MMC Life System Development (Phase I)—
A NASA/Pratt & Whitney Life Prediction
Cooperative Program

Erwin V. Zaretsky, editor

MMC Life System Development (Phase I)— A NASA/Pratt & Whitney Life Prediction Cooperative Program

Erwin V. Zaretsky, editor
Lewis Research Center
Cleveland, Ohio

Preface

Aircraft propulsion research has not come to a halt, despite the economic troubles facing the broader aerospace industry. Today, researchers are focusing their efforts on ambitious performance goals for turn-of-the-century military and civil aircraft propulsion systems, goals set by projects such as the High-Speed Civil Transport. One such program is coordinated by the National Aeronautics and Space Administration (NASA) and the Department of Defense (DOD). The Integrated High-Performance Turbine Engine Technology Initiative (IHPTET) seeks to double thrust-to-weight ratios to 20:1 by the year 2003.

Tomorrow's aircraft engines will undoubtedly run hotter and weigh less than their present-day counterparts and will depend on advanced materials to reach those ends. Metal-matrix composites (MMC's), typically consisting of a titanium alloy matrix and ceramic reinforcement, are generally held as leading candidates because they are light and they maintain their strength at higher operating temperatures. But before researchers can tap the potential offered by MMC's, they need to perfect suitable design and analysis methods. Recognizing this, NASA Lewis Research Center and Pratt & Whitney (P&W), a division of United Technologies, Inc., entered a four-year cooperative effort, hoping to lay the foundations of knowledge that will make these materials more reliable and ultimately less exotic. Each organization assumed its own costs for this MMC life prediction cooperative program.

So far, researchers believe that titanium-based MMC's can replace current metallic materials in fan blades, spacers, cases, shafts, and rods. However, new compressor rotor designs incorporating MMC rings within an integrally bladed rotor may provide the most significant improvements in weight and rotor speed over baseline nickel and titanium materials. Thus, P&W and Lewis researchers focused their attention on three rings made from a titanium-alloy MMC designated SiC(SCS–6)/Ti-15V-3Cr-3A1-3Sn. Chosen for its extensive data base, this material represents the MMC's that would be used in an aircraft engine but is not the specific grade. P&W and Lewis combined their data bases for this material. The resulting data base (see the appendix to this publication) contains cyclic and static strength and fatigue data at temperatures that include stress, strain, and creep relationships. Researchers chose a foil-fiber-foil process to make rings for testing.

Teams at both Lewis and P&W worked independently to avoid influencing each other's results. Robert deLaneuville, team leader at P&W, coordinated the engine manufacturer's contributions to the joint program. P&W developed a mechanistic, empirically supported life system that models the behavior of the MMC system; the Lewis team approach, coordinated by me, was more analytical than empirical. Both groups used their analytical codes to predict the burst load and fatigue life of rotating rings.

The four-year study, which began in 1988, had several objectives: assessing life and fracture prediction methods; determining the actual fracture strength and lives of the MMC rings; and evaluating nondestructive evaluation (NDE) methods for predicting the reliability of MMC materials.

The cooperative program generated five independent life analysis methods for predicting the life and fracture strength of the three 15.2-cm (6-in.) diameter rings made from the test MMC material. Each method seeks to accurately predict the structural integrity as well as the cyclic life of the component because aircraft engines go through a cycle each time they throttle up or down that causes stresses and temperatures to vary during flight.

Within the cooperative program a group comprising both P&W and Lewis researchers weighed how closely different NDE techniques described the MMC rings. The NDE team concluded that several NDE techniques can assist structural and design engineers in analyzing MMC's. For example, in addition to locating the

composite core before final machining, low-resolution computed tomography (CT) offers spatial density information that can be incorporated into finite element modeling for stress analysis and life prediction.

The details and results of this program are contained in the nine chapters and the appendix of this reference publication. We were successful in fracture testing the rings and predicting, with reasonable engineering certainty, the MMC ring strength. However, because of quality assurance problems during ring manufacture, we did not fatigue test the rings. The five independent life predictions ranged from 1000 to 15 000 stress cycles. This scatter in the life prediction results indicates a need to benchmark MMC life analysis with full-scale component life tests.

The NASA Lewis Advanced High-Temperature Engine Materials Technology Program (HiTEMP) under-wrote the Lewis effort. The results of this program have been shared with the aerospace industry through the HiTEMP annual meetings held in Cleveland, Ohio. As a result, other aircraft engine companies requested that the MMC Life Prediction Cooperative Program be continued with their added participation. On February 3 and 4, 1993, a meeting was held at NASA Lewis between ourselves, the engine companies, and the U.S. Air Force Wright Laboratory for the purpose of continuing this cooperative effort. This meeting resulted in a greatly expanded effort comprising Lewis and Wright Laboratory, representing U.S. Government participation, and five aircraft engine manufacturers (Allied Signal, Allison, General Electric, Pratt & Whitney, and Williams). The Ohio Aerospace Institute (OAI) is the program coordinator. The planned program duration is five years with the potential for an additional five years. Funding for the phase II program is from Wright Laboratory and Lewis with in-kind contributions from the participating engine companies.

Erwin V. Zaretsky, P.E.
Chief Engineer for Structures
NASA Lewis Research Center

MMC Life Prediction Program Phase I NASA Lewis/P&W team—front row: Tom Farmer, Joe Stephens, Erv Zaretsky, Chris Chamis, Bob DeLaneuville, Bob Rowe; second row: Brad Cowles, Steve Arnold, Hugh Grey, Jennifer Heine, Marv Hirshberg, Fred Holland, George Baaklini, John Fox, Phil Gravett, Bill Doehnert, Tom Little; third row: Gary Halford, Mike Castelli, Brad Lerch, Rick Tucker, Sue Cunningham, Ron Haake, Larry Pinson, Ron Cairo, John Gayda, Gil Gillespie, Rod Ellis.

Contents

Chapter 1
Overview of MMC Life System Development (Phase I)

Erwin V. Zaretsky* and Robert E. deLaneuville[†]

1.1 Symbols

A cross-sectional area, m^2 (in.^{2})

B intercept of elastic strainrange–life relations

C intercept of inelastic strainrange–life relations

C' intercept of inelastic line for combined creep-fatigue cycles

CTE   coefficient of thermal expansion

E modulus of elasticity, MPa (ksi)

e Weibull modulus

F inelastic strain fraction

K cyclic strain-hardening coefficient

L life, cycles

$L_{0.1}$ life at 99.9 percent probability of survival, cycles

MF   multiaxiality factor

N number of applied cycles

R ratio of algebraic minimum to maximum

r radius, m (in.)

S probability of survival

T temperature, °C (°F)

TF   triaxiality factor

V stressed volume, m^3 (in.^{3})

ε strain, m/m (in./in.)

σ normal stress, MPa (ksi)

τ shear stress, MPa (ksi)

Subscripts:

a,b stressed components

alt   alternating

cc creep strain in tension, creep strain in compression

cp creep strain in tension, plastic strain in compression

el   elastic

f failure with zero mean stress

fm failure with mean stress

―――――――――――――――――――――

i	microcrack initiation with zero mean stress
ij	pp, pc, cp, or cc
in	inelastic
L	load
max	maximum
p	microcrack propagation with zero mean stress
pc	plastic strain in tension, creep in compression
pp	plastic strain in tension, plastic strain in compression
t	total
u	ultimate (tensile strength)
y	yield (0.2 percent offset)
ε	strain
σ	stress

Superscripts:

b	power for elastic strainrange–life relations
C	stress-life exponent
c	power for inelastic strainrange–life relations
n	cyclic strain-hardening exponent ($\approx b/c$)

1.2 Introduction

Pratt & Whitney Aircraft (P&W) and the NASA Lewis Research Center entered into a nonbinding cooperative program to study a silicon-carbide-fiber-reinforced, titanium-metal-matrix composite (MMC) designated SCS–6/Ti-15-3 for silicon carbide/titanium–15 wt% vanadium–3 wt% chromium–3 wt% aluminum–3 wt% tin. This MMC was selected because the processing parameters were established, the alloy was available in full form, the mechanical properties were reproducible, and the material and related technology were proprietary to P&W, allowing for publication of the results at program completion. Each organization assumed its own costs as appropriate. The program was under the auspices of the NASA Advanced High-Temperature Engine Materials Technology Program (HiTEMP).

The objectives of the NASA/P&W program were to verify and improve analyses for predicting the life and performance of MMC structures, to develop a data base required to exercise currently existing codes, to verify existing code predictions with performance data to be generated by P&W, and to develop enabling technology sufficient to design, with reasonable engineering and scientific certainty, a dynamic structure made from silicon carbide/titanium MMC for 500 cycles (550-hr hot time).

The program, which began January 1, 1988, originally was planned to be a two-year effort with an option for extending the effort depending on performance requirements and program success. Because of delays in material procurement and delivery, the program was extended to four years.

The program was organized around the following technical activities: life prediction systems, nondestructive evaluation (NDE), test plans and procedures, and processing aspects. Each activity had a P&W and NASA Lewis lead person assigned to it. P&W had three MMC rings manufactured and then tested them. P&W paid for two rings and NASA Lewis paid for the third.

P&W developed a mechanistic, empirically supported life system that models the behavior of the candidate MMC system. NASA Lewis developed generic technology and used its analytic codes to predict burst loads on rotating rings. The data base developed by NASA Lewis included cyclic and static strength and fatigue data at temperatures that included stress, strain, and creep relationships. Test temperatures were limited to room temperature and 316 and 538 °C (600 and 1000 °F), with the understanding that use temperatures may reach 649 °C (1200 °F).

The thermomechanical processing history of the material was made available to the parties. Both NASA Lewis and P&W performed tensile, creep, and low-cycle fatigue (LCF) testing. The results of P&W testing were not disclosed until after the P&W and NASA analyses had been completed. At the completion of the analysis and testing, the results were exchanged and compared. Differences between analysis and experiment are being used to refine the modeling effort.

P&W compiled the MMC material data base for SCS–6/Ti-15-3. These data were used to predict the fracture strength and cyclic life of the three MMC rings during the cooperative program.

Assessing the quality of the MMC rings became a major part of the coordination of efforts at P&W and NASA Lewis. Both parties completed NDE inspection before and after each ring was tested. With this information they investigated the effect of detectable indications on the strength and cyclic life of the MMC rings. The work described herein assessed the life and fracture prediction methods developed by P&W and Lewis, determined the fracture strength and lives of three rings made from SCS–6/Ti-15-3 materials, and evaluated nondestructive evaluation (NDE) methods in predicting the reliability of MMC material.

1.3 Life Prediction Systems

Five life prediction systems were used and/or developed under this program, each independent of the other. The following is a summary of these systems.

1.3.1 Pratt & Whitney Life Analysis

The P&W life prediction system relies on the matrix material characterizing the fatigue behavior of the MMC (Gravett, 1993). This assumption has been supported by test data and failure mechanisms identified in isothermal and out-of-phase thermomechanical fatigue (TMF) specimens. These specimens typically show an area of matrix cracking before failure. The matrix cracking propagates through the MMC, leaving the fibers intact. Opening the crack faces causes the stress in the unbroken fibers to increase near the crack. As the crack propagates, the local fiber stresses increase, causing fiber failure and eventual composite failure.

An MMC anisotropic, coefficient-of-thermal-expansion (CTE), thick-cylinder model was used to characterize the state of stress in the matrix at the fiber/matrix interface during cyclic loading (fig. 1.1). Applying the Smith-Watson-Topper stress parameter

$$\sigma_{effective} = \sqrt{\sigma_{max} \frac{\Delta\varepsilon}{2} E}$$

to the fiber/matrix interface stress characterized the matrix behavior independent of laminate fiber volume, stress ratio, and load history. Low-cycle fatigue at 427 °C (800 °F) was analyzed along with previous LCF and TMF data and showed a similar collapse of applied stresses into a single band of data characterizing the matrix (fig. 1.2). Predicting test specimen life by using this model resulted in a mean actual/predicted life of 1.03 and an $L_{0.1}$ scatter factor[1] of 3.19.

Because the collapsed effective matrix stress is independent of fiber volume, stress ratio, and load history, this MMC life prediction system can be used to predict the fatigue behavior of any reasonable laminate and loading. This method was extended to predict the isothermal LCF life of Ti-15-3 matrix material. The monolithic material was modeled as a laminate with a fiber content of 0.0 vol%. Even though the monolithic material was not included in the model generation, the predictions are reasonably accurate but consistently lower than the test data. This result was expected because MMC's typically have microcracks in the fiber/matrix interaction zone that act as crack initiators, thus reducing the fatigue life of the composite from that of a "perfect" composite. This reduced life was apparent when the composite matrix properties were used to predict the life of the monolithic material, which had no microcracks (fig. 1.3). With this life prediction system life

analyses can be performed for laminate geometries and loadings at which no test data exist—a feature that will prove valuable when designing engine components where optimization of MMC capabilities is required but testing is limited.

The Smith-Watson-Topper stress parameter can be used similarly to predict the LCF life of various R-ratio data. Correlation to past data for 38-vol% fiber was reasonably accurate except for high stresses (fig. 1.4). The lack of correlation to the high-stress specimen was attributed to a fiber-dominated failure. R-ratio testing of a 34-vol%-fiber MMC has since complicated the analysis with a totally different fatigue response at high R-ratios. Variations in R-ratio had little effect on the LCF fatigue life of the composite, perhaps because high mean stress in the matrix at high R-ratios causes more damage than is modeled. Because the life system predicts a considerable effect of R-ratio on life, the prediction is not very conservative for high R-ratios (fig. 1.5). The results were similar for a simple mission specimen that had cycles with R-ratios of 0.1 and 0.5. The matrix stresses in the 34-vol%-fiber specimens were higher than those in the 38-vol%-fiber specimens; therefore, another fatigue stress parameter with a greater mean stress effect may be more appropriate for modeling the matrix response in an MMC.

1.3.2 NASA Life Analysis I

In the life prediction system called NASA Life Analysis I (Chamis et al., 1988), an analytical procedure is used to computationally simulate the cyclic behavior of high-temperature, metal-matrix composites (HTMMC's) and its degradation effects on the structural response. MMC mechanics are coupled with a multifactor-interaction constituent material relationship to perform an incremental iterative nonlinear analysis. The procedure is implemented in a stand-alone computer code that can be used to computationally simulate the thermomechanical behavior of HTMMC's from the fabrication process through thermomechanical cycling and that accounts for the interface/interphase region. This code, called METCAN (Metal-Matrix Composite Analyzer), performs the computational simulations from the constituent material level to the laminate level and encompasses all the capabilities shown within the dashed line in figure 1.6.

The various factors that influence constituent material behavior and ultimately MMC behavior are incorporated through a multifactor-interaction relationship (fig. 1.7). The important points to note in figure 1.7 are that the individual effects of the thermal and mechanical load cycles N_T and N_M are explicitly included; that the temperature T and the stress σ induced by these cycles are also explicitly included; that the combined thermomechanical cyclic effects on the thermomechanical behavior of MMC's are therefore automatically included; and that the various effects are normalized with respect to reference properties, which are usually taken as room-temperature properties.

---

[1]Scatter factor—factor by which mean life is divided to obtain a $L_{0.1}$ life.
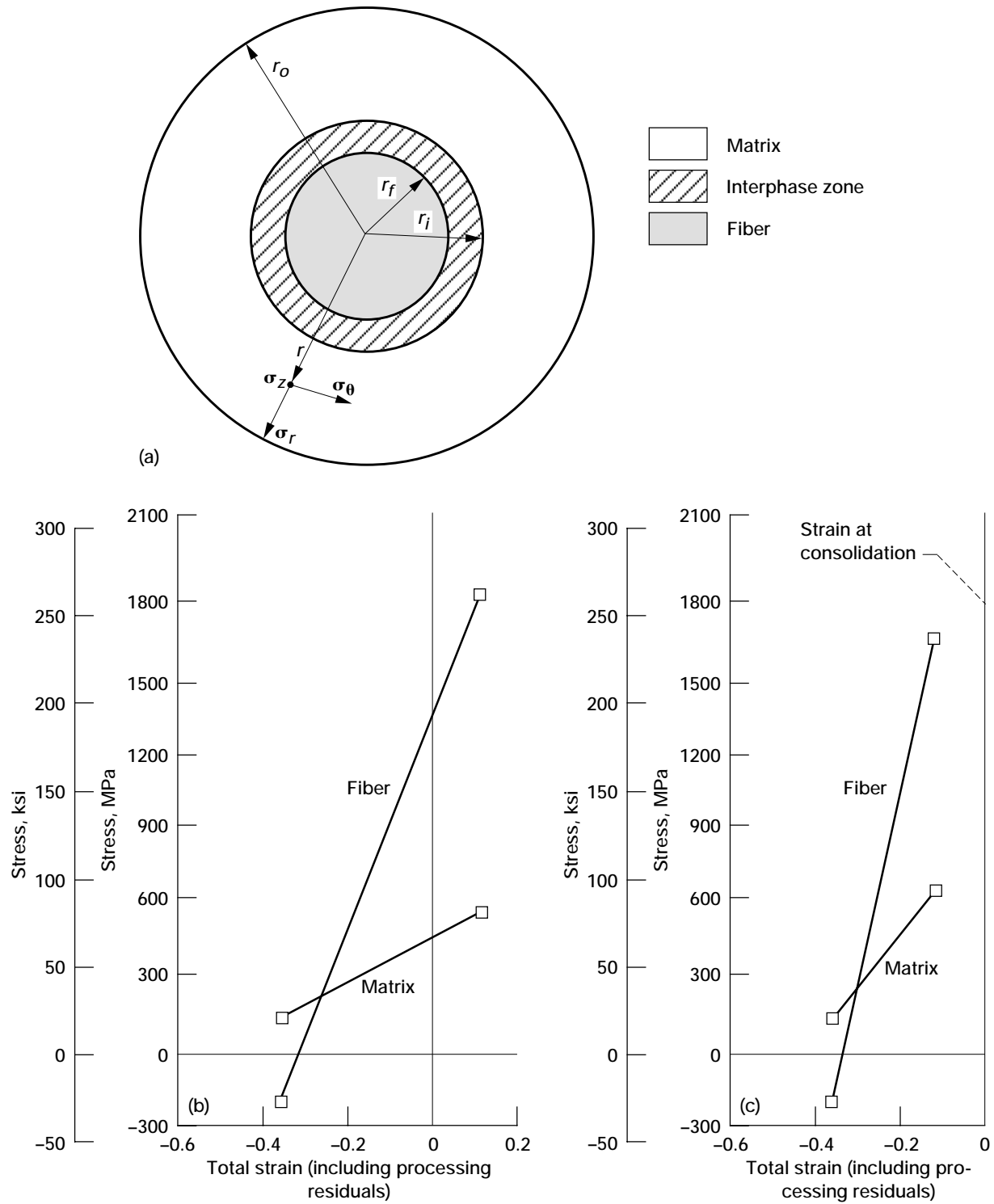
Figure 1.1.—Matrix-dominated fatigue failures. (a) MMC anisotropic, CTE, thick-cylinder model. (b) LCF loading. (c) Out-of-phase TMF loading.
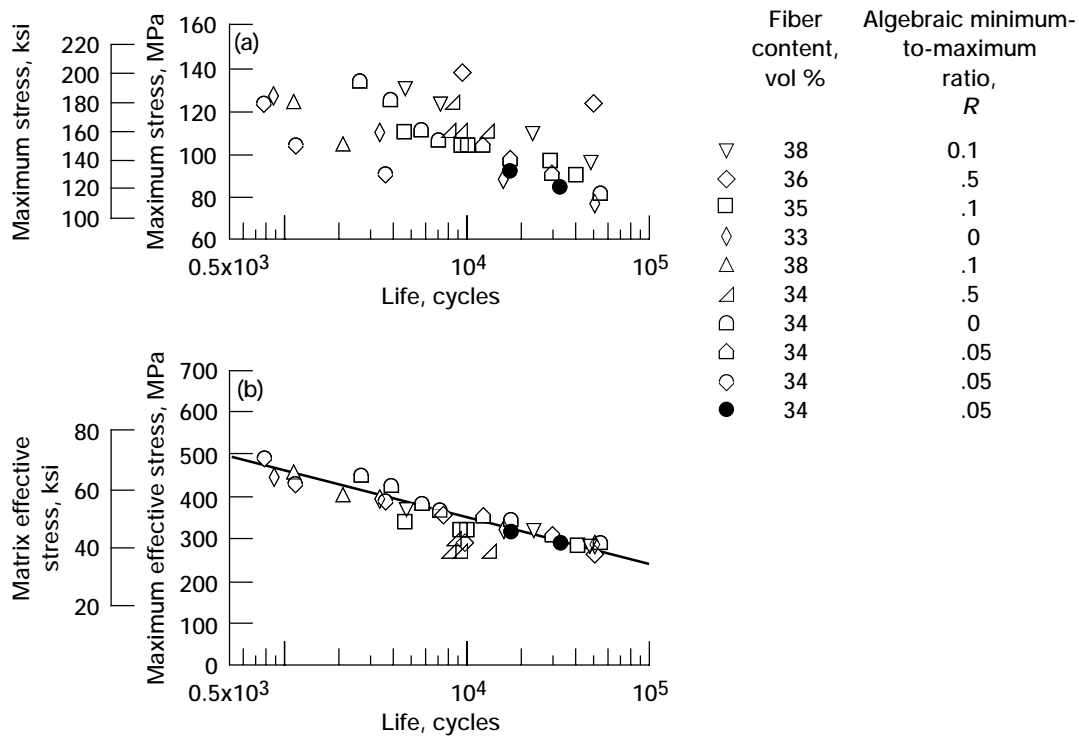
Figure 1.2.—Consolidation of SCS–6/Ti-15-3 longitudinal fatigue data by Smith-Watson-Topper parameter. (a) Maxmum laminate tension stress with variation in fiber content, *R*-ratio, and load history. (b) Stress matrix in fiber direction at interface; temperature, 427 °C (800 °F).
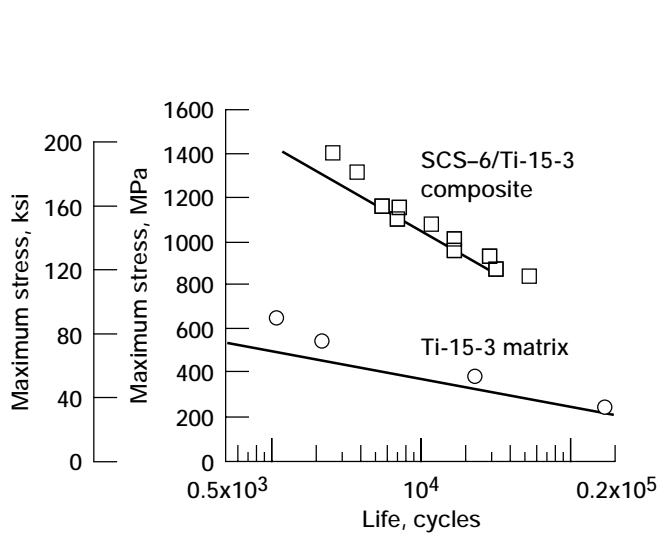
Figure 1.3.—Prediction of matrix and composite life by Smith-Watson-Topper parameter. SCS–6/Ti-15-3 composite versus Ti-15-3 matrix; composite fiber content, 34 vol %; temperature, 427 °C (800 °F).
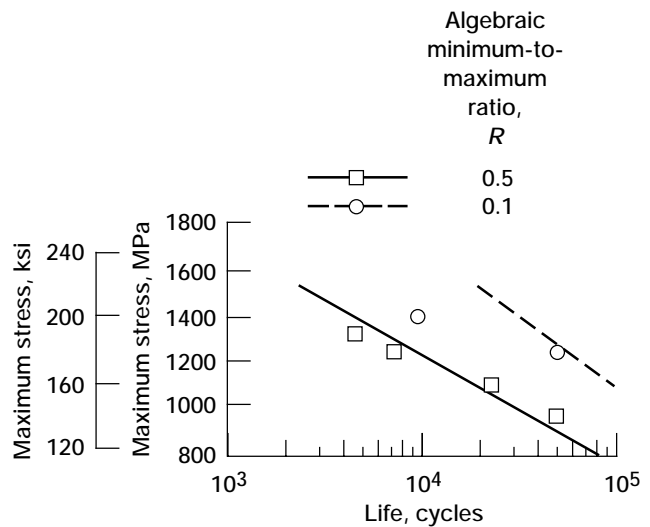
Figure 1.4.—Smith-Watson-Topper parameter correlation to variations in *R*-ratio at fiber content of 38 vol %. SCS–6/Ti-15-3 longitudinal fatigue data; correlation to *R*-ratio data; temperature, 427 °C (800 °F).
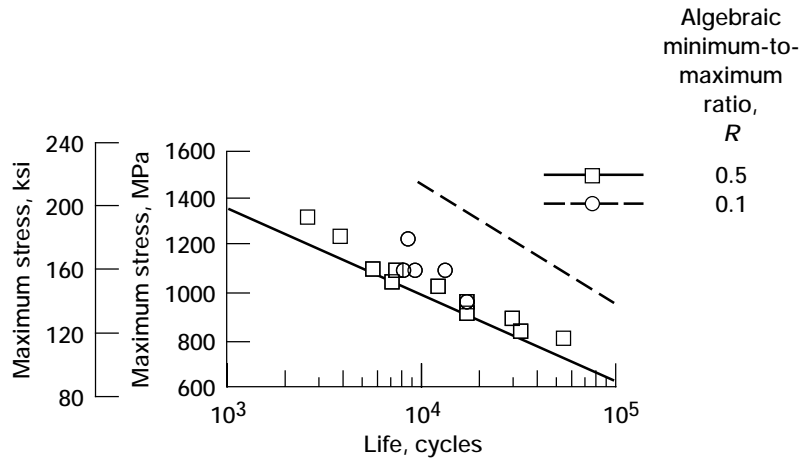
Figure 1.5.—Smith-Watson-Topper parameter correlation to variations in *R*-ratio at fiber content of 34 vol %. SCS–6/Ti-15-3 longitudinal fatigue data; correlation to *R*-ratio data; temperature, 427 °C (800 °F).
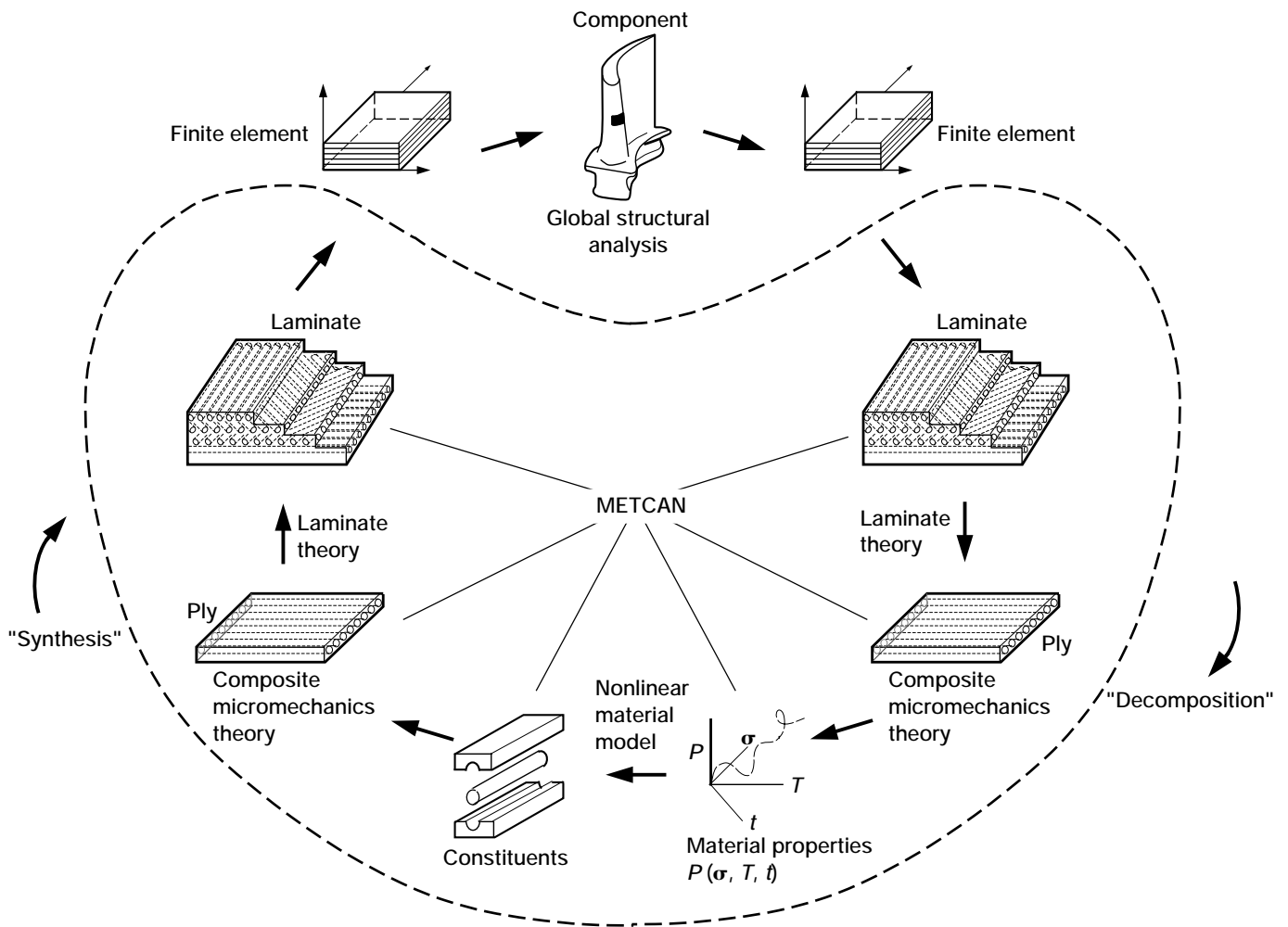
Figure 1.6.—Integrated multiscale computational simulation.

$$\frac{P}{P_0} = \left[\frac{T_F - T}{T_F - T_0}\right]^n \left[\frac{S_F - \sigma}{S_F - \sigma_0}\right]^m \left[\frac{\dot{S}_F - \dot{\sigma}_0}{\dot{S}_F - \dot{\sigma}}\right]^l \left[\frac{\dot{T}_F - \dot{T}}{\dot{T}_F - \dot{T}_0}\right]^k \left[\frac{\dot{R}_F - \dot{R}}{\dot{R}_F - \dot{R}_0}\right]^p \cdots$$

$$\left[\frac{N_{MF} - N_M}{N_{MF} - N_{M0}}\right]^q \left[\frac{N_{TF} - N_T}{N_{TF} - N_{T0}}\right]^r \left[\frac{t_F - t}{t_F - t_0}\right]^s \cdots$$
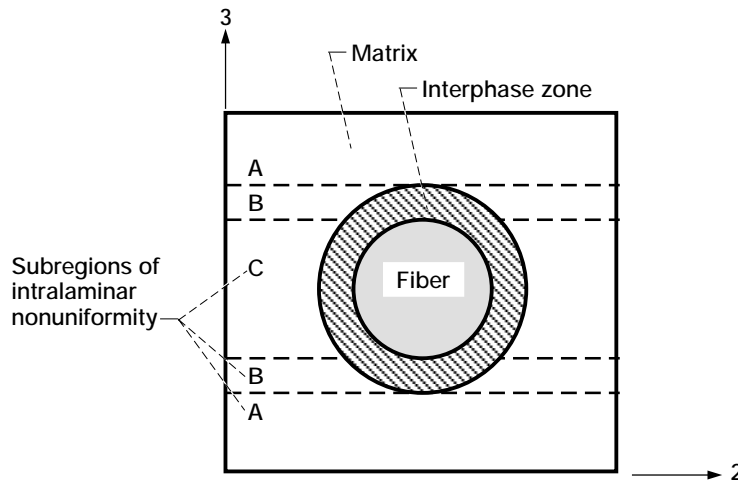
Rationale:

- Gradual effects during most of range, rapidly degrading near final stages
- Representative of in situ behavior for fiber, matrix, interphase zone, and coating
- Introduction of primitive variables
- Consistent in situ representation of all constituent properties in terms of primitive variables
- Room-temperature values for reference properties
- Continuous interphase growth
- Simultaneous interaction of all primitive variables
- Adaptability to new materials
- Amenability to verification inclusive of all properties
- Ready adaptability to incremental computational simulation

Notations:

P – property; T – temperature; S – strength; R – metallurgical reaction; N – number of cycles: t – time; overdot – rate; subscripts: 0 – reference; F – final; M – mechanical; T – thermal

Figure 1.7.—Multifactor-interaction relationship for in situ constituent material behavior.

METCAN performs the following steps to computationally simulate the mechanical cyclic behavior of the MMC. These steps and the required convergences are automatically performed and are transparent to the user.

(1) Calculates the microstresses from global thermal and structural analyses by using the respective cyclic loads as inputs to these global analyses. Performs global analyses by using finite-element analysis of the structural component (top part (outside the dashed line) of fig. 1.6).

(2) Enters the magnitude of these microstresses and the respective number of mechanical cycles in the multifactor relationship in figure 1.7.

(3) Applies the next cycle loads to the structure and/or laminate and simulates the desired behavior by using the incremental-iterative procedure mentioned previously.

1.3.3 NASA Life Analysis II

In the life prediction system called NASA Life Analysis II (Arnold and Witt, 1993), a load deflection curve for the MMC ring is calculated for the fracture analysis by using a three-dimensional, finite-element model consisting of the matrix cladding and the composite core. (The ideal cross section of MMC ring is shown in figure 1.8.) This analysis obtains a limit load. The matrix cladding is assumed to be isotropic and

16.774 (6.604)
16.764 (6.600) diam

A   A

13.721 (5.402)
13.716 (5.400) diam

0.140 (0.055)
(all-around monolithic)
0.114 (0.045) (Ti-15-3-3-3)

1.549 (0.610)
1.524 (0.600)
diam

30- to 35-vol%
SCS–6 SiC fiber
in Ti-15-3-3-3

Section A–A
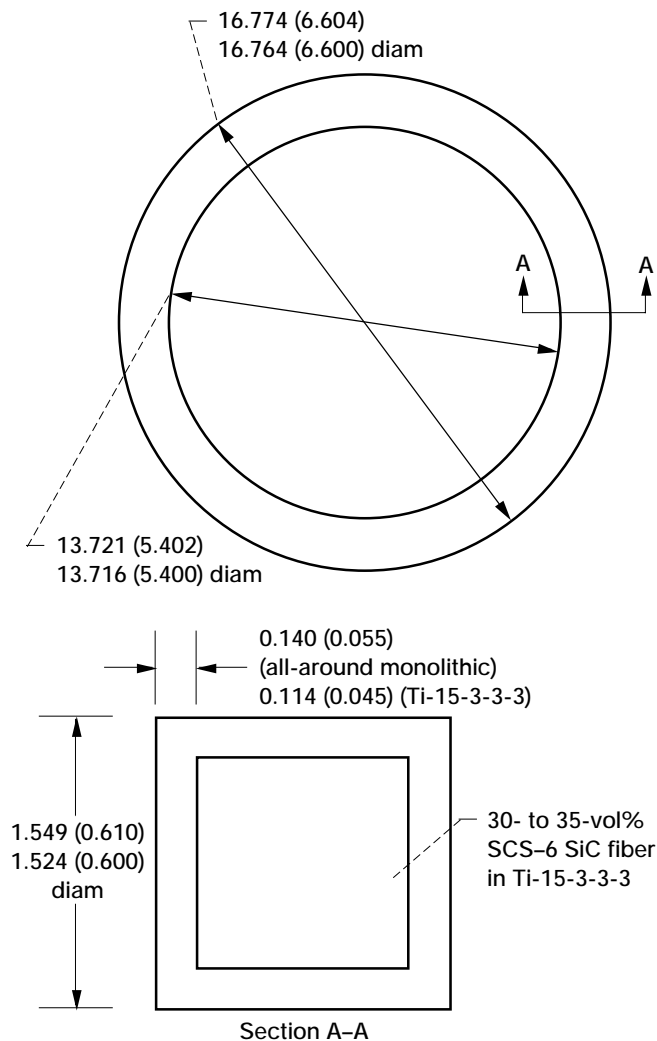
Figure 1.8.—SCS–6/Ti-15-3 ring dimensions. (Dimensions are in centimeters (inches).)

elastic–perfectly plastic. The composite core is idealized as a pseudohomogeneous, transversely isotropic material; the material response is described by an anisotropic, elastic–perfectly plastic (and in another case a bilinear hardening) constitutive model. Residual macrostresses are accounted for by considering the cooldown cycle and the CTE mismatch between the matrix cladding and the composite core. Residual microstresses are accounted for in the coefficients of the constitutive model. Also, when the core behaves as a bilinear hardening material, a strain failure criterion is imposed when the limit load is calculated.

The fatigue life is calculated by performing a coupled deformation and damage analysis. The deformation analysis is the same as described above, wherein the composite core is assumed to behave elastically–perfectly plastically.

The damage analysis is conducted by employing a transversely isotropic continuum-damage-mechanics, stress-based

model and the concept of effective stress. The procedure is as follows:

(1) Conduct a three-dimensional, elastic–perfectly plastic, finite-element analysis and obtain the stress-strain history for the MMC ring.
(2) Using the above stress history for the present cycle and the initial damage measurement, calculate the amount of additional material degradation for the next N cycles.
(3) With this new damage measurement degrade the associated elastic moduli.
(4) Repeat steps 1, 2, and 3 until failure occurs.

Several deformation and damage analyses, each with added levels of complexity, are conducted:

(1) A decoupled analysis, in that no stress redistribution is taken into account, is performed. The output will be a graph of the ratio of internal pressure to limit pressure versus N_f for various radial locations in the ring.
(2) For a given ratio of internal pressure to limit pressure, a detailed coupled deformation and damage analysis is conducted, accounting for stress redistribution in the manner described above. Also the analysis is conducted
    (a) With and without residual stress effects
    (b) With and without accounting for damage in the cladding
    (c) With and without the cusp

1.3.4 NASA Life Analysis III

In the life prediction system called NASA Life Analyses III (Halford et al., 1989), the fatigue life of an MMC is assessed through consideration of the matrix's fatigue properties and how these properties are affected by the matrix material being an integral part of a small, but more complex, structural element (i.e., an MMC). The very presence of fibers, interfacial layers, foreign substances used to aid in fabrication, manufacturing defects and voids, free surfaces with exposed fibers, sharp external edges, ply interfaces, residual stress, localized multiaxial stress-strain states, etc., will exert quantifiable influences on the matrix material's response. The mathematical formulation of all individual influences is, as yet, incomplete (Halford et al., 1989).

This approach to MMC fatigue life prediction was adopted by Halford et al. (1989) because only the metallic matrix material is prone to the phenomenon of cycle-dependent fatigue crack initiation and growth. Brittle ceramic fibers and interfacial material, per se, do not undergo cycle-dependent fatigue cracking (at least within the temperature regime of interest). Further, the properties of the interfacial layer are largely unknown and virtually unmeasurable, leaving only the matrix as the vehicle for tracking fatigue damage in an MMC. This approach *does not necessarily imply* that MMC fatigue failures will be matrix dominated.

The fatigue resistance of the matrix material is characterized in terms of total mechanical strainrange (based on effective or von Mises strain) versus cycles to complete separation of axially loaded coupon specimens (fig. 1.9). Complete coupon separation is called macrocrack initiation, a culmination of the sequence of microcrack initial and microcrack propagation states of fatigue as outlined below (Halford et al., 1989):

$$N_f = N_i + N_p$$

LCF: $$N_i \sim 0.1 N_f$$

$$N_p \sim 0.9 N_f$$

HCF: $$N_i \sim 0.9 N_f$$

$$N_p \sim 0.1 N_f$$

Initiation: $$\Delta\varepsilon \approx 0.99 B N_i^{-b} + 0.25 C N_i^{-c}$$

Propagation: $$\Delta\varepsilon \approx 0.79 B N_p^{-b} + 0.94 C N_p^{-c}$$

where

$$\Delta\varepsilon = \Delta\varepsilon_{el} + \Delta\varepsilon_{in}$$

$$\Delta\varepsilon = B N_f^b + C N_f^c$$

The breakout of stages is advantageous because different factors influencing fatigue affect these two different stages in different ways. Typically, the baseline matrix fatigue data would be isothermal and free of mean stresses ($V_\sigma = \sigma_{mean}/\sigma_{alt} = 0$). The specimen surface would be smooth and free of stress-concentrating defects. Under these circumstances the lower cyclic life regime would be dominated by the plastic strainrange, and the macrocrack initiation life would be dominated by microcrack propagation. Correspondingly, after a transition regime the higher cycle life regime would be dominated by the elastic strainrange, and microcrack initiation would overshadow microcrack propagation. A schematic baseline strainrange-versus-fatigue-life curve is shown in figure 1.9.

The isothermal MMC fatigue model deals with each specific detail listed above that is quantitatively known to influence matrix fatigue. For an isothermally loaded ring, Halford
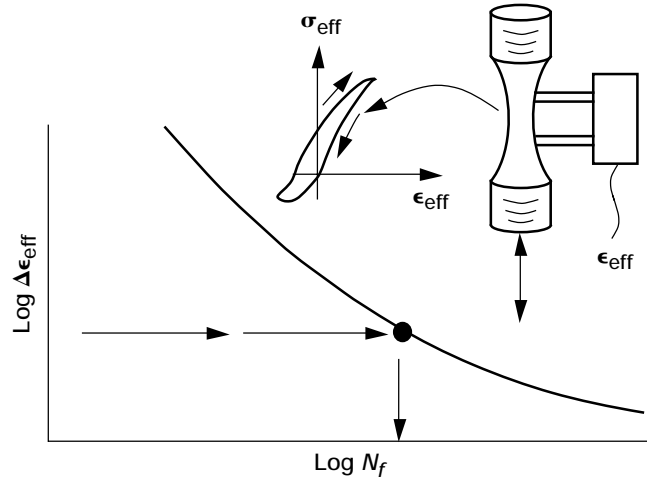
Figure 1.9.—Total strainrange versus macrocrack initiation life for matrix.

(1993) calibrated most quantifiable influences on fatigue by using MMC coupon fatigue data that essentially mimic the major features of the structurally loaded component. Thus, the MMC data take the place of an analytically calculated MMC fatigue response. The current MMC zero-to-maximum-load-controlled ($V_{load} = \text{Load}_{mean}/\text{Load}_{alt} = 1.0$) fatigue results can be derived from the completely reversed ($V_\varepsilon = V_\sigma = 0$), strain-controlled matrix fatigue results by applying a single calibration factor that is interpretable as an internal strain concentration factor.

The Halford et al. (1989) model did not specifically address statistical or probabilistic considerations owing to the complete lack of calibrating data at the time. Little has changed in this regard during the intervening years with the possible exception of the highly limited MMC data generated at several laboratories. Nevertheless, the existing data were analyzed as though they were from a single population. The analysis was taken one step further from a rigorous approach by assuming that the variation in fatigue results was independent of the life or the strainrange level. Consequently, the single parameter chosen to represent the variation in fatigue data was the ratio of the measured strainrange as read from the fatigue curve at the experimentally measured life.

1.3.5 NASA Life Analysis IV

Zaretsky (1987) developed an expression for predicting life at a given survivability of a stressed component b relative to the known life of a stressed component a:

$$L_b = L_a \left(\frac{\tau_a}{\tau_b} \right)^C \left(\frac{V_a}{V_b} \right)^{1/e} \qquad (1.1)$$

This equation gives the component's life relative to that of another similar component when both have the same survivability. The system life can then be calculated from the individual component lives as follows:

$$\left(\frac{1}{L_s}\right)^e = \sum_{i=1}^{n}\left(\frac{1}{L_i}\right)^e \qquad (1.2)$$

where L_s is the total system life and L_i is the ith component life. Zaretsky's method can be extended further to examine relative component survivability at equal life. This is given by

$$S_b = S_a^{\left(L_b/L_a\right)^e} \qquad (1.3)$$

Finally, the component's survivability is equal to the product of all the elements' survivabilities:

$$S_s = \prod_{j=1}^{n} S_i \qquad (1.4)$$

The methodology can easily be incorporated into the finite-element method to determine the life and survivability of a structural component. The entire component is analogous to a system. The finite-element model of the component discretizes its geometry into element volumes. These elements are considered to be the base members of the "system." The time to crack initiation for each element is calculated from the element stress levels and volumes as described previously to determine the component's incipient failure time.

A relative comparison approach is used in this methodology. A critical element in the model is selected on the basis of a maximum stress state. The selected stress failure criterion can be based on the material used in the component. If no fatigue data are available, the stressed element can be arbitrarily assigned a life and a survivability that are used to normalize the life and survivability of the other elements. This approach allows easy, qualitative comparisons between designs. Also, only one set of coupon fatigue tests at operating temperatures is necessary to fix the Weibull parameters and to establish quantitative component lives if the stress-life exponent of the material is already known. However, if the stress-life exponent is not known, at least two additional sets of coupon fatigue tests will be necessary.

The MMC material was considered for purposes of analysis as if it were a monolithic material having an effective or characteristic modulus of elasticity and Poisson's ratio. These values were experimentally determined. However, in this method, volume-based element survivability may be influenced by the finite-element mesh size (Holland et al., 1993).

The method for determining the fracture strength of the MMC ring is similar to that used to predict the life. By using a finite-element analysis based on an assumed ring pressure at the ring inner diameter, the probability of failure at each finite-element mesh is determined from previously obtained coupon data and stressed volume (Holland et al., 1993).

1.4 Results and Discussion

1.4.1 Ring Tests

Testing of ring 1 consisted of a room-temperature strain gage survey and a 427 °C (800 °F) static test to failure. The results of the strain gage survey show that the ring response remained linear to 1130 N-m (10 000 in.-lb) per actuator and correlated well with the analytical predictions. The strain variation between the top and bottom surfaces was very small. The test to failure verified that stiffness predictions are accurate and that MMC components can exhibit a nonlinear behavior before ultimate failure. The deflection response of the ring correlated with the predicted behavior with only slight variations in deflection from the predicted response up to failure. The internal ring pressure at failure for ring 1 was 190 MPa (27.5 ksi).

Ring 2 exhibited a slightly different behavior during the strain gage survey. Unexpectedly, this ring showed a 16 percent lower stiffness than predicted and a small amount of nonlinear deformation at loads well below 1130 N-m (10 000 in.-lb). At 427 °C (800 °F) the plasticity was identifiable but occurred at a much lower load than for ring 1. The internal pressure to failure of ring 2 was 155 MPa (22.5 ksi), or approximately 82 percent that of ring 1. Post-test inspection of ring 2 revealed extensive damage to the MMC core due to processing, which may explain the lower internal pressure at failure for this ring.

Testing of ring 3 consisted of a room-temperature test to failure. Because the failure test was conducted at room temperature, strain gage information was recorded up to ring failure load. This ring exhibited very little nonlinear behavior until just before failure. The deflection response was linear. Near failure, however, measured strain began to increase rapidly, possibly caused by the onset of fiber failure across the MMC core. The internal pressure to failure of ring 3 was 241 MPa (34.9 ksi) at room temperature. The internal pressure to failure for the three rings tested is summarized in table 1.1.

Comparing the stiffness of the three rings revealed that rings 1 and 2, both of which were tested at 427 °C (800 °F), has similar stiffness. Ring 3 showed slightly higher stiffness, a significantly higher yield point, and a significantly higher failure load than rings 1 and 2. This behavior was expected because coupon test specimens of Ti-15-3 are stronger at room temperature than at 427 °C (800 °F). The scatter and differences exhibited by the three rings were similar to those of the coupon specimens tested by Pratt & Whitney.

TABLE 1.1.—PREDICTED LIFE AND INTERNAL PRESSURE TO FAILURE OF

TABLE 1.1.—PREDICTED LIFE AND INTERNAL PRESSURE TO FAILURE OF
SCS–6/Ti-15-3 RING

[Nominal ring diameter, 15 cm (6 in.); temperature, 427 °C (800 °F).]

Reference	Internal pressure to failure				Predictred life at 83-MPa (12-ksi) internal pressure, cycles
	Predicted		Experimental		
	MPa	ksi	MPa	ksi	
Arnold and Witt (1993)	207–221	30–32	155, 190 (235 at room tem-perature)[a]	22.5, 27.5 (34.1 at room temperature)[a]	1 500
Gravett (1993)	228	33.1			15 000
Chamis et al. (1993)	218	31.6			12 500
Holland et al. (1993)	140	20.3			4 750
Halford (1993)	276	40.1			1 600

[a]From Gravett and deLaneuville (1993).

1.4.2 Fracture and Life Predictions

The program was based on the premise that cyclic tests would be performed on two of the three rings at 427 °C (800 °F). Because of lower strength and manufacturing defects inherent in the rings, no fatigue or endurance tests were conducted. However, using each of the life prediction systems previously described, life predictions were made at a cyclic internal ring pressure of 83 MPa (12 ksi). The initial results of the analysis are summarized in table 1.1. The references describing the analysis in more detail and refinement are cited in the table. Although there were inherent differences in the approaches of the various investigators, there are some similarities in the predicted results. Arnold and Witt (1993) and Halford (1993) predicted lives of 1500 and 1600 cycles, respectively, but Holland et al. (1993) predicted 4200 cycles. Gravett (1993) and Chamis et al. (1993) predicted lives of 15 000 and 12 500 cycles, respectively. However, the spread of approximately 10 to 1 among the predictions needs to be resolved. The ring fracture predictions had less scatter in the results than was obtained with the life predictions, approximately 2 to 1 among the various investigators. The average internal pressure at ring fracture was 172 MPa (25 ksi). The preliminary values reported by Arnold and Witt (1993), Gravett (1993), and Chamis et al. (1993) were 214, 228, and 218 MPa (31, 33.1, and 31.6 ksi), respectively. Halford (1993) reported 276 MPa (40.1 ksi) and Holland et al. (1993), 140 MPa (20.3 ksi). The ring fracture data were not sufficient to draw any reasonable conclusion regarding the approaches to MMC strength prediction by any of the investigators. Hence, further component data and comparisons are required to establish design methodology for life and reliability when using these MMC materials.

1.4.3 Nondestructive Evaluation

NDE efforts by Baaklini et al. (1993) were directed toward identifying the capabilities and limitations of x-ray computed tomography (CT), radiography, acousto-ultrasonics, and pulse-echo ultrasonics in characterizing the subscale rings. CT, radiography, and pulse-echo ultrasonics were used to characterize a small sample of a subscale ring and to detect damage in tensile specimens due to failure or due to straining and then unloading right before failure. Acousto-ultrasonics was used to characterize specimens flexurally cycled up to 14 000 cycles and was found to be sensitive to degradation due to flexural cycling.

Radiography and pulse-echo ultrasonic data showed the ability to detect density/porosity variations, flaws, and cracks. Although radiography is more suited for fiber architecture and misalignment detection than ultrasonics, the latter is more suited for the detection of delamination and disbonding.

The use of low-resolution CT at 250- to 350-μm resolution demonstrated the capability of providing quantitative three-dimensional density information. CT cross-sectional density information differentiated between the monolithic skin of "alloy C" and the composite core. Density variations within the composite core were imaged. These variations may be due to poor consolidation, fiber bunching, or poor bonding.

High-resolution CT (10- to 50-μm resolution) provided microstructural information on the composite system. Delaminations, clusters of pores, and clusters of cracks in the 40-μm $(1.6 \times 10^{-3}$-in.) range can be detected. The high-resolution CT technology can be used to handle large MMC engine components with complex shapes.

Low-resolution CT scans were performed on the three MMC rings. Approximately 36 CT sections were provided for each
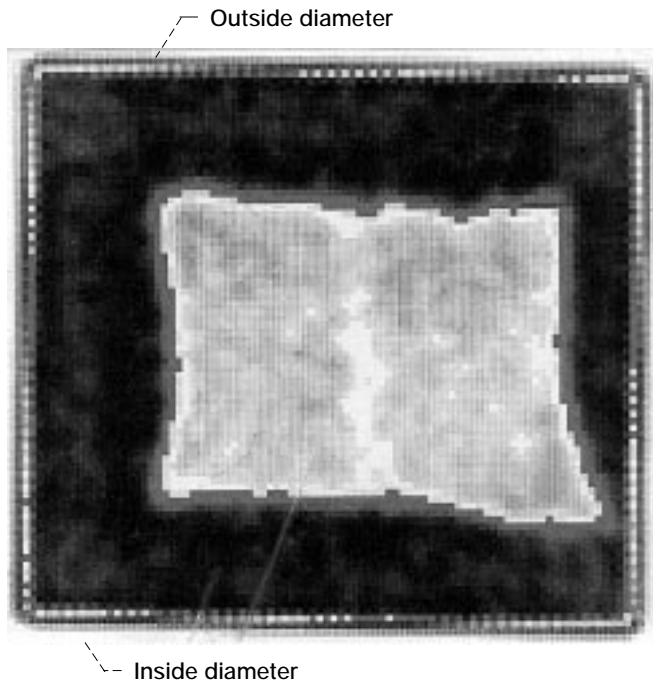
Figure 1.10.—CT scan of cross section of unmachined SCS–6/Ti-15-3 MMC ring at 0° reference.

Figure 1.11.—Geometry of NAS–1 MMC ring modeled at P&W (average of 35 CT scans). (Dimensions are in centimeters (inches).)

ring. A representative cross section is shown in figure 1.10. A high-resolution CT system was not used because of part size limitations (less than 10-cm (4-in.) diameter), x-ray source penetration capability (2.5 cm (1 in.) of SiC/Ti-15-3), and long scan time.

The CT scans revealed that the fabrication of the rings was less than ideal. The MMC core was not uniformly distributed inside the monolithic casing. Additionally, during consolidation the MMC core formed a cusp inside the casing. As a result of these scans P&W performed the final ring machining by not exposing the MMC, resulting in a nonuniform cross section (fig. 1.11). This cross section represents the ring geometry analytically modeled by P&W and NASA Lewis.

Density variations for the three rings did not vary significantly from theoretical values. Rings 2 and 3 were similar in density except that the density variation within ring 3 was greater than that within ring 2. Ring 1 was slightly less dense than rings 2 and 3 and had a more uniform core. The worst density nonuniformity occurred in rings 2 and 3 toward the outer diameter. Cusp-height data indicated that similar distortions took place in all three rings.

Radiography and pulse-echo ultrasonics are viable two-dimensional techniques for fast and complementary evaluation of subscale rings. Acousto-ultrasonics is useful for comparative analysis with a standard ring or for intermittent evaluation during the operational life of the ring. CT can help in locating the composite core before final machining takes place, preventing machining through the fiber layers and pre-

cisely describing the three-dimensional shape of the composite core throughout the ring. Further, spatial density variations similar to the ones detected in the previous CT slice may have a significant effect on matrix-dominated properties. Identifying the precise three-dimensional geometry of the monolithic skin and of the composite core, in addition to the three-dimensional density maps, can aid in building more realistic finite-element models for stress analysis and life prediction of the MMC engine component (Baalkini et al., 1993).

1.5 Summary of Results

Pratt & Whitney Aircraft and the NASA Lewis Research Center studied a silicon-carbide-fiber-reinforced, titanium-metal-matrix composite (MMC) designated SC5–6/Ti-15-3, for silicon carbide/titanium–15 wt% vanadium–3 wt% chromium–3 wt% aluminum–3 wt% tin, as a model material for use in aircraft engines. Five separate and distinct analyses were performed to predict the life and fracture strength of a nominal 15-cm (6-in.) diameter ring made from this MMC material. Nondestructive evaluation methods were evaluated in an attempt to predict the reliability of MMC materials. Fracture tests were performed with two MMC rings at 427 °C

(800 °F) and a third at room temperature. The following results were obtained:

(1) At 427 °C (800 °F) the internal pressures to failure for rings 1 and 2 were 190 and 155 MPa (27.5 and 22.5 ksi), respectively. The average pressure was 172 MPa (25 ksi). At room temperature ring 3 failed at an internal pressure of 241 MPa (34.9 ksi). The ratio of failure pressures between room temperature and 427 °C (800 °F) was similar to the ratio of fracture strengths with coupon specimens at the same respective temperatures.

(2) The five analytical predictions of the internal pressure to failure at 427 °C (800 °F) varied from 140 to 276 MPa (20.3 to 40.1 ksi), or a scatter of 2 to 1. Three predictions were between 214 and 228 MPa (31 and 33.1 ksi).

(3) Nondestructive evaluation using x-ray computed tomography revealed that the fabrication of the rings was less than ideal. The MMC core had varying density and was not uniformly distributed inside the monolithic casing.

(4) The five analytical predictions of ring cyclic life at 83-MPa (12-ksi) internal pressure varied from 1500 to 15 000 cycles, or a spread of 10 to 1. No ring life data were obtained for comparison because of manufacturing flaws in the rings.

References

Arnold, S.M., and Witt, T.E., 1993, "A Deformation and Life Prediction of a Circumferentially Reinforced SiC/Ti-15-3 Ring," *Reliability, Stress Analysis, and Failure Prevention*, R.J. Schaller, ed., DE–Vol. 55, American Society of Mechanical Engineers, New York, pp. 231–238.

Baaklini, G.Y., Percival, L., Yancey, R.N., and Kautz, H.E., 1993, "NDE of Titanium Alloy MMC Rings for Gas Turbine Engines," *Reliability, Stress Analysis, and Failure Prevention*, R.J. Schaller, ed., DE–Vol. 55, American Society of Mechanical Engineers, New York, pp. 239–250.

Chamis, C.C., Murthy, P.L.N., and Hopkins, D.A., 1988, "Computational Simulation of High Temperature Metal Matrix Composites Cyclic Behavior," NASA TM–102115.

Chamis, C.C., Murthy, P.L.N., and Singhal, S.N., 1993, "Computational Simulation of Hot Composite Structures," *Reliability, Stress Analysis, and Failure Prevention*, R.J. Schaller, ed., DE–Vol. 55, American Society of Mechanical Engineers, New York, pp. 317–330.

Gravett, P.W., 1993, "A Life Prediction Method for Matrix Dominated Fatigue Failures of SCS–6/Ti-15-3 MMC," *Reliability, Stress Analysis, and Failure Prevention*, R.J. Schaller, ed., DE–Vol. 55, American Society of Mechanical Engineers, New York, pp. 223–230.

Gravett, P.W., and deLaneuville, R.E., 1993, "Analysis and Results of an SCS–6/Ti-15-3 MMC Reinforced Ring Structure Under Internal Radial Loading," *Reliability, Stress Analysis, and Failure Prevention*, R.J. Schaller, ed., DE–Vol. 55, American Society of Mechanical Engineers, New York, pp. 191–212.

Halford, G.R., Lerch, B.A., Saltsman, J.F., Arya, V.K., and Caruso, J.J., 1989, "Low-Cycle Fatigue Prediction for Metal Matrix Composites," *HiTEMP Review 1989: Advanced High-Temperature Engine Materials Technology Program*, NASA CP–10039, pp. 64–1 to 64–9.

Halford, G.R., 1993, "MMC Ring Fatigue and Fracture Life Prediction," *Reliability, Stress Analysis, and Failure Prevention*, R.J. Schaller, ed., DE–Vol. 55, American Society of Mechanical Engineers, New York, pp. 307–316.

Holland, F.A., Zaretsky, E.V., and Melis, M.E., 1993, "Probabilistic Failure Prediction of SCS–6/Ti-15-3 MMC Ring," *Reliability, Stress Analysis, and Failure Prevention*, R.J. Schaller, ed., DE–Vol. 55, American Society of Mechanical Engineers, New York, pp. 297–306.

Zaretsky, E.V., 1987, "Fatigue Criterion to System Design, Life, and Reliability," *Journal of Propulsion and Power*, Vol. 3, No. 3, pp. 76–83.

Chapter 2

Analysis and Results of SCS–6/Ti-15-3 MMC Reinforced Ring Structure Under Internal Radial Loading

Phillip W. Gravett* and Robert E. DeLaneuville*

2.1 Introduction

For advanced turbine engine designs such as shown in figure 2.1 to realize the potential benefits offered by metal-matrix composites (MMC's), design and analysis methods must be developed and demonstrated. An example of an MMC application in such an engine is shown in figure 2.2. In this application the MMC ring is used to reinforce the bladed rotor.

In 1987 the NASA Lewis Research Center and Pratt &Whitney recognized this need and defined a cooperative effort to address it. Because design system and fabrication development efforts were occurring elsewhere, the team decided to focus on developing analysis methods that would be experimentally verified by testing MMC ring articles representative of advanced design requirements. MMC analysis methods for damage and fatigue prediction have been investigated at Pratt & Whitney and NASA Lewis. Efforts at NASA Lewis include a differential continuum damage mechanics model (Robinson and Pastor, 1992), a strain-based fatigue approach (Halford et al., 1989), a statistically based element survivability model (Zaretsky, 1987), and a procedure consisting of MMC mechanics coupled with a multifactor-interactions constituent material relationship in an incremental iterative nonlinear analysis (Chamis et al., 1988). In this chapter Pratt & Whitney's analysis and modeling procedures are presented, and the predicted behavior is compared with the actual structural response.

*United Technologies—Pratt&Whitney Government Engines and Space Propulsion, West Palm Beach, Florida 33410.

2.2 Program Definition

A four-year cooperative effort was defined in which analysis methods would be developed and then verified and improved by testing flat-panel coupon specimens and subscale subcomponent rings. The selected materials system was silicon carbide/Ti-15V-3Cr-3Al-3Sn, designated SCS–6/Ti-15-3. Although titanium–15 wt% vanadium–3 wt% chromium–3 wt% aluminum–3 wt% tin (Ti-15V-3Cr-3Sn-3Al) is not of primary interest for gas turbine engine applications because of its temperature capability, oxidation resistance, and burn resistance limitations, it was selected as the matrix system for this program because its processing parameters were established, the reproducibility of its mechanical properties had been demonstrated, and it was available and in the form required for panel and ring processing.

Two common methods for testing rings are (1) spinning the ring in a spin rig fixture and allowing the centrifugal forces to induce hoop stress or (2) applying a uniform pressure to the ring inside diameter surface, inducing radial compressive and tensile hoop stresses. The latter method was chosen for its known applied loads, the availability of the test rig, and the cost effectiveness of the test.

To assess the accuracy of the analysis method, the state of stress within the MMC ring must be accurately determined. Two major factors complicating this analysis are the stress maldistributions caused by the load fixture and the thermal expansion mismatch between the MMC core and the monolithic sheath. To accurately determine stress maldistributions in the MMC core, the ring and load fixture were modeled as a three-dimensional, solid, finite-element model. A two-dimensional, axisymmetric, finite-element model was used to
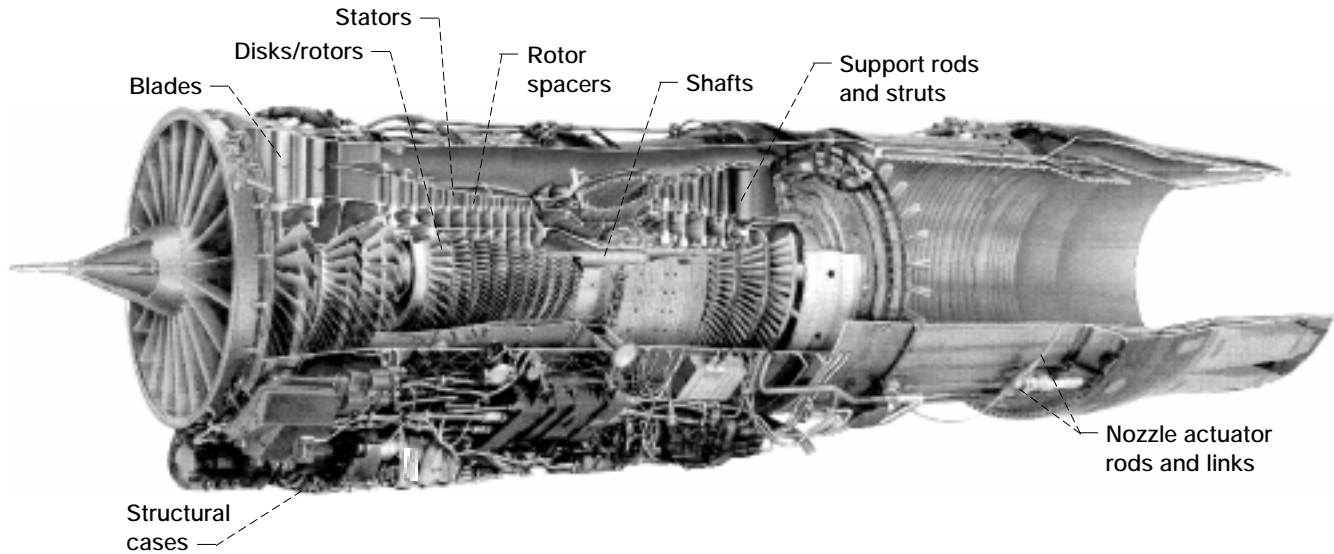
Figure 2.1.—Applications of titanium-matrix composites.

determine the thermal stresses induced from processing at high temperature and to determine the plasticity in the monolithic cladding and matrix core materials.

2.3 Ring Fabrication

In the MMC ring fabrication approach selected in this program, a foil-fiber-foil process, a helical fiber preform was inserted into a slot in a Ti-15-3 pancake disk. The slot was capped with a punch, and the assembly was pressed and then hot isostatically pressed to consolidate the MMC ring (fig. 2.3), resulting in a fiber content of 33 vol % for the MMC core. After consolidation the assembly was machined to rough dimensions and inspected by using computed tomography (CT) to locate and describe the geometry of the MMC core encapsulated in the monolithic Ti-15-3 cladding (fig. 2.4(a)). Machining to final dimensions was directed by the results of the CT inspection. The rings were then heat treated at a temperature below the consolidation temperature to stabilize the matrix material microstructure (Lerch et al., 1990) and to relieve thermal residual stresses due to processing. This heat treatment has been shown to eliminate the residual stresses produced during fabrication (Gayda et al.,1989), leaving the composite with a zero reference residual stress state at the heat treatment temperature. This fabrication process was selected because Textron Specialty Materials, the selected fabricator for this program and supplier of the SCS–6 fiber, had previously demonstrated the capability to consistently fabricate MMC rings by this technique.

The three rings fabricated as part of this program were subsequently nondestructively evaluated (NDE) by CT (Baaklini et al., 1991), ultrasonic transmission (UT), and x-ray radiography. CT inspection indicated that the ring cross section, designed to be rectangular, was irregular in shape and exhibited some density variation both radially and axially within the fiber-reinforced region (fig. 2.4(a)). UT inspection indicated relatively uniform density around the circumference of the ring, with minimal localized anomalies (fig. 2.4(b)). X-ray radiography revealed that the fiber path was uniformly hoop oriented as desired but also revealed some minor density variations (fig. 2.4(c)). None of these methods identified the processing defects discovered during post-test inspections or the magnitude of their effect on ring capabilities.

2.4 Ring Test Procedure

As previously indicated, the testing method chosen for this program was to apply a uniform pressure to the ring inside diameter surface to induce a tensile hoop stress. Applying pressure increased the ring diameter, resulting in directly measurable strains and deflections that could be recorded and analyzed with load values to determine ring stiffness and response. Hoop tensile failure of the rings could be induced if the applied pressure was raised to a high enough level.

Test apparatuses developed to load rings in this manner in order to obtain static modulus and failure data include a hydrostatic bladder burst rig, an expanding flange burst rig, and a hydraulic actuator burst rig. The only apparatus that satisfied the requirements of this program was the hydraulic actuator burst rig with its high-temperature capability. This burst rig consisted of 24 hydraulic actuators positioned around a high-temperature test chamber and capable of supplying a total of over 4.45 MN (10^6 lbf) of uniform load against the inside diameter of the composite ring (fig. 2.5). The complete
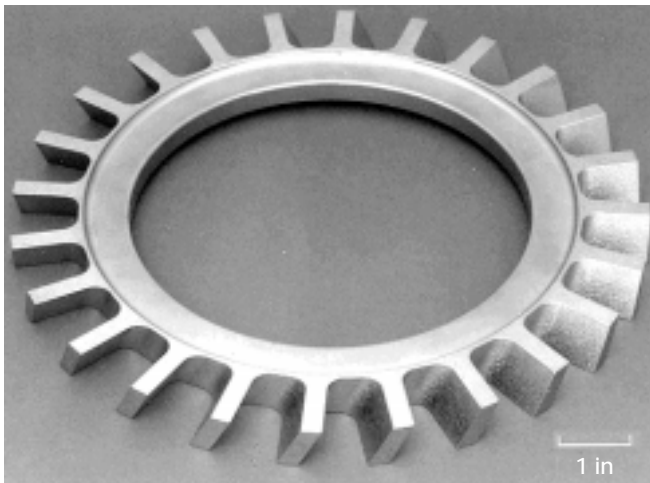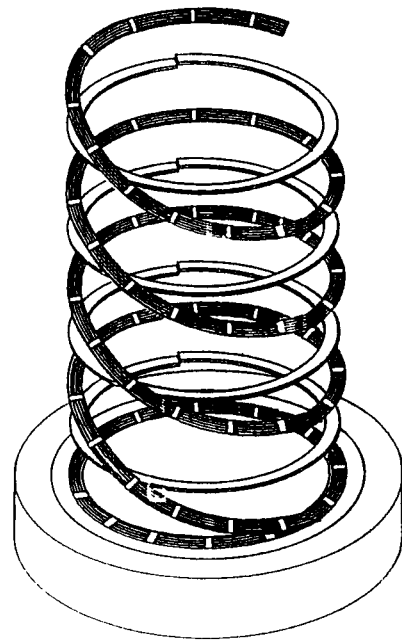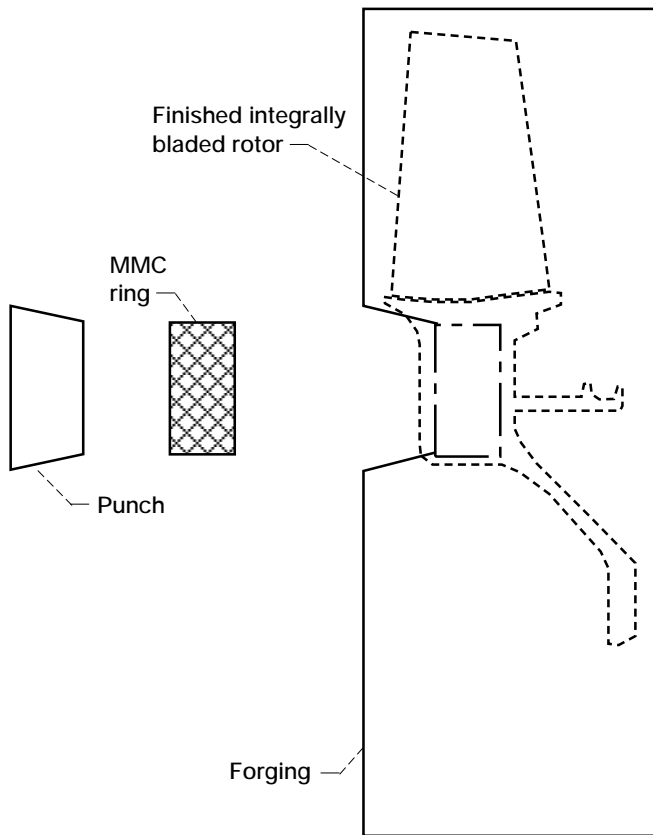
Figure 2.2.—MMC-reinforced integrally bladed rotor.
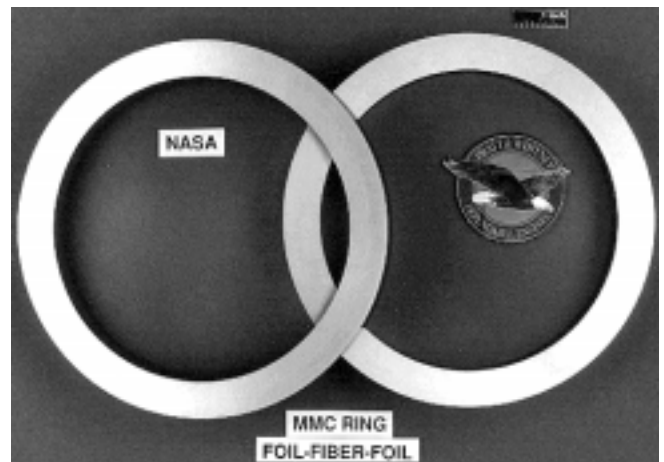
Figure 2.3.—MMC ring fabrication.

Data file; s0079_v_100_00010
Scaling factor = 7

8000   21000
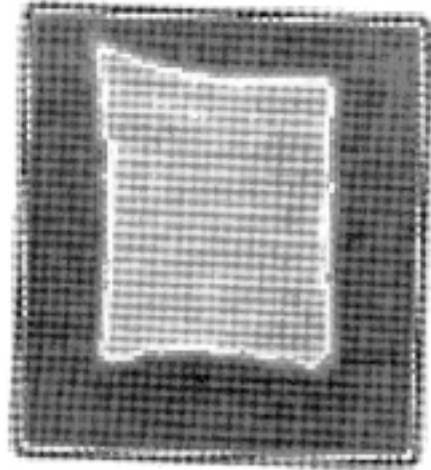
(a)
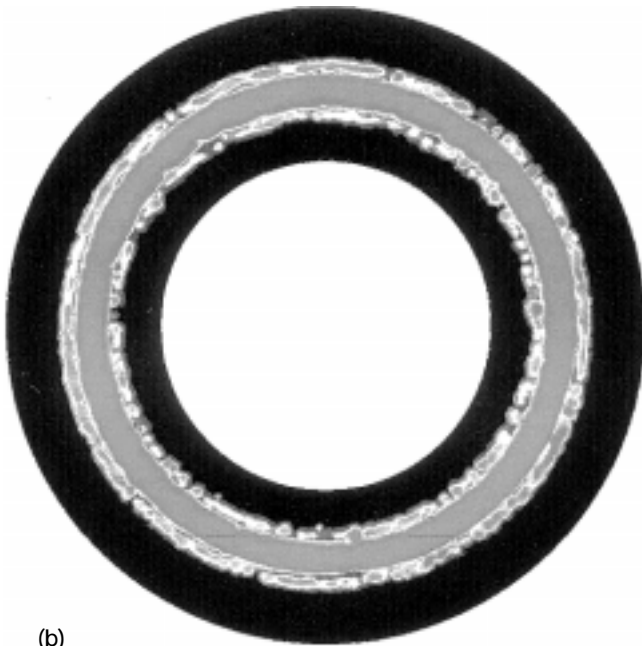
(b)

(c)

Figure 2.4.—Nondestructive evaluation techniques used on MMC ring. (a) Computed tomography results. (b) Ultrasonic transmission results. (c) X-ray radiography results.
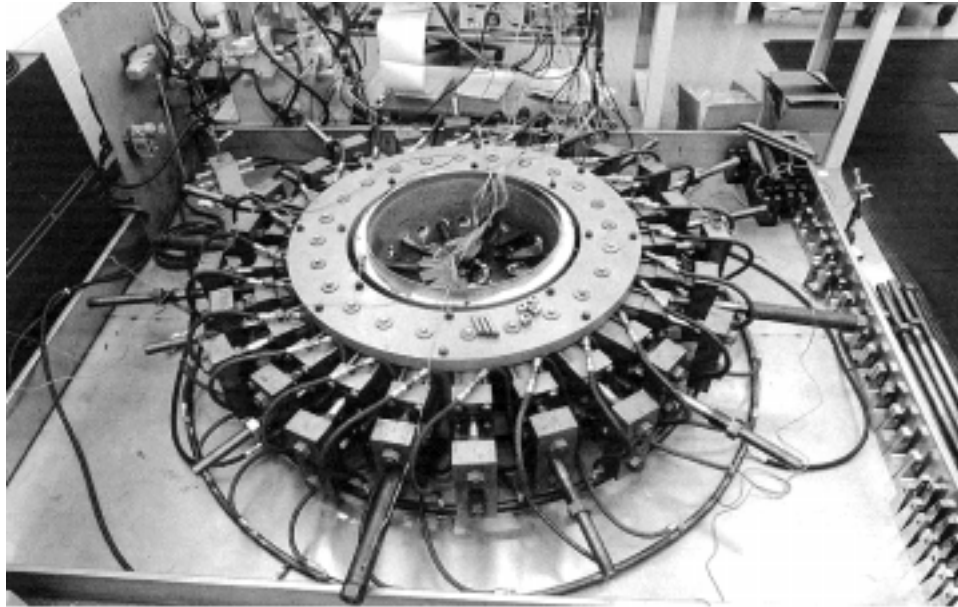
Figure 2.5.—Hydraulic actuator ring burst load test rig.

system was load controlled by a Measurements Group, Inc., System 4000 data acquisition system and could also be operated in a tension-tension, low-cycle-fatigue mode to temperatures above 815 °C (1500 °F).

For these particular tests, only 12 of the 24 load actuators were used because of the geometric constraints of the ring diameter and load fixture. A clevis and load shoe arrangement was used to uniformly transfer the load from the actuator to the ring. Twelve equally dimensioned load shoes were cut from an Inconel 718 ring, which matched the internal surface of the MMC ring. The load shoes mated with the ring inside diameter, and load was transferred from the clevis to the shoe through a pin (fig. 2.6). To reduce stress maldistribution due to the edges of the load shoes, a 0.254-mm (0.010-in.) thick compliant steel band was added between the load shoes and the ring surface.

High-temperature characterization of the ring loading response during testing to failure was the objective of this program. However, much more information can be acquired from a room-temperature test. Therefore, a room-temperature strain gage survey was conducted on all rings before high-temperature failure testing. After the strain gages and linear variable displacement transformers (LVDT's) had been attached to the ring outside diameter (OD), the test rig was assembled and the ring was loaded to 44.5 kN (10^4 lbf) per actuator. This information was used to correlate to modeling and to verify the accuracy of the analysis method. Data gathered from the test included the applied load from the actuators and discrete strains and displacements of the ring. Strain gages were used to measure the radial and hoop strains induced by the loading and were placed at the ring inside

diameter (ID), midspan, and OD. In addition to the strain gages, LVDT's were used to measure the radial displacement of the ring OD. The LVDT's were placed outside the test chamber and connected to the ring with steel wires or glass rods.

After the strain gage survey the strain gages were removed and the temperature was increased to 427 °C (800 °F), except for ring 3, which was tested at room temperature. Because high-temperature strain gages could not be used, the LVDT's were used to determine the ring deflection response at 427 °C (800 °F). The rings were then loaded at 8.9-kN (2×10^3-lbf) increments to record load and deflection information until ultimate failure occurred. The results of these tests are given in section 2.6.

2.5 Analysis Methods

A complex component designed with a region of MMC embedded within the structure requires a much more rigorous analysis than would a monolithic component. The inherent problem is the thermal mismatch between the MMC and the monolithic material surrounding it. Consolidating the structure at high temperature induces significant thermal residual stresses that greatly affect the stresses in the materials and the load levels, causing plastic deformation and failure. In this section a method for determining the mechanical properties of the MMC material is discussed, and then a procedure for determining the response to loading, and failure, of an MMC ring embedded within a monolithic material structure is reviewed.
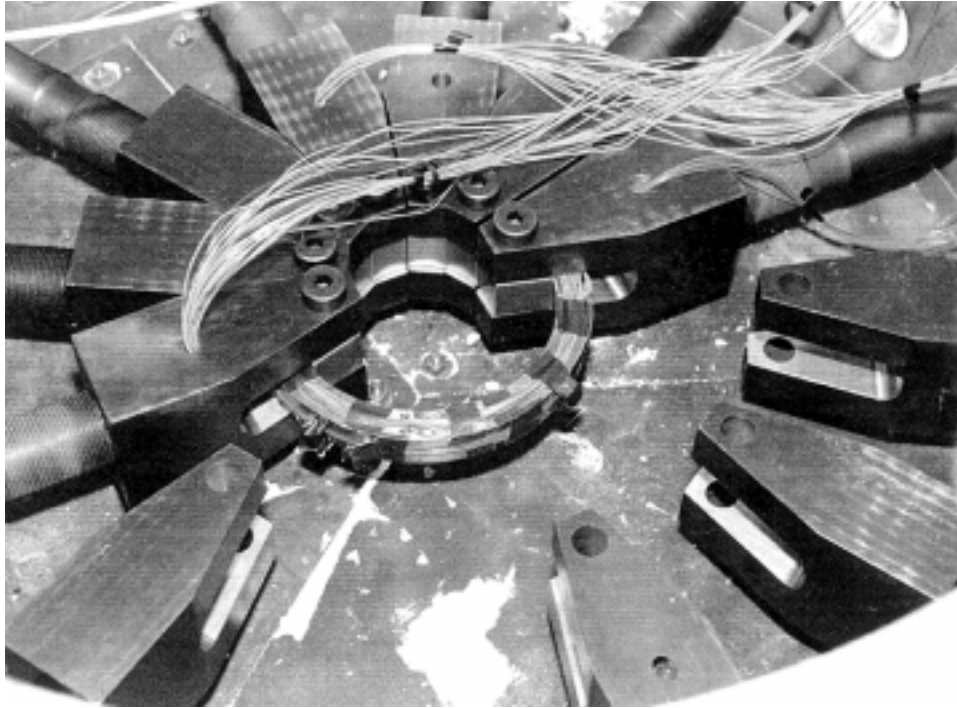
Figure 2.6.—MMC ring assembled in test rig.

2.5.1 Material Mechanical Properties

Because MMC's are produced by combining two very different materials, a high-stiffness, high-strength, brittle fiber and a moderately stiff ductile matrix, they can be considered a micromechanical structure. Analyzing this micromechanical structure involves the same inherent thermal mismatch problem that large structures have. To determine the thermal mismatch effects and the mechanical properties of the MMC, an anisotropic, coefficient-of-thermal-expansion (CTE), thick-concentric-cylinder model (CCM; Pangborn et al., 1988) was used along with the standard rule of mixtures (ROM). The CCM is a simple micromechanical model of one fiber in a cylinder of matrix material (fig. 2.7). Fiber and matrix properties at the analysis conditions are required for use in this micromechanical model.

Primary MMC tensile mechanical properties can be determined from its constituent properties by using the CCM and the ROM. Typically, the longitudinal stress-strain curve of an MMC can be summarized in two straight lines, called the bilinear effect. The point where the two lines intersect is the breakpoint (fig. 2.8). The CCM, being an elastic model, is used directly to determine the primary elastic modulus of the MMC in the longitudinal fiber direction, the Poisson's ratio, and the CTE. The ROM is used to calculate the transverse-direction elastic modulus, the shear modulus, and minor Poisson's ratios. Because the matrix material was modeled as elastic–perfectly plastic, the loss of matrix stiffness beyond the breakpoint resulted in an overall MMC stiffness reduction for the secondary modulus.
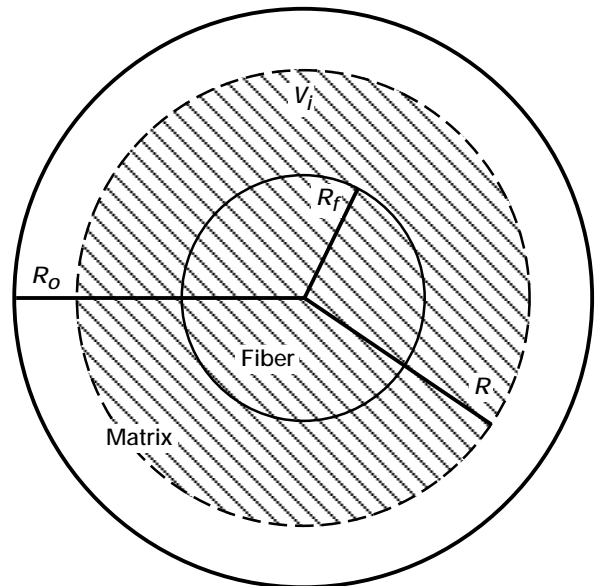
Figure 2.7.—Thick-concentric-cylinder micromechanical model, where $R_o = R_f / \sqrt{V_f}$ and $V_i = (R^2 - R_f^2)/(R_o^2 - R_f^2)$.
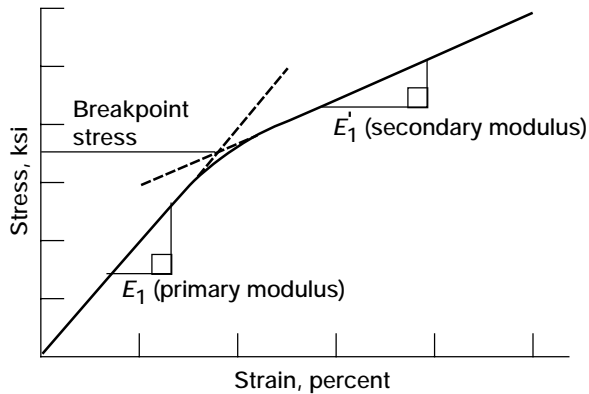
Figure 2.8.—Typical MMC stress-strain curve.

The process developed to determine the breakpoint stress for an MMC relies on an empirical correlation of available fiber contents and temperatures gathered from coupon test data. The CCM is used to calculate the radius in the matrix at which the von Mises stress is equal to the 0.2-percent yield stress at the applied mechanical load corresponding to the experimental test specimen breakpoint. Thermal residual stresses are accounted for in this analysis. This radius is used to calculate a matrix yield area ratio, which is the total matrix area divided by the area of matrix over the yield stress. A population of these matrix yield area ratios is calculated from the coupon test data and used to determine a value that best fits the experimental data. This matrix yield area can then be used to determine the breakpoint stress for any combination of fiber content and temperature. With the primary and secondary moduli and the breakpoint stress defined, the longitudinal stress-strain response is defined and can be used in the finite-element analysis.

Beyond the material breakpoint the validity of the CCM is reduced by plastic deformation and loss of stiffness in the matrix. The ROM was used to calculate the material properties in this deformation region. The matrix properties were reduced to calculate the secondary elastic modulus in the longitudinal and transverse directions and the shear modulus. Because very few compression test data exist, the primary properties in compression were assumed to be identical to the tensile properties. The breakpoint could be determined again by using the CCM, and secondary properties were modified to reflect the trends identified from more conventional materials. These properties can be directly input into various finite-element analysis programs for structural analysis.

Material properties for the monolithic cladding were based on unpublished data from Ti-15-3 foil consolidated and heat treated. This information was used, instead of standard plate or sheet Ti-15-3 data, because it more closely represents the monolithic cladding material after MMC ring consolidation and heat treatment. Nonlinear isotropic material properties were defined from available data for stress-strain curves out to 2-percent plastic strain at 21 and 427 °C (70 and 800 °F).

2.5.2 Finite-Element Structural Model

The most obvious complication in analyzing an MMC component is the different material properties of the fiber and matrix. However, these properties are only a small part of the analysis required to accurately predict stresses in an MMC component. Although accurate modeling of the MMC ring core geometry and material properties is important, calculating thermal residual stresses is one of the most important aspects of MMC component analysis. Thermal residual stresses play a major role in the determination of MMC and monolithic structural stresses. In this section the finite-element model and analysis procedure for determining the ring deflection response due to loading at room and high temperatures is discussed.

2.5.2.1 Average ring cross section.—Although designed to be rectangular and uniformly distributed, a composite core manufactured by current processes will not be of uniform shape or placement within the ring. CT scans were performed in 10° increments around the three rings to characterize the shape and placement of the MMC core (fig. 2.4(a)). The shape and placement of the MMC core were digitized from the CT scans, and the coordinates of key points were averaged from all scans to provide a "typical" cross-sectional geometry for each of the three MMC rings. This cross-sectional geometry was used to accurately model the MMC core in each ring. These cross sections are presented in figure 2.9. The sensitivity of ring stresses to composite core skewness and cladding thickness variations was not known.

2.5.2.2 Linear, three-dimensional, finite-element analysis.—The load applied at the ID of the MMC rings was not continuous but rather was discretely applied through the load shoes on the 12 hydraulic actuators. Because a two-dimensional, axisymmetric, finite-element model assumes a uniform circumferential load, a three-dimensional model was created to evaluate the variation in stress due to the discrete loads applied by the load shoes. The geometry and mesh breakup of this model are presented in figure 2.10. The model includes half a load shoe and a 15° wedge of the compliant band and MMC ring. The compliant band and MMC ring are constrained with cyclic symmetry (i.e., rollers on the front and back surfaces). The load shoe is constrained with rollers on the faces above and below the load pin. The back face is a free surface and modeled that way. The load shoe is also constrained to have uniform radial displacement along the pin contact surface. This constraint is specified to more accurately model the resistance of the load fixture clevis and pin to rotation out of plane. The load distribution for the pin contact surface is assumed to vary sinusoidally in the circumferential direction (a saddle load) of the hole. To simulate pin bending, the load is assumed to be uniform along the pin centerline but absent over the middle 30 percent of the span.

An orthotropic, nonlinear plastic analysis with a three-dimensional, finite-element model of this size is not practical
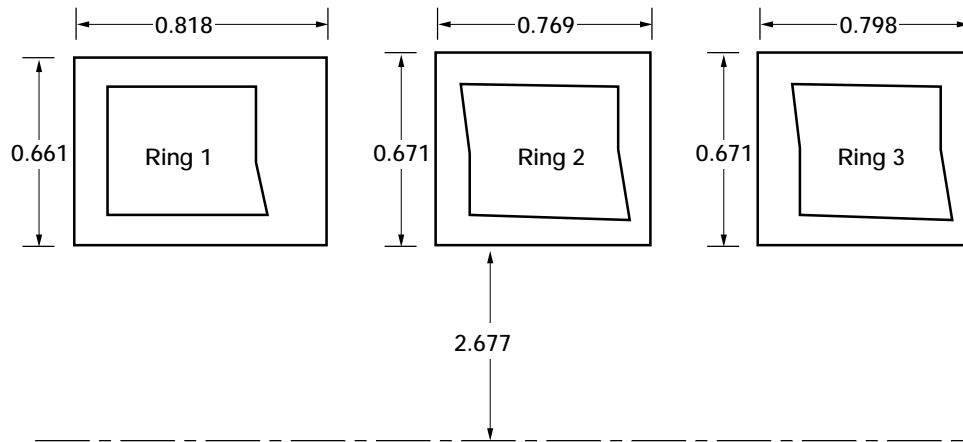
Figure 2.9.—Average cross-sectional geometry of MMC ring. (Dimensions are in centimeters (inches).)
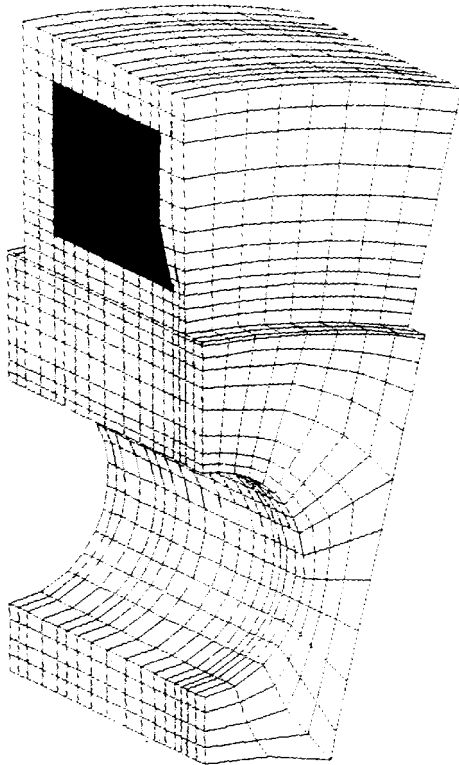
Figure 2.10.—MMC ring model for linear, three-dimensional, finite-element analysis.

for most turbine engine hardware, so an alternative approach was devised. Including plasticity in a linear solution requires the value of the secant modulus that will intersect the plastic portion of the stress-strain curve at the correct location. Determining this value is an iterative process that would not be efficient with this model. Instead, a shell model of ring 1 was created for this purpose. Elastic analyses at the same load levels were performed using the finite-element and shell mod-

els to develop a set of hoop stress correlation factors for the monolithic sheath and the MMC core. Iterative runs were made with the shell model to determine the appropriate values of the secant modulus at various load levels for the sheath and the core. Knowing these values, the effects of plasticity could be included in an orthotropic, linear, three-dimensional, finite-element analysis. The model was run at load levels to the elastic limit at 21 °C (70 °F) and to predicted burst at 427 °C (800 °F). The stresses due to mechanical loading were combined with thermal residual stresses determined from the two-dimensional analysis described in the following section by using the superposition principle. As expected, ring stresses were highest at the center of the load shoe and lowest at the edge of the load shoe, with a total variation of approximately 5 percent from the mean stress.

2.5.2.3 Nonlinear, two-dimensional, finite-element analysis.—A two-dimensional, axisymmetric, finite-element analysis was performed to predict ring load response at 21 °C (70 °F) for the strain gage survey and at 427 °C (800 °F) for the tests to failure. The model (fig. 2.11) includes a two-dimensional, axisymmetric slice through the compliant band and MMC ring and the portion of the load shoe between the ring ID and the pin hole where the load is applied. The load shoe was constrained in the axial direction and constrained to have uniform radial displacement along the pin contact surface, again to model the actual resistance of the clevis and pin to rotation. The compliant band and MMC ring were constrained with axisymmetric boundary conditions. The MMC core was modeled by using orthotropic, axisymmetric elements.

When MMC rings are cooled after consolidation, thermal residual stresses are generated by the difference in thermal expansion and contraction rates between the monolithic cladding and the MMC core. The core goes into hoop compression and the cladding goes into hoop tension. This is an important phenomenon to model when completing an analysis of an MMC component. A two-dimensional, axisymmetric
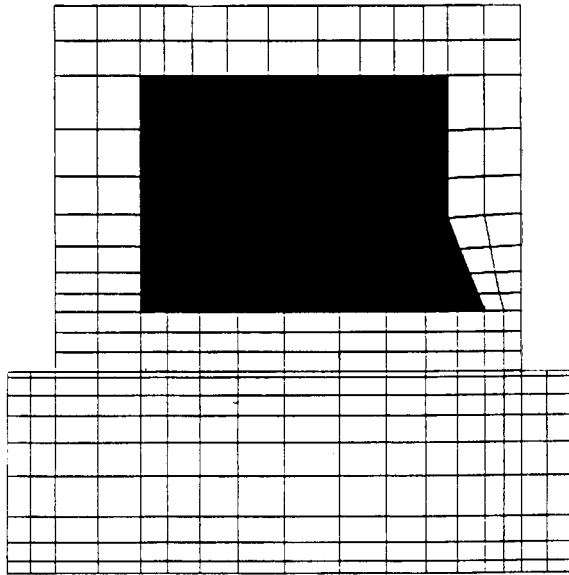
Figure 2.11.—MMC ring model for nonlinear, two-dimensional, finite-element analysis.

Stress, MPa (ksi)
279 (41)
248 (43)
316 (46)
335 (49)
354 (51)
372 (54)
391 (57)
409 (59)
428 (62)
447 (65)

Stress, MPa (ksi)
330 (48)
352 (51)
374 (54)
376 (58)
419 (61)
441 (64)
463 (67)
485 (70)
507 (74)
529 (77)

Figure 2.12.—Predicted MMC ring stress from finite-element analysis model.

finite-element model was created for each ring from the cross-sectional geometries shown in figure 2.9. The rings were considered to be stress free after heat treatment. Finite-element analysis was used to determine the thermal residual stresses created upon cooling to 427 and 21 °C (800 and 70 °F). These stresses were all within the elastic regime, so that a nonlinear plastic analysis was not required. Because nonlinear analysis is practical with a two-dimensional model, plastic effects could be included in the solution directly. Elastic-plastic behavior of the MMC core was modeled by using the bilinear stress-strain curve defined in section 2.5.1. The analysis allowed for different bilinear curves for each of the three orthonormal directions, as well as different curves for tension and compression. The model was run to determine thermal residual stresses and then continued at 8.9-kN (2×10^3-lbf) load levels to the predicted burst at 21 and 427 °C (70 and 800 °F). Results from the two-dimensional, finite-element analysis correlated well with mean stress from the three-dimensional analysis. Comparing these results led to the formulation of a 1.05 stress maldistribution factor to account for the nonuniform application of the load shoes.

2.5.2.4 MMC ring predicted response and failure.—The predicted stresses and deflections with applied loads calculated as described in the preceding sections correlated well with the measured values for all three MMC rings. As expected, the predicted stresses in the monolithic cladding and the MMC core were highest near the ring ID and lowest at the ring OD. See figure 2.12 for typical stress levels throughout the ring cross section. All predictions for the room-temperature strain gage surveys show that ring response was linear to the 44.5-kN (10^4 lbf) load level (figs. 2.13(a), 2.14(a), and 2.15(a)). Also, the predicted hoop strain was the highest
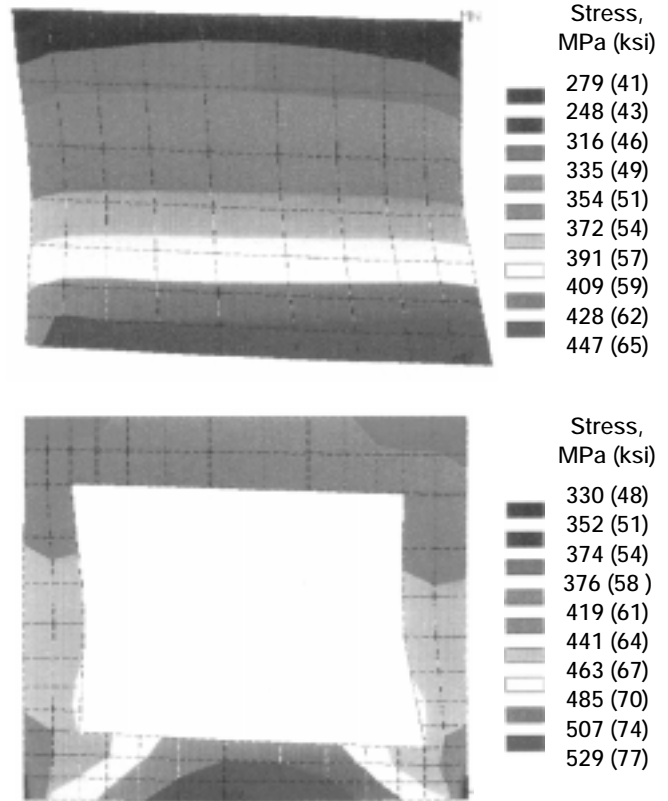
at the ring ID and 25 percent lower at the ring OD, corresponding to the predicted behavior. Ring load response for the 427 °C (800 °F) failure tests was predicted to be linear to a load level of 89.0 kN (2×10^4 lbf) per actuator (figs. 2.13(b), 2.14(b), and 2.15(b)). Above this load the monolithic material surrounding the MMC began to plastically deform at the ring ID. This yielding progressed toward the ring OD as the load level was increased. The MMC core surpassed its linear range in a similar manner. These two effects resulted in an overall nonlinear response of the ring to loading at high levels. Note that rings 1 and 2 were failure tested at 427 °C (800 °F), but ring 3 was failure tested at room temperature.

The peak hoop stress in the MMC core (fig. 2.12) occurred at approximately the center of the ID edge of the core. This location was predicted to be the initial failure location to which the failure criteria would be applied. Note that the monolithic cladding at this load level experienced significant plastic yielding at the ID and bordered on plasticity everywhere else. The predicted failure mode for the MMC rings was ultimate fiber strain. Element strains for the ID of the composite core were taken from the two-dimensional, axisymmetric, finite-element analyses and multiplied by the 1.05 stress maldistribution factor determined from the three-dimensional, linear analysis. Failure was assumed when the strain at the failure location exceeded the fiber failure strain,
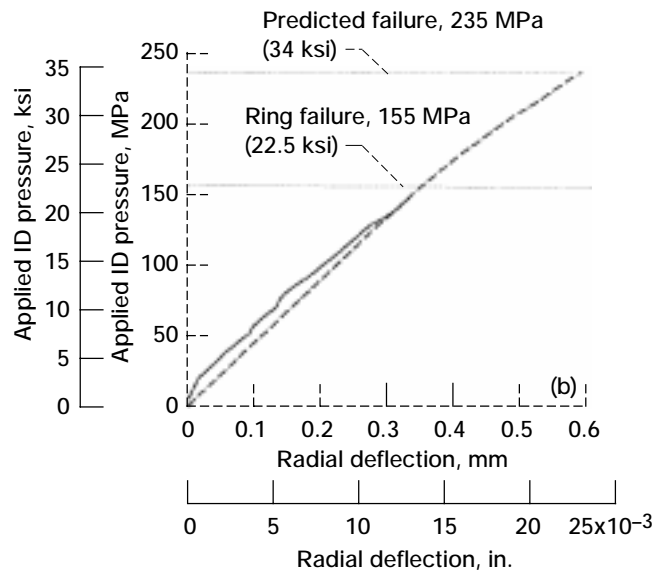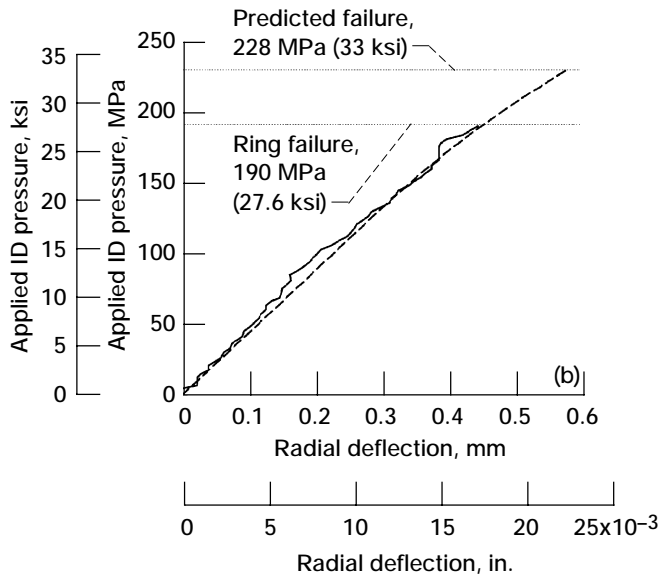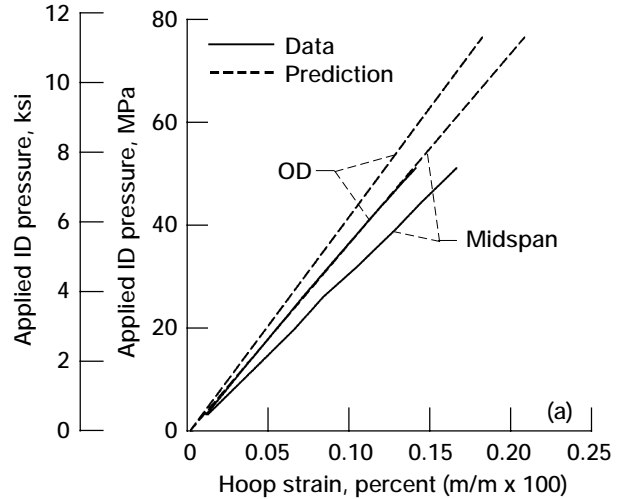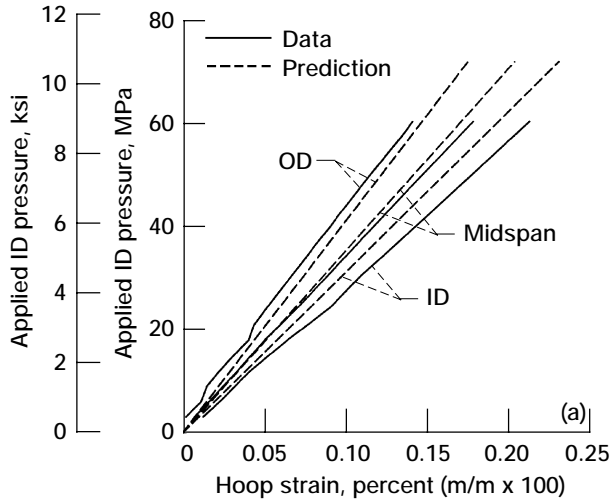
Figure 2.13—Load response and deflection for MMC ring 1. (a) Load response at 21 °C (70 °F). (b) Deflection and predicted OD displacement at 427 °C (800 °F).

Figure 2.14.—Load response and deflection for MMC ring 2. (a) Load response at 21 °C (70 °F). (b) Deflection and predicted OD displacement at 427 °C (800 °F).

accounting for the compressive thermal residual stress induced during processing. The fiber failure strain was based on test data for 33-vol % fiber SCS–6/Ti-15-3 coupons corrected for the compressive residual strain due to processing predicted by micromechanical modeling.

Results from the finite-element structural modeling of the MMC rings indicate that the distribution of the monolithic cladding around the MMC core had a significant effect on ring behavior.

2.6 Ring Test Results

Results of testing at both room temperature and 427 °C (800 °F) showed good correlation with load deflection pre-

dictions, although ultimate strength was far lower than predicted. The results of the strain gage survey and burst test for each ring are described here and the correlation with modeling is discussed.

Testing of ring 1 consisted of a room-temperature strain gage survey and a 427 °C (800 °F) static test to failure. The results of the strain gage survey show that the ring response remained linear to 44.5 kN (10⁴ lbf) per actuator and correlated well with the analytical predictions (fig. 2.13(a)), with a 7-percent variation in deflection at the ring ID and a 4-percent variation at the ring OD. As expected, the strain variation between the top and bottom surfaces was very small. The test to failure revealed characteristics about the behavior of MMC structures at high temperatures and loads. This test verified that stiffness predictions were accurate and that MMC

Predicted failure,
285 MPa (41.3 ksi)

Ring failure,
240 MPa
(34.8 ksi)

Midspan

OD

ID

Data
Prediction

(a)

Applied ID pressure, ksi
Applied ID pressure, MPa
Hoop strain, percent (m/m x 100)

Predicted failure,
285 MPa (41.3 ksi)

Ring failure,
240 MPa (34.8 ksi)

(b)

Applied ID pressure, ksi
Applied ID pressure, MPa
Radial deflection, mm
Radial deflection, in.
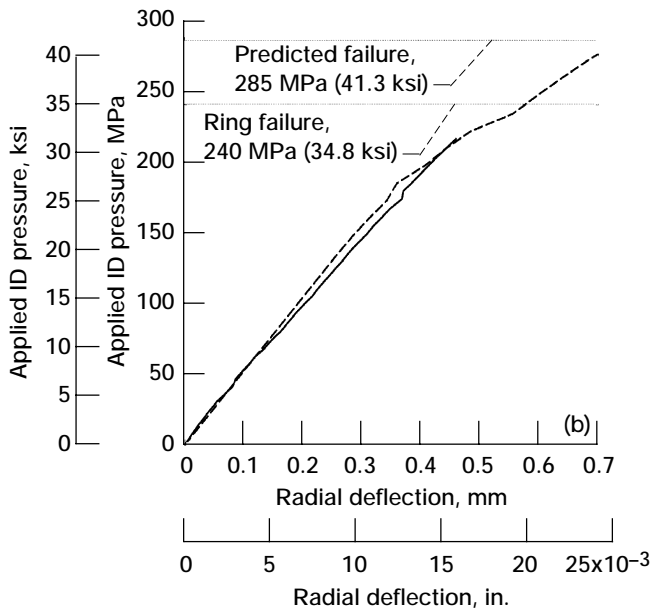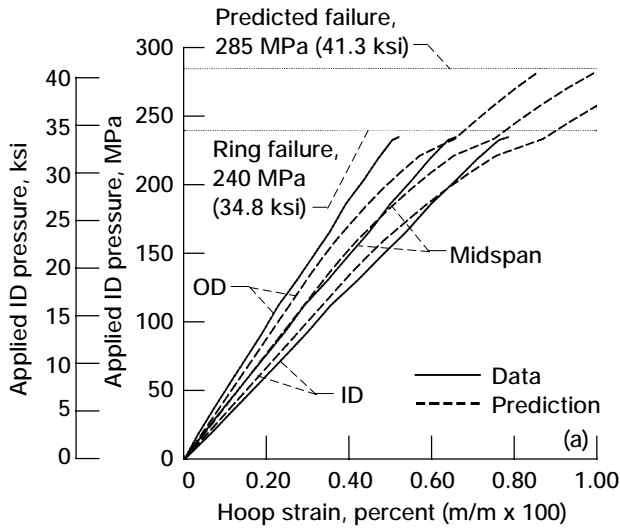
Figure 2.15.—Load response and deflection for MMC ring 3.
(a) Load response at 21 °C (70 °F). (b) Deflection and pre-
dicted OD displacement at 427 °C (800 °F).

Ring
3
1
2

Ring	Stress at failure, MPa (ksi)
1	190 (27.6)
2	155 (22.5)
3	240 (34.8)

Applied ID pressure, ksi
Applied ID pressure, MPa
Radial deflection, mm
Radial deflection, in.

Figure 2.16.—Comparison of MMC ring load response.

components can exhibit nonlinear behavior before ultimate
failure (fig. 2.13(b)). The deflection response of the ring
correlated well with the predicted behavior, with only slight
variations up to failure. However, the ultimate failure oc-
curred at 80 percent of the predicted failure load. The reason
for this discrepancy is discussed in section 2.7.

Ring 2 exhibited a slightly different behavior during the
strain gage survey. Unexpectedly, this ring showed a 16 per-
cent lower stiffness than predicted and a small amount of
nonlinear deformation at loads well below 44.5 kN (10^4 lbf)
(fig. 2.14(a)). At 427 °C (800 °F) the plasticity was identifi-
able but occurred at a much lower load than predicted
(fig. 2.14(b)). Also, ring 2 failed at 60 percent of predicted

capability. The cause of the reduced stiffness and strength
capability was not analytically identified, but post-test inspec-
tions revealed extensive damage to the MMC core in process-
ing, which could explain the inferior capabilities of ring 2, as
be discussed in more depth in section 2.7.

Testing of ring 3 consisted of a room-temperature test to
failure. Strain gage information was thus recorded to the ring
failure load. Surprisingly, this ring exhibited very little non-
linear behavior until just before failure (fig. 2.15(a)). The
deflection response was linear to the load at which the LVDT's
were disconnected for safety reasons (fig. 2.15(b)). Near fail-
ure, however, measured strain began to increase rapidly, pos-
sibly caused by the onset of fiber failure across the MMC
core. The strain gage and OD deflection measurements corre-
lated well with the linear region of the prediction. Predictions
were consistently within 10 percent of the measured results.
Although the ring displayed very little nonlinear behavior, the
predictions show nonlinear behavior beginning at 89-kN
(20×10^4-lbf) internal pressure. The predictions thus deviated
significantly from the measured response, by 30 percent at the
worst case. The cause of this deviation is most likely inaccu-
rate modeling of the secondary modulus of both the MMC
core and the monolithic cladding. Ultimate failure occurred at
85 percent of the predicted failure load.

Comparing the stiffness of the three rings revealed that
rings 1 and 2, both tested at high temperature, had similar
stiffness, but processing defects in ring 2 caused premature
failure (fig. 2.16). Ring 3 showed slightly higher stiffness, a
significantly higher yield point, and a significantly higher
failure load than rings 1 and 2. This behavior was not unex-
pected as the capabilities of Ti-15-3 are much greater at room
temperature than at 427 °C (800 °F).
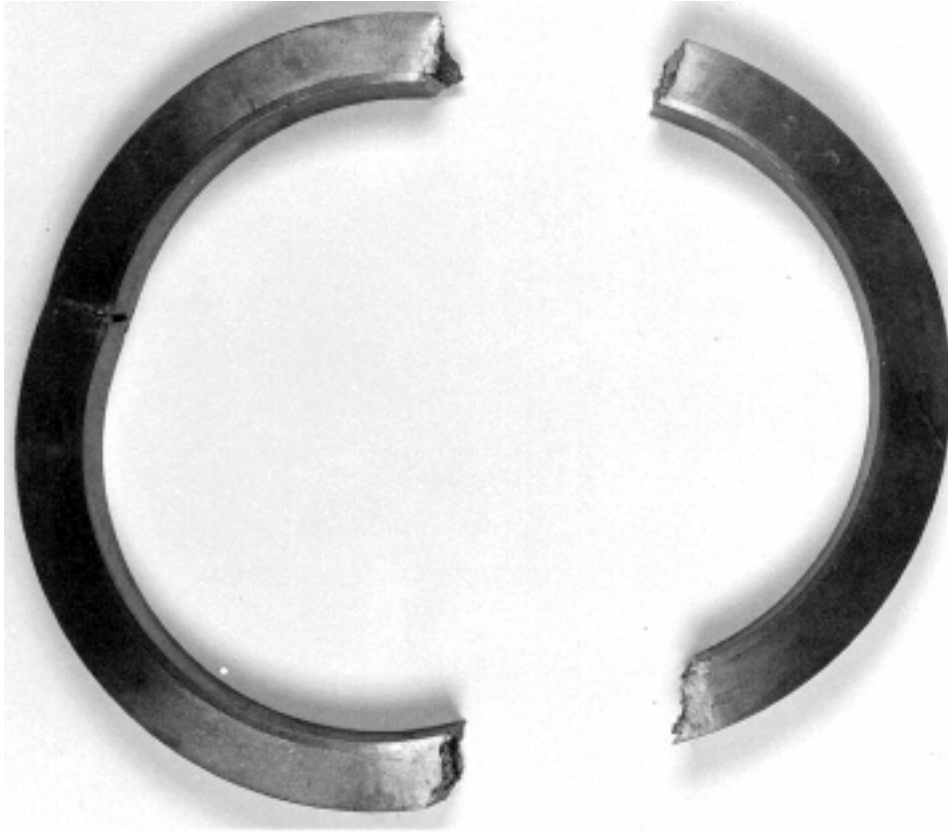
Figure 2.17.—MMC ring 1 after failure.

2.7 Post-Test Inspection

After testing, rings 1 and 2 were inspected at both Pratt & Whitney and NASA Lewis. Preliminary identifications of aspects of the fracture surfaces are discussed here. Although NASA has completed a more detailed review of the fracture surfaces and probable failure mechanisms, it is not included in this chapter. The brief assessment of ring 3 was based on visual observations.

Ring 1 fractured in three locations (fig. 2.17). The primary failure was due to the tensile overload in the hoop direction, and two secondary failures were incurred from the actuator load release after primary failure. Rings 2 and 3 each fractured in two locations, with the same primary and secondary failures as ring 1. Examination of the fracture surfaces of all three rings indicated a cusp in the MMC core at an ID corner. The MMC cusp protruded through the monolithic cladding to the surface of ring 1 (fig. 2.18), verifying the CT inspections that first identified and mapped the cusp. The cusps of rings 2 and 3 were smaller and did not significantly protrude into the cladding (fig. 2.19).

The primary fracture surfaces of all three rings were characterized by a flat-fracture tensile overload in the MMC core and a 45° shear failure of the monolithic cladding. The fiber

pullout appeared to be typical of that seen on fracture surfaces of flat-panel, tensile coupon test specimens at 427 °C (800 °F) (fig. 2.20). Fiber spacing for all three rings, however, was somewhat irregular and not typical of that produced by the well-controlled fabrication of flat panels. Fiber spacing in the axial direction was very uniform and well spaced, with the exception of one location on ring 1 where foils overlapped during processing. Fiber spacing in the radial direction was uniform, with very little spacing between fibers. This resulted in fibers contacting and in matrix cracks between fibers. The fiber spacing can be seen in figure 2.20. Also, regions of fiber bunching, with groups of fibers in contact with each other, were identified from other micrographs of the failure surface. The MMC core appeared to be well bonded to the outer monolithic cladding with no areas of delamination or separation. In spite of a rigorous inspection of the fracture faces, no evidence of the failure origin of rings 1 and 3 could be found.

Of great significance in ring 2 was a region of skewed fibers in the fracture surface. One-third to one-half of the ring cross section contained fibers locally skewed approximately 30° out of plane (fig. 2.21). Detailed post-test inspections completed at NASA identified areas in this region where matrix material coated the fiber fracture faces. This infiltration of matrix on the broken fiber faces could only have
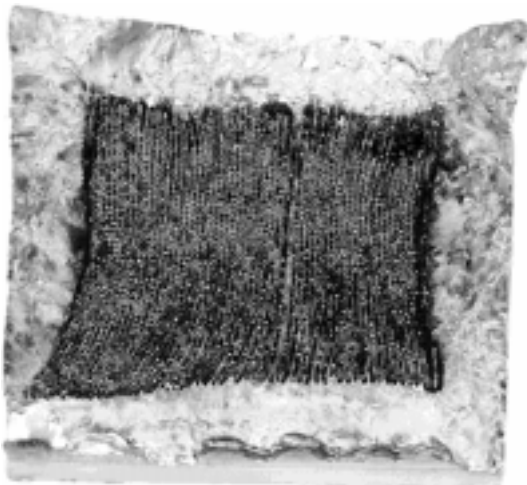
4x
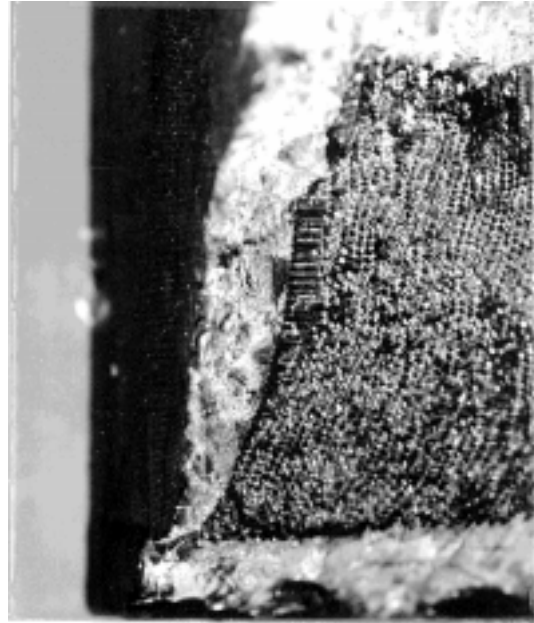
7x

Figure 2.18.—Primary fracture surface of MMC ring 1.
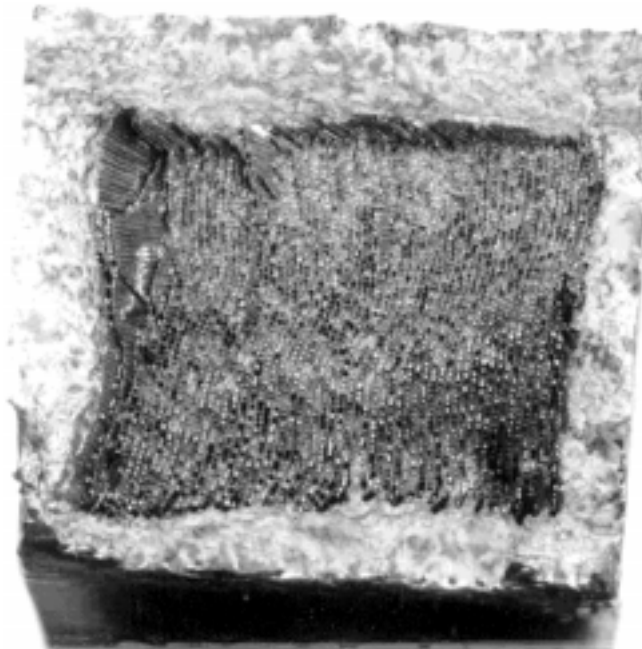
Figure 2.19.—Primary fracture surface of MMC ring 2.
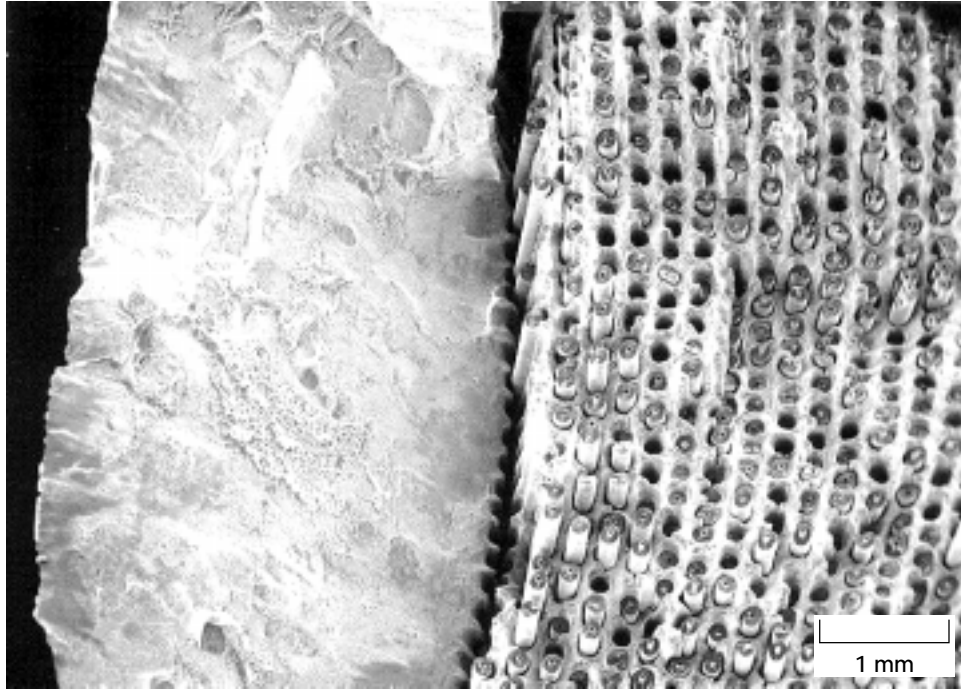
Figure 2.20.—Fiber spacing and bond integrity of MMC ring 1.
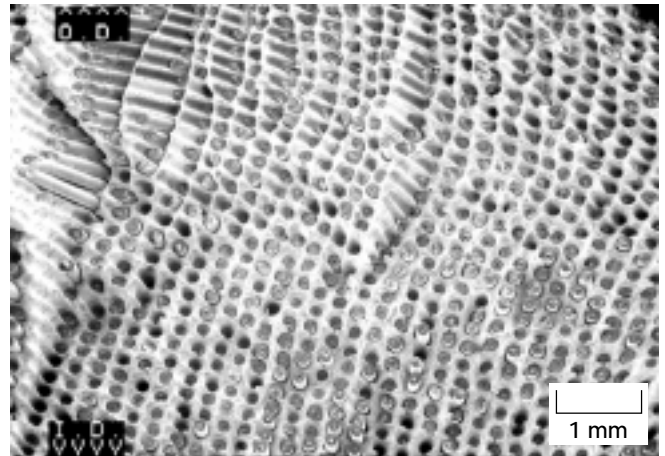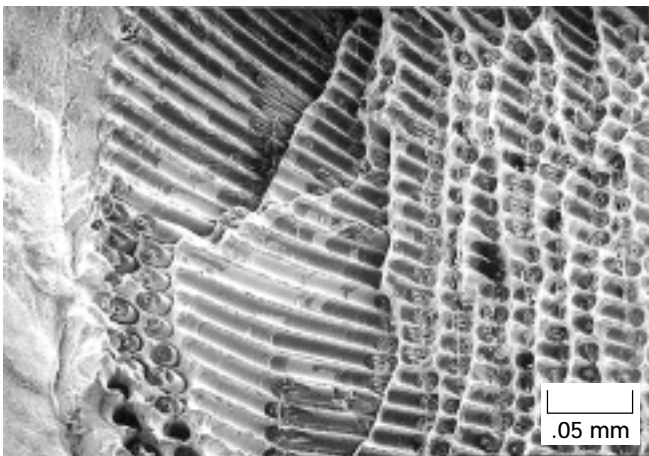
Figure 2.21.—Skewed fiber region in MMC ring 2.

occurred during ring fabrication and effectively eliminated the load capacity of 50 percent of the MMC core before testing began. The magnitude of this preexisting processing damage contributed to the significant reduction in MMC ring strength identified during testing.

2.8 Conclusions

Predicting the capabilities of a relatively large-volume turbine engine component by using finite-element methods and material properties derived from small-volume, flat-panel coupon specimens revealed much about the validity of this approach. Comparing the predicted strains and deflections with those measured during tests of metal-matrix-composite (MMC), silicon-carbide-reinforced subscale rings showed that finite-element analysis is a reasonably accurate method for determining the load response of MMC components. Although not clearly evident from these tests, accurate determination of thermal residual stresses induced by the thermal mismatch between the MMC and monolithic materials is important in predicting the nonlinear behavior of MMC components. Available small-volume, flat-panel coupon specimens proved adequate to define the elastic tensile material properties of the MMC material, but much more extensive material characterization testing is required to accurately model the nonlinear and out-of-plane properties exhibited by MMC material.

Analytical methods for predicting component failure based on flat-panel coupon test specimens were proven inadequate because of the material defects resulting from MMC ring fabrication. The lack of maturity in the ring fabrication process resulted in the creation of a number of defects that reduced the ring's load capacity. Those defects included unequal fiber spacing, fibers in contact with each other, fibers damaged during consolidation, and fibers skewed out of the primary loading direction. These types of defect are not accounted for in analysis methods but significantly affect component strength. Therefore, in addition to pure analytical failure predictions, a statistically based damage assessment

prediction method must account for defects not inherent to coupon test specimens.

Computed tomography proved invaluable in accurately mapping the actual interior geometry of the MMC core within the ring. This information was required when generating the finite-element model and removed any uncertainty in defining the ring interior. However, none of the nondestructive evaluation methods employed in this program were able to indicate the magnitude of defects identified during post-test inspections or the effect they would have on the ring's load capacity. Much more development and calibration of nondestructive methods must be done before MMC components can be installed and operated in advanced turbine engines.

References

Baaklini, G.Y., Doehnert, W.J., Hemann, J.H., and Yancey, R.N., 1991, "Characterization of MMC Subscale Engine Components Using X-Ray Computed Tomography," *HiTEMP Review 1991: Advanced High-Temperature Engine Materials Technology Program*, NASA CP–10082, pp. 33–1 to 33–14.

Chamis, C.C., Murthy, P.L.N., and Hopkins, D.A., 1988, "Computational Simulation of High Temperature Metal Matrix Composite Cyclic Behavior," NASA TM–102115.

Gayda, J., Gabb, T.P., and Freed, A.D., 1989, "The Isothermal Fatigue Behavior of a Unidirectional SiC/Ti Composite and the Ti Alloy Matrix," NASA TM–101984.

Halford, G.R., Lerch, B.A., Saltsman, J.F., Arya, V.K., and Caruso, J.J., 1989, "Low-Cycle Fatigue Prediction for Metal Matrix Composites," *HiTEMP Review 1989: Advanced High-Temperature Engine Materials Technology Program*, NASA CP–10039, pp. 64–1 to 64–9.

Lerch, B.A., Gabb, T.P., and MacKay, R.A., 1990, "Heat Treatment Study of the SiC/Ti-15-3 Composite System," NASA TP–2970.

Pangborn, R.N., Queeney, R.A., and Vedula, M., 1988, "Fibre Anisotropic Thermal Expansion and Residual Thermal Stress in a Graphite/Aluminum Composite," *Composites*, Vol. 19, No. 1, pp. 55–60.

Robinson, D.N., and Pastor, M.S., 1992, "Limit Pressure of a Circumferentially Reinforced SiC/Ti Ring," *Composite Engineering*, Vol. 2, No. 4, pp. 229–238. (Also, NASA CR–187211.)

Zaretsky, E.V., 1987, "Fatigue Criterion to System Design, Life, and Reliability," *Journal of Propulsion and Power*, Vol. 3, No. 1, pp. 76–83.

Chapter 3

Elevated-Temperature Damage Mechanisms and Fatigue Behavior of Unidirectional SCS–6/Ti-15-3 Composite

Michael G. Castelli* and John Gayda[†]

3.1 Introduction

Achieving the performance and thrust-to-weight goals of advanced gas turbine engine designs requires significant advances in material capabilities. It is anticipated that many of these advances will be enabled through the use of titanium-matrix composites (TMC's), which offer high ratios of strength to density. One potential use of TMC's is in advanced compressor rotor designs, where MMC reinforcement rings are embedded within integrally bladed rotors. Such designs offer attractive benefits, including both lower weight and higher rotor speeds than those achieved with conventional nickel and titanium rotors. However, before the benefits of introducing TMC's into such designs can be fully realized, several key issues—including component design, fabrication, inspection, and predictions of structural behavior—must be addressed and demonstrated.

To this end, NASA Lewis Research Center and Pratt & Whitney Aircraft (P&W) entered into a cooperative research program with the goal of developing and verifying fatigue life prediction models for metal-matrix composites—in particular, TMC's. Emphasis was placed on ultimately modeling the static burst and cyclic fatigue lives of subscale TMC reinforcement rings representative of those used in advanced compressor rotor designs. To support and guide the fatigue life modeling effort, a coupon-level experimental program was established with the goal of providing the necessary characterization data for the selected TMC system, silicon carbide/titanium–15 wt % vanadium–3 wt % chromium–3 wt % aluminum–3 wt % tin, designated SCS–6/Ti-15-3. The fatigue work conducted at NASA Lewis in support of this experimental program is the focus of this chapter.

The objective of the Lewis fatigue work was to thoroughly characterize the fatigue behavior and damage mechanisms of a unidirectionally reinforced SCS–6/Ti-15-3 composite. Although the SCS–6/Ti-15-3 system is not considered a viable material for gas turbine engine disk applications, it was selected as a model material in the NASA/P&W cooperative program because of its availability, established processing parameters, and reproducible mechanical properties. Isothermal fatigue behaviors of the [0°], [90°], and unreinforced systems were investigated at 427 °C (800 °F). This temperature was selected for the static burst and fatigue tests on the TMC rings. To examine the effects of cut or exposed fibers on the coupon edges and to more closely approximate conditions found in the TMC ring, clad [0°] specimens were also fabricated and tested. In addition, the thermomechanical fatigue (TMF) behaviors of the [0°] and [90°] systems were examined. Failure and damage mechanisms exhibited by the various coupons and types of fatigue cycle were compared and contrasted through the use of optical and scanning electron microscope fractography and metallography.

3.2 Material Details

The SCS–6/Ti-15-3 composite consisted of a Ti-15V-3Cr-3Al-3Sn alloy matrix reinforced with approximately 35 vol % of continuous SiC (SCS–6) fibers. The SCS–6 fiber has a

---

*Lewis Research Center Group, Sverdrup Technology, Inc., Brook Park, Ohio 44142.
[†]NASA Lewis Research Center, Cleveland, Ohio 44135.

nominal diameter of 140 μm (0.0055 in.). The composite test specimens were obtained from several eight-ply and one nine-ply unidirectionally reinforced panels fabricated by hot isostatic pressing alternate layers of Ti-15-3 foil and SCS–6 fiber mat. The one nine-ply panel had no special significance and was used simply because of its availability. The resulting panel thicknesses were approximately 2 mm (0.08 in.). An unreinforced Ti-15-3 alloy panel was also fabricated from Ti-15-3 foils by using the same consolidation process and parameters employed in composite production.

Coupon test specimens with a nominal geometry of 15.2 by 1.3 cm (6.0 by 0.5 in.) were cut from the composite panels parallel to (i.e., [0°]) and perpendicular to (i.e., [90°]) the fiber direction by means of wire electrodischarge machining. The heat-affected zone was removed by diamond wheel grinding the machined edges. After machining, the specimens were heat treated at 700 °C (1300 °F) for 24 hr in vacuum to stabilize the matrix microstructure. Note that because the specimens were cut out of large, flat panels, the machined edges exhibited cut or exposed fiber ends, which may influence the specimen's fatigue life.

Given that the NASA/P&W ring design consisted of a TMC ring embedded within an outer matrix cladding and did not have cut or exposed fibers, there was some concern as to the appropriateness and applicability of testing TMC coupons with cut or exposed fibers. Therefore, $[0°]_8$ clad, composite, coupon-size panels without cut or exposed fibers were also fabricated. These clad, composite test specimens were fabricated from Ti-15-3 foils 20 by 2.5 cm (8 by 1.0 in.) and SCS–6 fiber mats 20 by 1.2 cm (8 by 0.5 in.). Extra Ti-15-3 foil sheets were added to the top and bottom faces of the panels. These coupon-size panels were then consolidated by using the same consolidation process employed for the larger panels. Clad specimens were machined from these panels such that the machined edges in the gage section would not

intersect any fibers. After machining, the specimens were heat treated at 700 °C (1300 °F) for 24 hr in vacuum. The actual fiber distribution and Ti-15-3 case of a clad test specimen are shown in figure 3.1. The TMC core had a fiber content of approximately 35 vol % (identical to the unclad composite), and the Ti-15-3 case was approximately 0.5 mm (0.02 in.) thick on the broad face and 1 to 2 mm (0.04 to 0.08 in.) thick on the edge. The overall fiber content of the clad specimens was 19 to 21 vol %.

Cylindrical test specimens with a 4.8-mm (0.19-in.) diameter in the gage section were used to characterize the unreinforced Ti-15-3 alloy. This specimen design was selected (over the flat-plate design) to accommodate the compressive loads anticipated in the strain-controlled fatigue tests. These specimens were also heat treated at 700 °C (1300 °F) for 24 hr in vacuum after machining.

3.3 Test Details

All fatigue tests were conducted with servohydraulic test systems equipped with either hydraulic wedge or collet grips. The composite testing employed zero-tension (i.e., $R_\sigma = 0$), load-controlled triangular waveforms, with the exception of the $[0°]_9$ TMF, where a sine waveform was used. The zero-tension cycle was selected to prevent specimen buckling problems with the thin-plate composite coupon specimens. Axial strain measurements were made with a high-temperature extensometer mounted on the specimen edge. Direct induction heating was used for all composite testing.

The isothermal composite tests were conducted at 427 °C (800 °F) and a cyclic load frequency of 0.33 Hz. A number of $[90°]_8$ specimens were also tested at 0.0083 Hz to match the $[90°]_8$ TMF tests and to help balance the isothermal and TMF cycles with respect to the effects of environmental degradation and time-dependent phenomena. In-phase (IP) and out-of-phase (OP) TMF tests were conducted on the $[0°]_9$ and $[90°]_8$ systems. IP and OP loadings are defined as a 0° (IP), and 180° (OP), time-phase shift between the load and temperature waveforms. The $[0°]_9$ TMF tests were conducted at 93 to 38 °C (200 to 100 °F) and 0.0056 Hz; and the $[90°]_8$ TMF tests, at 200 to 427 °C (400 to 800 °F) and 0.0083 Hz.

Isothermal fatigue tests on the unreinforced Ti-15-3 alloy were conducted at 427 °C (800 °F) by using a strain-controlled command waveform. Although strain-controlled testing of the unreinforced Ti-15-3 may seem inappropriate as a comparison with the load-controlled composite tests, this choice was not without merit, as matrix deformation in the composite is very much a strain-limited condition resulting from the stiff elastic response of the fibers. As in the isothermal composite tests a 0.33-Hz triangular command waveform was employed. For these strain-controlled tests a minimum/maximum strain ratio of zero (i.e., $R_\varepsilon = 0$) was selected to represent matrix behavior in the composite. Furnace heating was used on the unreinforced specimens.
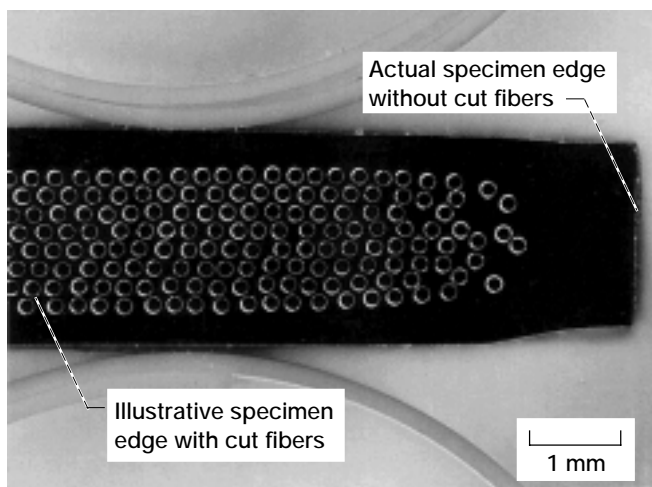
Figure 3.1.—Cross section of typical clad $[0°]_8$ specimen.

Actual specimen edge without cut fibers

Illustrative specimen edge with cut fibers

1 mm

3.4 Results and Discussion

3.4.1 Tensile Behavior

Before examining the fatigue behavior of both the composite and the unreinforced Ti-15-3 alloy, it is instructive to examine the tensile properties summarized in table 3.1. As expected, the modulus and strength of the $[0°]_8$ composite were superior to those of both the unreinforced Ti-15-3 alloy and the $[90°]_8$ composite, but the failure strain was quite low, reflecting the brittle nature of the SCS–6 fibers. For the $[90°]_8$ composite the initial elastic modulus was significantly greater than that of the unreinforced Ti-15-3 alloy; however, the yield strength (proportional limit), ultimate tensile strength (UTS), and elongation of the $[90°]_8$ composite were far less than the corresponding values for the unreinforced Ti-15-3 alloy. These low numbers for the $[90°]_8$ composite have been attributed to the weakness of the fiber/matrix interface (Johnson et al., 1990; Gayda and Gabb, 1992; Majumdar and Newaz, 1992a).

3.4.2 Isothermal Deformation Behavior

During isothermal fatigue testing of the composite and the unreinforced Ti-15-3 alloy at 427 °C (800 °F), notable differences in deformation behavior were observed. These fatigue data are summarized in table 3.2. For the unreinforced Ti-15-3 alloy, strain-controlled testing produced significant changes in mean stress. At the start of the test a zero-tension stress situation prevailed, but by half-life ($0.5 N_f$) a balanced tension-compression stress condition was established. This drop in mean stress was produced by plastic flow and stress relaxation.

Changes in strain response observed during load-controlled fatigue tests on the composites are typified in figure 3.2. In general, little or no change in strain range, and therefore compliance, was observed for the $[0°]_8$ composite, and the stress-strain response for any given cycle was nominally linear. At much higher stress levels and/or temperatures above 427 °C (800 °F) (not reported herein), the mean strain response has been observed to increase significantly during initial loading cycles (Gabb et al., 1990). Later in the cyclic life the $[0°]_8$ composite revealed some increase in peak strain (fig. 3.2). This increase has been attributed to a combination of load shedding from the matrix to the fibers brought about by matrix stress relaxation and the accumulation of damage by crack

initiation and propagation (Gabb et al., 1990). Fractography and metallography of the $[0°]_8$ specimens revealed multiple internal crack initiation sites at fiber/matrix (F/M) interfaces. Cracks were also found to originate from surface locations. Individual cracks typically propagated a distance of 1 to 2 fiber diameters before coalescing.

For the $[90°]_8$ composite a nonlinear stress-strain response, such as that shown in figure 3.3, was observed for cyclic stress ranges greater than approximately 140 MPa (20 ksi). This nonlinear response results predominantly from F/M debonding and, with increasing stress, from plastic flow of the matrix (Majumdar and Newaz, 1992b). Significant increases in peak strain and strain range were observed with continued cycling for all stress ranges. These increases are believed to be chiefly associated with additional F/M interface damage and propagation of fatigue cracks from the interfaces. It is also likely that matrix creep contributes to the strain accumulation. Fractography and metallography clearly revealed numerous oxidized fatigue cracks originating exclusively from F/M interface locations. The cut or exposed SCS–6 fibers on the machined edges of the coupon appeared to enhance internal oxidation by serving as conduits for oxygen transportation.

3.4.3 Isothermal Fatigue Behavior

In a stress-based isothermal fatigue life comparison (fig. 3.4), the advantage of fiber direction reinforcement of the Ti-15-3 alloy became evident. In this comparison fatigue life N_f was plotted against maximum stress S_{max}; the S_{max} at $0.5 N_f$ was used for the unreinforced Ti-15-3, strain-controlled tests. The $[0°]_8$ composite had the longest life, followed by the unreinforced Ti-15-3 alloy and then the $[90°]_8$ composite. Note that for the unreinforced Ti-15-3 alloy the stress range would be double that shown because a balanced tension-compression stress condition existed at $0.5 N_f$. The exceptionally low life of the $[90°]_8$ composite was clearly a function of several identified processes, including fiber/matrix debonding, strain ratchetting brought about by matrix creep, and environmental effects associated with interface oxidation of exposed fibers. To help sort out these effects, a comparison of the $[90°]_8$ composite data run at 0.33 and 0.0083 Hz is instructive. If environmental degradation and/or strain-ratchetting effects were distinctively dominant, the specimens loaded at the lower frequency should have exhibited shorter

TABLE 3.1—REPRESENTATIVE TENSILE PROPERTIES FOR
SCS–6/Ti-15-3 AT 427 °C (800 °F)

Material	Initial elastic modulus		Yield (0.2 percent)		Ultimate tensile strength		Failure strain
	GPa	psi	MPa	psi	MPa	psi	
$[0°]_8$	195	28.3×10^{-6}	– –	– – – – –	1510	220×10^3	0.88
$[90°]_8$	110	16.0	240	34.8×10^3	325	47	1.48
Ti-15-3 matrix	85	12.3	840	121.8	885	128	20.00

TABLE 3.2—ISOTHERMAL FATIGUE DATA FOR SCS–6/Ti-15-3 AT 427 °C (800 °F)

Material	Control mode	Life, N_f	Maximum stress, S_{max}		Minimum stress, S_{min}		Strain range, $\Delta\varepsilon$, percent	Frequency, Hz
			MPa	psi	MPa	psi		
[a][0°]$_8$	Load	12 352	1034	150×10³	52	7.5×10³	0.57	0.16
		17 599	965	140	48	7.0	.49	.16
		29 845	896	130	45	6.5	.48	.16
		2 669	1338	195	0	0	.70	.33
		3 905	1255	182			.69	
		5 769	1110	161			.60	
		7 207	1192	173			.59	
		17 522	972	141			.54	
		54 835	807	117	↓	↓	.44	↓
[a][90°]$_8$	Load	1 683	172	25×10³	0	0	0.31	0.33
		3 603	138	20			.22	.33
		9 863	110	16			.15	.33
		166	221	32			.45	.0083
		1 179	172	25			.26	
		1 340	152	22			.22	
		8 774	138	20			.16	
		5 265	131	19			.18	
		23 643	110	16	↓	↓	.12	↓
Ti-15-3 matrix[b]	Strain	100 000+	303	44×10³	−290	−42×10³	0.65	0.33
		22 971	428	62	−434	−63	1.00	
		2 150	538	78	−559	−81	1.45	
		100 000+	407	59	−393	−57	.87	↓
Clad [0°]$_8$[a]	Load	25 619	483	70×10³	0	0	0.41	0.33
		17 027	552	80			.42	
		18 314	648	94			.50	
		8 783	793	115	↓	↓	.60	↓

[a]$\Delta\varepsilon$ values taken at 0.5 N_f.

[b]S_{max} and S_{min} values taken at 0.5 N_f.

lives, given that the exposure times per cycle were significantly greater (120 s versus 3 s) and loading rates were greatly reduced. Such trends have been clearly evidenced in the [0°] system (Gabb et al., 1991). However, figure 3.4 shows that the cyclic lives of specimens loaded at the two frequencies were essentially equivalent, strongly suggesting that the weak F/M bond was predominantly responsible for the short lives of the [90°]$_8$ composite. This conclusion is also supported by the fractography and metallography noted above, which revealed that all observable cracks began at F/M interfaces.

Returning to the discussion of isothermal tests conducted in the fiber direction, one sees that adding a Ti-15-3 cladding to the [0°]$_8$ composite diminished fatigue lives on a stress basis. This result was anticipated given that the overall fiber content was lower for the clad composite specimens, even though the composite core had the same fiber content as the unclad specimens. To normalize these results, a strain-based fatigue life plot is presented in figure 3.5, where strainrange $\Delta\varepsilon$ at 0.5 N_f is plotted against fatigue life. The $\Delta\varepsilon$-versus-N_f plot reveals that the lives of the clad and unclad [0°]$_8$ composites were equivalent at higher strainranges but that the clad composite specimens had shorter lives at lower strainranges.

Examining fracture surfaces of the clad specimens provided insight to help explain this life deficit. At higher strainranges fatigue initiation sites were found in both the Ti-15-3 case and the composite core, and in general, the cracks that began in the Ti-15-3 case did not have sufficient time to propagate into the composite core before failure occurred. Thus, internal core crack initiation/propagation was the primary failure mechanism, identical to that observed in tests on composites without the Ti-15-3 case. In contrast, at low strainranges numerous fatigue cracks began at the surface of the Ti-15-3 case and had sufficient time to propagate into the composite core (fig. 3.6). The composite core was essentially free of internal crack initiation sites. These case-initiated cracks may have accelerated crack propagation in the composite core by producing a larger crack that resulted in a higher stress intensity at the crack tip. This increased stress intensity would be more likely to cause fiber failure when the crack front reached the composite core.

As expected, the $\Delta\varepsilon$-versus-N_f plot (fig. 3.5) also reveals that the [90°]$_8$ composite exhibited inferior fatigue life properties, analogous to trends established in the S_{max}-versus-N_f plot (fig. 3.4). However, in contrast to the S_{max}-versus-N_f
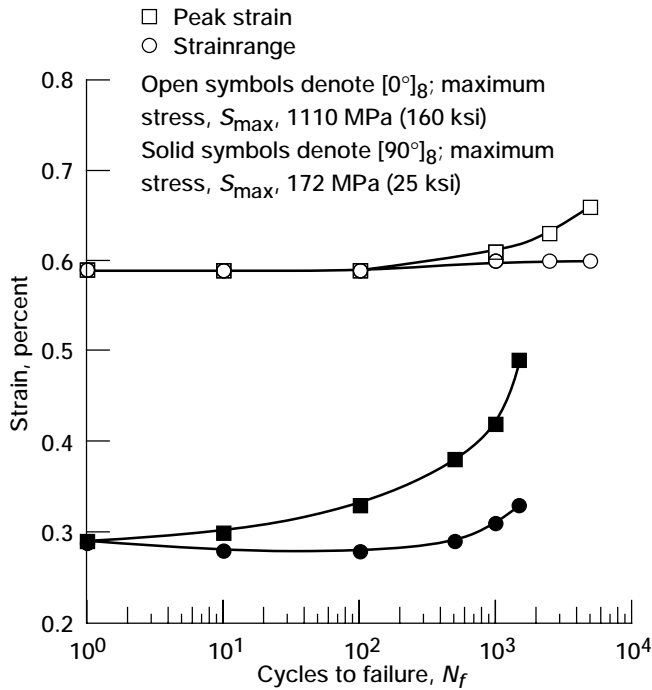
Figure 3.2.—Changes in strain responses typical of $[0°]_8$ and $[90°]_8$ SCS–6/Ti-15-3 during isothermal fatigue at 427 °C (800 °F).
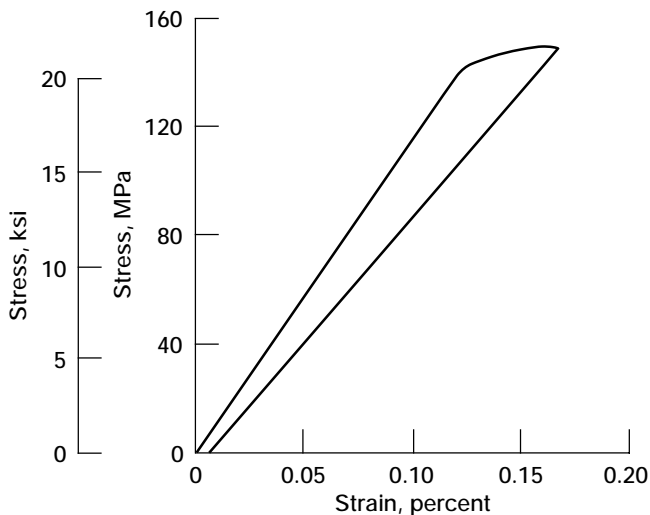
Figure 3.3.—Representative cyclic deformation response of $[90°]_8$ SCS–6/Ti-15-3 at 427 °C (800 °F). Cycle 1; maximum stress, S_{max}, 150 MPa (22 ksi).

Figure 3.4.—Stress-based, 427 °C (800 °F), isothermal fatigue life comparison for SCS–6/Ti-15-3.
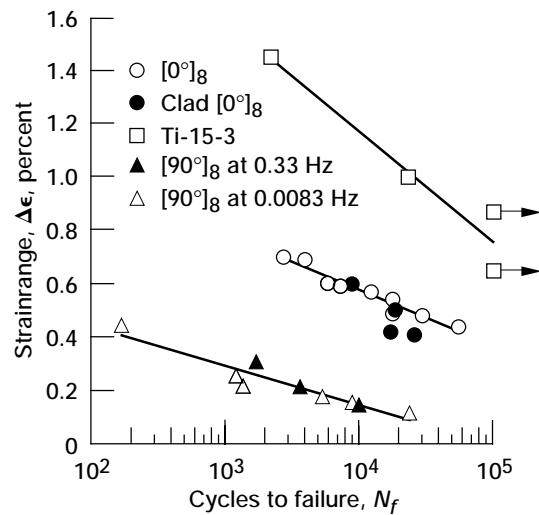
Figure 3.5.—Strain-based, 427 °C (800 °F), isothermal fatigue life comparison for SCS–6/Ti-15-3.

trends the strain-based plot reveals that the unreinforced Ti-15-3 alloy exhibited a significant life advantage over the $[0°]_8$ composite for a given strain. This advantage may be due in part to the vast differences in the mechanisms affecting crack initiation and propagation. At cyclic strainranges of less than 1 percent, crack initiation is a relatively long process for the

ductile, unreinforced Ti-15-3 alloy. However, for the $[0°]_8$ composite previous work (Gabb et al., 1991) has shown that crack initiation occurs rapidly and that most of the isothermal fatigue life is consumed during the propagation of matrix cracks. Further, at 427 °C (800 °F) there are multiple initiation sites throughout the cross section of the $[0°]_8$ composite, generally at the relatively brittle F/M interfaces. Taken in combination (i.e., the accelerated initiation of fatigue cracks at numerous F/M interfaces throughout the composite) and considering both the strain limitations of the SCS–6 fiber (fatigue strain $\varepsilon_f < 1$ percent) and the imposed zero-tension
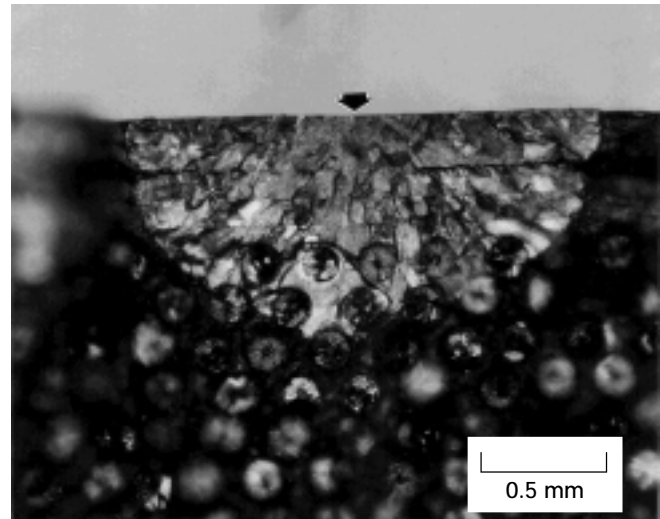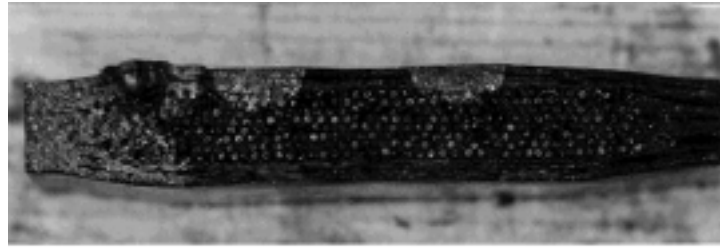
Figure 3.6.—Fracture surface of clad $[0°]_8$ SCS–6/Ti-15-3 specimen subjected to 427 °C (800 °F) isothermal fatigue at low strainrange. (Cracks begun in the Ti-15-3 case have propagated into the composite core.)

cycle, it is reasonable that the fatigue life of unreinforced Ti-15-3 alloy is greater than that of the associated $[0°]_8$ composite on a strain basis.

3.4.4 Thermomechanical Fatigue Behavior

Fatigue life results from the $[0°]_9$ TMF tests (Castelli et al., 1992) are plotted in figure 3.7 on a stress basis, along with a linear regression fit of the isothermal fatigue data generated at 427 °C (800 °F). The TMF data are also tabulated in table 3.3. Recall that the temperature cycle for the $[0°]_9$ TMF tests was 93 to 538 °C (200 to 985 °F). Given that the maximum temperature T_{max} for the TMF was 538 °C (985 °F) and that the isothermal data were generated at 427 °C (800 °F), additional isothermal data generated at 550 °C (1020 °F) (Gabb et al., 1990) are also included to better facilitate comparisons between isothermal and TMF conditions. In general, cyclic lives determined under TMF conditions were greatly reduced from those obtained under comparable isothermal conditions. Note that the IP and OP curves cross at an S_{max} of approximately 750 MPa (110 ksi), above which the IP conditions are life limiting and below which OP conditions appear to be more damaging. Three factors were identified as dominating the damage and failure mechanisms in the TMF

tests—environmental degradation, factors leading to enhanced strain ratchetting, and a coefficient-of-thermal-expansion (CTE) mismatch effect.

A CTE mismatch effect is present in many brittle and ductile composite systems because of the widely differing properties of the fiber and the matrix. Given that the CTE of the Ti-15-3 matrix ($\alpha_m \simeq 9.0 \times 10^{-6}$ °C^{-1} (5.0×10^{-6} °F^{-1}); Rosenberg, 1984) is more than twice that of the SCS–6 fiber ($\alpha_f \simeq 4.0 \times 10^{-6}$ °C^{-1}(2.2×10^{-6} °F^{-1}); Hillmer, 1991), internal stresses (tensile in the matrix and compressive in the fiber) are generated as the composite cools from elevated temperatures to room temperature. Work performed by Gabb et al. (1990) on this TMC system revealed that specimens subjected to 10 000 thermal cycles (from 300° to 550 °C (575 to 1020 °F)) under zero load did not exhibit degraded mechanical responses during subsequent tests. However, the CTE mismatch did promote highly localized cracks in the reaction zone and in the carbon-rich coating of the fibers. TMF conditions combine this cyclic CTE mismatch effect with the effects of mechanical loading, potentially enhancing the overall damage progression in the composite.

In-phase, zero-tension TMF (maximum load at maximum temperature) loading introduced conditions highly conducive to strain ratchetting. This effect was amplified over that
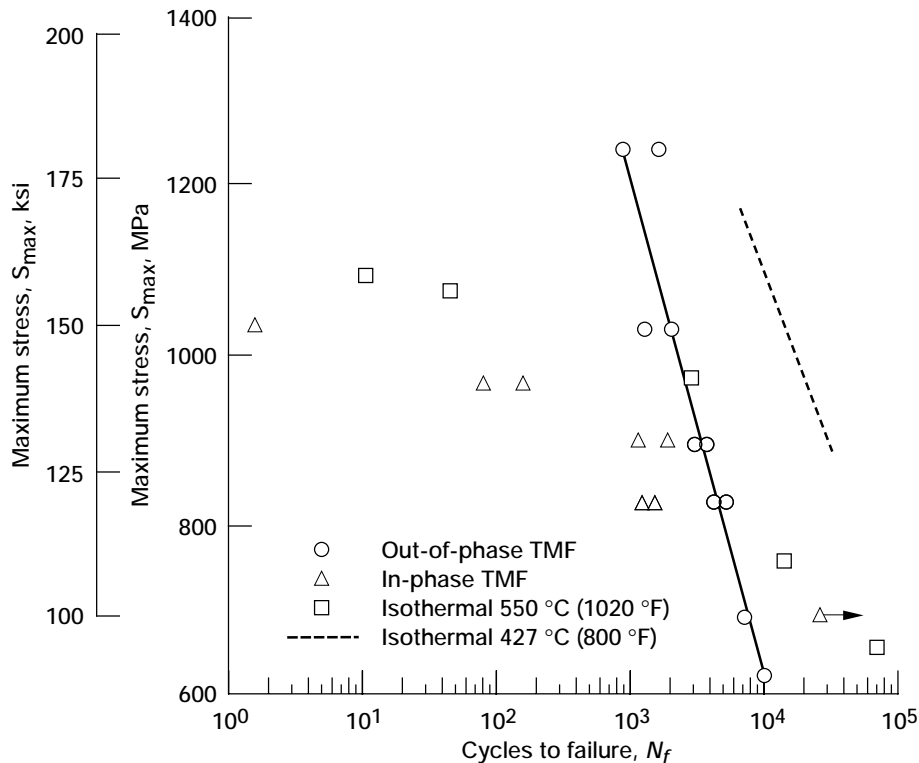
Figure 3.7.—Thermomechanical fatigue behavior of [0°]₉ SCS–6/Ti-15-3 with temperature cycle of 93 to 538 °C (200 to 1000 °F).

produced under zero-tension isothermal conditions because of the increasing elastic modulus and yield strength of the matrix (due to the decreasing temperature) during unload. Here, the "cold," nominally elastic unload reduced the degree of strain reversal, in turn enhancing the tensile strain-ratchetting effects associated with matrix load shedding. This effect is evidenced in figure 3.8, which shows the mechanical strain (total strain minus initial thermal strain) response from representative [0°]₉ IP and OP TMF tests. IP loadings produced notable increases in peak strain during initial loading cycles. Subsequently, the peak strain appeared to stabilize, exhibiting minimal or no detectable increases prior to failure; individual hysteresis loops were nominally linear. Also note that the strainrange did not increase, suggesting no change in the material's compliance. Fractography and metallography indicated that the IP damage and failure mechanisms were dissimilar to those revealed under isothermal and OP conditions. Fractographs revealed extensive fiber pullout and ductile matrix failure across the entire fracture surface. These features were very similar to those displayed by specimens subjected to tensile tests (Lerch and Saltsman, 1991), suggesting pure tensile overload failures in the IP tests. Metallographic sections clearly revealed extensive fiber cracking, in the absence of matrix cracking, in both the transverse (predominant) and longitudinal directions. This extensive fiber cracking is compatible with the fact that in an

IP TMF test the longitudinal CTE mismatch stresses combine with the mechanical loading stresses to produce a relative increase in the fiber stress range.

In contrast to IP loadings, OP loadings did not promote initial excessive strain ratcheting, as OP maximum loading occurs at the minimum temperature, where matrix load shedding and tensile strain ratchetting are not likely to occur. The strain response revealed only minor increases in peak strain at the onset of the test. Subsequently, a very gradual decreasing trend in peak strain was consistently detected in the OP tests as a possible result of a decreasing composite CTE. Matrix work hardening and/or the hardening effects associated with the precipitation of additional α-Ti phase may also have contributed to this decrease. Later in cyclic life ($N >$ 0.7N_f) the OP specimens displayed substantial increases in peak strain and strainrange (i.e., an increase in compliance), indicating damage accumulation. Fracture surfaces revealed flat fatigue cracks that began almost exclusively at surface and near-surface F/M interface locations. This perimeter of oxidized fatigue cracking (approximately two to three fibers into the cross section) surrounded an internal region that exhibited ductile matrix failure and fiber pullout indicative of tensile overload failure. Metallographic sections revealed that the primary cyclic fatigue damage consisted of matrix cracks normal to the load that began at surface and near-surface F/M interface locations. Little if any fiber damage was visible

TABLE 3.3.—THERMOMECHANI-
CAL FATIGUE DATA FOR
SCS–6/Ti-15-3

[Minimum stress, $S_{min} \approx 0$ MPa; load control.]

(a) $[0°]_9$ at 93 to 538 °C (200 to 985 °F) and 0.0056 Hz

Phasing	Life, N_f	Maximum stress, S_{max}	
		MPa	psi
IP[a]	1.5	1034	150×10³
	1.5	1034	150
	77	965	140
	150	965	140
	1 072	896	130
	1 870	896	130
	1 177	827	120
	1 595	827	120
	25 820	690	100
OP[b]	801	1241	180×10³
	1 540	1241	180
	1 178	1034	150
	1 919	1034	150
	2 954	896	130
	3 630	896	130
	4 333	827	120
	4 916	827	120
	7 145	690	100
	9 793	621	90

(b) $[90°]_8$ at 200 to 427 °C (400 to 800 °F) and 0.0083 Hz

Phasing	Life, N_f	Maximum stress, S_{max}	
		MPa	psi
IP	149	280	40×10³
	354	220	32
	1 455	180	26
	1 617	150	22
	3 440	140	20
	15 938	130	19
OP	1 013	280	40×10³
	1 585	250	36
	3 435	220	32
	20 938	150	22

[a]In phase.
[b]Out of phase.
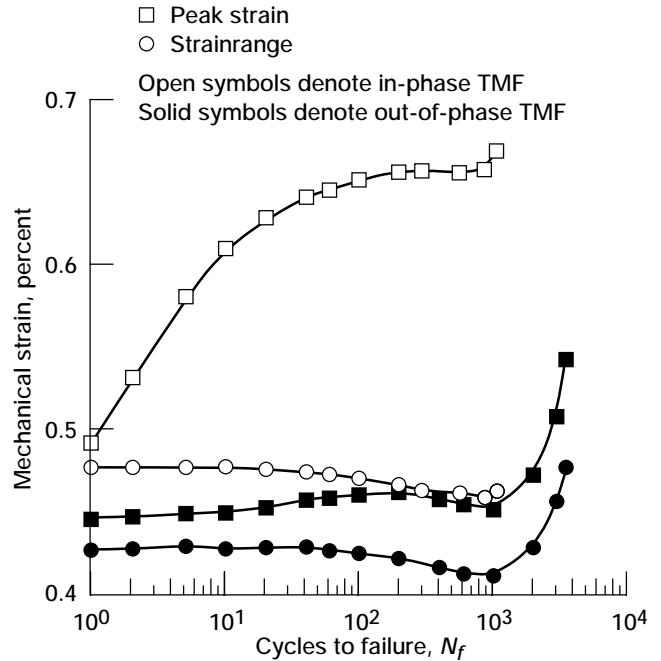
Figure 3.8.—Changes in strain response of $[0°]_9$ SCS–6/Ti-15-3 during in-phase and out-of-phase TMF with temperature cycle of 93 to 538 °C (200 to 1000 °F) and maximum stress S_{max} of 896 MPa (130 ksi).

away from the fracture surface. This observation of extensive matrix damage is compatible with the fact that in an OP TMF test the longitudinal CTE mismatch stresses combine with the mechanical loading stresses to produce a relative increase in the matrix stress range.

The results for the $[90°]_8$ composite TMF tests with a temperature cycle of 200 to 427 °C (400 to 800 °F) are tabulated in table 3.3 and plotted on a stress basis in figure 3.9, along with the 427 °C (800 °F) $[90°]_8$ isothermal data. The lives resulting from IP TMF were very similar to those produced under isothermal conditions at the maximum temperature of 427 °C (800 °F). In fact, given the zero-tension loading conditions investigated, the isothermal cycle appeared to be slightly more damaging at the higher stress levels. However, the comparative lives exhibited under OP TMF conditions were consistently greater by approximately an order of magnitude. These trends are obviously not consistent with those established by the $[0°]_9$ TMF results, indicating that the TMF damage mechanisms had changed. Many mechanisms leading to reduced $[0°]_9$ TMF lives relative to isothermal lives are either nonexistent or may be rendered ineffectual in the $[90°]_8$ system by the extremely weak F/M bond. Given that the F/M bond normal to the load direction is lost after the first cycle, $[0°]_9$ TMF mechanisms associated with load shedding from the matrix to the fiber and with CTE mismatch effects likely become inconsequential.
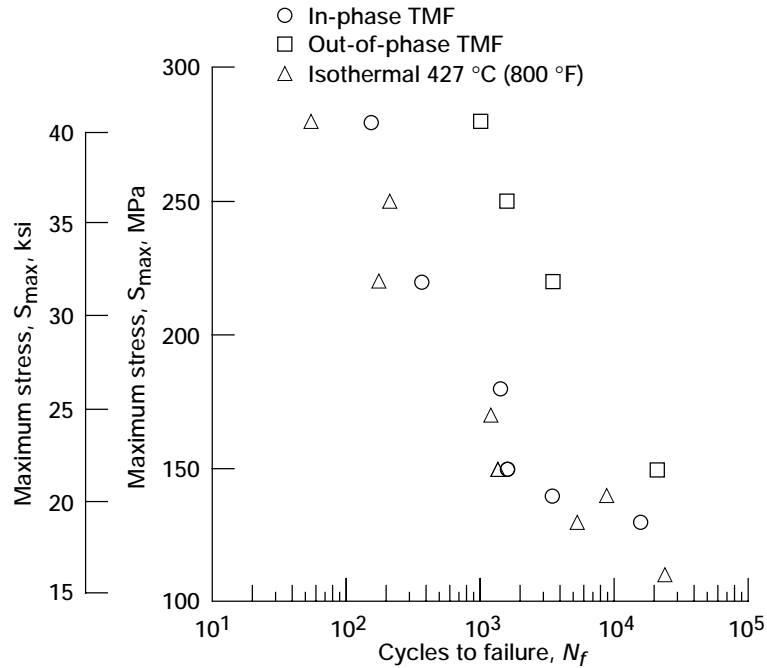
Figure 3.9.—Thermomechanical fatigue behavior of [90°]$_8$ SCS–6/
Ti-15-3 with temperature cycle of 200 to 427 °C (390 to 800 °F).

Mechanical strain responses are shown in figure 3.10 for IP and OP [90°]$_8$ TMF tests with S_{max} = 150 MPa (22 ksi). The first-cycle damage (i.e., stiffness degradation) was comparable for both the IP and OP loadings. However, the IP tests experienced a much higher rate of both strain ratchetting and stiffness degradation, as evidenced in figure 3.10. The IP tests experienced strain-ratchetting effects comparable to, but slightly less than, those typically observed during 427 °C (800 °F) isothermal loadings at 0.0083 Hz. Also, for equivalent values of S_{max} the 427 °C (800 °F) isothermal loading produced much greater first-cycle damage than that produced under IP TMF conditions (Castelli, 1992). For example, with an S_{max} of 150 MPa (22 ksi) the first-cycle stiffness degradation was approximately 10 percent for the IP TMF, but greater than 30 percent for the isothermal.

Optical and scanning electron microscope fractography confirmed the commonality in failure mechanisms between the 427 °C (800 °F) isothermal, IP TMF, and OP TMF. All TMF [90°]$_8$ fractographs revealed exclusive internal crack initiation at F/M interface locations. Oxidized F/M interface damage and fatigue crack propagation from the interfaces were identical to those for the isothermal tests. Again, the damage mechanisms appeared to be dominated by effects associated with the weak F/M interfaces and the exposed fiber ends serving as oxygen "pipelines" to the numerous internal cracks.
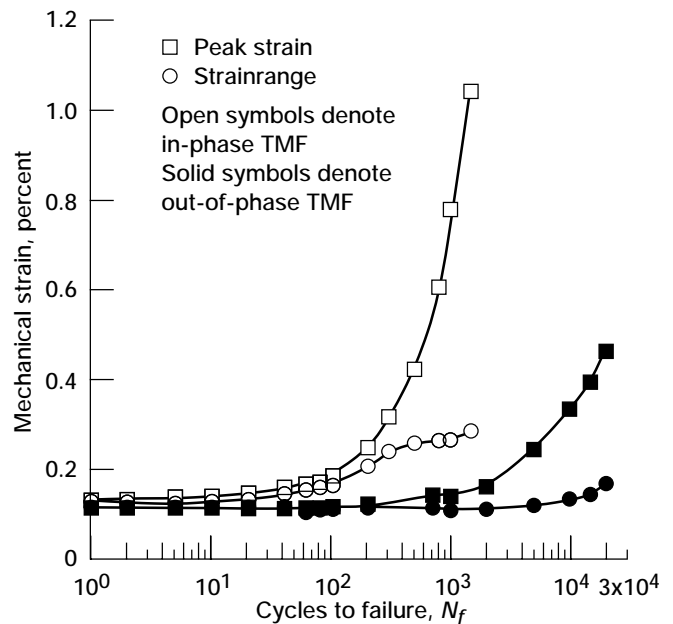

Figure 3.10.—Changes in strain response of [90°]$_8$ SCS–6/
Ti-15-3 during in-phase and out-of-phase TMF with tem-
perature cycle of 200 to 427 °C (390 to 800 °F) and max-
imum stress S_{max} of 150 MPa (22 ksi).

3.5 Summary of Results

A comprehensive coupon-level experimental investigation was conducted on unidirectionally reinforced SCS–6/Ti-15-3. This work was conducted to generate a self-consistent data base in support of a titanium-matrix composite (TMC) life prediction modeling effort ultimately aimed at predicting the burst strength and fatigue life of advanced TMC disks designed for gas turbine engine compressor rotor applications. These data were used for model development, characterization, and verification. The 427 °C (800 °F) isothermal fatigue and thermomechanical fatigue (TMF) behavior of the [0°] and [90°] systems were studied with emphasis placed on characterizing the key damage mechanisms. The following results were obtained:

(1) The 427 °C (800 °F) isothermal fatigue behavior of the [0°] TMC revealed significant strength and fatigue life improvements over the unreinforced Ti-15-3 matrix. However, these improvements only appeared in a stress-based comparison and were not evident in a strain-based comparison. Environmentally enhanced cracking was found to begin at internal fiber/matrix (F/M) interfaces and surface locations.

(2) Cladding the [0°] TMC with Ti-15-3 did not affect isothermal fatigue lives at higher strain levels, where numerous, small, core-initiated cracks predominated. In contrast, at lower strain levels large fatigue cracks began at the external surface of the case and propagated into the core, shortening the fatigue lives relative to that of the unclad material.

(3) The 93 to 538 °C (200 to 985 °F) [0°] TMF lives were significantly shorter than maximum-temperature isothermal lives. At high strains in-phase TMF produced extremely short lives, probably owing to fiber overload failures brought about by matrix stress relaxation. Metallography revealed a high degree of fiber cracking but no matrix fatigue cracking. At low strains out-of-phase TMF conditions became life limiting. Environmentally enhanced surface cracking was found to accelerate fatigue failure. Here, extensive matrix fatigue damage was observed with minimal fiber damage.

(4) The 427 °C (800 °F) isothermal fatigue behavior of the [90°] TMC exhibited significantly poorer fatigue properties than those of both the [0°] system and the unreinforced Ti-15-3 matrix; this was evidenced on both stress- and strain-based life comparisons. The poor fatigue properties were primarily attributed to the weak F/M interfacial bond. Fractography and metallography revealed numerous crack initiation sites exclusively at F/M interface locations. Environmental degradation was also enhanced by oxygen diffusion down exposed fiber ends.

(5) The 200 to 427 °C (400 to 800 °F) [90°] TMF conditions did not promote an additional reduction in cyclic life beyond that observed under maximum-temperature isothermal conditions. In-phase lives were essentially identical to 427 °C (800 °F) isothermal lives, and out-of-phase lives were typically an order of magnitude greater. On the basis of relative stiffness degradation the isothermal cycle was more damaging. Fractography of the [90°] TMF specimens revealed damage mechanisms identical to those experienced under isothermal conditions.

Although much has been learned concerning the elevated fatigue damage mechanisms in unidirectional TMC's, several issues remain that need to be addressed. The most obvious are the effects of fully reversed loading, loading in a strain-controlled environment, variation in fiber content, and multiaxial loadings. Each will quite likely have some influence on the fatigue damage mechanisms and resulting cyclic lives.

3.6 Conclusions

In this study to characterize the fatigue behavior of unidirectionally reinforced titanium-matrix composites (TMC's), the following conclusions were drawn:

(1) TMC fatigue behavior and damage mechanisms will vary with the loading direction in components. Cyclic loads oriented at 90° to the fiber reinforcement axis can degrade fatigue behavior by accelerating damage.

(2) Fatigue behavior and damage mechanisms can also vary with temperature conditions. TMF loading at 0° to the fibers provides lower life than isothermal loading by activating different damage mechanisms.

(3) Cladding the TMC cores to prevent cut and exposed fibers will not necessarily improve TMC fatigue resistance.

References

Castelli, M.G., 1992, "Thermomechanical Fatigue Behavior of a [90°]$_8$ SCS–6/Ti-15-3 Composite," *HiTEMP Review 1992: Advanced High-Temperature Engine Materials Technology Program*, NASA CP–10104, Vol. 2, pp. 52–1 to 52–14.

Castelli, M.G., Bartolotta, P.A., and Ellis, J.R., 1992, "Thermomechanical Testing of High-Temperature Composites: Thermomechanical Fatigue Behavior of SiC(SCS–6)/Ti-15-3," *Composite Materials: Testing and Design*, G.C. Grimes, ed., American Society for Testing and Materials, Philadelphia, PA, pp. 70–86.

Gabb, T.P., Gayda, J., and MacKay, R.A., 1990, "Isothermal and Nonisothermal Fatigue Behavior of a Metal Matrix Composite," *Journal of Composite Materials*, Vol. 24, pp. 667–686.

Gabb, T.P., Gayda, J., and MacKay, R.A., 1991, "Nonisothermal Fatigue Degradation of a SiC/Ti Composite," *Advanced Composite Materials: Processing, Microstructures, Bulk, and Interfacial Properties, Characterization Methods, and Applications*, M.D. Sacks, ed., American Ceramic Society, Westerville, OH, pp. 527–534.

Gayda, J., and Gabb, T.P., 1992, "Isothermal Fatigue Behavior of a [90°]$_8$ SiC/Ti-15-3 Composite at 426 °C," *International Journal of Fatigue*, Vol. 14, No. 1, pp. 14–20.

Hillmer, N.J., 1991, "Thermal Expansion of High Modulus Fibers," *International Journal of Thermophysics*, Vol. 12, No. 4, pp. 741–750.

Johnson, W.S., Lubowski, S.J., and Highsmith, A.L., 1990, "Mechanical Characterization of SCS–6/Ti-15-3 Metal Matrix Composites at Room Temperature," *Thermal and Mechanical Behavior of Ceramic and Metal Matrix Composites*, H.H. Moeller and W.S. Johnson, eds., American Society for Testing and Materials, Philadelphia, PA, pp. 193–218.

Lerch, B.A. and Saltsman, J., 1991, "Tensile Deformation Damage in SiC Reinforced Ti/15V-3Cr-3Al-3Sn," NASA TM–103620.

Majumdar, B.S. and Newaz, G.M., 1992a, "Inelastic Deformation of Metal Matrix Composites: Plasticity and Damage Mechanisms," Part I, NASA CR–189095.

Majumdar, B.S. and Newaz, G.M., 1992b, "Inelastic Deformation of Metal Matrix Composites: Plasticity and Damage Mechanisms," Part II, NASA CR–189096.

Rosenberg, H.W., 1984, "Ti-15-3 Property Data," *Beta Titanium Alloys in the 80's*, R.R. Boyer and H.W. Rosenberg, eds., The Metallurgical Society of American Institute of Mining, Metallurgical and Petroleum Engineers, Warrendale, PA, pp. 409–432.

Chapter 4
Life Prediction Method for Matrix-Dominated Fatigue Failures of SCS–6/Ti-15-3 MMC

Phillip W. Gravett*

4.1 Introduction

For advanced turbine engine designs to realize the potential benefits offered by metal-matrix composites (MMC's), design, analysis, and life prediction methods must be developed and demonstrated. Numerous methods have been developed for predicting MMC laminate life. Analytical models to predict fatigue crack initiation life for longitudinal plies of MMC based on the fatigue behavior of the titanium-matrix material include a local strain criteria (Hillberry and Johnson, 1992) and a linear life fraction model. Other models include a differential continuum damage mechanics model (Robinson and Pastor, 1992), a strain-based fatigue approach (Halford et al., 1989), and a maximum laminate stress model (Harmon et al., 1987). The matrix-based models are very similar to the methods described in this chapter and should give similar results.

The primary objective of developing an MMC life prediction system at Pratt & Whitney was to provide an automated life prediction system for use in designing high-temperature gas turbine engines. The life system must be accurate, efficient, and versatile enough to be applied to optimizing MMC geometry and component design. The main driver for developing an efficient life prediction system is the complex loading and temperature spectrum that gas turbine engine components experience during a typical fighter aircraft mission (fig. 4.1). This spectrum can include dozens of cyclic load reversals and constantly varying temperature. For this type of analysis Pratt & Whitney developed an integral analysis method and life prediction model that is maturing into a life prediction tool for use by design and structural analysis engineers. This complete life prediction system involves five

analysis steps (fig. 4.2): steps 1 to 3 for determination of MMC laminate stress-strain behavior, steps 4 and 5 for decomposition of laminate stresses to the constituent stresses, and step 6 for life prediction.

Extensive test data were generated in the cooperative program to support the development of analytical models and the verification of life prediction methods. Data were generated at NASA Lewis Research Center, Pratt & Whitney Government Engines and Space Propulsion, and the United Technologies Research Center. Flat-panel coupon specimens of fiber contents ranging from 33 to 40 vol % were tested in isothermal fatigue, thermomechanical fatigue, and bi-thermal fatigue, providing a wide range of composite geometries and conditions to exercise and verify the life prediction modeling.

4.2 MMC Mechanical Properties

Before a component stress analysis is performed, the material properties of the MMC must be determined from its constituent material properties. The methods developed address modeling the MMC on a micromechanical level with published closed-form-solution, representative-volume-element models (Agarwal and Broutman, 1980, pp. 15–71; and Pangborn et al., 1988) and modeling on a macromechanical level with standard laminate theory (Agarwal and Broutman, 1980, pp. 105–183). Closed-form solutions are required for a life prediction system, although not for a finite-element-method unit cell model, for efficiency in operating the system in a timely manner. Fighter aircraft engines typically go through numerous throttle excursions throughout a complex mission, causing component stresses to vary constantly during flight. To accurately predict the cyclic life of the component, each cyclic stress excursion must be analyzed and a life predicted.

*United Technologies—Pratt & Whitney Government Engines and Space Propulsion, West Palm Beach, Florida 33410.
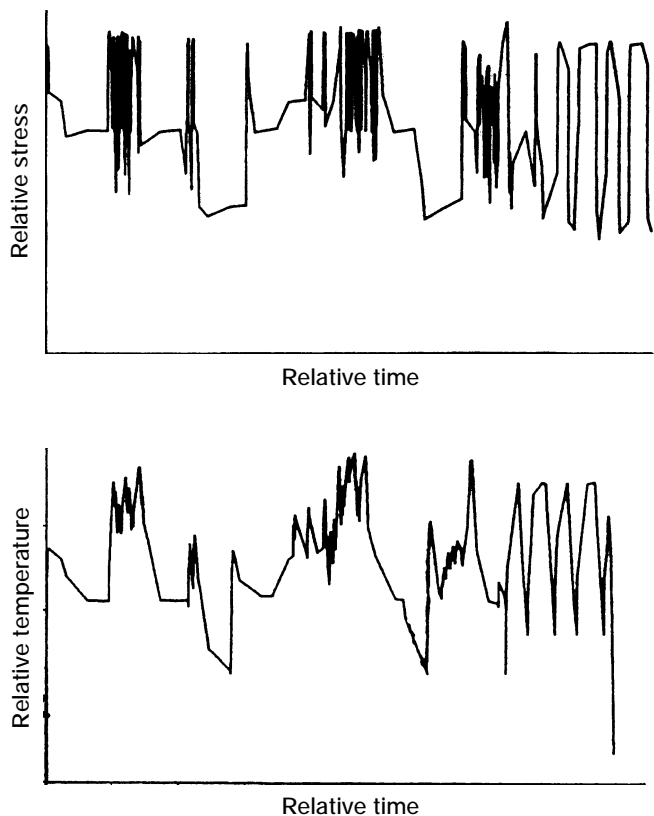
Figure 4.1.—Typical fighter aircraft engine spectrum.

The following is a review of the concentric-cylinder-model (CCM) and rule-of-mixtures (ROM) constitutive models used for longitudinal stress-strain properties and the laminate theory used for multiple-ply composites. These micro- and macro-mechanical models are used to determine the composite laminate stress-strain behavior and to decompose the laminate applied loads into the constituents' stresses for life prediction.

4.2.1 Micromechanical Modeling

Because MMC's are produced by combining two distinct constituent materials, a high-stiffness, high-strength, brittle fiber and a moderately stiff ductile matrix, they can be considered as a micromechanical structure. When reduced to the smallest two-dimensional representative volume element, this "structure" consists of a circular fiber surrounded by matrix material. The most common modeling of this representative volume element is by the rule of mixtures (Agarwal and Broutman, 1980, pp.15–71), which calculates properties on the basis of volume fractions of the fiber and matrix. A more versatile model is the concentric cylinder model, which assumes that the matrix is a cylinder surrounding a single fiber (fig. 4.3). This model calculates not only the longitudinal properties of the composite but also the variation of stress in the matrix surrounding the fiber under uniaxial loading. In

both models strain compatibility between fiber and matrix in the fiber direction requires no differential movement at the fiber/matrix interface (i.e., the interface is a perfect bond). For either model fiber and matrix properties are required at the analysis conditions to calculate MMC properties.

This micromechanical structure has an inherent thermal stress problem caused by the difference in coefficient of thermal expansion between fiber and matrix. Processed at high temperature and then cooled, MMC's have considerable thermal residual tensile stress in the matrix and compressive stress in the fiber at lower temperatures. These residual thermal stresses and strains can be combined with those induced from mechanical loading by using the principle of superposition. Because the matrix residual strain is tensile, the additional mechanical strain required to produce plastic yielding of the matrix is much less than the yield strain of the monolithic matrix material. This effect must be accounted for in determining the breakpoint described below. A benefit resulting from the thermal residual strain is a strain to failure in the MMC that is greater than that of the fibers alone. This is possible because the fiber thermal residual strain is compressive, thus increasing the mechanical strain that can be applied to the MMC before fiber ultimate failure.

Typically, the longitudinal stress-strain curve of an MMC can be summarized by using two straight lines. This process is called the bilinear effect, and the point where the two lines intersect is called the breakpoint (see fig. 2.8). Presently, Pratt & Whitney uses a thick-concentric-cylinder model with an anisotropic coefficient of thermal expansion (CTE) (Pangborn et al., 1988) to calculate MMC longitudinal mechanical properties. This CCM, being an elastic model, is used directly to determine the primary elastic modulus of the MMC in the longitudinal fiber direction along with Poisson's ratio and the CTE. The matrix material is modeled as elastic–perfectly plastic; therefore, the MMC stiffness beyond the material breakpoint is the result of the stiffness contribution of the fibers. Beyond the breakpoint the validity of the CCM is reduced by plastic deformation and loss of stiffness in the matrix; therefore, the ROM is used in this region. Transverse-direction elastic modulus, shear modulus, and minor Poisson's ratio are calculated by using the ROM.

The process developed to determine the breakpoint stress for an MMC relies on an empirical correlation from coupon test data gathered for available fiber contents and temperatures. The CCM is used to calculate the radius in the matrix at which the von Mises stress is equal to the 0.2-percent yield stress because the thermal residual stress and the mechanical load correspond to the test specimen's breakpoint load. This radius is used to calculate a matrix yield area ratio, which is the total matrix area divided by the matrix area over the yield stress (fig. 2.7). A population of these matrix yield area ratios is calculated from the coupon test data and used to determine a value that best fits the experimental data. This matrix yield area can then be used to determine the breakpoint stress for

Component analysis

3. Perform finite-element analysis to determine the stress-strain state.

Laminate analysis

2. Calculate the composite stress-strain state.

4. Calculate the stress and strain in each ply.

Microstructural analysis

1. Calculate the ply stress-strain properties and the thermal residual stress state.

5. Calculate the stress and strain in the fiber and fiber/matrix interface.

START
Matrix and fiber properties and composite layup

Life analysis

6. Perform the life analysis based on the microstructural stress and strain state.
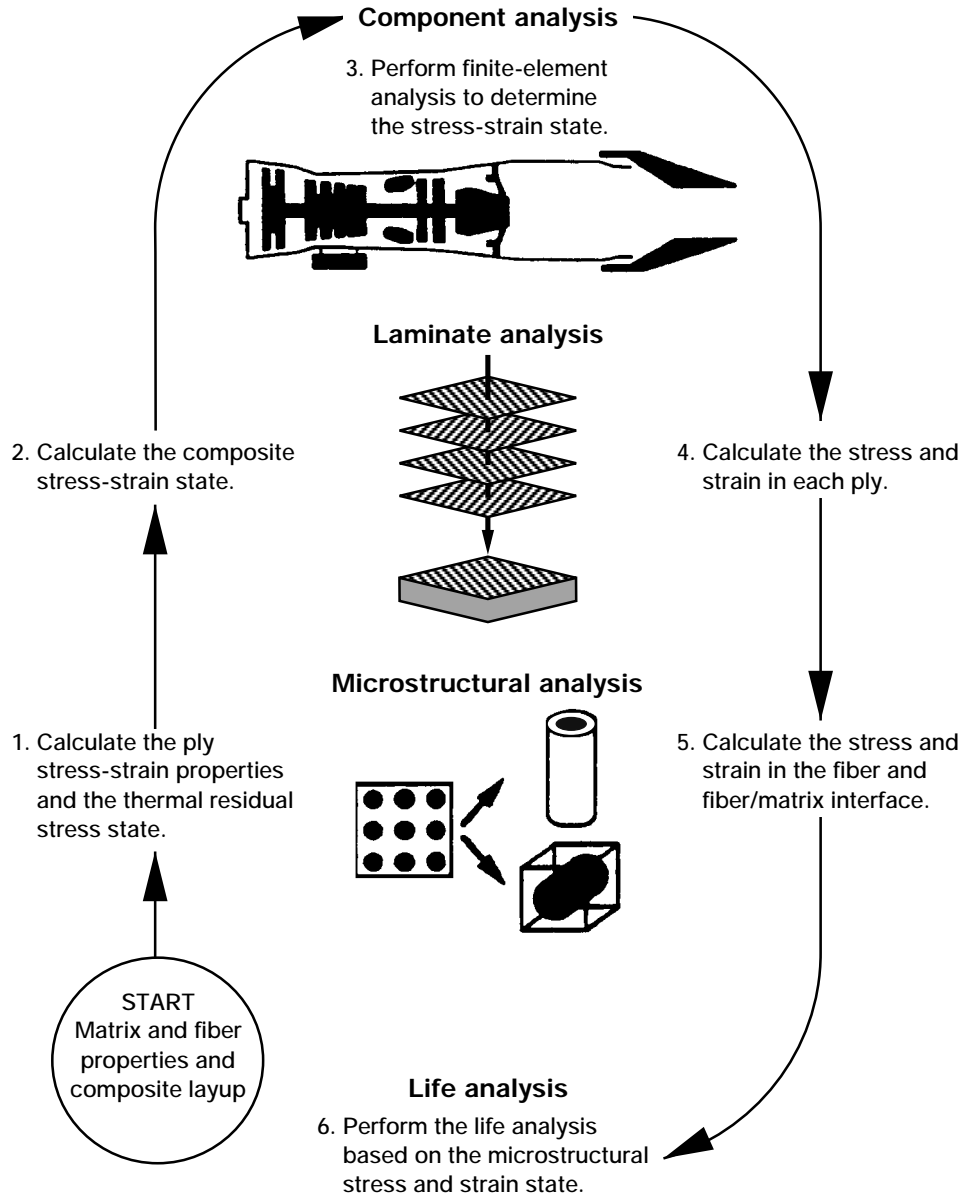
Figure 4.2.—MMC life prediction system analysis procedure.

any combination of fiber volume and temperature. With the primary and secondary moduli and the breakpoint stress defined, the longitudinal tensile stress-strain response of the MMC is fully defined.

4.2.2 Macromechanical Modeling

The longitudinal properties of unidirectional composites are controlled primarily by fiber properties, whereas the transverse properties are primarily matrix dominated. This results in an orthotropic material with high capability in the fiber direction and low capability in the transverse directions. This behavior is easily identified by the MMC data and modeling

described above. In many engineering applications complex applied loads require high material capability in several directions. This apparent limitation on the use of unidirectional composites is overcome by forming laminates from individual unidirectional layers consolidated in different directions. Laminates are formed from two or more unidirectional layers bonded together to act as an integral structural element. The bond between two layers in a laminate is assumed to be perfect; thus, displacements remain continuous across the bond.

To produce a structural element with the required properties for the component geometry and loading, the layer principal material directions are oriented to result in satisfactory MMC laminate properties for the application. In order to
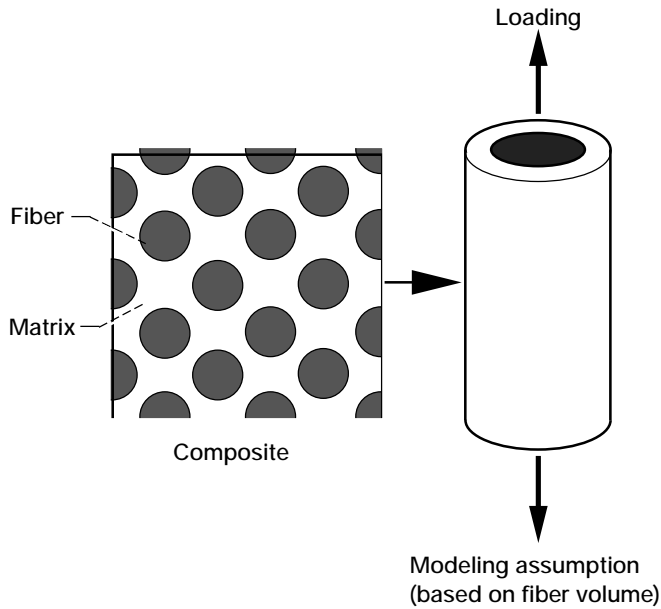
Figure 4.3.—Concentric cylinder MMC micromechanical modeling assumption.

analyze these multiple-layer laminates, classical laminate theory is used to determine the extensional stiffness of the system (Agarwal and Broutman, 1980, pp. 105–183). Classical laminate theory, in its most general form, determines the stress-strain relations for an orthotropic material with the generalized Hooke's law. After transformation of the stress-strain relations to global coordinates for individual layers of different orientations, mathematical assembly of the various layer properties is completed to construct the extensional stiffness matrix that defines the laminate properties. This matrix contains the stiffness information in the primary laminate directions.

As in micromechanical modeling, differences in directional thermal expansion caused by the variation in layer orientation after consolidation induce significant thermal residual stresses. These thermal residual stresses must be accounted for in determining layer stiffness and multiple breakpoint yielding. This procedure is used to determine the tensile stress-strain response of a multiple-angle-ply MMC laminate in the primary orientation for use in finite-element analysis of turbine engine components.

4.3 Fatigue Life Prediction Method

Fatigue life prediction in the Pratt & Whitney life prediction system is based on the matrix material dominating the longitudinal fatigue behavior of the MMC. This assumption has been supported by test data and failure mechanisms identified in unidirectional isothermal and out-of-phase thermomechanical fatigue specimens, which typically show an area of matrix cracking before failure (Gabb et al., 1990; Gayda and Gabb, 1991). This behavior can be seen as the characteristic flat fatigue crack regions surrounding the rough tensile overload region in figure 4.4. A typical scenario for this failure mechanism is that this matrix cracking propagates through the MMC, leaving the fibers intact. Opening the crack increases the stress in the bridging fibers between the crack faces. As the crack propagates, the local fiber stresses increase, eventually causing fiber failure, which leads to composite failure. Under these assumptions the matrix fatigue capabilities can be characterized by testing MMC coupon specimens. Likewise, MMC component life can be predicted from matrix fatigue capabilities. This is the process developed by Pratt & Whitney for characterization and life prediction of MMC's.
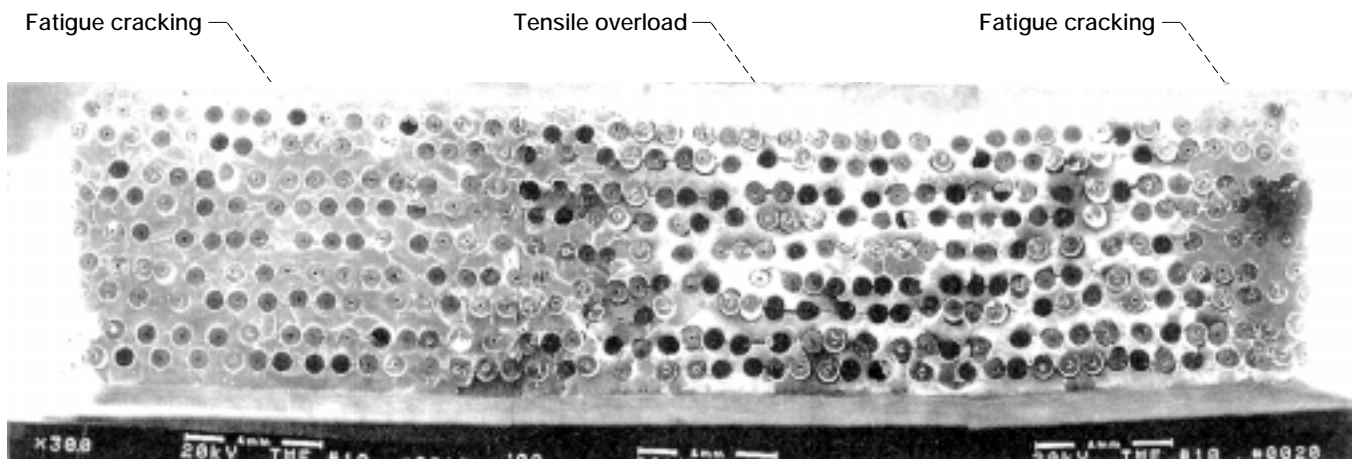
Figure 4.4.—Fatigue fracture surface characterized by fatigue cracking and tensile overload.

4.3.1 Life Prediction Model

Because matrix fatigue capabilities dominate composite fatigue behavior, matrix response to laminate loading must be determined in order to model damage within the composite. To model the matrix response, the MMC concentric cylinder model is used to characterize the state of stress in the matrix at the fiber/matrix interface due to processing of thermal residual stresses and loading. By using the heat treatment conditions as the temperature at which thermal residual stresses are relieved (Gayda et al., 1989) and the procedure described here, the stresses and strains for a laminate at all temperature-load conditions throughout a mission can be determined (fig. 4.5). Thermal residual stresses and strains are calculated from the CCM by analyzing the change in temperature from heat treatment to room temperature (point A in fig. 4.5). Because raising the temperature to test or operating conditions also relieves thermal residual stress, a similar analysis must be completed for this temperature change (point B in fig. 4.5). Stresses and strains induced from mechanical loading are combined with thermal residual stresses by superposition (point C in fig. 4.5). The states of stress in the matrix at the fiber/matrix interface at all the maximum and minimum loads during a mission are calculated with this procedure to determine the cyclic damage the matrix is incurring. Reduction of these data is described below.

Because each temperature-load combination produces a unique fiber/matrix stress response (fig. 4.6), the Smith-Watson-Topper stress parameter (Smith et al., 1970) is applied to the matrix stresses to determine a "corrected" matrix fatigue stress. The equation is as follows:

$$\sigma_{\text{matrix effective}} = \left[\sigma_{\text{matrix max}} \frac{\Delta \varepsilon}{2} E_{\text{matrix}} \right]^{1/2}$$

where

$\sigma_{\text{matrix max}}$ maximum stress on matrix during load cycle

$\Delta \varepsilon$ strainrange of matrix during load cycle

E_{matrix} elastic modulus of matrix

This parameter defines the empirical relation that relates failure at a given life under nonzero mean matrix cyclic stress to failure at the same life under zero mean matrix stress. This procedure effectively isolates the fatigue capability of the matrix from laminate geometry and laminate stress. It consolidates not only data for different load-temperature cycles but also data for laminates with different fiber contents, since matrix stress variations with fiber content are accounted for in the micromechanical models. A single fatigue curve can then be used to predict the fatigue capability of any MMC of the same materials at various loadings and fiber contents. The
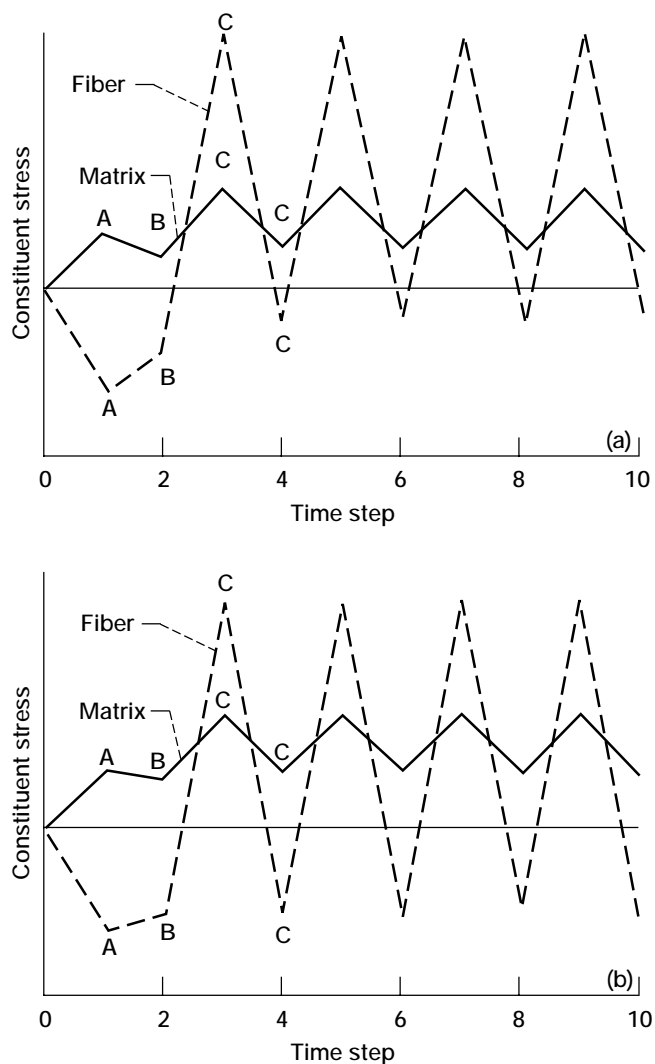
Figure 4.5.—Fiber and matrix thermal and mechanical stresses. (a) Low-cycle-fatigue loading. (b) Out-of-phase thermomechanical force loading.

closed-form-solution micromechanical model and the Smith-Watson-Topper stress parameter combine to make the life prediction system efficient to operate and versatile enough to be used for optimizing MMC geometries.

4.3.2 Life Prediction Verification

Under the cooperative program a test matrix was laid out to characterize the SCS–6/Ti-15-3 MMC at conditions representative of the rings to be tested near the end of the program. NASA Lewis Research Center, Pratt & Whitney, and the United Technologies Research Center contributed to this test matrix. The insignificant variation in results between test facilities reinforced confidence in the quality and maturity of the material and the test methods used in the program. This
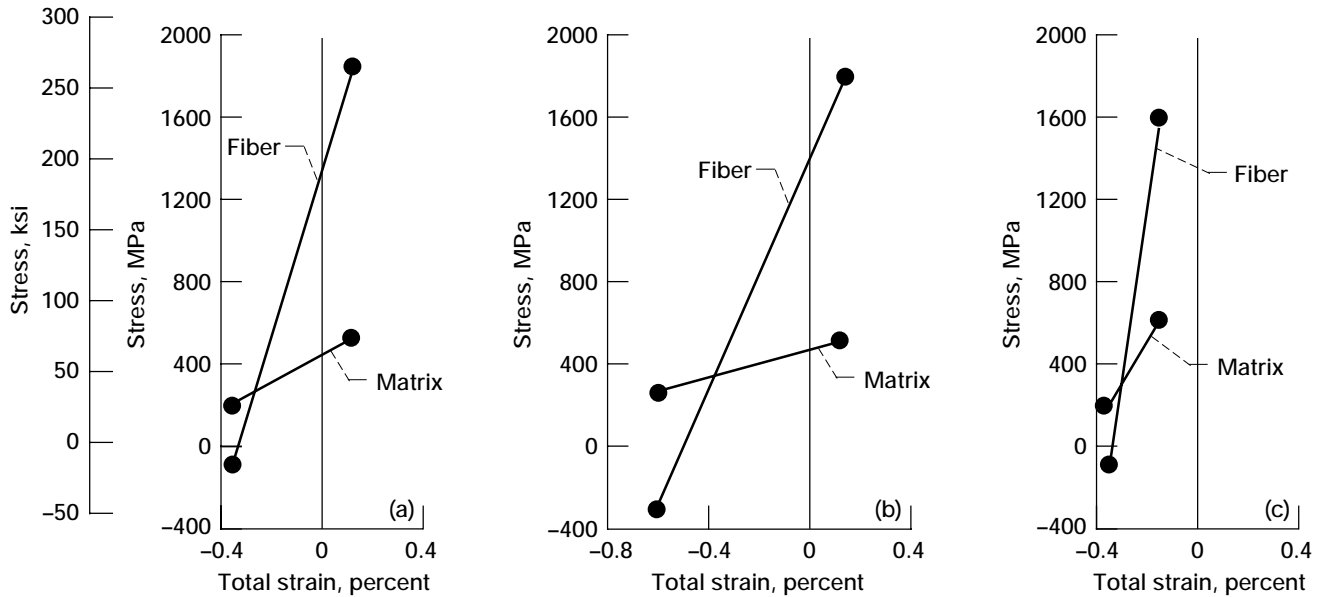
Figure 4.6.—Unique fiber/matrix stress response for each temperature-load history. (a) Low-cycle-fatigue loading. (b) In-phase thermomechanical fatigue loading. (c) Out-of-phase thermomechanical fatigue loading.

diverse material data base provided adequate data to characterize the MMC material and to verify the life prediction system.

Analyzing the data generated for this program by using the Pratt & Whitney-developed life prediction system gave promising results. Coupon specimens with fiber contents of 33, 34, 35, and 38 vol % were tested in isothermal fatigue at 427 °C (800 °F), in bi-thermal fatigue, and in thermomechanical fatigue (see chapter 2). The scatter in these test data was rather large, making it impossible to identify behavior trends (fig. 4.7). This scatter was mostly the result of the different load capacities of MMC's with various fiber contents. In addition, the various load histories induced unique stresses and strains in the fiber and matrix that caused different levels of damage. Reducing the data by using the life prediction modeling methods described in this chapter effectively eliminated this scatter. The life prediction modeling methods consolidated all the test data into a single band of data characterizing the matrix fatigue capability (fig. 4.8). Predicting the lives of the test specimens by using this model resulted in a mean ratio of actual to predicted life of 1.03 and a $L_{0.1}$ scatter factor[1] of 3.19; see figure 4.9 for a typical prediction. This level of accuracy is good relative to many fatigue life prediction systems developed for monolithic materials.

Fiber content, vol %	Load ratio (min/max), R		Fiber content, vol %	Load ratio (min/max), R
38	0.1		34	0.5
38	0.5		34	0.0
35	0.1		34	0.05
33	0.0		34	0.05(TMF)
38	0.1(TMF)		34	0.05
34	0.1			
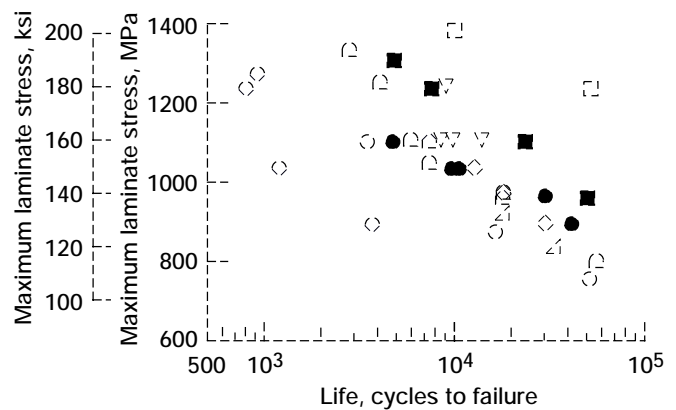
Figure 4.7.—SCS–6/Ti-15-3 isothermal, bi-thermal, and thermomechanical fatigue data.

---

[1]Probabilistic factor by which the mean life is divided to obtain a 0.1-percent-probability life.
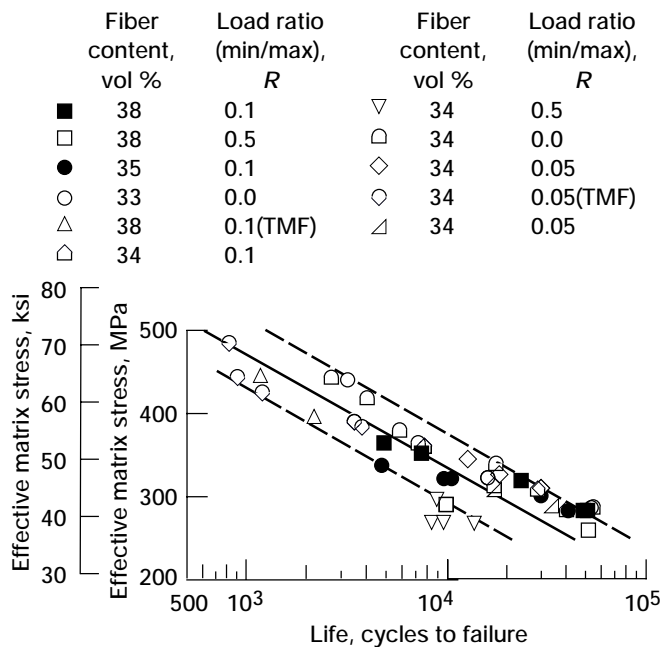
Figure 4.8.—SCS–6/Ti-15-3 data consolidated into single fatigue curve.

Figure 4.10.—Predictions from MMC life prediction system. Material, SCS–6/Ti-15-3; temperature, 427 °C (800 °F).

Figure 4.9.—Typical prediction of SCS–6/Ti-15-3 fatigue data. Fiber content, 34 vol %; load ratio (minimum applied load divided by maximum applied load), R, 0.1; temperature, 427 °C (800 °F).
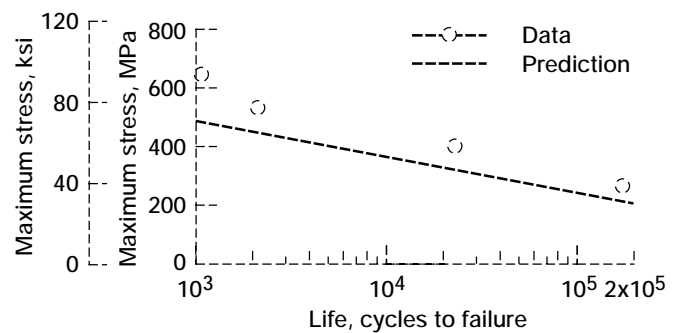
Figure 4.11.—Prediction of monolithic fatigue data with MMC life prediction system. Ti-15-3 fiberless composite; load ratio (minimum applied load divided by maximum applied load), R, 0.1; temperature, 427 °C (800 °F).

4.3.3 Life Prediction Applications

Because the corrected matrix stress fatigue response is independent of fiber content, stress ratio, and load history, this MMC life prediction system can predict the fatigue behavior of any relevant laminate and loading. Coupon test data at the temperatures of interest are required to empirically determine the fatigue characterization curves for life prediction. This life prediction system can predict fatigue life for laminate geometries and loadings at which no test data exist (fig. 4.10). This capability will prove valuable when designing engine components where optimization of MMC capabilities is required but testing is limited.

This method was taken to an extreme by predicting the isothermal low-cycle-fatigue life of Ti-15-3 matrix material consolidated with the same procedure as the MMC panels, creating a "fiberless composite." Even though the monolithic material was not included in the model generation, the predictions are quite accurate, although consistently lower than the test data (fig. 4.11). This result was expected, since MMC's typically have microcracks in the fiber/matrix interaction zone that act as crack initiators, thus reducing the fatigue life of the "real" composite from that of a defect-free composite. This implies that, in the absence of any MMC fatigue data, MMC laminate fatigue life can be approximated from "adjusted" monolithic fatigue data.

4.4 Conclusions

The metal-matrix-composite (MMC) fatigue life prediction method presented in this chapter was developed and refined with extensive test data generated for the Pratt & Whitney/

NASA Lewis Research Center cooperative program. This life prediction system is limited to matrix-dominated fatigue failures but proved very accurate at determining the fatigue capabilities of MMC's tested under these conditions. The system's accuracy is comparable to that of monolithic material life prediction systems. The life prediction system incorporates closed-form-solution MMC micromechanical models and a fatigue stress damage parameter. The resulting automated system operates efficiently and can easily be run by the typical component design or analysis engineer. This aspect of the life system is especially important, since the inherent values of any analysis tool are its suitability to the application and its usability by the engineer. The advantage of a life prediction system based on the response of the fiber and matrix is the independence from fiber content, loading, or temperature. With this versatility and the requirement for few characterization data, life prediction can contribute to optimizing MMC structures at the preliminary design level. Also, testing may be planned to more effectively characterize conditions and parameters specific to the failure modes of interest.

References

Agarwal, B.D., and Broutman, L.J., 1980, *Analysis and Performance of Fiber Composites*, John Wiley & Sons, Inc., New York.

Gabb, T.P., Gayda, J., and MacKay, R.A., 1990, "Isothermal and Nonisothermal Fatigue Behavior of a Metal Matrix Composite," *Journal of Composite Materials*, Vol. 24, No. 6, pp. 667–686.

Gayda, J., and Gabb, T.P., 1991, The Effect of Cut/Exposed Fibers on the Fatigue Life of a SCS–6/Ti-15-3 Composite, *HiTEMP Review 1991: Advanced High-Temperature Engine Materials Technology Program,* NASA CP–10082, pp. 37–1 to 37–7.

Gayda, J., Gabb, T.P., and Freed, A.D., 1989, "The Isothermal Fatigue Behavior of a Unidirectional SiC/Ti Composite and the Ti Alloy Matrix," NASA TM–101984.

Halford, G.R., Lerch, B.A., Saltsman, J.F., Arya, V. K., and Caruso, J.J., 1989, "Low-Cycle Fatigue Prediction for Metal Matrix Composites," *HiTEMP Review 1989: Advanced High-Temperature Engine Materials Technology Program*, NASA CP–10039, pp. 64–1 to 64–9.

Harmon, D.M., Saff, C.R., and Sun, C.T., 1987, "Durability of Continuous Fiber Reinforced Metal Matrix Composites," AFWAL–TR–87–3060, Air Force Wright Aeronautical Laboratories, Wright-Patterson Air Force Base, OH.

Hillberry, B.M., and Johnson, W.S., 1992, "Prediction of Matrix Fatigue Crack Initiation in Notched SCS–6/Ti-15-3 Metal Matrix Composites," *Journal of Composites Technology Research*, Vol. 14, No. 4, pp. 221–224. (Also NASA TM–104141.)

Pangborn, R.N., Queeney, R.A., and Vedula, M., 1988, "Fibre Anisotropic Thermal Expansion and Residual Thermal Stress in a Graphite/Aluminum Composite," *Composites*, Vol. 19, No. 1, pp. 55–60.

Robinson, D.N., and Pastor, M.S., 1992, "Limit Pressure of a Circumferentially Reinforced SiC/Ti Ring," *Composite Engineering*, Vol. 2, No. 4, pp. 229–239. (Also NASA CR–187211.)

Smith, K.N., Watson, P., and Topper, T.H., 1970, "A Stress-Strain Function for the Fatigue of Metals," *Journal of Materials*, Vol. 5, No. 4, pp. 767–778.

Chapter 5
Deformation and Life Prediction of Circumferentially Reinforced SCS–6/Ti-15-3 Ring

Steven M. Arnold* and Thomas E. Wilt[†]

5.1 Symbols

$\hat{a}$ scaling factor for stress dependency in fatigue damage exponent

D scalar variable representing damage

ΔD increment in damage

E Young's modulus, MPa (ksi)

G shear modulus, MPa (ksi)

H hardening modulus, MPa (ksi)

M stress amplitude constant

N number of cycles

N_f number of cycles to failure

ΔN increment in cycles

P internally applied pressure, MPa (ksi)

P_l limit (burst) pressure (i.e., pressure that would cause instantaneous failure), MPa (ksi)

u,v,w finite-element degrees of freedom associated with x,y,z coordinates, respectively

x,y,z coordinate system

α coefficient of thermal expansion

β exponent on normalized stress amplitude

ε_f strain to failure

ε_p inelastic strain

θ fiber orientation, deg

ν Poisson's ratio

σ_{fl} normal stress fatigue limit, MPa (ksi)

σ_m mean strength of material

σ_u ultimate strength of material

σ_y yield stress defined as deviation from proportionality, MPa (ksi)

ω strength of anisotropy, defined as ratio of longitudinal to transverse yield stress

ω_{fl}, η_{fl} ratio of longitudinal to transverse normal and shear fatigue limit stresses, respectively

ω_m, η_m ratio of longitudinal to transverse normal and shear stress amplitudes, respectively

ω_u, η_u ratio of longitudinal to transverse normal and shear static fracture stresses, respectively

---
*NASA Lewis Research Center, Cleveland, Ohio, 44135.
[†]University of Toledo, Toledo, Ohio, 43606.

Subscripts:

L   longitudinal

T   transverse

Superscripts:

*   effective (damage)

5.2 Introduction

The objective of the study described in this chapter was to perform an analysis encompassing both a static burst pressure prediction and a life assessment of a circumferentially reinforced silicon carbide/titanium–15 wt% vanadium–3 wt% chromium–3 wt% aluminum–3 wt% tin (SCS–6/Ti-15-3) cladded ring designed for application at 427 °C (800 °F). A major concern in developing a deformation and life prediction methodology for metal-matrix composites (MMC's) is the question of scaleup associated with characterizing a given theory with test results from relatively thin MMC panels (test coupons) and then applying this theory to relatively large-volume MMC structures. Therefore, to verify the analysis methodology for actual engine component designs, the test conditions for subscale rings were chosen to simulate typical gas turbine engine fan or compressor operating conditions.

The stress analysis was conducted using MARC, a nonlinear finite-element code, wherein both the matrix cladding and composite core are assumed to behave as elastic–perfectly plastic. The life assessment used the stress analysis results in conjunction with a recently developed multiaxial, isothermal, continuum damage mechanics model for the fatigue of unidirectional MMC's. This model is phenomenological and stress based and assumes a single scalar internal damage variable, the evolution of which is anisotropic. Uniquely, this life model includes damage accumulation in the stress analysis by employing the concept of effective stress. In this way the redistribution of stresses, on the structural level, due to damage initiation and propagation can be accounted for conveniently and consistently. In the present application the damage model was computationally decoupled from the finite-element solution, in that the life assessment calculations were performed by "postprocessing" the finite-element deformation analysis results separately. Each deformation analysis and subsequent postlife assessments represent various increments (or stages) of the total life. The specific methodology for this computationally decoupled fatigue damage simulation is described, and results are given in terms of the evolution of damage and design life curves.

5.3 Deformation Analysis

The ring was idealized according to the results of a nondestructive evaluation (NDE) analysis (Baaklini et al., 1993) and information from ring testing. Pratt & Whitney's hydraulic actuator burst rig was used for both the static burst test and the low-cycle tension fatigue tests. In the test rig 24 hydraulic actuators were positioned around a high-temperature test chamber; the actuators could apply over 4.45 MN (10^6 lbf) of uniform load against the inner diameter of the composite ring at temperatures exceeding 815 °C (1500 °F). The tests were performed under load control with a System 4000 data acquisition system. The actual cross section of ring 1, obtained from the average of 35 computed tomography (CT) scans is shown in figure 1.10 (chapter 1). Three SCS–6/ Ti-15-3 rings were tested, each having 57 plies with approximately 33 vol% fiber.

A deformation analysis was performed on the idealized composite ring to determine the load-versus-displacement response and thus the static burst pressure. A three-dimensional, finite-element model of one-quarter of the ring, consisting of a composite core surrounded by matrix cladding, was constructed (see fig. 5.1). The finite-element model had 1701 nodes and 1280 eight-noded, three-dimensional elements (MARC element number 7). A uniform pressure load was applied to all elements forming the inner diameter face of the ring. The boundary conditions were as follows: $w = 0$ for all nodes at $z = 0$ and symmetry conditions at each end of the quarter ring (i.e., $v = 0$ for all nodes at $y = 0$; $u = 0$ for all nodes at $x = 0$). In this analysis a number of simplifying assumptions were made with respect to residual stresses, ring geometry, and the material characterization.

All residual stresses generated during the fabrication cycle were assumed to be eliminated during heat treatment. Consequently, only those residual stresses due to cooldown from 700 °C (1292 °F) to room temperature and heatup to the application temperature of 427 °C (800 °F) were calculated. Residual macrostresses were accounted for by considering the mismatch in coefficients of thermal expansion (CTE) between the matrix cladding and the composite core; whereas residual microstresses (i.e., the CTE mismatch between fiber and matrix) were accounted for in the uniaxial tensile specimen data and consequently were assumed to be included in the coefficients of the constitutive model.

Perfect bonding was assumed between the composite core and the matrix cladding. The ring was assumed to be defect free, in that initial damage due to fabrication was not included in either the deformation or life analyses. Initial damage can easily be included once a relationship between density changes (CT measurements) and mechanical properties is established. The offset of the inner core was accounted for in the finite-element analysis, but not the presence of the cusp. The ring, as

(a)

(b)
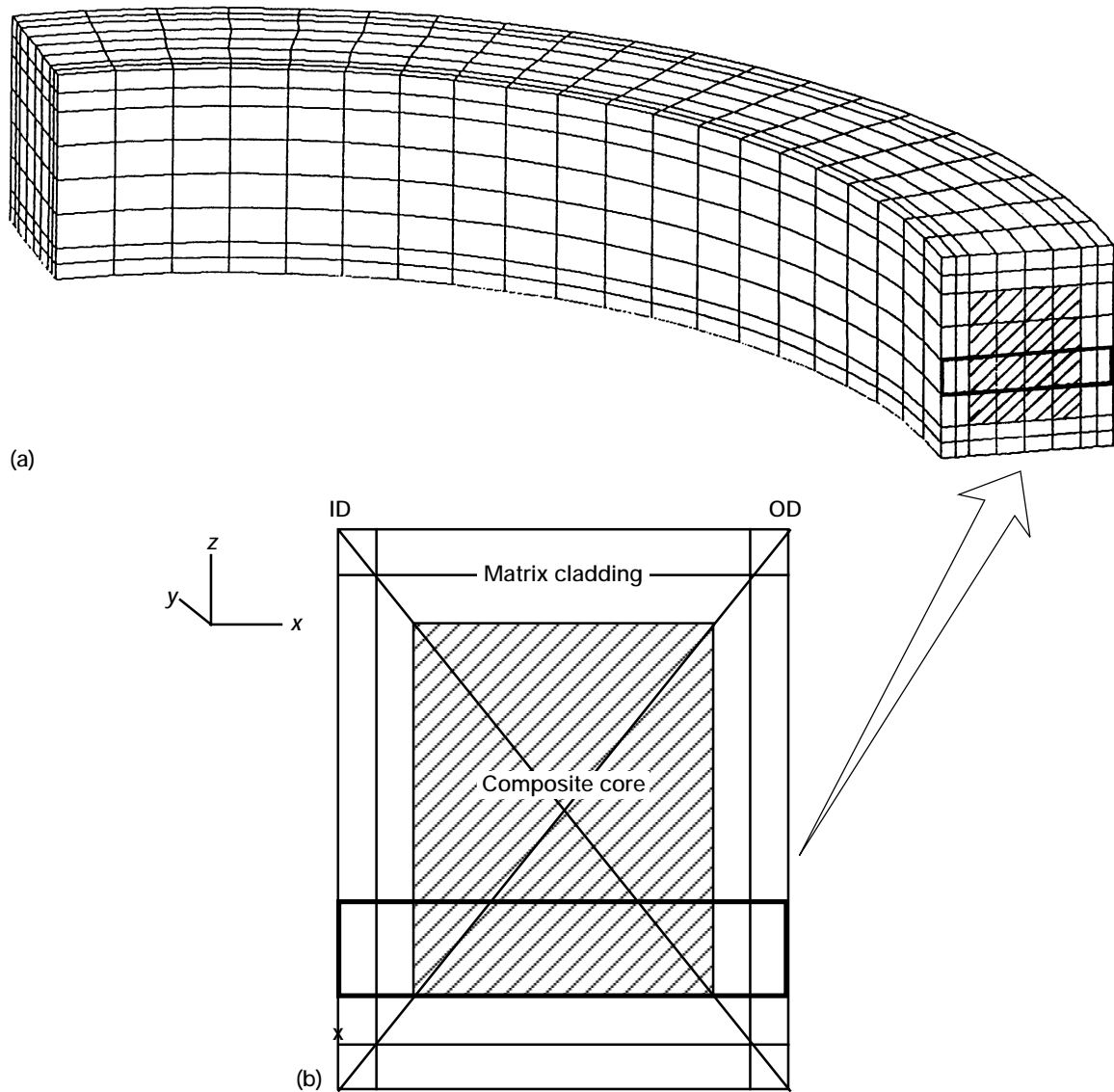
Figure 5.1.—Three-dimensional, finite-element model of MMC ring, with (a) representative cross section and (b) representative strip.

well as the load application, was assumed to be circular and axisymmetric. Finally, the fiber spacing was assumed to be periodic and any deviation was assumed to be included in the tensile data.

The matrix cladding was assumed to behave as elastic–perfectly plastic. The composite core was assumed to exhibit either perfectly plastic or bilinear hardening behavior. The mechanical composite properties were taken to be temperature independent because data characterizing the temperature dependence are limited, whereas CTE temperature dependence was incorporated.

5.4 Constitutive Model

The composite core was idealized as a pseudohomogeneous, transversely isotropic material described by an anisotropic elastic-plastic constitutive model (Robinson and Pastor, 1992; Hill, 1983). The matrix cladding was taken to be isotropic and elastic–perfectly plastic. A recent transversely isotropic–perfectly plastic constitutive model, put forth by Robinson and Pastor (1992), was used to characterize the matrix and the composite core. The associated material parameters are shown in table 5.1. The material parameters were obtained

TABLE 5.1.—MATERIAL PARAMETERS
[Poisson's ratio, ν, 32.]
(a) Matrix properties

Temperature		Young's modulus, E		Coefficient of thermal expanison, α	Yield stress, σ_y	
°C	°F	MPa	ksi		MPa	ksi
21	69.8	88	12.8	2.50×10^6	710	103.0
300	572	81	11.8	2.87	582	84.4
530	1022	74	10.7	3.09	450	65.3
700	1292	68	9.9	3.24	207	30.0

(b) Composite properties

Parameter	Perfect plasticity	Bilinear hardening
Young's modulus:		
Longitudinal, E_L, MPa (ksi)	184 (26.7)	198 (28.8)
Transverse, E_T, MPa (ksi)	114 (16.6)	114 (16.6)
Poisson's ratio:		
Longitudinal, ν_L	0.28	0.28
Transverse, ν_T	0.32	0.32
Yield stress, σ_y, MPa (ksi)	276 (40)	179 (26)
Hardening modulus, H, MPa (ksi)	0	19 306 (2800)
Strength of anisotropy, ω	5.0	5.54

(b) Concluded

Temperature		Coefficient of thermal expansion	
°C	°F	Longitudinal, α_L	Transverse, α_T
21	70	1.60×10^6	1.47×10^6
100	212	1.66	2.36
200	392	1.75	3.11
300	572	1.82	3.11
700	1292	1.82	3.11

Figure 5.2.—Correlation of perfectly plastic constitutive model with experimental data.
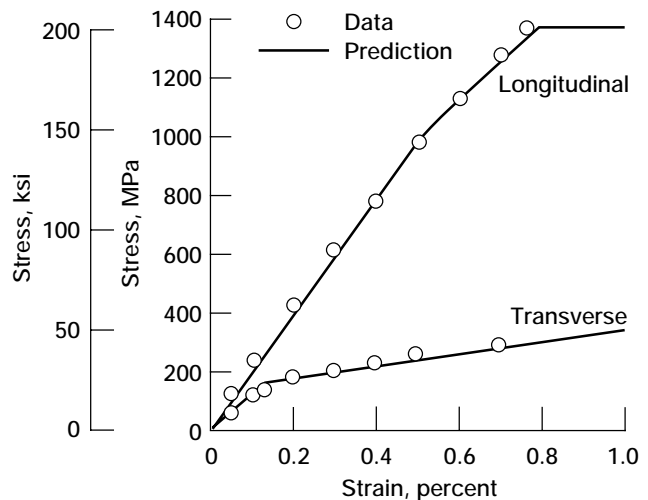
Figure 5.3.—Correlation of bilinear hardening constitutive model with experimental data.

from unpublished data generated during the Pratt & Whitney/ NASA Lewis cooperative program. Note that this model is also equivalent to the more general (in that hardening and other forms of anisotropy can be included) anisotropic model of Hill (1983). Henceforth, whenever bilinear hardening is referred to, the model used is Hill's with the associated material parameters given in table 5.1. Figures 5.2 and 5.3 illustrate the excellent correlation between experiment (Lerch and Saltsman, 1993) and theory for the longitudinal (0°) and transverse (90°) tensile responses when using an isothermal, transversely isotropic plasticity model. The two cases considered here are perfect plasticity (where $H = 0$, see fig. 5.2) and bilinear hardening (where $H \neq 0$, see fig. 5.3). Note, that for the perfectly plastic correlation a secant-like elastic longitudinal modulus of 184 GPa (26 700 ksi) resulted from the assumption that the longitudinal response was purely elastic until failure (i.e., $\varepsilon_f = 0.0078$ and $\sigma_u = 1436$ MPa (208.3 ksi)). On the other hand, in the bilinear case all material constants were obtained

by fitting the longitudinal tensile response, thus explaining the difference in the composite longitudinal elastic moduli in table 5.1.

5.5 Deformation Results

Various comparison calculations were made to gain confidence in the finite-element analysis and to assess the effect of the assumed constitutive behavior and residual stress state. First, analytical limit loads were calculated, using the upper and lower bound expressions given by Robinson and Pastor (1992) for a solid composite and a solid matrix ring.

TABLE 5.2.—COMPARISON OF LIMIT LOADS

Component	Analytical plane strain loads		Finite-element-method loads		Analytical plane stress loads	
	MPa	ksi	MPa	ksi	MPa	ksi
Solid core	305	44.3	269	39.0	256	37.2
Solid matrix	130	18.8	119	17.3	118	17.1
Cladded ring	– – –	– – –	207	30.0	– – –	– – –

Clearly, in these cases no CTE mismatch between matrix cladding and composite core, and thus no residual stress, was present. The calculated loads are shown in table 5.2. Next, analytical first yielding was compared with that calculated by using the finite-element method. Agreement was excellent.

Figure 5.4 shows the internal pressure versus radial displacement for the actual cladded ring (see fig. 1.10) and illustrates the effect of assuming an elastic-plastic rather than an elastic constitutive behavior response, as well as the effect of including, or excluding, the structural residual stress developed during consolidation. Clearly, the final limit load was unaffected by the residual stress, but first yielding was significantly affected. Also, including plasticity had a greater effect on the resulting limit load than did including residual
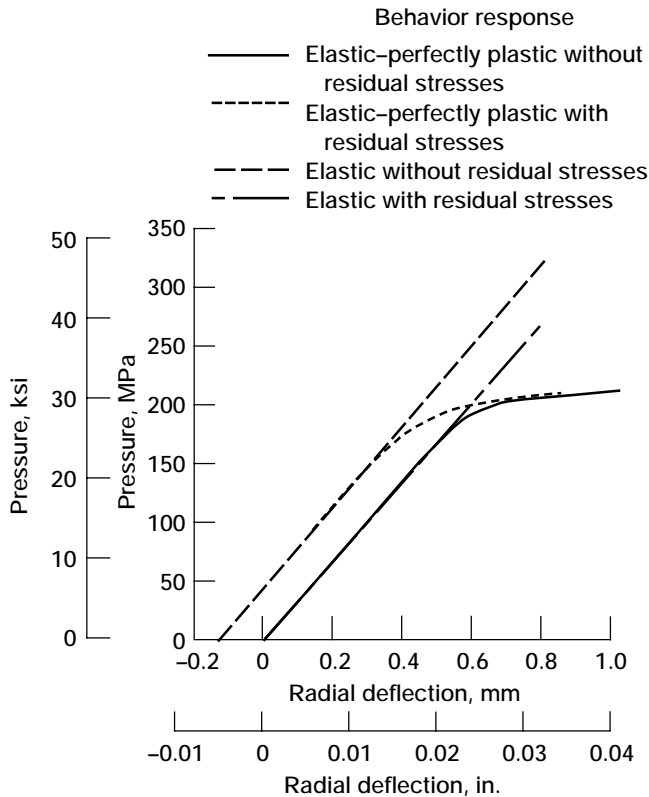
stress. That is, a burst pressure calculated by using an elastic analysis with an appropriate strain-to-failure criteria far exceeded that calculated by using an elastic-plastic analysis, and, as might be expected, the influence of residual stresses on the elastic stress analysis results far exceeded that of an elastic-plastic response.

Figure 5.5 shows pressure versus circumferential strain for a perfectly plastic and a bilinear hardening material. In both cases residual stresses have been included in the analysis. For the assumption of perfect plasticity the limit load (burst pressure) was approximately 207 MPa (30 ksi) at a circumferential strain of 0.89 percent. The strain-to-failure criterion was based on the failure strain of uniaxial test coupons, which occurred at approximately 0.78 percent. Applying a similar strain-to-failure criterion to the bilinear hardening response curve, at the inner diameter, resulted in a burst pressure of approximately 214 MPa (31 ksi). Considering the outer diameter response (fig. 5.6), the burst pressure was 227 MPa (33 ksi). The closeness of the inner and outer burst pressures gives confidence in the rapid failure of the entire ring, thus suggesting an average of the two limits (i.e., $P_l = 221$ MPa (32 ksi)).

Before Pratt & Whitney conducted the static burst test on the MMC ring, a prediction (based on the bilinear hardening response) of the deformation response and ultimate burst pressure was thought to be the most realistic. This statement was verified by comparing the experimentally obtained pressure versus the radial deflection response at the outer diameter (OD), for rings 1 and 2, with the predicted bilinear response at the OD (fig. 5.7). Clearly, the comparison is quite good. In addition, in figure 5.7 the inner diameter (ID) response curves for bilinear hardening and perfect plasticity illustrate the difference between the two assumptions. The better agreement with experimental results in the bilinear case was

Figure 5.4.—Internal pressure versus radial deflection for elastic–perfectly plastic and elastic constitutive response with and without residual stresses.
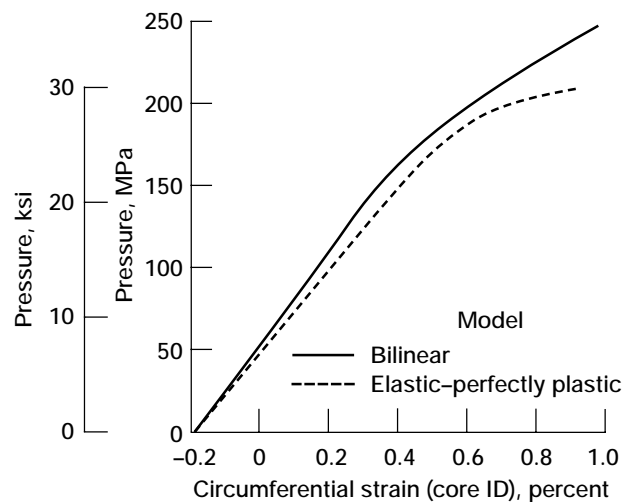
Figure 5.5.—Internal pressure versus circumferential strain for bilinear and elastic–perfectly plastic responses.
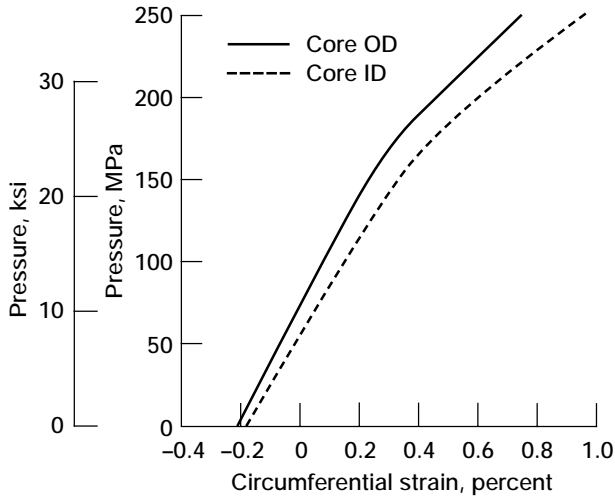
Figure 5.6.—Internal pressure versus circumferential strain: bilinear hardening response for composite core inner diameter (ID) and outer diameter (OD).
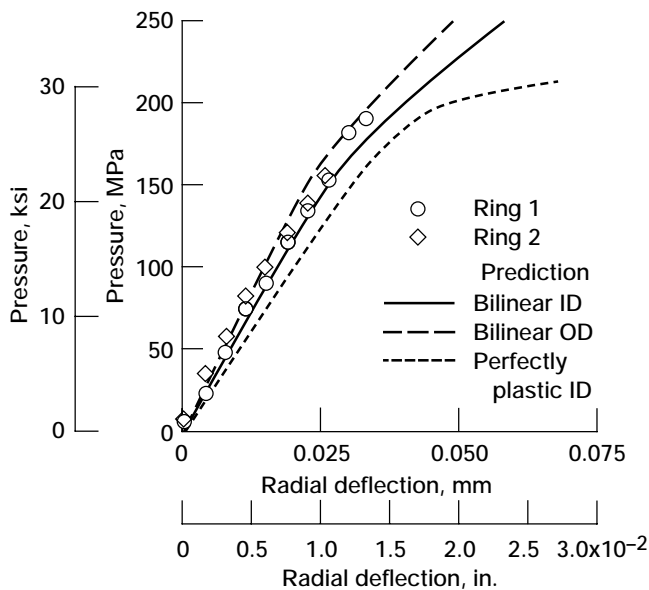
Figure 5.7.—Experimental and computed pressure versus radial deflection for rings 1 and 2.

probably due to the more accurate material characterization, as discussed in section 5.4. Also, note that the experimental data for ring 1 are bounded by the ID and OD bilinear responses. Finally, note that ring 1 had a burst pressure of 190 MPa (27.5 ksi), whereas that of ring 2 was 155 MPa (22.5 ksi). The lower burst pressure of ring 2 was attributed to manufacturing problems.

## 5.6 Damage Analysis (Fatigue Life)

Two classes of fatigue life assessment were performed. The first, and simplest, was a decoupled deformation and damage analysis (i.e., one in which no structural stress redistribution, caused by the evolution of damage, was incorporated), thus providing an upper and lower bound on ring life. The second was a coupled deformation and damage analysis and involved the additional complexity of incorporating structural stress redistribution through the degrading of appropriate material properties. Both life assessments employed a recently developed transversely isotropic continuum damage mechanics (CDM) model (Arnold and Kruch, 1991, 1992) applicable to unidirectional metallic composites and the previous three-dimensional, elastic-plastic, finite-element deformation analysis.

The multiaxial, isothermal, fatigue model is phenomenological and stress based and assumes a single scalar internal damage variable, the evolution of which is anisotropic and is associated with the initiation and propagation of transgranular effects. The development of this fatigue damage evolutionary law (model) is founded on the definition of an initially transversely isotropic fatigue limit surface, a static fracture surface, and a normalized stress amplitude function. The anisotropy of the model is defined through physically meaningful invariants reflecting the local stress and material orientation. Finally, the concepts of effective stress and remaining life are used to measure and interpret damage.

The deformation and damage procedure used in this study can be divided into the following five steps:

(1) A three-dimensional, elastic-plastic, finite-element deformation analysis was performed in which the ring was subjected to one complete load cycle. For the complete cycle the average stress state was recorded at different load levels (stress history) for each element in the "representative strip" of the ring cross section.

(2) For each element and its given stress history the maximum and minimum stress states were determined.

(3) The maximum and minimum stress states and the current amount of damage were then used as input for the fatigue damage model. (For the present application the fatigue damage model was implemented by using MATHCAD and used in a postprocessing life analysis. The input required for the model in MATHCAD was the above-mentioned maximum and minimum stress states and the current damage, as well as the material properties. The resulting output was the number of cycles to failure. In addition, for a given increment in damage (i.e., $\Delta D = 0.20$), the corresponding increment in cycles ΔN was calculated.)

(4) For the updated measure of damage D the associated elastic moduli and yield stress of each element were degraded (i.e., $E^* = E(1 - D)$, $G^* = G(1 - D)$, $\sigma_y^* = \sigma_y(1 - D)$).

(5) The material constants in the MARC input data were updated or modified to reflect the current state of damage. Next, step 1 was rerun, thus giving the new stress distribution, which simulated what would have occurred after an additional ΔN cycles had elapsed.

Steps 2 to 5 were then repeated until the ring had failed (burst). A second approach is also under development at this time in which the fatigue damage model has been directly linked with the MARC finite-element analysis program through the use of available "user" subroutines provided in MARC. This method requires no "postprocessing" after each load cycle, except for the finite-element analysis. The entire fatigue life analysis can be performed in a single run.

Note that when conducting a decoupled deformation and damage analysis in which stress redistribution is not accounted for, steps 1 to 4 were performed only once. That is, the number of cycles to ring failure was based on the initial damage-free cyclic stress history. Also note that in step 3, the number of cycles N between deformation analyses was determined by a trial-and-error procedure. It was found that if the amount of material damage D was limited to approximately 20 percent per analysis run, the amount of stress redistribution incurred within ΔN cycles was reasonable and did not adversely affect the damage accumulation within any given element. Consequently, the increment in damage in any given element was not allowed to exceed 20 percent. With this constraint the maximum number of cycles within a given increment was determined (using the element with the current shortest remaining life) and used as the "controlling" ΔN. This ΔN was then applied to all other elements for their damage calculations. The damage associated with each element was then updated as indicated in step 3.

In the deformation analysis conducted to predict the stress-strain distribution input to the damage analysis, an elastic–perfectly plastic matrix cladding and an elastic, bilinear hardening composite core were assumed. Also, no residual stresses of any kind were accounted for in the deformation/ damage analysis. For example, no thermal mismatch either between the matrix cladding and the composite core (macro-mismatch) or between the fiber and the matrix (micro-mismatch) was accounted for, nor was any residual stress due to incurred plastic deformation from one cycle analysis to another (i.e., each cycle analysis was considered to be independent). Finally, the cusp that resulted from fabrication and was discovered by NDE was not included in the deformation analysis. In the damage model the damage variable was taken to be a scalar (damage was assumed to be equivalent in all directions, i.e., isotropic) with an anisotropic evolution (dependent on loading direction relative to fiber direction). The concept of effective stress was used to allow integration, through the degradation of the elastic and plastic properties, of the damage measure D into the deformation analysis. Fiber

breakage ($D = 1$) was assumed to occur whenever the total strain within a given composite element reached 0.8 percent. This assumption was based on experimental evidence with uniaxial tensile specimens. Lastly, because limited data were available on the SCS–6/Ti-15-3 system at 427 °C (800 °F), creep damage and mean stress effects were neglected.

5.7 Damage Characterization

The required exploration and characterization experiments for the damage model are completely described by Arnold and Kruch (1991). Because of insufficient data the shear ratios η_u, η_{fl}, and η_m were all assumed to be 1.0 (i.e., isotropic in shear) and the longitudinal strength-life response (fig. 5.8) was used to obtain the constants, $\hat{a}$, β, M_L, $(\sigma_u)_L$, and $(\sigma_{fl})_L$. Then, while these constants were held fixed, the three transverse data points were fitted to obtain the "strengths" of anisotropy, ω_u, ω_{fl}, and ω_m. Figure 5.9 shows both the correlations (lines) and the experimental data (open symbols) for a 35-vol%-fiber, longitudinal and transverse SCS–6/ Ti-15-3 system and the Ti-15-3 matrix material at 427 °C (800 °F). Tables 5.3 and 5.4 list the specific individual material parameters used. The solid square symbol associated with the transverse (90°) response (fig. 5.9) was not used in the correlation data set for the composite response and therefore represents a check on the predictive capability of the present model at the coupon level. The accuracy was within a factor of 2.
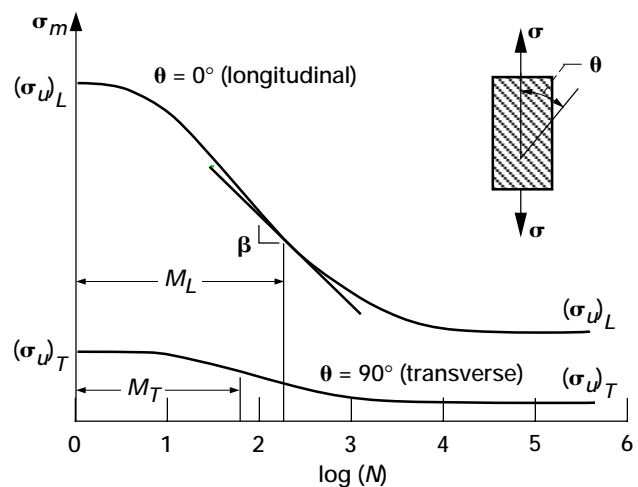
Figure 5.8.—Prototypical strength-life curves for unidirectional MMC loaded longitudinally ($\theta = 0°$) and transversely ($\theta = 90°$).
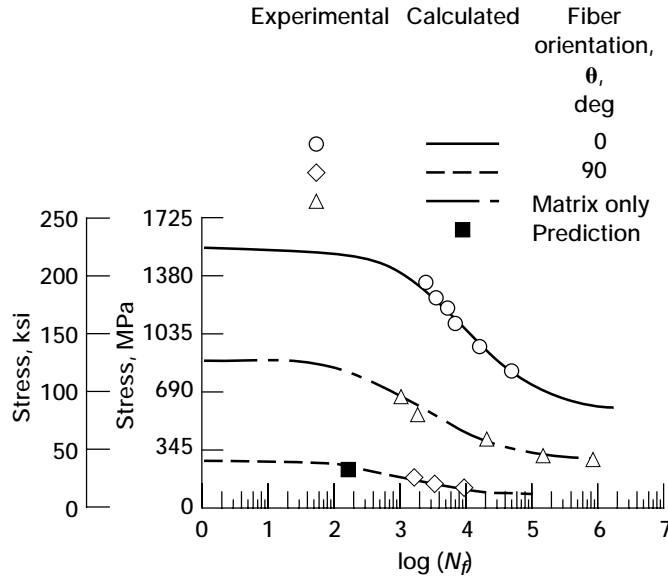
Figure 5.9.—Correlation of CDM model with SiC/Ti-15-3 composite and Ti-15-3 matrix coupon data.

TABLE 5.3.—MATERIAL PARAMETERS FOR CDM ANALYSIS

Parameter	SCS–6/Ti-15-3 composite material	Matrix material (Ti-15-3), isotropic simplification
Ultimate strength (longitudinal), $(\sigma_u)_L$, MPa (ksi)	1551 (225)	882 (128)
Normal stress fatigue limit (longitudinal), $(\sigma_{fl})_L$, MPa (ksi)	286 (41.5)	140 (20.3)
Exponent on normalized stress amplitude, β	1.842	2.27
Scaling factor for stress dependency, $\hat{a}$	0.065	0.2302
Stress amplitude constant, M, MPa (ksi)	22 371 (3244.5)	6205 (900)
Normal static fracture stress ratio, ω_u	5.5	1.0
Normal fatigue limit stress ratio, ω_{fl}	12.482	1.0
Normal stress ampltude, ω_m	11.8	1.0
Shear static fracture stress ratio, η_u; shear fatigue limit stress ratio, η_{fl}; and shear stress amplitude, η_m	1.0	1.0

TABLE 5.4.—STRAIN CRITERIA TO MATRIX MATERIAL FAILURE

Number of cycles to failure, N_f	Inelastic strain, ε_p, percent
250	1
1 000	.3
2 150	.1
23 000	.01
170 000	.005

5.8 Damage Results

Given the calculated burst pressure (or limit pressure, P_l) of 221 MPa (32 ksi), four normalized pressure ratios were examined (i.e., P/P_l of = 0.35, 0.56, 0.78, and 0.84). The pressure-ratio-versus-cycles-to-failure results of the decoupled deformation and damage solution are shown in figure 5.10. Only the results for the four elements of the composite core, in the representative section shown in figure 5.1, are given. As might be expected, failure began at the inner radius and proceeded outward. As a result, failure of the inner element gave the lower bound on ring life, whereas the outer element gave the upper bound. This type of analysis would be similar to a traditional fatigue initiation analysis.
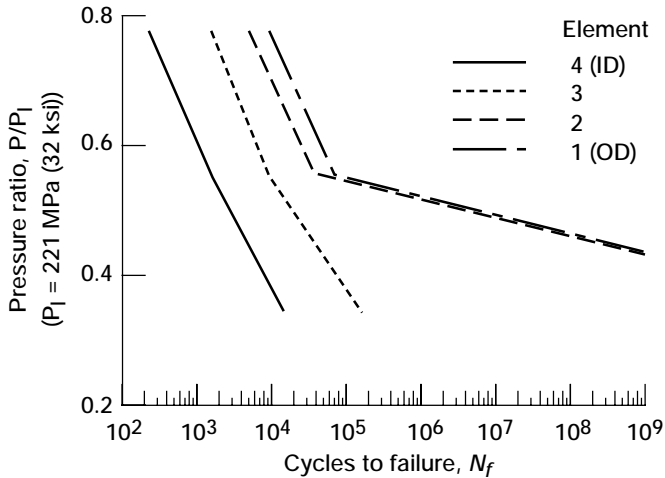
Figure 5.10.—Normalized internal pressure versus life for de-coupled deformation and damage analysis: bounds on life.
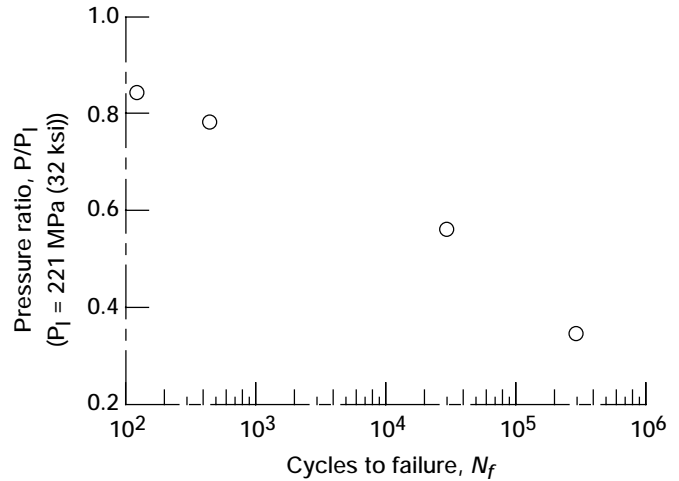
Figure 5.11.—Normalized internal pressure versus life for coupled deformation and damage analysis.
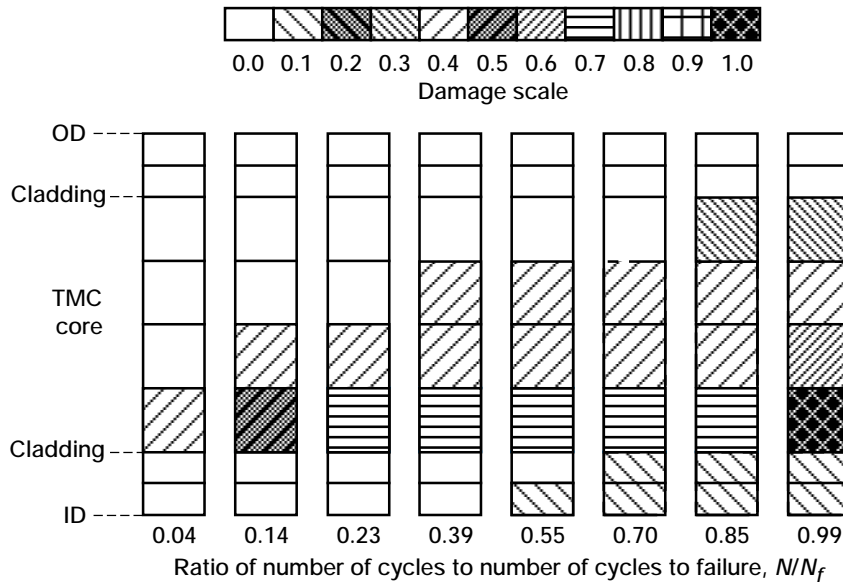
Figure 5.12.—Damage evolution in representative strip (defined in fig. 5.1) for pressure ratio P/P_l of 0.56. Cycles to failure, N_f, 39 950.

Figure 5.11 illustrates the results of a coupled deformation and damage analysis (i.e., one that accounts for redistribution of stress due to damage evolution). This type of analysis differs from the typical fatigue analysis because both initiation and propagation of fatigue cracks are incorporated into the damage model. Here, each data point represents a ring failure and not just failure of a given finite element, as in figure 5.10. Only for pressure levels very near the limit load were the results of the decoupled and coupled analyses comparable, thus indicating that at high load levels ring failure is dominated by inner radius failure within the composite core. The corresponding damage evolution throughout the ring life is shown

in figure 5.12 for $P/P_l = 0.56$, or $P = 124$ MPa (18 ksi). The figure illustrates clearly the damage state at various percentages of life N/N_f over the entire representative strip. Note that inner core radius damage began at 35 percent of ring life and that propagation of this damage consumed 65 percent of the life. Clearly, once the inner core element failed, the rate of damage progression accelerated dramatically for this particular load level. A number of significant advantages of the Arnold-Kruch CDM over other traditional fatigue models are indicated by comparing figures 5.10 and 5.11: (1) stress redistribution (due to damage evolution) and its effect on life are easily accounted for; (2) damage accumulation can be easily tracked;

and (3) a single life value can be obtained without resorting to multiple life assessment analyses (e.g., fatigue initiation failure coupled with a fracture mechanics propagation analysis).

Unfortunately, no experimental fatigue test results were available for comparison with the predicted design life curves because fabrication problems caused premature tensile failure of the remaining MMC rings in this phase of the program. Thus, no definitive statements can be made regarding the predictive capability of the Arnold-Kruch CDM at this time. Additional rings must be fabricated and tested so as to assess its accuracy at the component level. However, the accuracy at the coupon level appears to be reasonably good.

5.9 Summary of Results

A computational methodology, the Arnold-Kruch isotropic, continuum damage fatigue model (CDM), has been developed for predicting the fatigue life of typical aerospace components. Here, the CDM was used to analyze a circumferentially reinforced SCS–6/Ti-15-3 compressor ring designed for applications at 427 °C (800 °F). The analysis encompassed both a static burst pressure prediction and a decoupled and coupled deformation and damage life assessment of the cladded ring. A three-dimensional stress analysis was performed using MARC, a nonlinear finite-element code, wherein both the matrix cladding and the composite core were assumed to be behave as elastic–perfectly plastic. The composite core behavior was represented by Hill's anisotropic continuum-based plasticity model with bilinear hardening. Similarly, the matrix cladding was represented by an isotropic, perfectly plastic model.

The life assessment used the finite-element stress analysis results in conjunction with a recently developed multiaxial, isothermal, continuum damage mechanics model for the fatigue of unidirectional metal-matrix composites (MMC's). This model is phenomenological and stress based and assumes a single scalar internal damage variable, the evolution of which is anisotropic. The accumulation of damage was included in the stress analysis by employing the concept of effective stress. In the current application, however, the damage model was computationally decoupled from the finite-element solution. The specific methodology for this computationally decoupled fatigue damage simulation was outlined, and fatigue life predictions were given in terms of design life curves (pressure ratio versus number of cycles to failure). Finally, a graphical depiction of the damage evolution within a matrix-cladded, MMC ring was presented.

In general, the following conclusions can be drawn:

(1) Residual stresses do not affect the resulting limit load but do affect the load level corresponding to first yielding.

(2) The structural load-displacement (i.e., internal pressure versus radial deflection) response can be obtained reasonably accurately with only coupon data.

(3) No definitive conclusion regarding failure, static or fatigue, can be made at this time because of limited confidence in the fabrication quality of the MMC rings tested.

Work is continuing to fully automate the Arnold-Kruch CDM by embedding the fatigue life calculations within the finite-element solution algorithm, thereby, "computationally coupling" the deformation and damage (life) analyses. In addition, fatigue life predictions (simulations) will require so-called cyclic jump techniques to be incorporated into the solution scheme. Also, damage analysis using the finite-element method results in additional numerical difficulties, such as mesh-dependent damage propagation and localization phenomena.

References

Arnold, S.M., and Kruch, S., 1991, "Differential Continuum Damage-Mechanics Models for Creep and Fatigue of Unidirectional Metal Matrix Composites," NASA TM–105213.

Arnold, S.M., and Kruch, S., 1992, "A Differential CDM Model for Fatigue of Unidirectional Metal Matrix Composites, Damage Mechanics in Composites," D.H. Allen and D.C. Lagoudas, eds., AMD–Vol. 150, AD–Vol. 32, pp. 213–232.

Baaklini, G.Y., Percival, L., Yancey, R.N., and Kautz, H.E., 1993, "NDE of Titanium MMC Rings for Gas Turbine Engines," *Reliability, Stress Analysis, and Failure Prevention*, R.J. Schaller, ed., DE–Vol. 55, American Society of Mechanical Engineers, New York, pp. 239–250.

Hill, R., 1983, *The Mathematical Theory of Plasticity*, Oxford University Press.

Lerch, B.A., and Saltsman, J.F., 1993, "Tensile Deformation of SiC/Ti-15-3 Laminates," *Composite Materials: Fatigue and Fracture*, Vol. 4, ASTM STP 1156, W.W. Stinchcomb and N.E. Ashbaugh, eds., American Society for Testing and Materials, Philadelphia, PA, pp. 161–175.

Robinson, D.N., and Pastor, M.S., 1992, "Limit Pressure of a Circumferentially Reinforced SiC/Ti Ring," *Composite Engineering*, Vol. 2, No. 4, pp. 229–238. (Also NASA CR–187211.)

Chapter 6

Nondestructive Evaluation of Titanium Alloy MMC Rings for Gas Turbine Engines

George Y. Baaklini,* Larry D. Percival,† Robert N. Yancey,** and Harold E. Kautz*

6.1 Introduction

Metal-matrix composites (MMC's) consisting of a titanium alloy cladding and a ceramic-fiber-reinforced titanium alloy matrix core are being developed mainly for aeronautic propulsion components and are candidate compressor and turbine disk materials (Stephens, 1990). MMC's offer good oxidation resistance, low density, and high-temperature strength, in addition to operating at significantly higher temperatures than monolithic metals and superalloys. Using MMC's reduces engine cooling requirements, engine weight, and consequently fuel consumption (Petrasek, 1988, 1989). An increase in engine performance and a decrease in cost are expected. MMC's can be used from 800 °C to above 1370 °C (1475 °F to above 2500 °F). Problems associated with MMC's include mismatch in fiber/matrix coefficients of thermal expansion (CTE), analytical modeling difficulties in conjunction with composite development, and lack of matrix ductility and toughness (Stephens, 1990). In addition to developing high-CTE fibers for MMC's, failure and damage mechanisms must be identified so that better modeling and life prediction can be done.

Manufacture of high-temperature MMC engine components calls for developing new nondestructive evaluation (NDE) methods and for upgrading existing NDE techniques. Previous work (Baaklini, 1992; Yancey and Baaklini, 1994) in x-ray computed tomography (XCT) demonstrated capabilities and limitations for characterizing MMC specimens and subscale engine components, established related calibration data, and corroborated findings with scanning acoustic microscopy, radiography, and metallography. Acousto-ultrasonics (AU) also has been of increasing interest for NDE of high-temperature composite structures. Previous work in AU (Lott and Kunerth, 1990; Dos Reis, 1991; Kautz and Lerch, 1991; Kautz and Bhatt, 1991; Kautz, 1992; Tiwari and Henneke, 1994) showed that the AU signals recovered are sensitive to the strength, texture, and damage state in these materials. In addition, they found that when plate waves are excited, axial, shear, and flexure moduli can be determined. All of these AU studies were done with thin plates or tensile specimens.

This chapter examines capabilities and problems encountered in extending the AU technique to thick-cross-section hardware geometries and investigates the use and application of XCT, x-radiography, and immersion pulse-echo immersion ultrasonics for identifying fabrication flaws and for assessing thermomechanical degradation.

6.2 Experiment

6.2.1 Materials

Five MMC rings with titanium cladding, silicon carbide (SCS–6) fiber reinforcement, and titanium alloy matrix cores were evaluated. Axial thicknesses ranged from 10 to 25 mm (0.4 to 1.0 in.) and radial thicknesses, from 15 to 38 mm (0.6 to 1.5 in.). The outside diameter (OD) of these rings varied from 171 to 178 mm (6.75 to 7.0 in.). A part of an MMC ring is shown in figure 6.1.

Briefly, the manufacture of these rings started with a bundle of SCS–6 filaments (142 μm in diameter). The filaments were spirally wound with titanium ribbons (either Ti-15-3 for rings R1, R2, and R3 or alloy C for rings R4 and R5) as they were

*NASA Lewis Research Center, Cleveland, Ohio 44135.
†United Technologies—Pratt&Whitney Government Engines and Space Propulsion, West Palm Beach, Florida 33410.
**Advanced Research and Applications Corp., Dayton, Ohio.

P–E   Pulse-echo
A-U   Acousto-ultrasonics
Width   Radial thickness
Height   Axial thickness
R   Receiving transducer
S   Sending transducer
S/R   Sender receiver
OD   Outside diameter
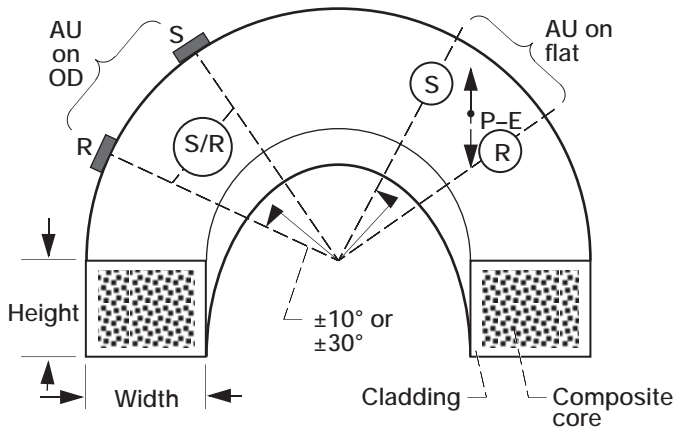
Figure 6.1.—Sketch of part of MMC ring showing application of different ultrasonic procedures.

inserted in a slotted titanium-base disk to fabricate the ring. Titanium caps were welded to the top of the slotted disk for sealing. The sealed disks were consolidated by hot isostatic pressing. The consolidated composite disks were then machined into compressor rings with 34-vol % fiber designed for applications at 427 °C (800 °F).

Nondestructive evaluation was performed (1) before and after rings R1 to R4 were burst tested under an applied internal radial load (Gravett, 1993) at room temperature or at 427 °C (800 °F) and (2) only before metallographic sectioning of R5.

6.2.2 Pulse-Echo Immersion Ultrasonics

All ultrasonic inspections were conducted at 5.0 MHz to achieve high signal-to-noise ratios and high resolution. All ultrasonic scans presented herein used a threshold setting amenable to resolving 0.8-mm-equivalent-diameter (0.032 in.), flat-bottom holes (FBH's) with acceptable signal-to-noise ratio.

The pulse-echo immersion ultrasonics (P–E) inspections were conducted with the transducers normalized and focused on the surface of the MMC ring. Either a KB6000 or a Sonic Mark VI was used as a pulser/receiver. Calibration was conducted by adjusting, with time-corrected gain, the amplitude responses from 1.2-mm-diameter (0.48 in.) FBH's ranging in depth from 19 to 38 mm (0.75 to 1.5 in.) in blocks of titanium alloy similar to the matrix material in the MMC rings (see Nondestructive Testing Methods Specifications, 1979). A compatibility check was conducted on each MMC ring to determine variability, relative to overall attenuation, between the MMC specimen and

the monolithic calibration materials. This test involved monitoring the back-surface response from both the MMC specimen and a calibration block of equivalent thickness. The instrument gain required to bring the back-surface responses to 80 percent of screen height on the ultrasonic instrument was measured. Any difference in gain between the two materials was compensated for during the scan. Two scans were then conducted at two sensitivity settings. The first scan was set at the calibrated gain for a 1.2-mm-diameter (0.48 in.) FBH sensitivity. The second scan was conducted with an additional 7-dB gain, an increase that provides for an equivalent 0.8-mm-diameter (0.032 in.) FBH calibration. The following equation (Halmshaw, 1987) was used to make the 7-dB gain calculation:

$$\Delta\text{dB} = 20\log\big(A_1/A_2\big)$$

where A_1 is the area of a 1.2-mm-diameter (0.048 in.) FBH and A_2 is the area of an 0.8-mm-diameter (0.032 in.) FBH.

Measurements were not taken at an equivalent 0.4-mm-diameter (0.016 in.) FBH because of signal-to-noise problems. A relatively good area on a MMC ring would show a signal response 24 dB or more below the calibration gain; it would appear as a light color (white) on the P–E image. A P–E image is a plane view image displaying the variations in amplitude of the ultrasonic signal in ranges of gray as it maps an object while focusing at a specified depth. Each range in the P–E image represents a change of 3 dB in response. P–E was applied to rings R1 to R5; however, only selected results are discussed.

6.2.3 Acousto-Ultrasonics

Acousto-ultrasonics was done with two ultrasonic transducers on the same surface (fig. 6.1). One transducer, the sender, introduced ultrasound and the other, the receiver, detected it after reverberating in the specimen. Broadband immersion transducers with elastomer pads for coupling to the ring surface were deployed. Waveforms were digitized, stored, and processed as described by Kautz and Lerch (1991) and Kautz (1992). Data were collected with a combination 5.0-MHz sender and 2.25-MHz receiver and with a sender-receiver of 1.0 or 0.5 MHz.

For the stress-wave factor (SWF) and the pulse arrival measurements, data were collected, both before and after the mechanical test, with the transducer pairs coupled to the outer curved surface (OD) of the rings. In this configuration (fig. 6.1) the transducer position and separation were referenced with respect to angular position from a fiducial mark. Velocities in the fiber direction were measured only after the mechanical tests, by coupling the transducers to one of the flat faces of the rings (fig. 6.1). In this case the position on the ring was still noted in terms of angle displacement, but transducer separation was measured in centimeters as a linear displacement across the

face. Through-height (i.e., flat to flat) P–E velocity measurements (normal to fibers) were also made. A 10.0-MHz center frequency broadband transducer was coupled to the ring with a gel. Although AU was applied to rings R1, R2, and R3, only results from rings R1 and R3 are discussed.

6.2.4 X-Radiography and X-Ray Computed Tomography

The XCT system is a laminography/dual energy (LAM/DE) computed tomography scanner. LAM/DE uses a translate-rotate scan geometry. Thus, the XCT scanning process consisted of translating the ring past the x-ray beam, rotating it, and translating it past the x-ray beam again until the ring had been rotated 180°. LAM/DE includes a 420-kV isovolt x-ray source and a $CdWO_4$ linear array detector with a 128-mm field of view. The thickness of the XCT slice was 2 mm, the image pixel size was 250 μm, the pixel integration time was 55 ms, and the total scan time per slice was 20 to 30 min. A conventional radiography system (400-μm focal spot size) with high energy capability (up to 3.2 kW) was also used.

6.3 Results

6.3.1 Pulse-Echo Ultrasonics

Figure 6.2 shows a post-test ultrasonic P–E scan of a portion of the SCS–6/alloy C ring R4, which had been static tested to failure at 427 °C (800 °F). This ring segment, located approximately 180° from the burst location, contains internal damages due to the burst test. Metallography identified the "black" regions near the inner diameter of the ring in figure 6.2 as areas of damaged fibers. Figure 6.3 shows a metallographic cross section at a typical black region where a "notch" corresponding to ultrasonic findings guided metallographic sectioning. This cross section shows 18 damaged fibers, all located near the inner diameter (ID) of the ring section. Higher magnifications of two of these fibers show varying degrees of damage (fig. 6.4).

Figure 6.5 is an ultrasonic P–E scan of a portion of ring R5. The matrix of this ring showed an increased ultrasonic response relative to other rings scanned at the same sensitivity before burst tests. This ring was not burst tested. Ultrasonics, destructive testing, and metallographic sectioning revealed a great number of matrix pull-away conditions throughout the ring. Apparently, greater ultrasonic backscatter is produced by poor consolidation of the matrix material. Figure 6.6 is a micrograph of a polished typical area within the ring. Most of the fibers in figure 6.6 depict the matrix pull-away condition at the fiber/matrix interface. Figure 6.7 shows higher magnification of this matrix pull-away condition. The cause of this condition has since been identified and successfully eliminated by a change in the consolidation sequence.

Pulser	5 MHz
Receiver	5 MHz
Calibrated gain	31 dB
Scan gain	42 dB
Index	0.25 mm

Response, dB

■	0
■	–3
■	–6
■	–9
■	–12
■	–15
■	–18

5 mm

Figure 6.2.—Selected section of P–E scan of SCS–6/alloy C ring R4. (Black regions indicate material damage.)

Notch

ID side

1 mm
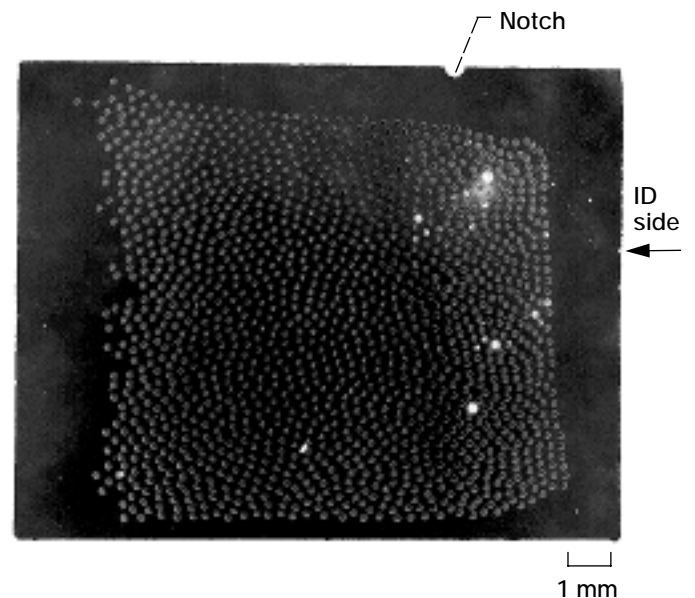
Figure 6.3.—Typical metallographic cross section showing fiber damage where ultrasound exhibited black regions in ring R4. (The notch was used to pinpoint ultrasound-indicated damage. Bright white fibers are the damaged fibers.)

10 μm
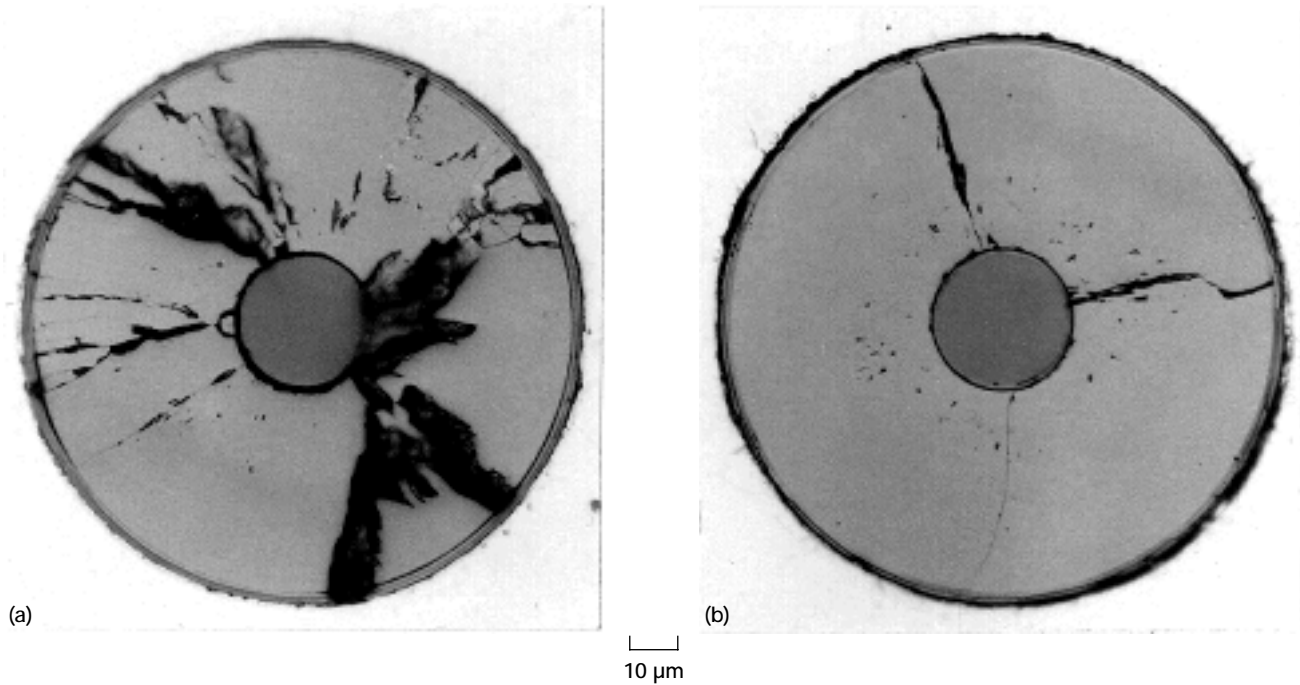
Figure 6.4.—Damaged fibers from figure 6.3 depict (a) a crushed fiber and (b) a cracked fiber.

Pulser   5 MHz
Receiver   5 MHz
Calibrated   32 dB
  gain
Scan gain   39 dB
Index   0.25 mm

Response,
dB

■   0
■   −3
▦   −6
▦   −9
▦ −12
▒ −15

2.5 mm
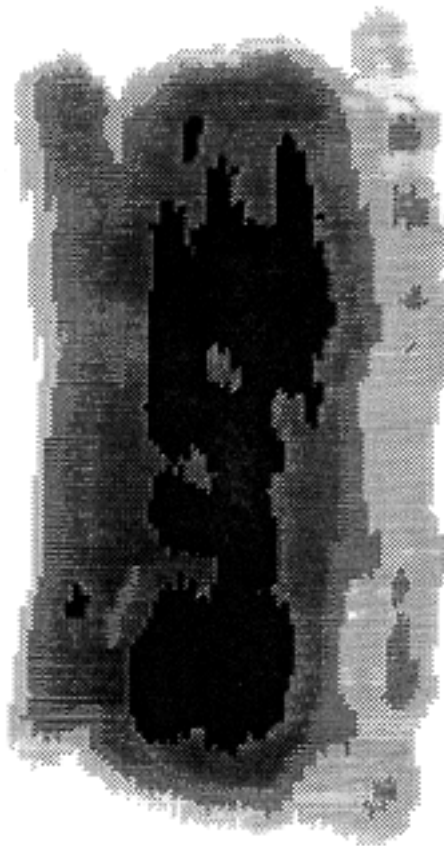
Figure 6.5.—Selected section of ultrasonic P–E scan of
SCS–6/alloy C ring R5. (Black regions indicate material
damage.)
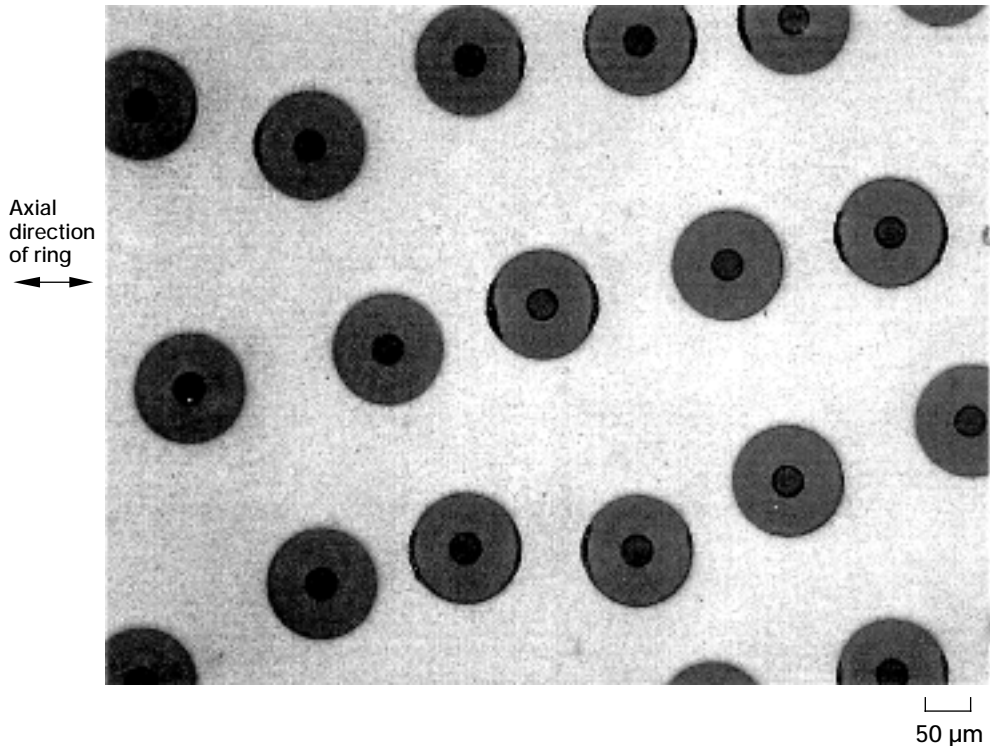
Figure 6.6.—Selected micrograph showing matrix pull-away condition of material damage characterized by ultrasound in figure 6.5.
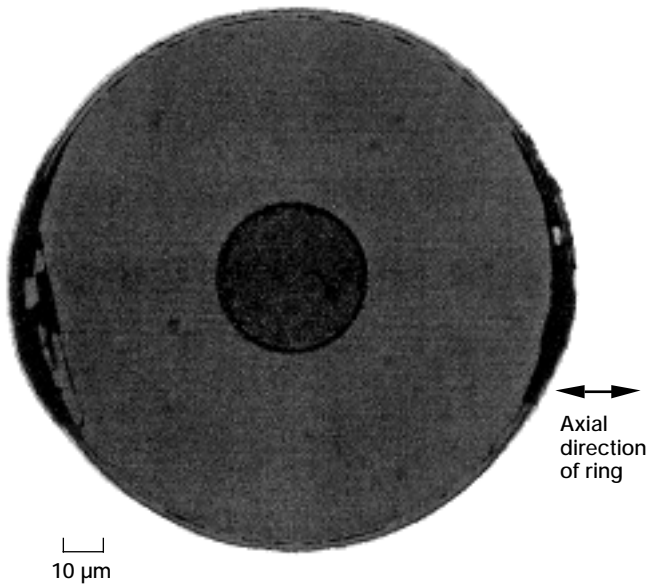
Figure 6.7.—High-magnification micrograph of typical matrix pull-away condition in ring R5.

6.3.2 Acousto-Ultrasonics

6.3.2.1 Stress-wave factor.—The acousto-ultrasonic SWF was calculated as the integral of the frequency spectrum magnitude. Although much ultrasonic or SWF energy passed from the OD to the ID of the rings and back, much was also trapped in the outer cladding. Because the energy passing into the composite core took longer to get to the receiver than that remaining in the outer cladding, the two paths could be separated by arrival time.

Figure 6.8 shows the SWF's for a 5.0-MHz sender and a 2.25-MHz receiver coupled to the outer surface of rings R1 and R3, respectively. The sender and receiver were ±10° apart with respect to a fiduciary mark. For both rings R1 and R3 the SWF was greater after the burst test, evidence that the burst test strained the cladding-composite interface and caused greater reflection of ultrasound back into the cladding. This reflected energy was attenuated less in going from sender to receiver, thereby giving a greater SWF.

Similarly, figure 6.9 shows the SWF for only the initial portion (lower frequency) of the signals used in figure 6.8. This portion is strongly weighted by ultrasound that has passed in and out of the composite and thus does not show the increase in SWF after the burst test. Although there is more scatter in these data, figure 6.9(b) seems to indicate an actual decrease in SWF after the burst test.
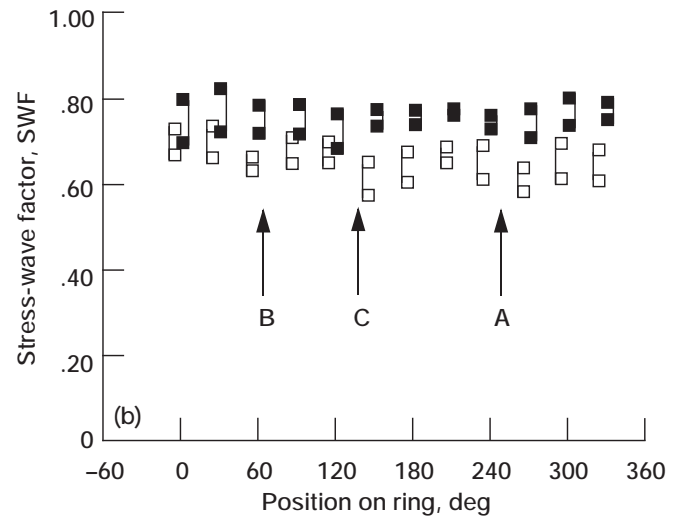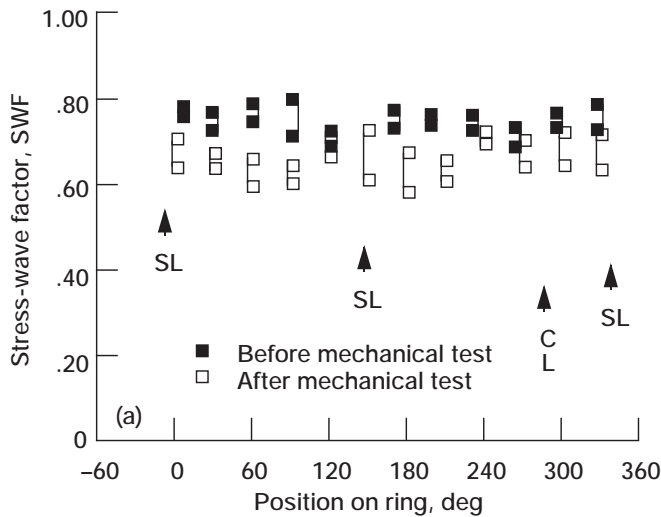
Figure 6.8.—Stress-wave factor of higher frequency component of signal in (a) ring R1 and (b) ring R3. (SWF = ratio of integrated area of magnitude spectrum of 0.8 to 3 MHz to that of 0 to 5 MHz; SL = separation location; CL = crack location; A, B, C = anomaly locations in radiographs.)
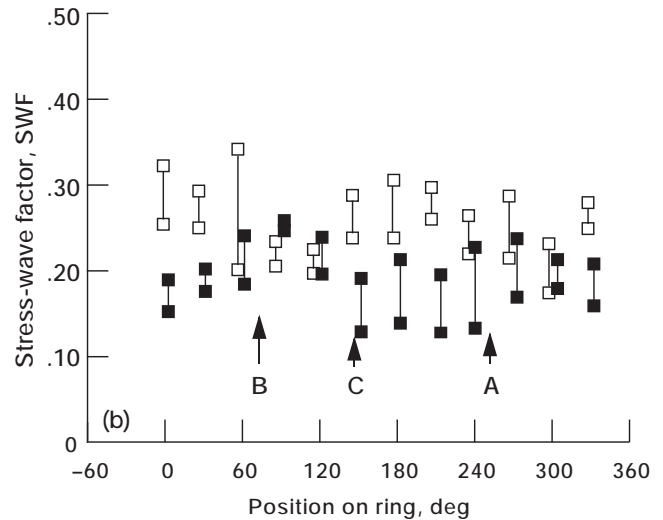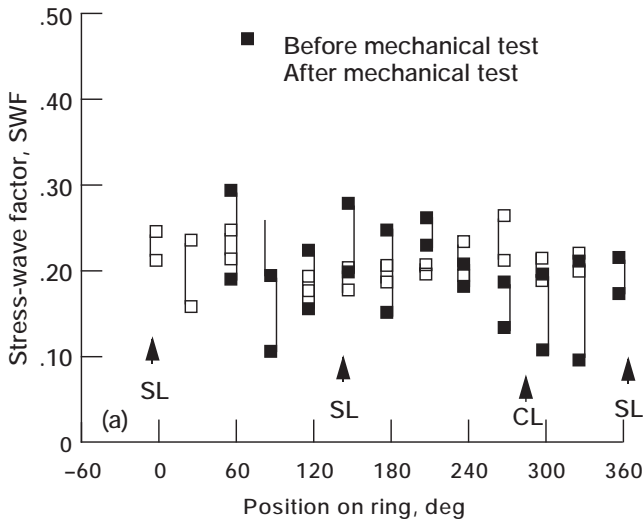
Figure 6.9.—Stress-wave factor of lower frequency component of signal in (a) ring R1 and (b) ring R3. (SWF = ratio of integrated area of magnitude spectrum of 0.2 to 0.8 MHz to that of 0 to 5 MHz; SL = separation location; CL = crack location; A, B, C = anomaly locations in radiographs.)

6.3.2.2 Ultrasonic velocity.—In earlier work (Kautz and Lerch, 1991; Kautz, 1992), 1.0-MHz transducers were found to excite the first symmetric Lamb mode in SCS–6/Ti-15-3 MMC's. The velocity of this mode is sensitive to the axial modulus in the propagation direction. When pairs of 1.0-MHz transducers were coupled at ±30° from the fiduciary position on the outer face of the rings, the collected signals were dominated by discrete pulses. Figure 6.10 shows estimates of the reciprocals of pulse arrival time as a function of position on rings R1 and R3 before and after the burst test. Figure 6.10(a) suggests a loss of modulus along the fiber direction near the crack in the failed ring R1. Figure 6.10(b) demonstrates a general loss in the modulus along the fiber direction in ring R3 after the burst test.

Figure 6.11 shows results obtained with 1.0-MHz transducers, but only after the burst test. For these data, which were collected on the flat face of the rings, it was possible to calculate velocity. The magnitude of these velocities is 0.6 to 0.8 cm/μs, as would be expected for the first symmetric Lamb mode mentioned previously. Figure 6.11 also includes the 10.0-MHz P–E results. All the velocities in figure 6.11(a) exhibit degradation near the crack in ring R1, as noted also with figure 6.10. Velocities in ring R3 (figs. 6.10(b) and 6.11(b)) do not show sensitivity to anomalies A, B, and C, which were found with radiography to be low-density regions.

In earlier work Kautz and Bhatt (1991) and Kautz (1992) used 0.5-MHz transducers to excite the first antisymmetric Lamb mode in SiC/Ti-15-3 MMC's. The velocity of this mode

66
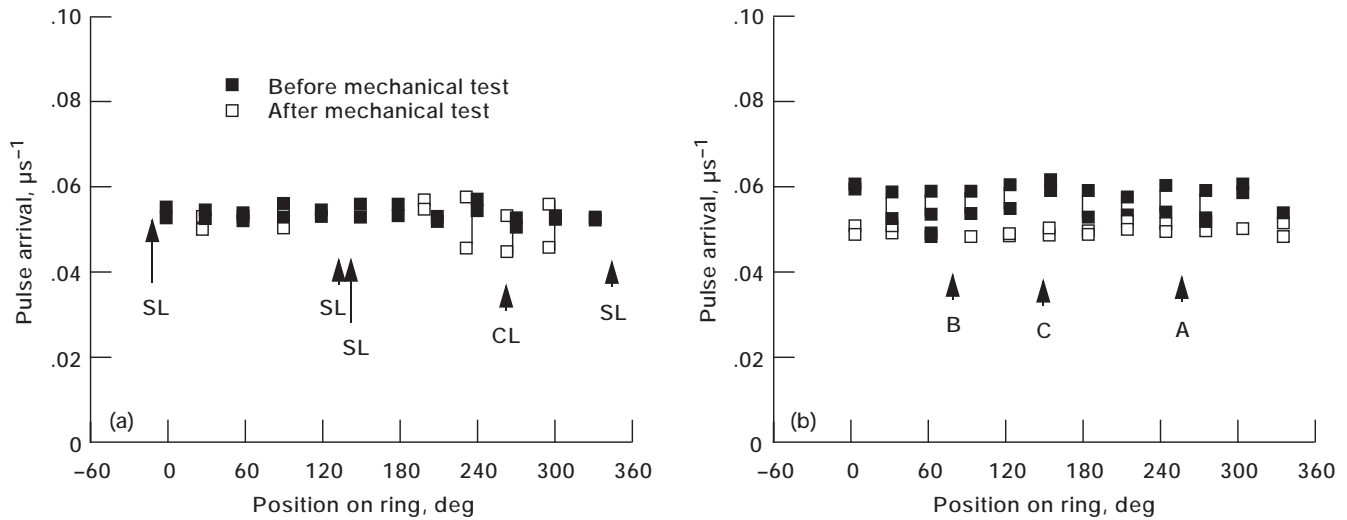
Figure 6.10.—Pulse arrival versus position along outside diameter of (a) ring R1 and (b) ring R3. (SL = separation location; CL = crack location; A, B, C = anomaly locations in radiographs.)
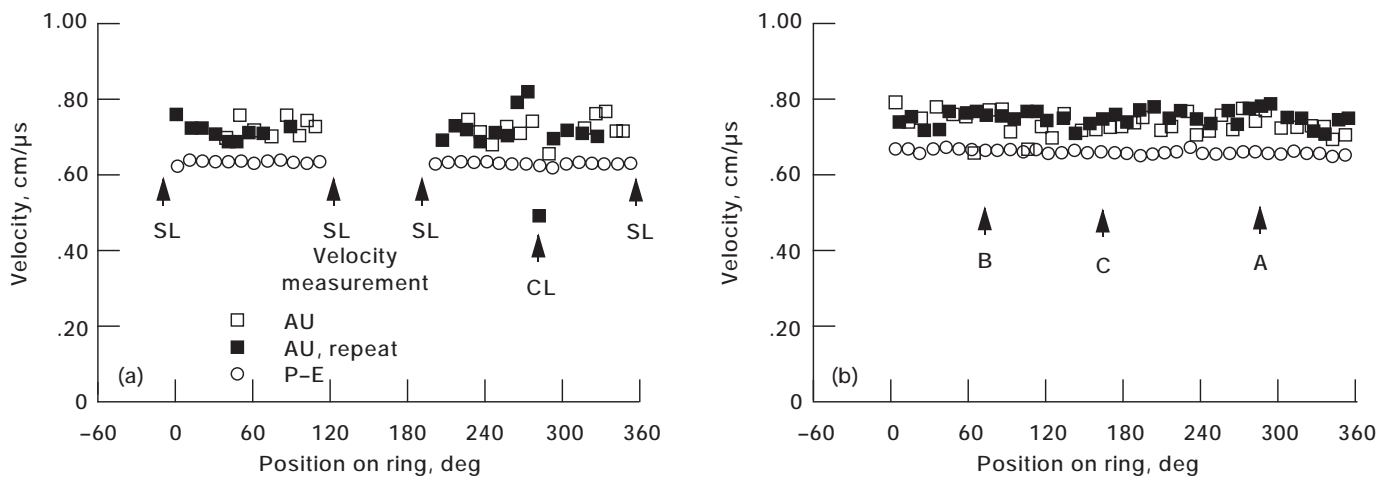
Figure 6.11.—Velocities in (a) ring R1 and (b) ring R3. (SL = separation location; CL = crack location; A, B, C = anomaly locations in radiographs.)

is sensitive to shear and flexure stiffness in the propagation direction. Figure 6.12 shows velocities from pairs of 0.5-MHz transducers coupled to the flat sides of the rings. These velocities ranged from 0.3 to 0.4 cm/μs, supporting the assumption that these are shear wave velocities. Figure 6.12(a) indicates degradation of the shear velocity near the crack in ring R1. Unlike the axial cases figure 6.12(b) suggests some degradation in the shear velocity near anomalies A, B, and C, which were identified by radiography.

   6.3.2.3 Comparison of SWF to velocity results.—AU waveforms showed that the ultrasound was trapped in the cladding layer. It is likely that the pulses used for the velocity calculations also remained in this layer. Because the cladding approximates a plate, it is not surprising that plate waves were

detected. Apparently, some ultrasonic energy did pass to the core fibers. This is evidenced in figure 6.11 by the fact that velocities along the fiber direction are greater than velocities normal to the fiber direction.

6.3.3 X-Radiography and X-Ray Computed Tomography

   Figures 6.13 and 6.14 show through-the-thickness conventional radiographs of rings R2 and R3 along with selected XCT slices. Conventional radiography showed a thinner cladding toward the ID of ring R2 than toward the OD. Similarly, the four XCT slices show not only a smaller cladding on the ID side than on the OD side but also details of the density variations within each slice. Conventional radiography also
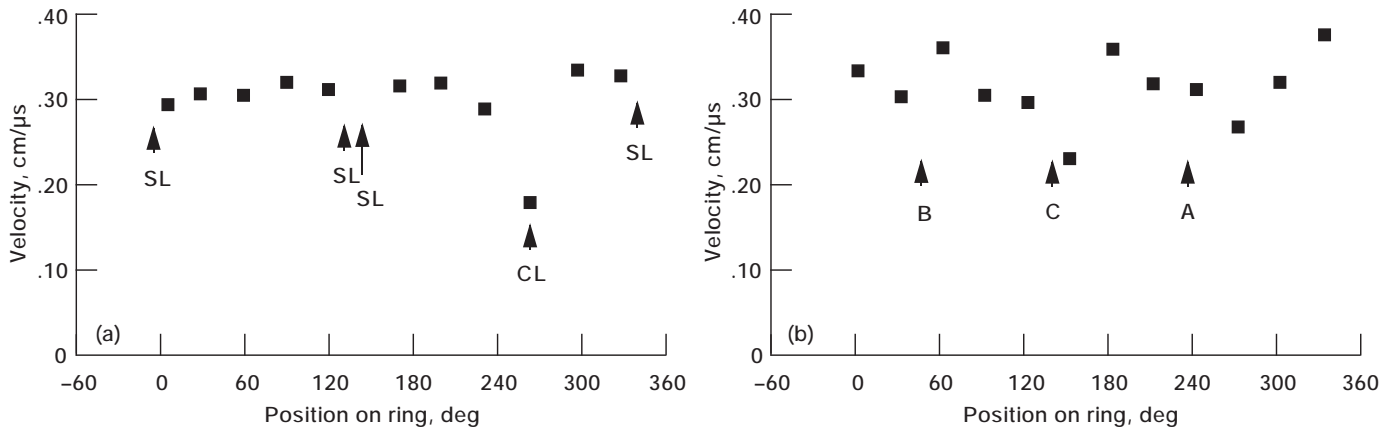
Figure 6.12.—Shear velocities for (a) ring R1 and (b) ring R3. (SL = separation location; CL = crack location; A, B, C = anomaly locations in radiographs.)
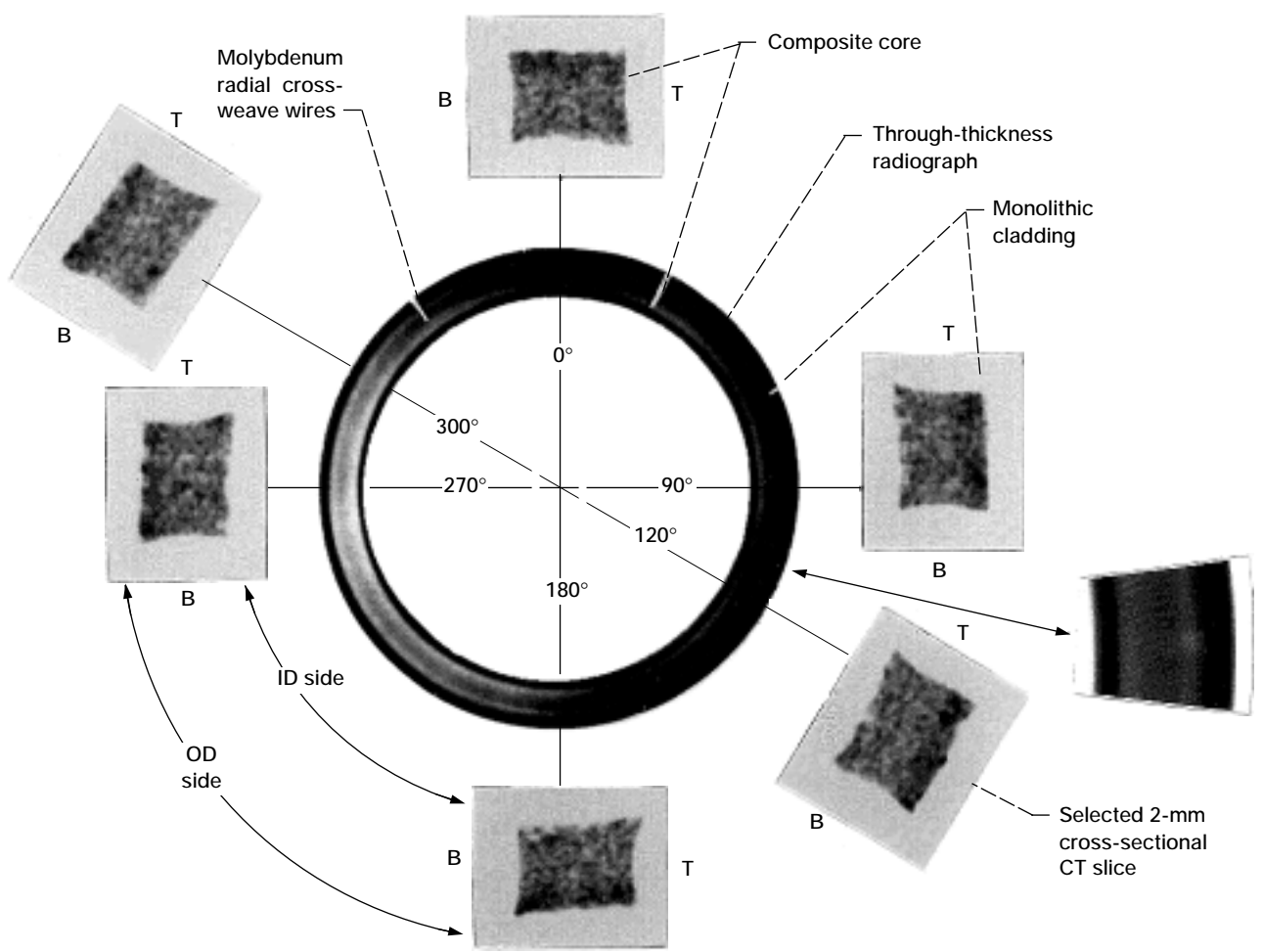
Figure 6.13.—Radiography and x-ray computed tomography of ring R2. Annulus dimensions: OD, 171 mm; ID, 133 mm; thickness, 24 mm; annulus materials, SCS–6/Ti-15V-3Cr-3Al-3Sn. (T is top side; B is bottom side. Lighter regions indicate higher density in tomography (darker in radiography).)
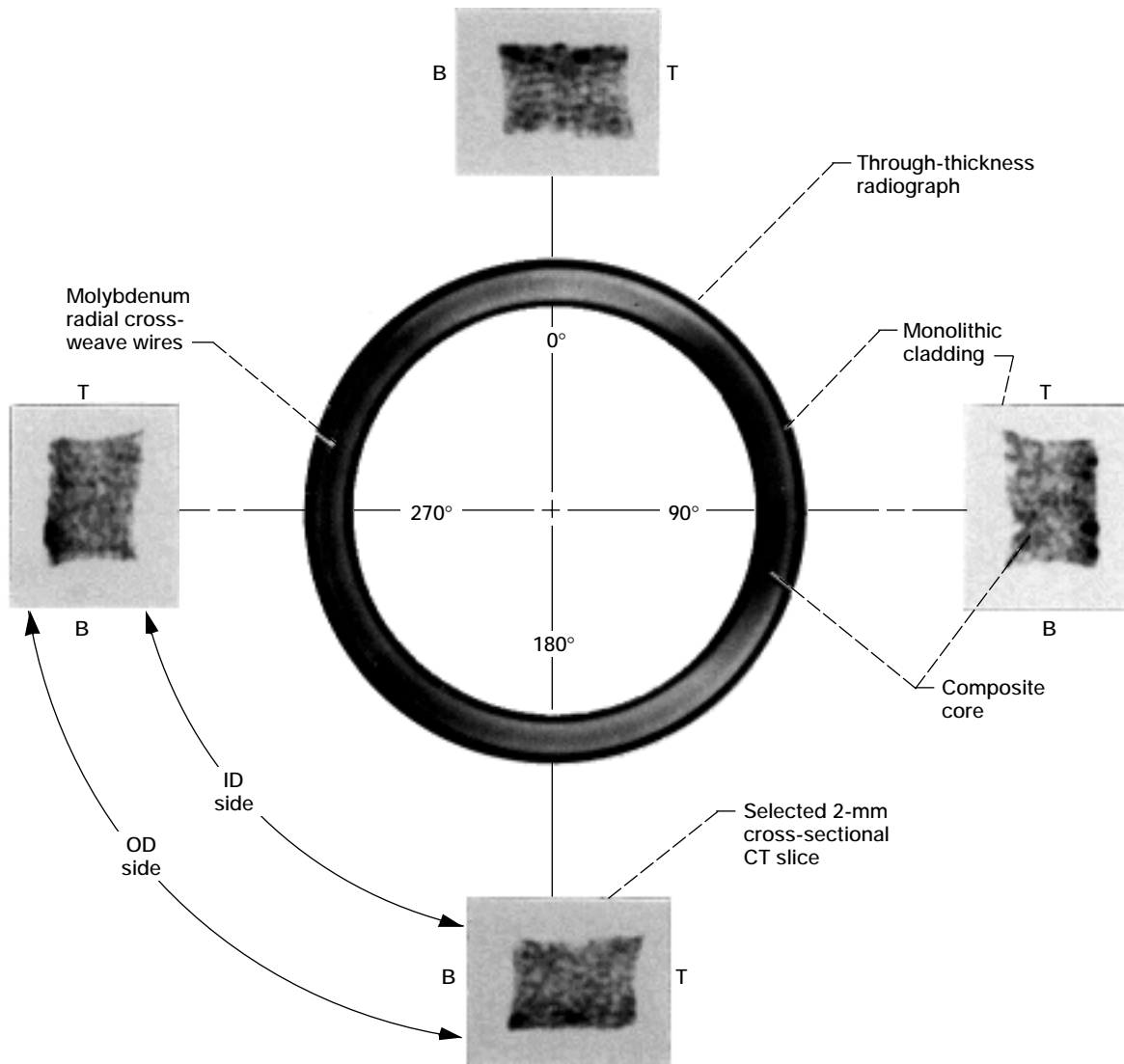
Figure 6.14.—Radiography and x-ray computed tomography of ring R3. Annulus dimensions: OD, 171 mm; ID, 133 mm; thickness, 24 mm; annulus materials, SCS–6/Ti-15V-3Cr-3Al-3Sn. (T is top side; B is bottom side. Lighter regions indicate higher density in tomography (darker in radiography).)

showed the density variations within the composite core and featured the presence of sizable low-density anomalies such as the one highlighted in figure 6.13 before the 120° marker.

The XCT slices in figures 6.13 and 6.14 depict the presence of a protruding cusp in the core, located near the top side and toward the ring ID. XCT slices further demonstrate a lower fiber content and/or poorer consolidation in the core area toward the OD side than toward the ID side. The core of the composite was supposed to be rectangular and uniform and surrounded by uniform cladding.

A magnified XCT image in figure 6.15 shows density variations in a slice of ring R1 before testing. The density variations along line AA show a 10-percent change between the case and the core and a 3-percent change within the composite core. Figure 6.15 reveals the processing/consolidation problems that resulted in the protruding cusp seen previously in rings R2 and R3. The horizontal white band in the core section indicates a manufacturing flaw (i.e., an extra strip).

Figure 6.16 presents radiographs with different magnifications of ring R2 before and after the burst test in order to compare results on the same figure. XCT slices taken before (A and D) and after (B and C) the burst test at approximately the same locations are also shown in figure 6.16. One location was near the burst area (i.e., the primary fracture (PF) area), and the other was near the secondary fracture (SF) area, which is diametrically opposite the PF. Radiography of ring R2 before testing detected a defect condition that may have led to the primary failure because the location of that defect coincides
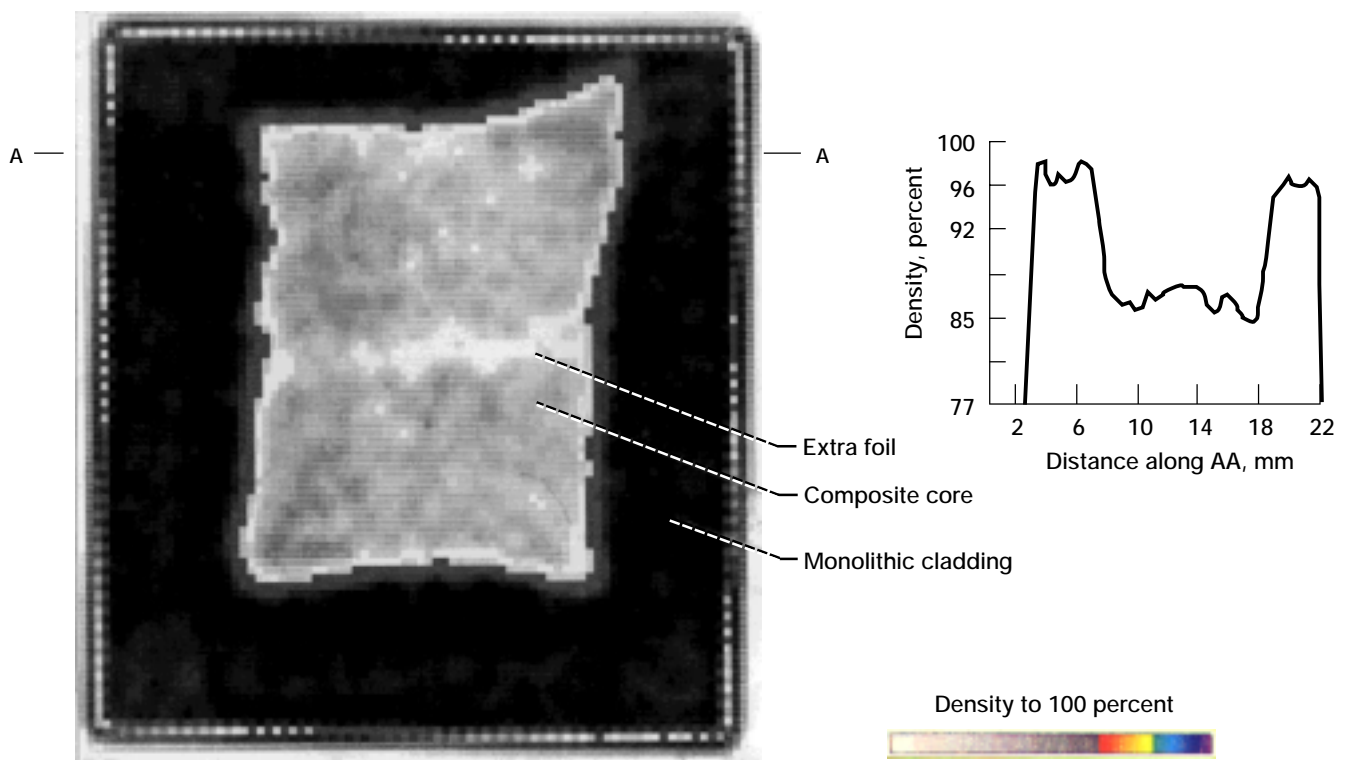
Figure 6.15.—Selected XCT cross section from ring R1 showing density variations.
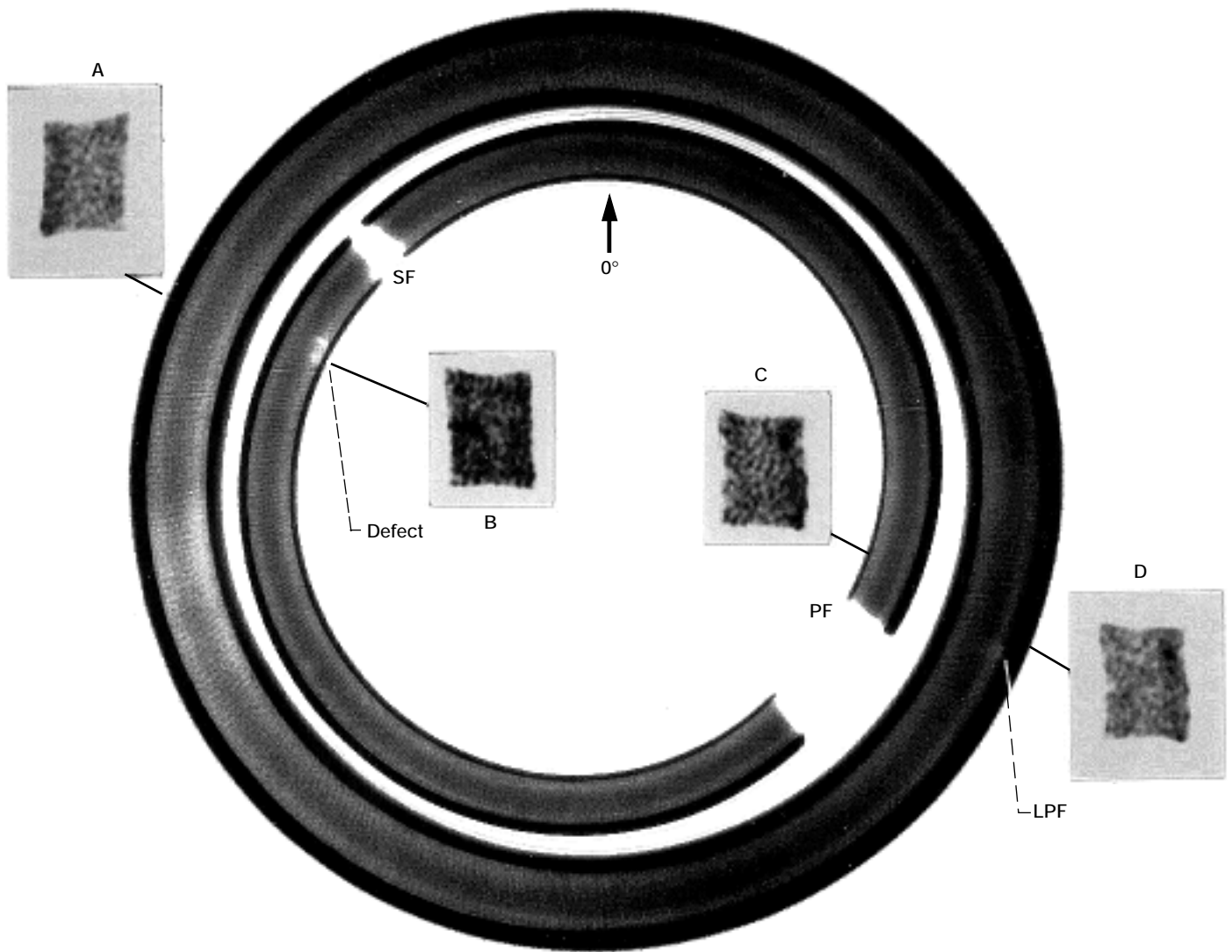
Figure 6.16.—Radiography and selected x-ray tomography slices of ring R2 before (outer ring) and after (inner ring) burst test. (Slices A and D were taken before burst testing; slices B and C, afterward. PF = primary fracture; SF = secondary fracture; LPF = location of primary fracture. Lighter regions indicate higher density in tomography (darker in radiography).)

with the location of the primary fracture designated LPF in figure 6.16. The defect has a low radiographic density, which may indicate poor consolidation in the composite core and poor cladding-composite interface bonding. Radiography also showed poor consolidation and/or higher fiber content in the OD side of the core before and after testing. A defect appears in the radiograph taken after testing. This type of defect was also found with ultrasonics. Characterizing the defects, the difference in the degree of damage between XCT slices B and C, and the damage evolution between slices A and B and between slices C and D requires further work. NDE findings need to be correlated with detailed metallographic characterization.

6.4 Discussion

In the MMC rings studied, focused P–E inspection at 5.0-MHz center frequency can detect damaged fibers and fiber/matrix interface anomalies. Further work is needed to evaluate types, sizes, and numbers of combined damage conditions. Different frequency domains and ultrasonic methodologies must be investigated before life prediction of hoop-reinforced MMC rings can be greatly aided by ultrasonics.

AU data showed that much of the ultrasonic energy was trapped inside the cladding. However, because the SWF increased after the burst test, it seems that some energy leaked into the core MMC material in the AU tests before burst testing. After failure the cladding acted as a "waveguide" from sender to receiver.

AU velocity measurements along or perpendicular to the fiber direction, and P–E velocity measurements across the fiber direction, showed a degradation at the crack location in ring R1. Velocity measurements before burst testing showed, at best, a discontinuity across the crack region. However, they did not unambiguously predict where the ring would crack because no such discontinuity was observed at the ring separations. Nevertheless, AU velocity measurements are beneficial for degradation assessment during ring life. Shear-like velocity measured on ring R3 seemed to show some degradation at the three locations (A, B, and C) where radiography showed the presence of anomalies.

XCT density information is recognized as a means of guiding structural analysis. Distortions in composite constituents, which may cause nonuniform material responses at high temperatures and under different loading conditions, have been detected by XCT and incorporated in life prediction models (Gravett, 1993; Halford, 1993; Chamis et al., 1993; Holland et al., 1993). Consequently, design and test engineers can concurrently decide whether to continue testing defective components or section them for detailed evaluation in order to further identify sources of manufacturing problems. NDE coupled with destructive verifications will certainly accelerate the improvement of composite components.

XCT information helps manufacturers avoid machining through fibers, as in the case of the protruding cusp in all rings. The manufacturer now uses XCT images to guide component machining to final dimensions.

Three-dimensional XCT density information on composite components can guide geometric modeling of composite constituents, composite stiffness modeling, and damage evolution modeling. Engineering tomography, which incorporates XCT density information in finite-element modeling, should help in predicting life and serviceability of composite components.

Predicting component life cannot be based only on coupon test results because the mechanical behavior of components is affected by different fabrication processes that are unique to specific component fabrications. Additionally, such issues as the nature of the loading, the mean residual stresses, the multiaxial state of stress, and the size effects are component-dependent distinctive characteristics (Halford, 1993). Thus, XCT, specifically, and often NDE modalities in general, help reduce engineering approximation approaches, improve statistical interpretation (imaging modalities are the source of a very large data base) of life and deterministic life prediction analyses, and ameliorate and accelerate damage tolerance assessment.

Results from coupon testing and evaluation, coupled with material characterization of related subscale components, can immensely improve component structural modeling and life prediction. This modeling and prediction would be otherwise unattainable because of the enormous cost attached to modeling based on direct testing of subscale components.

6.5 Conclusions

The capabilities of x-ray computed tomography and ultrasonics in characterizing metal-matrix-composite, subscale engine rings were investigated and found viable. Spatial density information, which can be incorporated in finite-element modeling of composite spatial stiffness and in geometric modeling of composite constituents, was provided and used in life prediction for MMC rings. It can be inferred that x-ray computed tomography is a viable technique for accelerating the development of composite components. X-ray computed tomographic imaging can identify problems with manufacturing processes, guide machining of components to final dimensions, and lead structural and design engineers to realistic component-life-prediction models.

Pulse-echo immersion ultrasonics can detect damaged fibers and fiber/matrix interface anomalies. However, more

innovative techniques, such as signal processing, are needed to unambiguously decouple combined damage conditions.

Acousto-ultrasonics can assess cladding-composite interface discontinuities or degradations and, with shear waves propagating perpendicular to fiber directions, can evaluate localized damage states.

References

Baaklini, G.Y., 1992, "X-ray Attenuation Measurements for High Temperature Materials Characterization and In-Situ Monitoring of Damage Accumulation," NASA TM–105577.

Chamis, C.C., Murthy, P.L.N., and Singhal, S.N., 1993, "Computational Simulation of Hot Composite Structures," *Reliability, Stress Analysis, and Failure Prevention*, R.J. Schaller, ed., DE–Vol. 55, American Society of Mechanical Engineers, New York, pp. 317–330.

Dos Reis, H.L.M., 1991, "Acousto-Ultrasonic Evaluation of Ceramic Matrix Composite Materials," NASA CR–187073.

Gravett, P.W., 1993, "A Life Prediction Method for Matrix Dominated Fatigue Failure of SCS–6/Ti-15-3 MMC," *Reliability, Stress Analysis, and Failure Prevention*, R.J. Schaller, ed., DE–Vol. 55, American Society of Mechanical Engineers, New York, pp. 223–230.

Halford, G.R., 1993, "MMC Ring Fatigue and Fracture Life Prediction—An Engineering Model," *Reliability, Stress Analysis, and Failure Prevention*, R.J. Schaller, ed., DE–Vol. 55, American Society of Mechanical Engineers, New York, pp. 307–315.

Halmshaw, R., 1987, "*Non-Destructive Testing: Metallurgical and Materials Science Series*," Edward Arnold, Baltimore, MD, p. 130.

Holland, F.A., Zaretsky, E.V., and Mellis, M.E., 1993, "Probabilistic Failure Prediction of an SCS–6/Ti-15-3 MMC Ring," *Reliability, Stress Analysis, and Failure Prevention*, R.J. Schaller, ed., DE–Vol. 55, American Society of Mechanical Engineers, New York, pp. 297–305..

Kautz, H.E., and Bhatt, R.T., 1991, "Ultrasonic Velocity Technique for Monitoring Property Changes in Fiber-Reinforced Ceramic Matrix Composites," *Proceedings of the 15th Annual Conference on Composites and Advanced Ceramic Materials*, *Pt. 1, Ceramic Engineering and Science Proceedings*, Vol. 12, pp. 1139–1151. (Also NASA TM–103806.)

Kautz, H.E., and Lerch, B.A., 1991, "Preliminary Investigation of Acousto-Ultrasonic Evaluation of Metal-Matrix Composite Specimens," *Materials Evaluation*, Vol. 49, pp. 607–612. (Also NASA TM–104339.)

Kautz, H.E., 1992, "Detecting Lamb Waves With Broadband Acousto-Ultrasonic Signals in Composite Structures," *Research in Nondestructive Evaluation*, Vol. 4, No. 3, pp. 151–164. (Also NASA TM–105557.)

Lott, L.A., and Kunerth, D.C., 1990, "NDE of Fiber-Matrix Bonds and Material Damage in Ceramic/Ceramic Composites," *Nondestructive Evaluation of Modern Ceramics*, pp. 135–139.

"Nondestructive Testing Methods Specification," 1979, Pratt & Whitney Specification SIM–1, Change K, pp. 1–25.

Petrasek, D.W., 1988, "High Temperature Engine Materials Intermetallic Matrix Composites," *HiTEMP Review 1988*: *Advanced High-Temperature Engine Materials Technology Program*, NASA CP–10025, pp. 67–81.

Petrasek, D.W., 1989, "Intermetallic Matrix Composites," *HiTEMP Review 1989*: *Advanced High-Temperature Engine Materials Technology Program*, NASA CP–10039, pp. 8–1 to 8–13.

Stephens, J.R., 1990, "HITEMP Program Overview," *HiTEMP Review 1990*: *Advanced High-Temperature Engine Materials Technology Program*, NASA CP–10051, pp. 1–1 to 1–23.

Tiwari, A.T., and Henneke II, E.G., 1994, "Real Time Acousto-Ultrasonic NDE Technique to Monitor Damage in SiC/CAS Ceramic Composites Subjected to Dynamic Loads," *Proceedings of ASTM Second Symposium on Cyclic Deformation, Fracture, and NDE of Advanced Materials*, ASTM STP 1184, M.R. Mitchell and O. Bucks, eds., American Society for Testing and Materials, Philadelphia, PA, pp. 363–375.

Yancey, R.N., and Baaklini, G.Y., 1994, "Computed Tomography Evaluation of Metal-Matrix Composites for Aeropropulsion Engine Applications," *Journal of Engineering for Gas Turbines and Power*, Vol. 116, No. 3, pp. 635–639.

Chapter 7
Probabilistic Failure Prediction of SCS–6/Ti-15-3 MMC Ring

Frederic A. Holland, Jr.,[*] Erwin V. Zaretsky,[*] and Matthew E. Melis[*]

7.1 Symbols

c	stress-life exponent
e	Weibull modulus in fracture
e_{avg}	average Weibull modulus
e_L	Weibull modulus in fatigue
F	probability of failure
L	life, cycles to failure
L_a	life of each finite-element volume, cycles to failure
L_b	life of specimen, cycles to failure
L_i	life of ith component, cycles to failure
L_s	total system life, cycles to failure
L_{10}	life at 10-percent probability of failure, cycles to failure
N	fatigue life, cycles to failure
N_o	characteristic life, cycles to failure
n	number of samples
P_i	probability of ith event occurring
p_i	internal pressure, MPa
r	ring radius, mm
r_i	inner radius of ring, mm
r_o	outer radius of ring, mm
S	probability of survival
S_i	probability of survival of ith component
S_s	probability of survival of total system
t	ring thickness, mm
V	volume, m^3
V_e	effective volume, m^3
V_1	volume of test specimen, m^3
V_2	volume of finite element, m^3
x	fracture strength or fatigue life
x_o	characteristics or scale value
x_u	minimum expected value of x
σ	strength or stress, MPa
σ_{max}	maximum stress, MPa
σ_o	characteristic strength, MPa

*NASA Lewis Research Center, Cleveland, Ohio 44135.

Subscripts:

1   coupon sample

2   finite element

7.2 Introduction

Advances in material capabilities promise significant improvements in aircraft performance. These improvements are possible through the application of metal-matrix composites (MMC's). Fiber-reinforced MMC's have certain advantages over monolithic metals: higher strength/density ratios and stiffness at high temperatures. However, a clear understanding of the failure of these materials, especially in thermomechanical fatigue, has yet to be achieved. Combining ceramic fibers and a metal matrix presents a mismatch in the thermal expansion coefficients and possible unfavorable chemical reactions between the two materials. These interactions are major concerns in considering the performance of these materials in service.

MMC's have been considered for reinforcement rings in jet engine compressor rotors. Incorporating MMC's into advanced rotor designs offers reduced weight and higher operating speeds. However, before the advantages of MMC's can be safely exploited in structural applications, the ability to predict the material's thermomechanical behavior must be demonstrated. Therefore, Pratt & Whitney Aircraft and the NASA Lewis Research Center formed a cooperative program to study a silicon-carbide-fiber-reinforced, titanium-metal-matrix composite, SiC/titanium–15 wt % vanadium–3 wt % chromium–3 wt % aluminum–3 wt % tin, designated SCS–6/Ti-15-3. The objective of the work reported in this chapter was to determine the applicability of a probabilistic methodology for predicting the fracture strength and fatigue life of an SCS–6/Ti-15-3 metal-matrix composite ring at 427 °C (800 °F) by using Weibull parameters.

7.3 Statistical Method

The Weibull distribution function has been useful in predicting component life. The Weibull function linearizes most engineering data distributions, making it possible to estimate a population of infinite size from small amounts of data (Weibull, 1939, 1951). This distribution is really a family of distributions because a variety of density functions can be obtained by changing the parameters. This cumulative distribution function can be expressed as

$$\ln \ln \frac{1}{S} = \ln\left(\frac{x - x_u}{x_o - x_u}\right)^e \qquad (7.1)$$

If the scale value is zero, the three-parameter Weibull equation becomes a two-parameter equation. The Weibull slope, or modulus, e is a measure of the variability of x. The higher the value of e, the less variability. In this investigation the variable x is fatigue life or fracture strength. From equation (7.1) the survival can be expressed as

$$S = \exp\left[-\left(\frac{x - x_u}{x_o - x_u}\right)^e\right] \qquad (7.2)$$

If n number of samples are tested to failure and the maximum failure values (i.e., stresses, lives) are ranked in ascending order, the probability of failure associated with the ith value is often expressed by Bernard's formula (Kapur and Lamberson, 1977):

$$P_i = \frac{i - 0.3}{n + 0.4} \qquad (7.3)$$

The effective volume V_e of a nonuniformly stressed body is the theoretical equivalent volume that a uniformly stressed body has at the same probability of failure. For uniaxial stress it is expressed as

$$V_e = \int_V \left(\frac{\sigma}{\sigma_{max}}\right)^e dV \qquad (7.4)$$

The effective volume of a nonuniformly stressed body can be considered an equivalent specimen volume under uniform uniaxial stress of magnitude σ_{max}, where the reliability of the effective volume is equal to the specimen reliability. This concept was introduced earlier by DeSalvo (1970). The effective volume has also been considered as defining the structure's "dangerous area" (i.e., the region in which fracture is likely to begin (Matsusue et al., 1981)). If a component is uniformly stressed (i.e., is constant), its effective volume is its entire stressed volume. The relationship between fracture strength and effective volume for the same probability of survival can be approximated with the following equation:

$$\frac{\sigma_2}{\sigma_1} = \left(\frac{V_{e,1}}{V_{e,2}}\right)^{1/e} \qquad (7.5)$$

7.4 Analytical Method

Zaretsky (1987) developed an expression for predicting life at a given survivability of a stressed component 2 relative to the known life of a stressed component 1:

$$L_2 = L_1\left(\frac{\sigma_1}{\sigma_2}\right)^c\left(\frac{V_{e,1}}{V_{e,2}}\right)^{1/e_L} \qquad (7.6)$$

This equation gives the component's life relative to a similar component when both have the same survivability. The system life can then be calculated from the individual component lives as follows:

$$\left(\frac{1}{L_s}\right)^{e_L} = \sum\left(\frac{1}{L_i}\right)^{e_L} \qquad (7.7)$$

Zaretsky's method can be extended to predict the relative component survivability at equal life. The survivability of component 2 is given by

$$S_2 = S_1^{\left(L_2/L_1\right)^{e_L}} \qquad (7.8)$$

Finally, the component's survivability is equal to the product of all the elements' survivabilities, assuming independent and mutually exclusive mechanisms.

$$S_s = \prod_{i=1}^{n} S_i \qquad (7.9)$$

The methodology is easily incorporated into the finite-element method to determine the life and survivability of a structural component. The entire component is analogous to a system. The finite-element model of the component is a discretization of the geometry into element volumes. These elements are considered to be base members of the analogous system. The life of each element is calculated from the elemental stress levels and volume as described previously to determine the component's incipient failure life. Finite-element analysis is combined with probabilistic methods in the Ceramic Analysis and Reliability Evaluation of Structures (CARES) computer program (Nemeth et al., 1990). CARES uses the results of the MSC/NASTRAN or ANSYS finite-element analysis programs to calculate the reliability of brittle components.

A relative comparison approach is selected on the basis of a maximum stress state. The selected stress failure criterion can be based on the material used in the component. If no fatigue data are available, the stressed element can be arbitrarily assigned a life and a survivability that are used to normalize the life and survivability of the other elements. This approach allows easy, qualitative comparisons between designs. Also, only one set of coupon fatigue tests at operating temperatures is necessary to fix the Weibull parameters and to establish quantitative component lives if the stress-life exponent of the
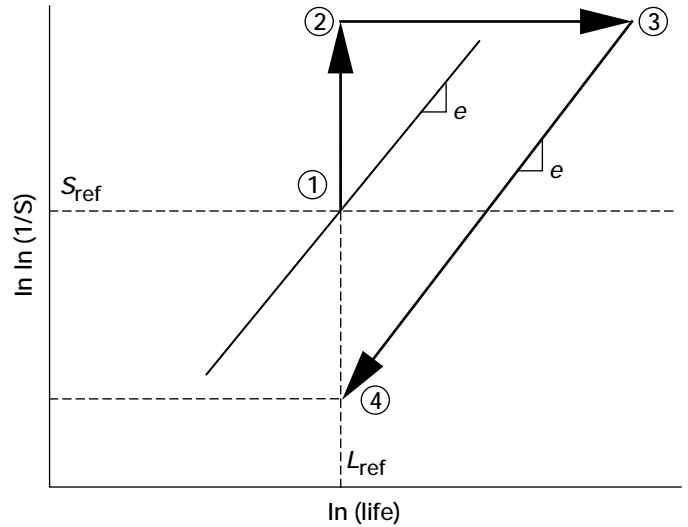
Figure 7.1.—Element survivability methodology.

material is already known. However, if the stress-life exponent is not known, at least two additional sets of coupon fatigue tests are necessary.

The methodology for predicting element survivability at a fixed life is illustrated in figure 7.1. The critical element's (usually the maximum stressed element) life and survivability are set at unity and 90 percent, respectively (point 1). This is the analysis point to which all the other elements' lives and survivabilities will be referenced. Other designs can also be referenced to this point by using the same critical volume and stress. The expected survivability at any number of stress cycles can be determined, as shown in the figure, by drawing a line through the reference point with a slope equal to e_L.

Next, an element's survivability is adjusted strictly on the basis of volume effects (point 2). This adjustment is done independently of the stress levels. Because stress is not involved, element life is not affected, and the adjustment results in purely vertical displacement from the reference point. In the example shown, the second element's volume is greater than the critical volume and contains more potential crack initiation sites. Therefore, the adjusted survivability is lower.

The element's life is then adjusted strictly on the basis of element stress relative to the critical stress (point 3). This adjustment is independent of volume considerations. Consequently, element survivability is not affected, and the life adjustment results in purely horizontal displacement at a constant survivability. In the example shown, the second element's stress is lower than the critical stress. Therefore, its life is greater and shifts to the right.

A new material Weibull line is now drawn through the adjusted life/survivability point. Because the compared element's material is the same as the critical element's material, the line is drawn parallel to the original line. However, if the elements had dissimilar materials, the new line would be drawn

with the new Weibull slope. Thus, designs incorporating different materials can be compared with respect to survivability.

The compared element's survivability is adjusted once more to the critical element's assigned life of unity (point 4). Now the displacement is along the Weibull line and gives the survivability of an element relative to that of the critical element, with both elements having the same life. Repeating this procedure for all the elements in the finite-element model gives the survivability for any section of the design at any time.

The method for determining fracture strength of the MMC ring is similar to that used to predict life. By using a finite-element analysis based on an assumed ring pressure at the ring inner diameter, the probability of failure of each finite-element mesh is determined from previously obtained coupon data and stress volume.

$$S_2 = \left(S_1\right)^{V_1/V_2} \tag{7.10}$$

The component survivability at a given pressure is equal to the product of all the element survivabilities.

7.5 Test Specimens and Material

SCS–6/Ti-15-3 was selected for the NASA/Pratt & Whitney cooperative program because its parameters are established, the alloy was available in full form, its mechanical properties are reproducible, and the material and related technology are nonproprietary.

Reduced-section specimens were used to obtain fundamental data. The specimens included two dogbone types (63.5-mm (2.5-in.) and 419.1-mm (16.5-in.) radii) and a tangent radius specimen. Examples of the dogbone and tangent radius specimens are shown in figures 7.2 and 7.3, respectively. The gage section parameters for these specimens are summarized in table 7.1. The specimens were made from SCS–6/Ti-15-3 [0°]. In general, the cyclic lives of the 419.1-mm (16.5-in.) radius specimens were found to be similar to those produced by the 63.5-mm (2.5-in.) radius geometry.

Three SCS–6/Ti-15-3 [0°] MMC's were manufactured for testing. The ring and loading fixture are shown in figure 7.4. The ideal ring cross section and dimensions are shown in figure 7.5. A more accurate representation of the ring cross section is shown in figure 7.6, where the observed cusp is a manufacturing anomaly. The original intent of the program was to test a single ring in fracture and the remaining two rings in fatigue at 427 °C (800 °F). This plan was altered when the second ring to be tested failed by fracture. None of these rings were fatigue tested.
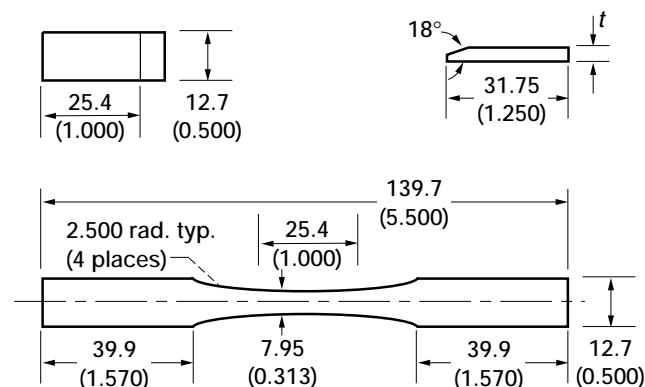
Figure 7.2.—Test specimen and tab details. (Dimensions are in millimeters (inches).)
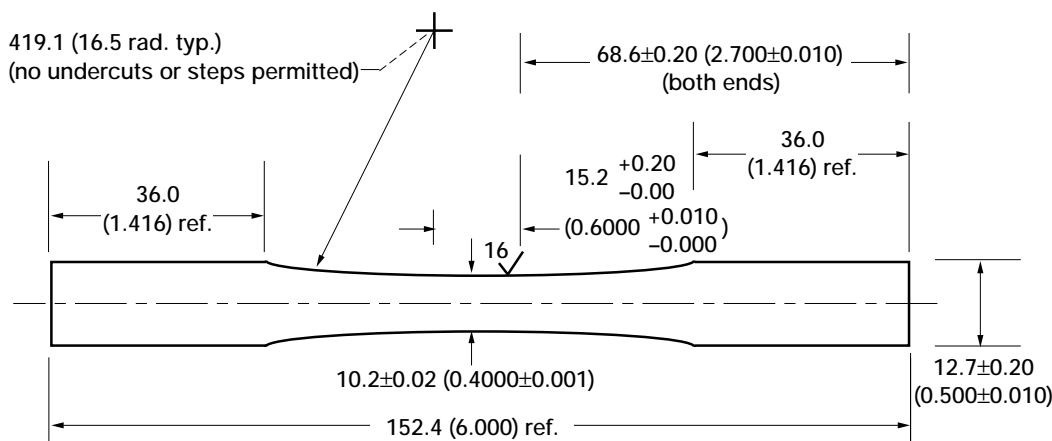
Figure 7.3.—MMC test specimen. Dogbone 419.1-mm (16.5-in.) radius; thickness as furnished. (Dimensions are in millimeters (inches).)

TABLE 7.1.—TEST SPECIMEN GAGE SECTION PARAMETERS
[Test type, fracture.]

Specimen type	Length		Width		Thickness		Volume	
	cm	in.	cm	in.	cm	in.	cm^3	in.^{3}
Tangent radius	2.5	1.0	0.63	0.25	0.203	0.08	0.33	0.02
Dogbone	3.6	1.5	1.02	.40	.229	.09	.88	.054
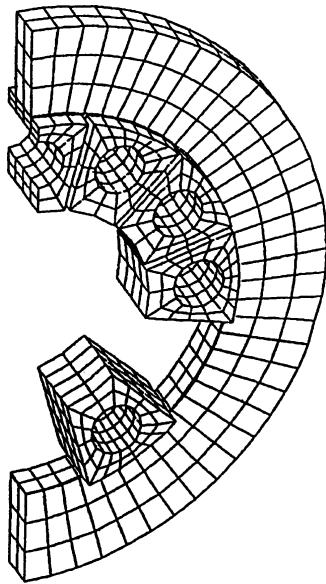
Figure 7.4.—MMC ring and test fixture.
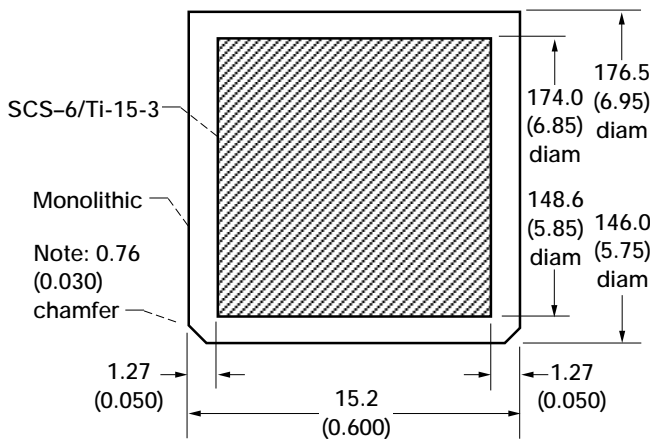
Figure 7.5.—Cross section of MMC test ring. (Dimensions are in millimeters (inches).)
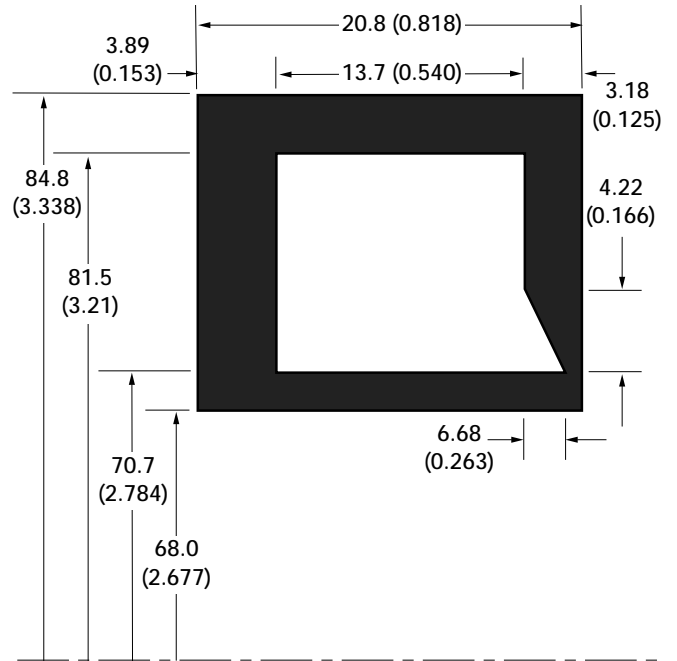
Figure 7.6.—Geometry of NAS–1 MMC ring modeled at Pratt & Whitney (average of 35 computed tomography scans). (Dimensions are in millimeters (inches).)

7.6 Results and Discussion

7.6.1 Fatigue Life Prediction

Six fatigue tests were performed at NASA Lewis over a range of maximum stress levels to obtain a stress-life relationship for the MMC samples. A flat dogbone specimen was used in this series of experiments whose gage section dimensions are given in table 7.1. The specimens were fatigue tested using an *R*-ratio of 0 (minimum to maximum stress ratio) and a triangular waveform at 0.33 Hz. This relationship between maximum stress and life (cycles to failure) is shown in figure 7.7. Linear regression analyses of the data resulted in a stress-life exponent of 6.0.

7.6.1.1 Estimation of Weibull parameters.—We assumed that the failure of the MMC could be adequately modeled by Weibull statistics. However, there were insufficient data to obtain accurate Weibull parameters. Only three fatigue tests were available from Pratt & Whitney that had been performed under identical conditions using a 152.4-mm (6.0-in.) tangent radius specimen. These conditions were cycled at 427 °C (800 °F) between a maximum stress of 1103 MPa (160 ksi) and a minimum stress of 551.6 MPa (80 ksi). A Weibull plot of these data is shown in figure 7.8, where a Weibull modulus of 4 and a characteristic life of 11 487 cycles were obtained by linear regression analyses. These Weibull parameters, although based on a very small sample size, were taken as the best available estimates.
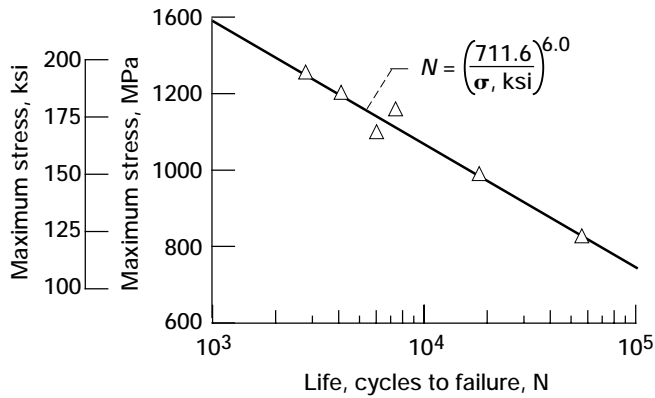
Figure 7.7.—Stress-life relation for SCS–6/Ti-15-3 MMC specimens. Source, NASA; specimen, 25.4- by 6.35-mm (1.0- by 0.25-in.) gage section dogbone; fiber content, 34 vol %; temperature, 427 °C (800 °F).

$$N = \left(\frac{711.6}{\sigma, \text{ksi}}\right)^{6.0}$$
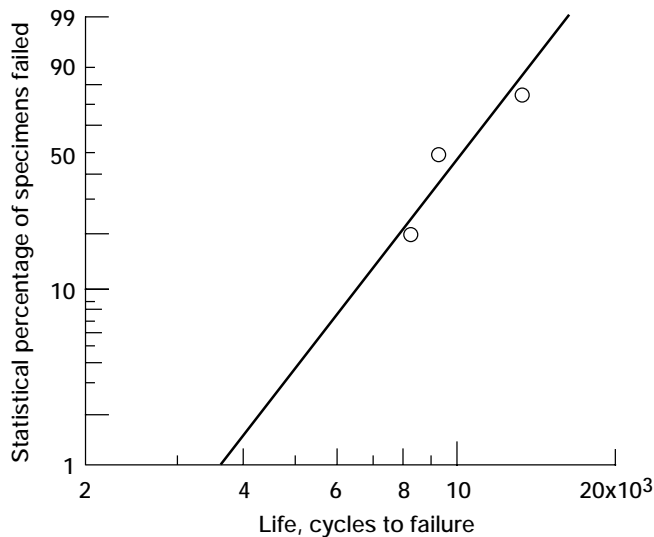
Figure 7.8.—Estimate of fatigue life distribution based on Weibull analysis of SCS–6/Ti-15-3 MMC specimen data. Source, Pratt & Whitney; specimen, 152-mm (6.0-in.) tangent radius; maximum stress, 1103 MPa (160 ksi); temperature, 427 °C (800 °F); fiber content, 34 vol %; Weibull modulus, e, 4.0; characteristic fatigue life, 11 487 cycles.

7.6.1.2 Finite-element method.—A finite-element model of the ring cross section is shown in figure 7.9. Tangential and radial stresses were induced in the ring as a result of internal pressure. However, the radial stresses were compressive and were assumed not to contribute to failure. The tangential stress distribution of the ring core is shown in figure 7.10. The cladding was assumed to be weaker than the MMC core. To simplify the analysis, we assumed that the core and the cladding are two separate systems. The cladding was considered only in that it affects the stress state of the core. Failure of the entire ring system was assumed to occur only when the MMC core failed.
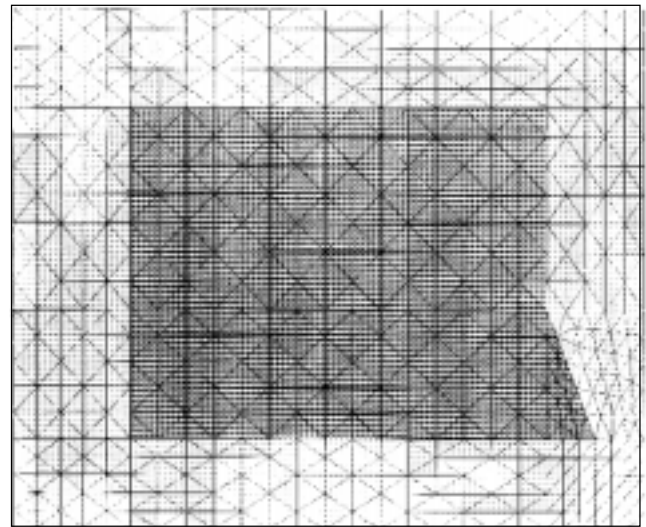
Figure 7.9.—Finite-element model of ring cross section consisting of MMC core and surrounding cladding.
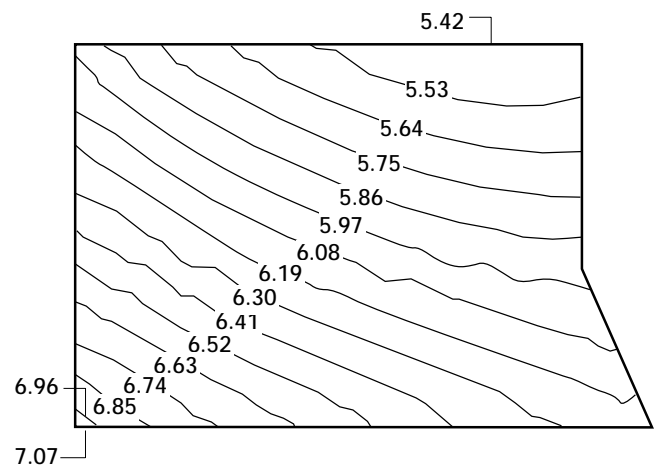
Figure 7.10.—Tangential stress distribution in SCS–6/Ti-15-3 MMC ring core for internal pressure of one stress unit based on finite-element analysis.

According to finite-element analysis the internal pressure was about 1/7th that of the maximum induced stress in the ring. Life calculations were based on a maximum induced stress in the ring of 1081.1 MPa (156.8 ksi), which required an internal pressure of approximately 154.4 MPa (22.4 ksi). The volume of each finite element was calculated, and the maximum stress in each element was assumed to be constant throughout the entire volume. The life of each finite-element volume L_2 was then calculated by using equation (7.6). The life of the specimen L_1 corresponded to a 90-percent probability of survival. The total life of the ring was then computed by using equation (7.7). This life was based on a 10-percent probability of failure and is termed the L_{10} life. The predicted stress-life relationship for the ring is shown in figure 7.11. To compute the life of the ring for
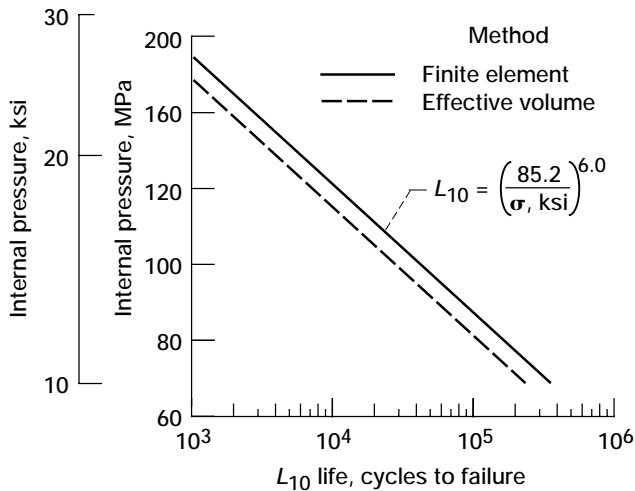
Figure 7.11.—Predicted effect of internal pressure on fatigue life of SCS–6/Ti-15-3 MMC ring based on 10-percent failure probability.

any given survival probability based on the L_{10} life, the following relationship can be derived from the Weibull cumulative distribution function:

$$\frac{L}{L_{10}} = \left(\frac{\ln \dfrac{1}{S}}{\ln \dfrac{1}{0.9}} \right)^{1/e_L} \qquad (7.11)$$

Simplifying,

$$L = 1.755 \, L_{10} \left(\ln \frac{1}{S} \right)^{0.25} \qquad (7.12)$$

At the time of this writing, no experimental data were available for comparison.

7.6.1.3 Effective-volume method.—A simple approach to predicting ring reliability was to use an effective volume. In this approach, in addition to assuming that the MMC ring core was homogeneous, we also assumed that the ring was geometrically symmetrical. To further simplify the analysis, we neglected the effect of the cladding. This assumption allowed the ring to be modeled as a uniform thick-walled cylinder under internal pressure, where the tangential stress distribution is given by a textbook equation (Ugural and Fenster, 1987):

$$\sigma_t = \left(\frac{r_i^2 p_i}{r_o^2 - r_i^2} \right) \left(1 + \frac{r_o^2}{r_i^2} \right) \qquad (7.13)$$

This stress distribution was substituted into equation (7.4) for

σ, and the effective volume was determined to be 37.0 μm^3 (2.26 in.^{3}).

The stress distribution in the thick-walled cylinder model correlated very well with the finite-element model. Both models predicted the maximum stress in the MMC core to be about seven times the internal pressure. The predicted stress range in the core was about $5.4p_i$ to $7.0p_i$ from finite-element analysis and $6.0p_i$ to $7.0p_i$ from the thick-walled cylinder model. The maximum stress in the ring corresponding to a 90-percent probability of survival, or 10-percent probability of failure, was determined by using the effective volume and coupon sample data in equation (7.5). This stress value was then used in equation (7.6) to estimate the ring fatigue life. The predicted ring stress-life relationships obtained from the finite-element and effective-volume methods are shown in figure 7.11. The effective-volume approximation was more conservative. For a 50-percent probability of failure (L_{50}) and a maximum internal pressure of 154.4 MPa (22.4 ksi), the effective-volume and finite-element methods predicted ring fatigue lives of 2700 cycles and 4800 cycles, respectively. No ring fatigue data were available for comparison.

7.6.2 Fracture Strength Prediction

7.6.2.1 Estimation of Weibull parameters.—No fracture data were available for the MMC material with 33-vol % fiber content at the ring test temperature of 427 °C (800 °F). Only two fracture strengths were obtained from laboratory tests at NASA Lewis at 300 °C (572 °F), and three experimental strengths were obtained at 550 °C (1022 °F). An average value of 16 was obtained for the Weibull slope (fig. 7.12(a)). The average characteristic strength was about 1379 MPa (200 ksi), which was estimated to be the strength at 427 °C (800 °F), the ring test temperature. Tensile tests performed at Pratt & Whitney for a 38-vol %-fiber MMC produced only three fracture strengths at 21 °C (70 °F) and 427 °C (800 °F) each. The average Weibull slope was also 16 (fig. 7.12(b)). Therefore, this value was taken as the best estimate of the Weibull slope.

7.6.2.2 Finite-element method.—Several approaches to calculating the ring reliability are based on static strength. One of the simplest, using hand calculations, is to first assign a probability of survival to the maximum-stressed finite element and then calculate the stress associated with this volume and probability of survival. The internal ring pressure necessary to induce this calculated stress can be determined and input in the finite-element code. The stress values of each element can then be used to calculate the probability of survival by using equation (7.8), where the coupon sample is used as a gage. The total probability of survival is then the multiplication of the element reliabilities (eq. (7.9)). Having the reliability at the associated load and assuming that the Weibull modulus is the same for the structure as for the coupon sample, a predicted fracture strength distribution can be determined.
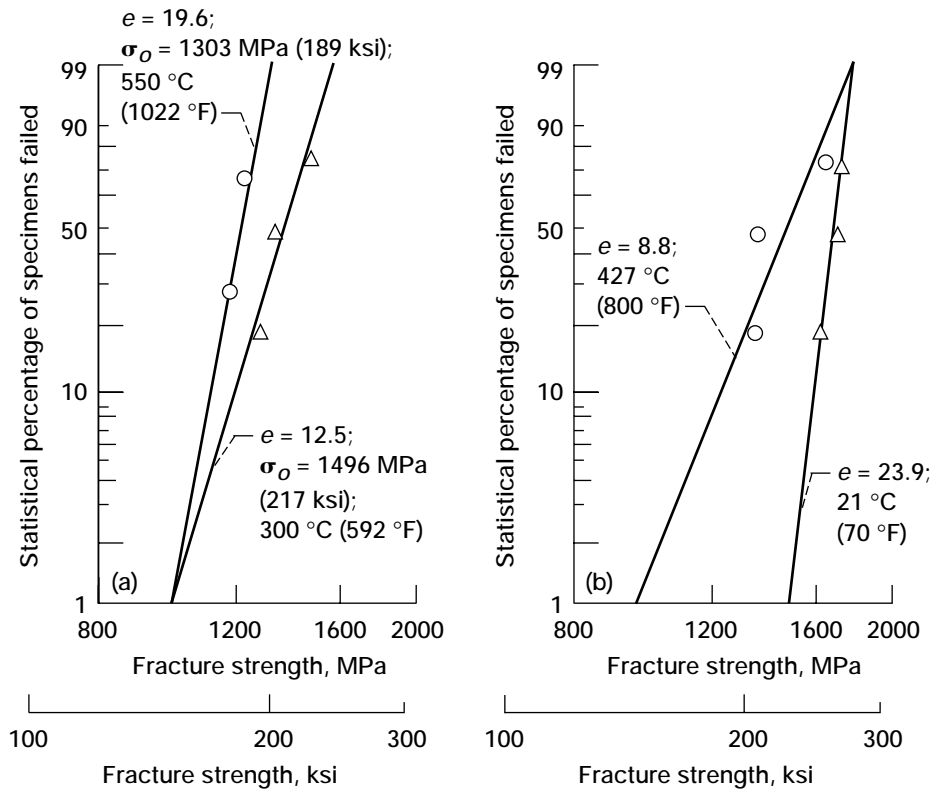
Figure 7.12.—Weibull analysis of SCS–6/Ti-15-3 MMC longitudinal fracture strength
data. (a) Source, NASA; fiber content, 33 vol %; average Weibull modulus, e_{avg}, 16.
(b) Source, Pratt & Whitney; fiber content, 38 vol %; average Weibull modulus, e_{avg}, 16.

By following this methodology, a 90-percent probability of survival was assigned to the maximum-stressed finite element in the ring. The element strength corresponding to this reliability was computed by first calculating the specimen strength at the same probability of survival and scaling this value by following equation (7.5). An alternative method is to use a single equation derived from equations (7.1) and (7.10):

$$\sigma = \sigma_o \left(-\frac{V_{e,1}}{V_{e,2}} \ln S \right)^{1/e} \qquad (7.14)$$

The entire volume of the finite element is considered as an effective volume because we assumed that the stress variation through the finite element is negligible. Next, the internal pressure on the ring necessary to create this stress was determined. The stresses in the remaining finite elements were adjusted in proportion to the adjusted stress of the maximum-stressed element. These stresses were used in determining the corresponding probability of survival for the coupon samples.

The reliability of each element was then determined by adjusting the calculated reliability of the coupon samples based on the volume effect. The total ring reliability was then computed by using equation (7.9). We assumed that the predicted fracture strength distribution of the ring had the same Weibull modulus as the coupon samples. Having this slope and the reliability at a given load, the following equation for the fracture strength distribution was determined for the ring in terms of the internal pressure p_i (ksi):

$$F(p_i) = 1 - \exp\left[-\left(\frac{p_i}{20.8} \right)^{16} \right] \qquad (7.15)$$

where 16 is the Weibull modulus and 20.8 is the predicted characteristic strength of the ring in kips per square inch.

7.6.2.3 Effective-volume method.—The ring fracture strength was computed by using the effective-volume method as in the fatigue life prediction. Instead of calculating the reliability for each element, a single effective volume was used

Figure 7.13.—Predicted fracture strength distributions for SCS–6/Ti-15-3 MMC ring using finite-element and effective-volume methods.

TABLE 7.2.—FATIGUE FRACTURE STRENGTH PREDICTIONS FOR SCS–6/Ti-15-3

Method	Fatigue,[a] cycles	Internal burst pressure of ring	
		MPa	ksi
Finite element	130 500	143.4	20.8
Effective volume	185 000	164.1	23.8
Experiment	(b)	[c]172.4	[c]25.0

[a]Maximum stress, 82.7 MPa (12 ksi).
[b]Not applicable.
[c]Average value from 155.1 and 189.6 MPa (22.5 and 27.5 ksi).

levels, the results should be viewed as preliminary. These results are summarized in table 7.2.

7.7 Summary of Results

Two-parameter Weibull analysis was used to predict the fracture strength and fatigue life of an SCS–6/Ti-15-3 metal-matrix composite (MMC) ring from coupon sample data. The fracture strength and fatigue life of the ring were assumed to be volume dependent. Fracture strengths were predicted in terms of maximum allowable ring internal pressure. Two methods were used. One simple method was to calculate an effective volume for an idealized ring on the basis of a theoretical approximation of the stress distribution. The fracture strength and fatigue life of the coupon samples were then scaled to the effective volume of the ring. The other method used finite-element analysis to determine a more realistic stress distribution in the actual, geometrically imperfect ring. The total ring reliability was then determined by multiplying the element reliabilities while using coupon samples as a gage. The following results were obtained:

(1) Fracture strength predictions for the MMC ring by the effective-volume and finite-element methods differed by about 5 and 17 percent, respectively, from the median of the experimental data. For a 50-percent probability of failure the effective-volume method predicted a ring internal failure pressure of 164.1 MPa (23.8 ksi), whereas the finite-element method predicted 143.4 MPa (20.3 ksi). The median value from the experimental data was calculated as 173.1 MPa (25.1 ksi) from experimental failure pressures of 155.1 MPa (22.5 ksi) and 189.6 MPa (27.5 ksi).

in equation (7.5) to determine the strength of the entire ring from coupon sample data. Assuming the Weibull slope to be the same as for the coupon samples, a fracture strength distribution was estimated. The predicted fracture strength distributions obtained from the finite-element and effective-volume methods are compared in figure 7.13. The finite-element method was the most conservative, but the effective-volume method correlated very well. For a 50-percent probability of failure the effective-volume method predicted a ring internal burst pressure of 164.1 MPa (23.8 ksi), whereas the finite-element method predicted 140.0 MPa (20.3 ksi). The experimental ring failure pressures were 155.1 and 189.6 MPa (22.5 and 27.5 ksi). Weibull analysis of these experimental data gave a median ($F = S = 0.5$) strength of 173.1 MPa (25.1 ksi), just slightly larger than the average experimental failure pressure of 172.4 MPa (25.0 ksi). The fracture strength predicted by the effective-volume method was –5 percent different from the average experimental result, and the finite-element method resulted in a –17-percent difference. Because data were lacking at both the coupon sample and component

(2) The effective-volume and finite-element methods predicted ring fatigue lives of 2700 and 4800 cycles, respectively, at 50-percent probability of failure and 154.4-MPa (22.4-ksi) maximum ring internal pressure. No ring fatigue data were available for comparison.

References

DeSalvo, G.J., 1970, "Theory and Structural Design Applications of Weibull Statistics," WANL–TME–2688, Westinghouse Astronuclear Laboratory, Pittsburgh, PA.

Kapur, K.C., and Lamberson, L.R., 1977, *Reliability in Engineering Design*, John Wiley & Sons, Inc., p. 300.

Matsusue, K., Takahara, K., and Hashimoto, R., 1981, "Strength Evaluation Test of Hot-Pressed Silicon Nitride at Room Temperature," NAL–TR–676, National Aerospace Laboratory, Tokyo, Japan.

Nemeth, N., Manderscheid, J., and Gyekenyesi, J., 1990, "Ceramics Analysis and Reliability Evaluation of Structures (CARES)," NASA TP–2916.

Ugural, A.C., and Fenster, S.K., 1987, *Advanced Strength and Applied Elasticity*, Elsevier Science Publishing Co., Inc., New York.

Weibull, W., 1939, "The Phenomenon of Rupture in Solids," *Ingeniors Vetenskaps Akademien*, No. 153.

Weibull, W., 1951, "A Statistical Distribution of Wide Applicability," *Journal of Applied Mechanics*, Vol. 18, No. 3, pp. 293–297.

Zaretsky, E.V., 1987, "Fatigue Criterion to System Design, Life, and Reliability," *Journal of Propulsion and Power*, Vol. 3, No. 1, pp. 76–83.

Chapter 8
MMC Ring Fatigue and Fracture Life Prediction—An Engineering Model

Gary R. Halford*

8.1 Symbols

A	cross-sectional area or classical fatigue ratio, alternating to mean
B	intercept of elastic strainrange–life relations
C	intercept of inelastic strainrange–life relations
C′	intercept of inelastic line for creep-fatigue cycles
F	inelastic strain fraction
K	cyclic strain-hardening coefficient
L	radial load per shoe, N (lbf)
MF	multiaxiality factor
N	number of applied cycles
R	ratio, algebraic minimum to maximum
TF	triaxiality factor
V	ratio, mean to alternating
ε	strain, m/m (in./in.)
σ	stress, MPa (ksi)

Subscripts:

cc	creep strain in tension, creep strain in compression
cp	creep strain in tension, plastic strain in compression
el	elastic
f	failure with zero mean stress
fm	failure with mean stress
i	microcrack initiation with zero mean stress
ij	*pp*, *pc*, *cp*, or *cc*
in	inelastic
L	load
p	microcrack propagation with zero mean stress
pc	plastic strain in tension, creep strain in compression
pp	plastic strain in tension, plastic strain in compression
t	total
u	ultimate (tensile strength)
y	yield (0.2-percent offset)
ε	strain
σ	stress

---

*NASA Lewis Research Center, Cleveland, Ohio 44135.

Superscripts:

b   power for elastic strainrange–life relations

c   power for inelastic strainrange–life relations

n   cyclic strain-hardening exponent ($\approx b/c$)

8.2 Introduction

The framework of an engineering creep-fatigue durability model has recently been presented (Halford et al., 1993) that addresses the key crack initiation and growth issues involved in the high-temperature, low-cycle fatigue resistance of [0°], continuous-fiber-reinforced, metal-matrix composites (MMC's). Because the model was originally proposed for dealing with thermomechanical fatigue, adapting it to isothermal loading conditions was a relatively simple matter. The model has been used herein to estimate the 427 °C (800 °F) radial static burst pressure and low-cycle fatigue life of cyclically loaded, continuous-fiber-reinforced MMC rings (fibers aligned with the circumferential, maximum principal stress direction, i.e., [0°]).

The program was part of a four-year cooperative effort between Pratt & Whitney's Government Engines and Space Propulsion Group and the National Aeronautics and Space Administration's Lewis Research Center. Overall results of that program are the subject of this chapter. Several other durability models were developed over the course of the program and have been reported on by their creators in other chapters.

8.3 Framework of Model

The MMC material was treated as if it were a conventional structural element whose weakest, most highly stressed regions are the likely origins of failure initiation (fig. 8.1). As with conventional structures the durability of an MMC was expected to be governed by localized stress, strain, and temperature conditions and their variation with time. Micromechanical structural analysis techniques were used to calculate local conditions. At this stage of the model's development it is assumed that a local analysis will suffice for dealing with global behavior of a specimen. Although the metallic matrix was used as the vehicle for tracking fatigue damage evolution, due consideration was also given to the stress-strain and fracture characteristics of the brittle fibers and to the structural interactions of fiber, interface, and matrix. These interactions are represented schematically in figure 8.2.

The engineering durability model has three major elements:
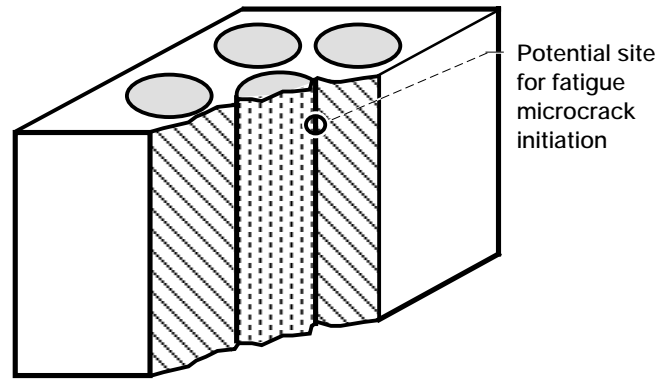
Figure 8.1.—Composite material as ministructure.

(1) Creep-fatigue equations reflect both the flow and failure behavior of the in situ matrix material. Equations are calibrated from test results of unreinforced matrix material, which may differ slightly from its in situ counterpart. The measured macrocrack initiation fatigue life (usually defined as complete separation of a coupon-sized axial specimen) of the matrix material is apportioned into microcrack initiation and microcrack propagation phases.

(2) The matrix flow and failure responses are altered by the presence of fibers and interfaces. Some influences act solely on the microcrack initiation phase of the matrix fatigue life, others act on the microcrack propagation phase, and some affect both.

(3) Overriding influences, such as a maximum tensile strain limit of brittle fibers, could cause individual fiber fractures and ensuing catastrophic failure of the surrounding matrix.

The matrix material's isothermal creep-fatigue flow and failure behavior are characterized in terms of the total strain version of strainrange partitioning (TS–SRP) (Saltsman and Halford, 1988a). The term "creep fatigue" is used because the cycles emphasize creep deformation superimposed on strain-limited fatigue cycling. Because the specimens are typically tested in a laboratory air atmosphere, they are also subject to oxidation. It is tacitly implied that creep-fatigue experiments in air produce results which reflect the interactions of all three important failure behavior factors: fatigue, creep, and oxidation.

In addition to documenting creep-fatigue-oxidation failure characteristics, it is also necessary to establish the cyclic, viscoplastic flow behavior of the matrix. The TS–SRP life prediction approach is applicable to any generalized, time-dependent, creep-fatigue cycle. Generality is achieved through the use of existing unified viscoplastic models (Bodner and Partom, 1975; Walker, 1981; Robinson and Swindeman, 1982; Freed, 1988) to represent the flow behavior. On occasion, we have had to resort to simpler, less general, empirical power-
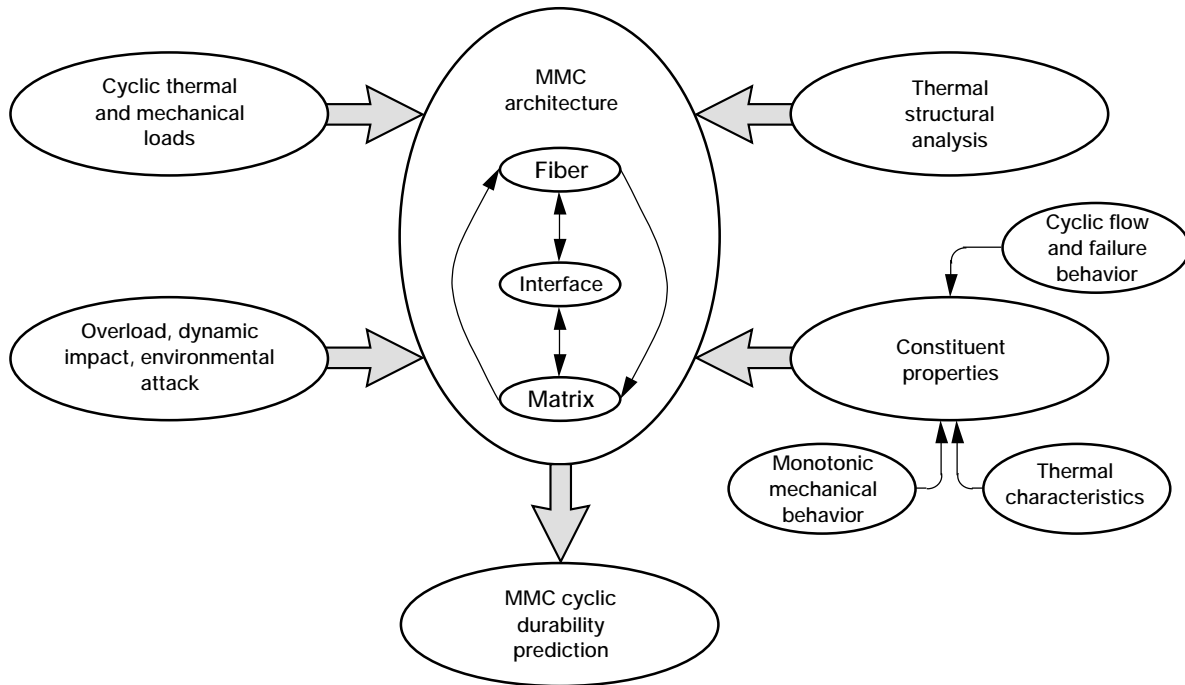
Figure 8.2.—Framework for engineering creep-fatigue life prediction modeling of MMC's.

law relations to document the required cyclic flow behavior (Halford et al., 1991a,b).

8.3.1 Failure Behavior Equations for Matrix Material

8.3.1.1 Macrocrack initiation.—Once the flow and failure characteristics of the matrix material have been established, the total, mechanical strainrange-versus-fatigue-life equation can be written for any arbitrary isothermal creep-fatigue cycle. Herein, the macrocrack initiation life is equal to the fatigue life defined for coupon-sized axial specimens.

Figure 8.3 graphically displays the total, mechanical strainrange-versus-fatigue-life relation for matrix material based on the TS–SRP representation. Step-by-step procedures for calibrating the constants in the TS–SRP model are given by Saltsman and Halford (1988a). The resultant creep-fatigue prediction equations are for the matrix material and are applicable for the specifically stated loading conditions (i.e., the isothermal temperature and strain-versus-time history). Should a significantly different set of loading conditions be imposed, new sets of equation constants can be readily calculated from the already established flow and failure characteristics.

The life prediction equation shown at this stage represents conditions involving no fibers, no geometric discontinuities (i.e., no stress concentrations), zero mean stress, a uniaxial stress-strain state, and continuously repeated loadings of constant total strainrange, frequency, temperature, etc.
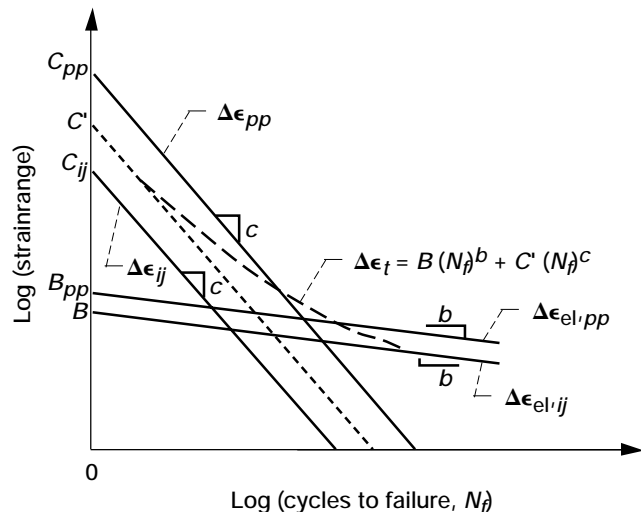
Figure 8.3.—Creep-fatigue life equations and strain-life curves for matrix material, where $ij = pp, pc, cp, cc$. Condensed from Saltsman and Halford (1988a).

Modifications of the equation to deal with specific influencing factors associated with a composite are discussed in section 8.3.2. Some influences can be described analytically, and quantitative computations of the expected effect on thermo-mechanical fatigue life are possible. Other influences are not yet at the quantifiable stage and for the meantime will require

empiricism and calibration of computations with experimental creep-fatigue results on the composite material.

Some influencing factors of the fibers will affect microcrack initiation more than microcrack propagation, and vice versa. It is convenient therefore to distinguish analytically these two important components of the total macrocrack initiation life. Approximate equations for the microcrack initiation and propagation portions of the total fatigue life are given here. First, the total strainrange can be decomposed into its elastic and inelastic components:

$$\Delta\varepsilon_t = \Delta\varepsilon_{el} + \Delta\varepsilon_{in} \tag{8.1}$$

Second, power-law relations between strainrange components and fatigue life (zero mean stress conditions) are commonly observed; that is,

$$\Delta\varepsilon_{el} = B(N_f)^b \tag{8.2}$$

and

$$\Delta\varepsilon_{in} = C(N_f)^c \tag{8.3}$$

Thus, for macrocrack initiation

$$\Delta\varepsilon_t = B(N_f)^b + C(N_f)^c \tag{8.4}$$

8.3.1.2 Microcrack initiation and propagation.— Macrocrack initiation fatigue life can be decomposed into its microcrack initiation and microcrack propagation phases:

$$N_f = N_i + N_p \tag{8.5}$$

There is widespread acceptance of the notion that microcracks begin very early in low-cycle fatigue, leaving the vast majority of life to be spent in microcrack propagation, and that microcracks begin late in high-cycle fatigue, making the microcrack propagation phase a small fraction of the total life. Although somewhat arbitrary, it is not unreasonable to assume that at the very low life of $N_f = 10$

$$N_i \approx 0.1 N_f \tag{8.6a}$$

and

$$N_p \approx 0.9 N_f \tag{8.6b}$$

and that at the arbitrarily high cyclic life of $N_f = 10^7$

$$N_i \approx 0.9 N_f \tag{8.6c}$$

and

$$N_p \approx 0.1 N_f \tag{8.6d}$$

Power-law relations between N_f and N_i and between N_f and N_p can be written by using the sets of coordinates of equations (8.6a) and (8.6c) and equations (8.6b) and (8.6d), respectively. That is, $N_f = 10(N_i)^{0.863}$ and $N_f = 0.733(N_p)^{1.19}$. When written in this simple form the sum of the microcrack initiation and propagation lives falls short of the total macrocrack initiation life N_f by about 40 percent at $N_f = 10^4$ cycles. At either higher or lower lives (10 and 10^7 cycles to failure), this error diminishes to zero. Substituting these relations into equation (8.4), with $b = -0.12$ and $c = -0.60$ (Manson, 1965), yields the following approximate relations: for microcrack initiation

$$\Delta\varepsilon_t \approx 0.76B(N_i)^{-0.1} + 0.25C(N_i)^{-0.5} \tag{8.7}$$

and for microcrack propagation

$$\Delta\varepsilon_t \approx 1.04B(N_p)^{-0.14} + 1.20C(N_p)^{-0.7} \tag{8.8}$$

8.3.2 Influences of Fibers and Interfaces on Matrix Flow and Failure Behavior

The fact that fibers are present in a composite imparts changes in both the flow and failure response of the matrix. The most significant mechanical influences on the surrounding matrix are listed in table 8.1. Each factor is identified as to whether it influences the microcrack initiation phase or microcrack propagation phase of the macrocrack initiation life. A few of the influences can now be handled analytically; others require development. Those influences that have been identified are discussed below. Several of these influences are initiated during the fabrication cycle of heating, consolidation, and cooling to ambient conditions. Because of the number of influencing factors and their known variabilities, the model should eventually be addressed in terms of probabilistics.

8.3.2.1 Coefficient-of-thermal-expansion mismatch strains.—The coefficient-of-thermal-expansion (CTE) mismatch between matrix and fiber causes postfabrication residual stresses in the MMC. Typically, the matrix residual stress is tensile, and the fiber is in compression. For isothermal fatigue at room temperature the CTE mismatch strain caused by cooling from a fabrication or heat treatment temperature usually produces a detrimental tensile residual stress in the matrix. This stress will act as a mean stress in subsequent fatigue loading if the residual stress does not relax cyclically

TABLE 8.1.—FACTORS ASSOCIATED
WITH FIBERS MECHANICALLY
INFLUENCING MATRIX
FATIGUE RESPONSE

Factor	N_i	N_p
CTE mismatch strains	Yes	Yes
Residual (mean) stresses	Yes	Yes
Multiaxial stress state	Yes	Yes
Off-axis fibers	Yes	Yes
Internal stress concentrations	Yes	No
Multiple initiation sites	Yes	Yes
Nonuniform spacing	Yes	Yes
Interfacial layers	Yes	No
Fractured fibers	Yes	No
Fiber debonding	No	Yes
Fiber crack retardation	No	Yes
Fiber bridging	No	Yes

because of inelasticity in the matrix (or relax because of creep at elevated temperatures).

8.3.2.2. Mean stresses.—Procedures for dealing with mean stresses in strain-based fatigue life models are given by Saltsman and Halford (1988b):

$$\left(N_{fm}\right)^{-b} = \left(N_f\right)^{-b} - V_\sigma \qquad (8.9)$$

where V_σ is the ratio of mean to alternating stress and is equal to the inverse of the classical fatigue ratio A. The procedures use the modifications made by Halford and Nachtigal (1980) to the Morrow (1968) mean stress approach. For strain-controlled cycles involving detectable amounts of inelasticity, any initially present mean stresses will tend to cyclically relax, thus numerically reducing the value of V_σ. During creep-fatigue loading the numerical value of V_σ may be nonzero but is ineffective in altering fatigue in accordance with a transition equation given and discussed by Halford and Nachtigall (1980).

8.3.2.3 Multiaxial stress state.—Fibers cause multiaxial stress-strain states within the matrix (even though the loading on the unidirectional MMC is uniaxial) as a result of their differing elastic and plastic stress-strain properties and their differing thermal conductivities and expansion coefficients. Effects on cyclic life due to deviations from uniaxial stress-strain states can be handled by a relatively simple procedure given by Manson and Halford (1976, 1977).

The multiaxiality factor MF is a measure of the degree of hydrostatic stress normalized by the corresponding von Mises effective stress. The MF is used in assessing fatigue life just as a stress concentration factor would be used (i.e., the nominal effective strainrange is multiplied by the MF to obtain the local effective strainrange, which in turn affects the local microcrack initiation life). The equations for the multiaxiality factor are

$$MF = TF \qquad TF \geq 1 \qquad (8.10a)$$

$$MF = \frac{1}{2 - TF} \qquad TF \leq 1 \qquad (8.10b)$$

where

$$TF = \frac{\sigma_1 + \sigma_2 + \sigma_3}{\frac{1}{\sqrt{2}}\left[\left(\sigma_1 - \sigma_2\right)^2 + \left(\sigma_1 - \sigma_3\right)^2 + \left(\sigma_2 - \sigma_3\right)^2\right]^{1/2}} \qquad (8.10c)$$

and σ_i denotes the principal stresses ($i = 1,2,3$)

The multiaxiality factor within the matrix material at the location shown in figure 8.1 for unidirectional loading of a unidirectional fiber layup for the SCS–6/Ti-15-3 MMC system was determined to be only 1.04 (Halford et al., 1989). Multiplying 1.04 times the computed effective strainrange yields the strainrange for entering the equation for matrix total strainrange versus macrocrack initiation life. This factor would give rise to a calculated decrease in fatigue life of only about 10 percent provided that all other influencing factors are constant. Higher multiaxiality factors would result in lower predicted fatigue lives.

8.3.2.4 Off-axis fibers.—Relatively small deviations of fiber orientation from [0°] can cause large losses in fatigue resistance. Hashin and Rotem (1973) have shown that a shift from 5° to 10° off-axis loading decreases isothermal fatigue strength by approximately a factor of 2. The corresponding loss in cyclic life was measurable in terms of multiple factors of 10. A 60° off-axis loading resulted in a loss of nearly a factor of 10 in fatigue strength.

8.3.2.5 Internal stress concentrations and multiple initiation sites.—An internal microstress concentration factor produces higher local internal stresses and strains and promotes earlier microcrack initiation. Once the microcrack grows away from the local concentration, however, the concentration effect diminishes and the microcrack propagation portion of life is relatively unaffected.

Internal crack initiation at local stress-strain concentrations can occur in MMC's at multiple initiation sites, thus leading to shorter paths for cracks to follow before linking together and hastening the macrofracture of the composite. If the number of microcrack growth paths is decreased by an average of a factor of 2, the micropropagation phase of life should also decrease by a factor of 2.

8.3.2.6 Nonuniform fiber spacing.—Structural analysis can be used to determine the influence of nonuniform fiber spacing on the stress-strain response behavior of the in situ matrix. The alteration of the local stresses and strains will cause corresponding changes in the calculated microcrack initiation life. However, little effect on the microcrack propagation life would be expected for this influencing factor.

8.3.2.7 Interfacial layers.—Additional examples of using structural analyses to ascertain effects of fibers and interfaces on matrix stress-strain response are found in Jansson and Leckie (1990) and Arnold et al. (1990), who assessed the influence of compliant interfacial layers between fibers and matrix. An obvious influence of the rather weak bonding between fibers and matrix (resulting from the low strength of the interfacial layer in the SCS–6/Ti-15-3 system) is to decrease the ability of the fibers to "bridge" crack faces (i.e., to hold the faces closer together once a crack has formed). The net result is a decreased resistance to crack propagation and a lowered apparent fracture toughness.

8.3.2.8 Additional influencing factors associated with cracks or debonding.—Further analytic development of the proposed framework will be required to quantitatively model the effect on microcrack propagation life of some influencing factors not yet discussed. Of particular interest are those factors directly associated with microcracks within an MMC (i.e., fractured fibers and fiber debonding (the concepts proposed by Chen and Young (1991), among others, offer a promising approach), fiber crack retardation, and fiber bridging (see applicable work of Ghosn et al., 1991)). The more highly localized the stress and strain are, the less likely it is that they will significantly influence microcrack propagation.

8.3.2.9 Metallurgical interactions.—The presence of distributed nonmetallic fibers can influence the metallurgical state of the matrix material. Heat treating the matrix in the presence of fibers can result in a somewhat different microstructure, yield strength, ultimate tensile strength, ductility, and hardness than those obtained by heat treating the unreinforced matrix metal (Lerch et al., 1990). This influence will compound the problem of isolating the true cyclic flow and failure behavior of the in situ matrix material.

Another crucial factor is the potential for increased internal oxidation of the MMC made possible by the interfacial layers acting as diffusional pipelines within the interior of the MMC. Internal oxidation will dramatically reduce an MMC's resistance to high-temperature fatigue resistance by promoting early microcrack initiation and faster microcrack propagation.

8.4 Influences of Matrix on Fibers and Interfaces

It is also necessary to examine the mechanical influence of the matrix on the response characteristics of the reinforcing fibers. Fibers of primary concern (e.g., SCS–6) are elastic and brittle. They fail progressively throughout the fatigue life of the MMC because tensile stresses are continually shed from the matrix material as it cyclically deforms. Cyclic relaxation of mean (residual) stresses and matrix strain hardening or softening results in various behavior scenarios depending on the combination of operative conditions. Various possibilities are discussed in section 8.5.

8.5 Implications of Modeling Framework to MMC Coupon Tests

Some isothermal fatigue coupon results for the SCS–6/Ti-15-3 MMC system were generated during the NASA/Pratt & Whitney cooperative ring effort. These results have been examined in light of the above points of view and have been extended to predicting the radial burst strength and the isothermal low-cycle fatigue life of cyclically loaded rings.

These coupon results (fig. 8.4) are for 427 °C (800 °F) with the load ratio $R_L \approx 0$ and cyclic frequencies between about 0.03 and 0.3 Hz, depending on the strainrange and the testing laboratory. Fiber content ranged from 34 to 38 vol %. The MMC results were compared with isothermal, strain-controlled ($R_\varepsilon = -1$) data reported by Gayda et al. (1990) for matrix material processed in the same fashion as the composite. Frequencies ranged from 0.03 to 1.0 Hz and were highest at the lowest strainranges. The MMC exhibited substantially lower strain fatigue resistance than the unreinforced matrix. The reduction is a factor of approximately 2 in strainrange for a fixed life or a factor of about 40 in life for a given strainrange. Among the dozen influential factors previously discussed, few could be responsible for the significantly large loss in fatigue resistance caused by the presence of fibers in the Ti-15-3 matrix. The most pertinent influences are discussed in the following paragraphs.

Any mean stresses in the matrix owing either to the nature of loading or to residual fabrication stresses are expected to cyclically relax to zero for Ti-15-3 at 427 °C (800 °F). Gayda et al. (1990) have reported experimental results supporting this argument for axially loaded specimens of a 33-vol %, $[0°]_4$ SCS–6/Ti-15-3 MMC. They have also generated cyclic strain-controlled data for unreinforced specimens of the matrix material and showed that for $R_\varepsilon = 0$ tests the initially large tensile mean stress quickly relaxed to zero (i.e., $V_\sigma \to 0$),
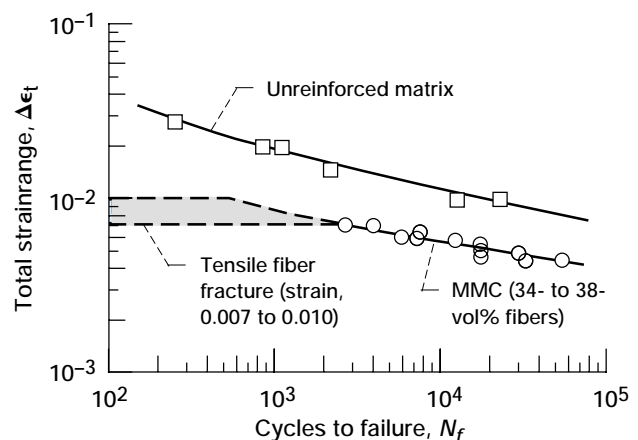

Figure 8.4.—Comparison of isothermal fatigue resistance of SCS–6/Ti-15-3 MMC (previously unpublished NASA and Pratt & Whitney data) with that of Ti-15-3 unreinforced matrix material from Gayda et al. (1990).

resulting in hysteresis loops identical to those for $R_\varepsilon = -1$ tests. Thus, from the standpoint of the effect of mean stresses in the matrix, it is not expected that the matrix material would initiate and propagate microcracks earlier in the MMC than if it were fatigued alone.

However, a larger peak tensile stress is experienced by the fibers because they carry a greater portion of the tensile load after the matrix tensile mean stresses have relaxed. Hence, the fibers are forced to operate closer to their peak tensile strain capacity (0.007 to 0.010), and the MMC becomes less tolerant of subsequent matrix cracking that will further erode load-bearing area and transfer more and more tensile stress (and hence, strain) to the fibers. The cyclic durability resistance of the MMC thus would be compromised—not by fatigue cracking per se but by the cyclic flow response characteristics of the matrix and the limited strain capacity of the brittle fibers.

An additional portion of the discrepancy can be explained by examining differences in control modes used in the two test series. The MMC fatigue tests used load control and only tensile loads were imposed ($R_L = 0$), whereas the matrix fatigue tests were conducted under completely reversed strain control ($R_\varepsilon = -1$). Had the MMC fatigue tests been conducted with the same range of load and hence the same range of strain with $R_L = -1$ (to keep the results of fig. 8.4 more comparable), the peak tensile stress (or strain) experienced by the fibers would have been 50 percent lower. Consequently, much more extensive matrix fatigue cracks and considerable fiber cracking would have had to occur before the remaining load-carrying fibers were pushed to their peak tensile strain limit. Using this line of reasoning, the MMC specimens could have endured more loading cycles, thus resulting in lives closer to those exhibited by the unreinforced matrix material.

Additional qualitative explanation for the discrepancy is found in the microcrack propagation phase of cyclic life, which can be shortened in the MMC as a result of two important factors. First, cracks can begin in the MMC internally and later link, thus decreasing cyclic life. Second, internal oxidation at 427 °C (800 °F) can occur along the interfaces and any interior cracks. A loss of a factor of 4 in microcrack propagation life by these means is certainly within the realm of possibility. Furthermore, Gayda et al. (1990) have observed by fractography that the microcrack initiation phase of specimen fatigue life is essentially bypassed in this MMC system, likely owing to the nature of the interfacial material and its relatively poor bonding to either fiber or matrix. At a cyclic strainrange giving a life of 10^7 cycles to failure for the unreinforced matrix material, the microcrack initiation phase is expected to be 90 percent of the total macrocrack initiation life in accordance with equation (8.6c). Thus, an additional factor-of-10 loss in life can be attributed to the loss of microcrack initiation life. The two life losses are multiplicative (i.e., $4 \times 10 = 40$, which is in general agreement with the losses observed in fig. 8.4). It is not now possible to quantify the degree of loss with any confidence in accuracy. A series of strain-controlled

($R_\varepsilon = -1$), low-cycle fatigue tests of MMC coupons is planned. The results are expected to provide a better understanding of the causes of the large life losses observed in this MMC material for $R_L = 0$.

8.6 Application of Model Framework

8.6.1 Static Ring Burst Tests

The dimensions of the three rectangular-cross-section rings varied somewhat owing to the manufacturing process. Dimensions of a radial cross section of ring 1 are shown in figure 1.11 (chapter 1). Only the core of the ring was fiber reinforced. Fibers were circumferentially oriented by using a nominal fiber content of 33 vol %. The corresponding core was 1.37 cm (0.54 in.) wide, 16.3 cm (6.42 in.) in outside diameter, and 14.15 cm (5.57 in.) in inside diameter, resulting in a radial thickness of about 1.11 cm (0.437 in.). Because of the rather substantial monolithic titanium cladding surrounding the core, the overall fiber content of a cross section varied from about 14.4 vol % for ring 1 to 17.5 vol % for ring 2. Rings 2 and 3 had similar-appearing cross sections.

Radial mechanical loading was applied to each ring through 12 equally spaced and independently loaded shoes. The radial-segmented shoes imparted a "pressure" loading to the ring's inner-diameter (ID) surface (fig. 7.4, chapter 7). Each shoe was connected to a pinned clevis that was attached, in turn, to a hydraulic cylinder located well beyond the ring's outside-diameter (OD) surface. The hydraulic cylinders were manifolded to a common hydraulic supply. The net result of this manner of loading was to place the ring in nominally circumferential tension. However, the radial thickness was sufficient to produce a substantial radial gradient of applied strain, with the ID surface experiencing a strain about 20 percent greater than the average circumferential strain along the radial thickness. This gradient will cause the material near the ID surface to initiate failure. Because the material at the ID surface is ductile Ti-15-3, failure will not occur there but more likely will begin in the brittle SCS–6 fibers contained in the core, which is located about 0.272 cm (0.107 in.) radially beyond the ring's ID surface. At the location of the first rows of fibers the circumferential strain for ring 1 will be only about 13.5 percent higher than the average. Ring 1 was statically burst tested at 427 °C (800 °F).

It is assumed that burst under static radial loading will begin when the local stress reaches the ultimate tensile strength of the core composite material. The failure initiation location will be at the core ID, where the local strain (and hence, stress for a nominally elastic, brittle-fiber MMC) is 13.5 percent higher than the calculated average circumferential ring stress. When the core material is at an average stress of 13.5 percent less than its ultimate tensile strength, the Ti-15-3 cladding material will, on average over its cross-sectional area, be very near its yield strength (higher at the ID, lower at the OD).

Equating the internal forces (average circumferential stresses σ_{core} and σ_{clad} times their respective areas A_{core} and A_{clad}) to the externally applied loads (expressed as a function of the radial load applied per shoe) gives for ring 1

$$3.8625\, L = 2\left(\sigma_{\text{core}} \times A_{\text{core}} + \sigma_{\text{clad}} \times A_{\text{clad}}\right) \qquad (8.11\text{a})$$

$$3.8625\, L = 0.4716\, \sigma_{\text{core}} + 0.6098\, \sigma_{\text{clad}} \qquad (8.11\text{b})$$

At commencement of burst $\sigma_{\text{core}} = \sigma_{u,\text{MMC}}/1.135 = 27.1$ MPa (185.5 ksi) at 427 °C (800 °F) and $\sigma_{\text{clad}} = \sigma_{y,\text{Ti-15-3}} = 17.9$ MPa (122 ksi). Thus, burst is calculated to occur at a load per shoe L of 186 kN (41.9 kips), corresponding to an average pressure applied to the ring ID surface 5.34 MPa (36.5 ksi).

Experimentally, ring 1 burst at an ID surface pressure of 4.02 MPa (27.46 ksi), considerably below the calculated burst pressure of 5.34 MPa (36.5 ksi). Ring 2 had slightly different dimensions than ring 1 and failed at an ID surface pressure of 3.29 MPa (22.5 ksi), also considerably below its calculated burst pressure. Calculations of burst pressures did not account for the details of the degrading defects found by post-test destructive evaluation. Rings 1 and 2 had irregular fiber spacing, touching fibers, and numerous matrix cracks between fibers that could have contributed to more severe local stress-strain conditions and hence lower-than-expected static strength. In addition, ring 2 had small regions of highly misoriented fibers (up to 30° off-axis) that appeared to be failure initiation sites and may have caused its relatively low burst strength. This unusual defect was traceable to the specific manufacturing techniques, which were not communicated to participants in the cooperative program. These strength-limiting defects, although having shown up as indications of irregularity during nondestructive evaluation, were not judged (prior to testing) as being as serious as was later determined. Ring 3 was suspected of having been compromised by similar manufacturing defects, and we decided not to perform the originally planned cyclic loading tests.

8.6.2 Ring Fatigue Life Prediction

Although ring fatigue tests have yet to be conducted, an example fatigue life can be predicted for postulated loading conditions by using the model framework presented herein. For this purpose the dimensions and details of all three rings were used, resulting in the following relation between the radial load per shoe L and the average circumferential strain ε. Thus,

Ring 1	$\varepsilon = 0.000192\, L$
Ring 2	$\varepsilon = 0.000190\, L$ (8.12)
Ring 3	$\varepsilon = 0.000183\, L$

For a cyclic loading test wherein L fluctuates between zero and a prescribed maximum value, L becomes ΔL and ε becomes $\Delta\varepsilon$, the total strainrange. Thus, a link is established between the applied loading variable and the primary parameter, $\Delta\varepsilon$, for calculating MMC fatigue life (fig. 8.4).

Owing to the simple ring geometry, the circumferential orientation of the fibers, and the zero-to-maximum-load-controlled loading, the MMC coupon specimens and the MMC material contained in the ring experienced essentially identical operating conditions. This simple fact means that the many influencing factors discussed in section 8.3 will affect the ring just as they would affect an MMC coupon in a laboratory test. Consequently, the laboratory-generated fatigue data can be applied directly to predicting ring fatigue life. The problem becomes trivial under these unique circumstances, and there is very little that is unique to the life prediction calculations for an MMC ring in contrast to a monolithic ring. The primary difference has to do only with the location at which failure is expected to originate.

Fatigue failure of a cyclically loaded, MMC-cored ring is expected to originate at the same location that initiated static burst failure (i.e., at the ID of the MMC core, where the strainrange is 13.5 percent greater than the average circumferential strainrange). Thus, the strain in equation (8.12) must be increased by this percentage:

Ring 1	$\Delta\varepsilon = 0.000218\, \Delta L$
Ring 2	$\Delta\varepsilon = 0.000216\, \Delta L$ (8.13)
Ring 3	$\Delta\varepsilon = 0.000208\, \Delta L$

A cyclic load ΔL of 139 kN (31.3 kips) per shoe (average pressure of 3.28 MPa (22.4 ksi) applied to the ID surfaces of the rings) gives rise to total strainranges of 0.00683, 0.00676, and 0.00650, respectively, for rings 1 to 3. Corresponding cyclic fatigue lives, determined directly from figure 8.4, are 2935, 3130, and 4000.

In calculating the fatigue life no consideration has been given to potentially important factors, such as statistical distribution of fatigue lives and size effects. The volume of

composite material is nearly 600 times greater in a ring than in a single fatigue test coupon. The greater volume of the rings and the greater complexity of their manufacture would certainly invite a higher probability of life-degrading defects. Calibrated statistical and probabilistic models to cover these factors are currently lacking.

8.7 Summary of Results

A framework of a deterministic engineering model has been proposed for a life prediction system applicable to isothermal creep-fatigue loading of unidirectional, continuous-fiber-reinforced, metal-matrix composites (MMC's). A local micromechanics stress-strain approach was adopted to impart the maximum degree of generality. The classically fatigue-prone metal matrix was selected as the vehicle for tracking the cycle-dependent changes (mean stress relaxation, hardening, softening, microcrack initiation, and microcrack propagation). The presence of fibers and interfacial layers was taken into account by the influence they exert on the stress-strain and failure response behavior of the matrix material. Similarly, the influence on the fiber of the interfacial and matrix materials was considered. Considerably more analytical and experimental research is needed to expand on the framework and bring the approach to its full potential. Examples of isothermal fatigue data for SCS–6/Ti-15-3 illustrated important aspects of the modeling framework. The approach was projected to the calculating radial burst strength and anticipated fatigue strength of cyclically loaded MMC rings.

References

Arnold, S. M., Arya, V.K., and Melis, M.E., 1990, "Elastic/Plastic Analyses of Advanced Composites Investigating the Use of the Compliant Layer Concept in Reducing Residual Stress Resulting From Processing," NASA TM–103204.

Bodner, S.R., and Partom, Y., 1975, "Constitutive Equations for Elastic-Viscoplastic Strain-Hardening Materials," *Journal of Applied Mechanics*, Vol. 42, No. 2, pp. 385–389.

Chen, E.J.H., and Young, J.C., 1991, "The Microdebonding Testing System—A Method of Quantifying Adhesion in Real Composites," *Composites Science and Technology*, Vol. 42, No. 1–3, pp. 189–206.

Freed, A., 1988, "Thermoviscoplastic Model With Application to Copper," NASA TP–2845.

Gayda, J., Gabb, T.P., and Freed, A.D., 1990, "The Isothermal Fatigue Behavior of a Unidirectional SiC/Ti Composite and the Ti Alloy Matrix," *Fundamental Relationships Between Microstructure & Mechanical Properties of Metal-Matrix Composites*, P.K. Liaw and M.N. Gungor, eds., The Minerals, Metals & Materials Society, pp. 497–514.

Ghosn, L.J., Kantzos, P., and Telesman, J., 1991, "Modeling of Crack Bridging in a Unidirectional Metal Matrix Composite," NASA TM–104355.

Halford, G.R., and Nachtigall, A.J., 1980, "The Strainrange Partitioning Behavior of an Advanced Gas Turbine Disk Alloy, AF2–1DA," *Journal of Aircraft*, Vol. 17, No. 8, pp. 598–604.

Halford, G.R., Lerch, B.A., Saltsman, J.F., Arya, V., and Caruso, J.J., 1989, "LCF Life Prediction for MMCs," *HITEMP Review 1989: Advanced High-Temperature Engine Materials Technology Program*, NASA CP–10039, pp. 64–1 to 64–9.

Halford, G.R., Verrilli, M.J., Kalluri, S., Ritzert, F.J., Duckert, R.E., and Holland, F., 1991a, "Thermomechanical and Bithermal Fatigue Behavior of Cast B1900 + Hf and Wrought Haynes 188," *Advances in Fatigue Lifetime Predictive Techniques,* ASTM STP 1122, M.R. Mitchell and R.W. Landgraf, eds., American Society for Testing and Materials, Philadelphia, PA, pp. 120–142.

Halford, G.R., Saltsman, J.F., Verrilli, M.J., and Arya, V., 1991b, "Application of a New Thermal Fatigue Life Prediction Model to Two High-Temperature Aerospace Alloys," *Advances in Fatigue Lifetime Predictive Techniques,* ASTM STP 1122, M.R. Mitchell and R.W. Landgraf, eds., American Society for Testing and Materials, Philadelphia, PA, pp. 107–119.

Halford, G.R., Lerch, B.A., Saltsman, J.F., 1993, "Proposed Framework for Thermomechanical Life Modeling of Metal Matrix Composites," NASA TP–3320.

Hashin, Z., and Rotem, A., 1973, "A Fatigue Failure Criterion for Fiber Reinforced Materials," *Journal of Composite Materials*, Vol. 7, pp. 448–464.

Jansson, S., and Leckie, F.A., 1990, "Reduction of Thermal Stresses in Continuous Fiber Reinforced Metal Matrix Composites With Interface Layers," NASA CR–185302.

Lerch, B.A., Gabb, T.P., and MacKay, R.A., 1990, "Heat Treatment Study of the SiC/Ti-15-3 Composite System," NASA TP–2970.

Manson, S.S., 1965, "Fatigue: A Complex Subject—Some Simple Approximations," *Experimental Mechanics*, Vol. 5, No. 7, pp. 193–226.

Manson, S.S., and Halford, G.R., 1976, "Treatment of Multiaxial Creep-Fatigue by Strainrange Partitioning," *Symposium on Creep-Fatigue Interaction,* MPC–3, R.M. Curran, ed., American Society of Mechanical Engineers and the Metals Properties Council, New York, pp. 299–322.

Manson, S.S., and Halford, G.R., 1977, "Discussion of paper by J. J. Blass and S.Y. Zamrik in Symposium on Creep-Fatigue Interaction, ASME, 1976, pp. 129–159," *Journal of Engineering Materials and Technology*, Vol. 99, pp. 283–286.

Morrow, J., 1968, "Fatigue Properties in Metals," *Fatigue Design Handbook*, Section 3.2, J.A. Graham, ed., Society of Automotive Engineers, Inc., Warrendale, PA, pp. 21–29.

Robinson, D.A., and Swindeman, R.W., 1982, "Unified Creep-Plasticity Constitutive Equations for 21/4Cr–1Mo Steel at Elevated Temperature," ORNL Report TM–8444, Oak Ridge National Laboratories, Oak Ridge, TN.

Saltsman, J.F., and Halford, G.R., 1988a, "An Update on the Total Strain Version of SRP," *Low Cycle Fatigue,* ASTM STP 942, H. D. Solomon, G.R. Halford, L.R. Kaisand, and B.N. Leis, eds., American Society for Testing and Materials, Philadelphia, PA, pp. 329–341.

Saltsman, J.F., and Halford, G.R., 1988b, "Life Prediction of Thermomechanical Fatigue Using the Total Strain Version of Strainrange Partitioning (SRP)—A Proposal," NASA TP–2779.

Walker, K.P., 1981, "Research and Development Program for Nonlinear Structural Modeling With Advanced Time-Temperature Dependent Constitutive Relations," NASA CR–165533.

Chapter 9
Computational Simulation of Hot Composite Structures

Christos C. Chamis,[*] Pappu L.N. Murthy,[*] and Surendra N. Singhal[†]

9.1 Introduction

Composite structural behavior is generally complex because of the multiple inherent scales and the behavior coupling within and between scales. Coupling for high-temperature, metal-matrix-composite (HT–MMC) structures is compounded because of the presence of nonlinear dependencies, such as those on temperature, stress, and time. Predicting HT–MMC behavior requires analyses at multiple inherent composite material/structures scales. These analyses must be integrated progressively from the constituent scale (fiber, matrix, and interphase to the global structural component. The various scales involve micromechanics (intraply), macromechanics (interply), laminate (multiple plies), local region (plate type of finite element), and structural component (assemblage of many finite elements), obviously complicating the task. One approach is to solve the fundamental governing field equations for all the participating variables by employing a computer as an integral part of the solution. Because this approach can be used to simulate the behavior or process as well as a specific event, it is called computational simulation.

Recent research at NASA Lewis is directed toward the development of computational methodologies and corresponding stand-alone computer codes for predicting the nonlinear behavior of HT–MMC's at all the inherent scales. The simulation starts with constituents and the fabrication process and progresses to determine the effects induced by the severe service loading environments. By using the fundamental physics of how the material and structure behaves, three computational simulation procedures (codes) have been developed: (1) Metal-Matrix Composite Analyzer (METCAN) for predicting the behavior of HT–MMC's from micromechanics scale to laminate scale, (2) Metal-Matrix Laminate Tailoring (MMLT) for tailoring HT–MMC behavior for optimum specific performance, and (3) High-Temperature Composite Analyzer (HITCAN) for predicting HT–MMC structural response for hot structural components.

This chapter briefly describes these three computational codes and presents illustrative results from their applications to simulate specific HT–MMC behavior. Select references are cited where these codes are described in detail with validation and verification results for that purpose. The chapter also demonstrates the effectiveness of this hierarchical computational capability (1) to predict the material behavior of a silicon-carbide-fiber-reinforced, titanium-matrix (SCS–6/Ti) laminate and (2) to tailor the fabrication process for a P100-graphite-fiber-reinforced, copper-matrix laminate for maximum in-service load capacity. These two demonstrations are included as background to establish the credibility of the hierarchical approach for predicting static and fatigue life of an SCS–6/Ti composite ring.

9.2 Behavior of HT–MMC From Micro-mechanics Scale to Laminate Scale

The behavior of HT–MMC's from micromechanics scale to laminate scale is computationally simulated by using the procedure embedded in the in-house computer code METCAN. The structures of METCAN, its simulation capabilities, and typical results to illustrate the applications of these capabilities are summarized here.

---

*NASA Lewis Research Center, Cleveland, Ohio 44135.
†Lewis Research Center Group, Sverdrup Technology, Inc., Brook Park, Ohio 44142.

The structure of METCAN parallels the fabrication process for metal-matrix composites (fig. 9.1). METCAN (fig. 1.6, chapter 1) can predict all aspects of HT–MMC behavior, including the fabrication process, by using mostly room-temperature properties for the fiber and the matrix. The formalism embedded in it, an initial version, and the concepts are demonstrated in Hopkins (1984). The micromechanics to represent the simulation at the constituent materials scale are described in detail in Hopkins and Chamis (1985). Fundamental to the computational simulation in METCAN is the introduction of the multifactor interaction model (MFIM) to represent the various nonlinearities and their mutual interactions in the constituents. The equation form of the MFIM and the reasons for its selection are summarized in figure 1.7. A discussion of its ability to represent constituent material behavior and the subsequent influence of this behavior on the response of structural components made from HT–MMC are discussed in Chamis and Hopkins (1985).

The METCAN computational sequence for the simulation of a typical composite behavior starting from the fabrication process is shown in figure 9.2(a). The sequence consists of (1) cooldown from processing temperature to room temperature, (2) heatup to use temperature from room temperature, and (3) mechanical loading to obtain stress-strain history to fracture. The minimum types of tests for calibrating METCAN for a specific HT–MMC (fig. 9.2(b)) are (1) monotonic longitudinal tensile test, (2) monotonic transverse tensile test, (3) interlaminar shear creep rupture test, (4) thermal cyclic test of crossply laminates, and (5) mechanical cyclic test of crossply laminates. Once METCAN has been calibrated with these
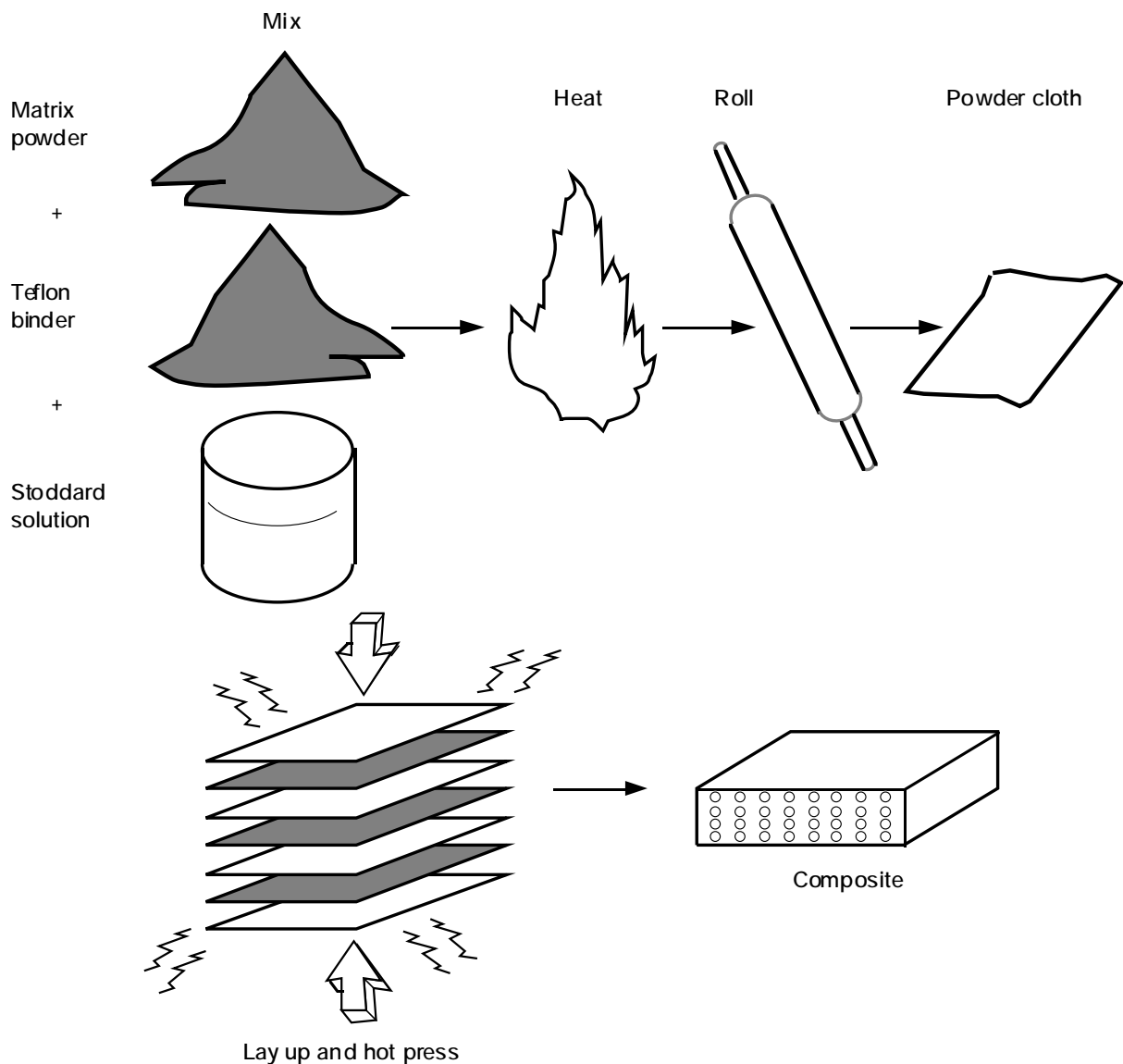
Figure 9.1.—Metal-matrix composite fabrication process.

Step 1 Cool down from processing temperature T_p
to room temperature T_0

Step 2 Heat up to use temperature T_u from room temperature

Step 3 Apply mechanical load to obtain stress-strain data

(a)

(b)
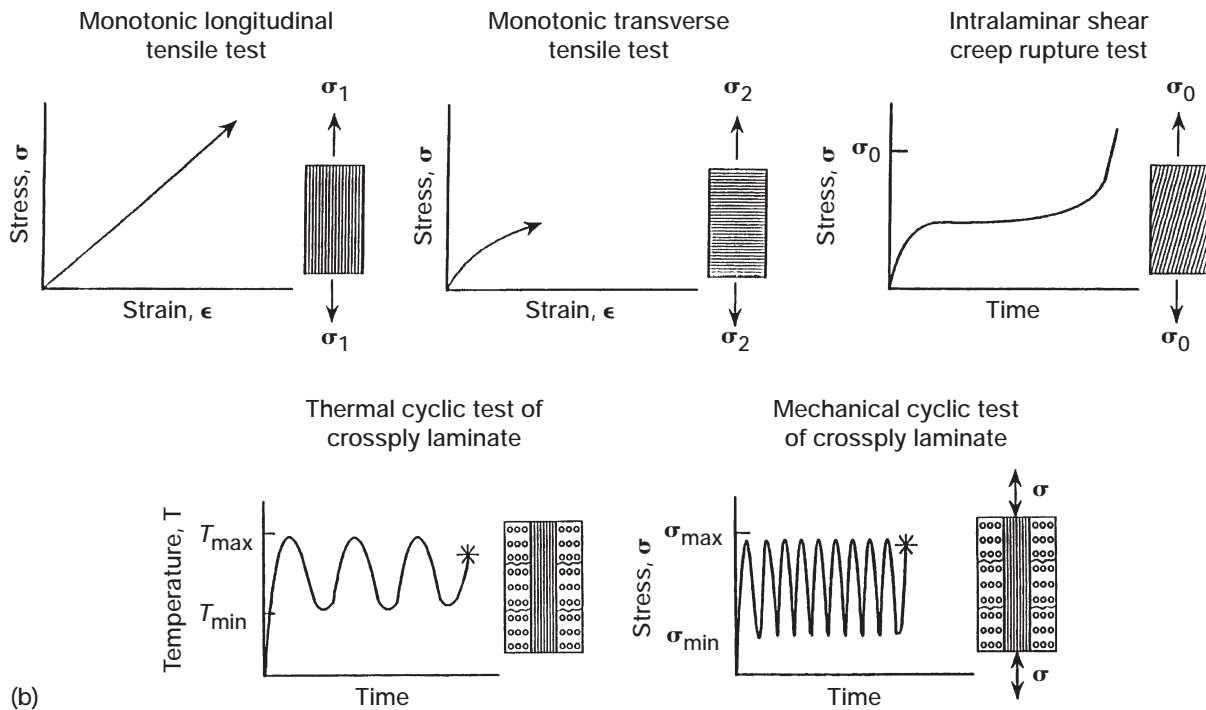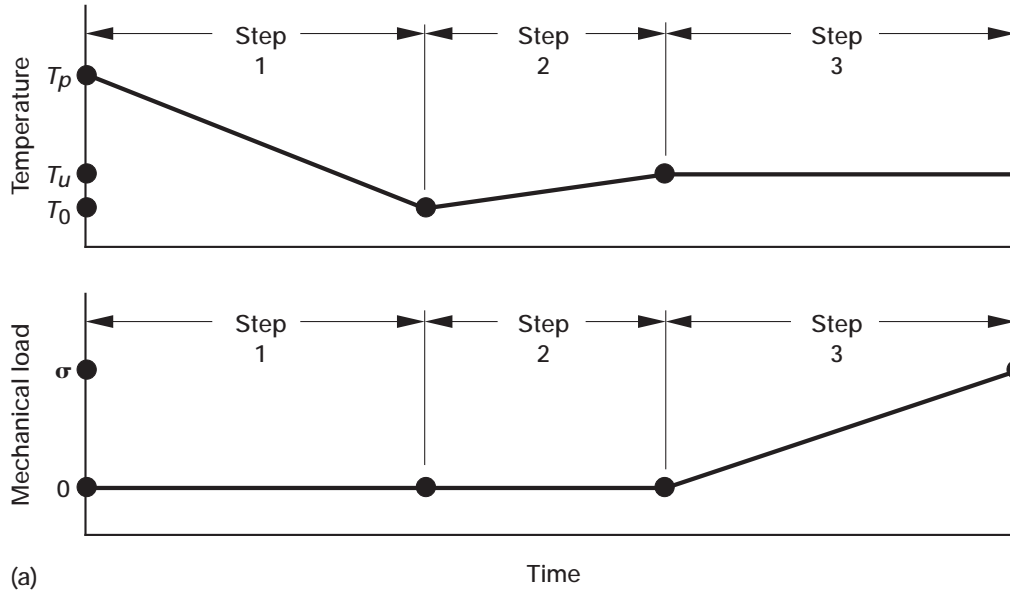
Figure 9.2.—METCAN computational simulation sequence and minimum number of tests. (a) Computational simulation sequence. (b) Minimum number of tests for calibrating METCAN for specific HT–MMC.

(a) Strength, ksi / Strength, MPa vs Temperature, °C (°F): 21 (73), 315 (600), 427 (800)

Legend: Experiment, METCAN

**(b)** Stress, ksi / Stress, MPa vs Strain, percent
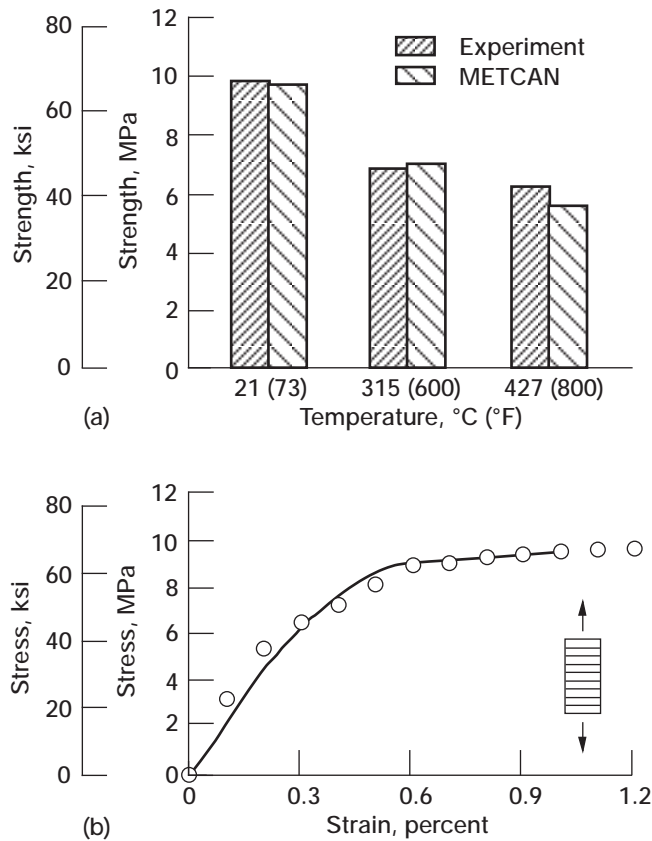
Figure 9.3.—Illustrative results from Chamis et al. (1990). Fiber content, 34 vol%. (a) METCAN accurately simulates transverse strength of SiC/Ti-6-4. (b) METCAN accurately simulates transverse stress-strain curve of SiC/Ti-6-4. Temperature, 21 °C (73 °F).

TABLE 9.1.—CONSTITUENT (FIBER-MATRIX) MATERIAL PROPERTIES USED IN METCAN

Material property	Fiber		Matrix	
	SiC^a	SiC^b	Ti-15-3[a]	Ti-6-4[b]
Density, ρ, kg/m³ (lb/in.³)	3048 (0.110)	2992 (0.108)	4765 (0.172)	4710 (0.170)
Melting temperature, T_m, °C (°F)	2687 (4870)	2482 (4500)	1649 (3000)	1649 (3000)
Elastic modulus in direction 11, E_{11}, GPa (psi)	428 (62×10^6)	414 (60×10^6)	83.0 (12×10^6)	117 (17×10^6)
Elastic modulus in direction 22, E_{22}, GPa (psi)	428 (62×10^6)	414 (60×10^6)	83.0 (12×10^6)	117 (17×10^6)
Shear modulus in direction 12, G_{12}, GPa (psi)	179 (26×10^6)	138 (20×10^6)	36 (5×10^6)	48.3 (7×10^6)
Poisson's ratio in direction 12, ν_{12}	0.19	0.30	0.32	0.30
Coefficient of thermal expansion in direction 11, α_{11}, ppm/deg C (ppm/deg F)	4.86 (2.7)	4.86 (2.7)	8.46 (4.7)	9.36 (5.2)
Coefficient of thermal expansion in direction 22, α_{22}, ppm/deg C (ppm/deg F)	4.86 (2.7)	4.86 (2.7)	8.46 (4.7)	9.36 (5.2)
Strength in direction 11, S_{11}, MPa (ksi)	345 (500)	345 (500)	41.4 (60	51.0 (74)
Strength in direction 22, S_{22}, MPa (ksi)	345 (500)	345 (500)	41.4 (60	51.0 (74)
Strength in direction 12, S_{12}, MPa (ksi)	207 (300)	178 (250)	24.8 (36)	30.4 (44)

[a]Lerch (1995).
[b]Chamis et al. (1990).

tests, the entire spectrum of HT–MMC behavior (under various thermal and mechanical static and time-dependent loads) can be predicted by using METCAN. Obviously, the computational simulation with METCAN minimizes the costly and time-consuming experimental effort that would otherwise be required.

The verification and validation of METCAN's capabilities with both experimental results and three-dimensional, finite-element analysis predictions has been an ongoing in-house activity (Chamis et al., 1988, 1990; Murthy et al., 1989; typical comparisons are shown in fig. 9.3). The constituent material properties of SCS–6/Ti-6-4 (i.e., silicon carbide fiber and titanium matrix) used for these simulations are listed in table 9.1. METCAN predictions for transverse strengths of SCS–6/Ti-6-4 at three temperatures (21, 315, and 427 °C; 73, 600, and 800 °F) for a fiber content of 34 vol% are shown in figure 9.3(a). Differences between METCAN predictions and experimental results are minimal, and the observed experimental degradation in strength with increasing temperature is accurately predicted by METCAN. The room-temperature, stress-strain behavior predicted by METCAN (fig. 9.3(b)) matches almost exactly with experimental data.

METCAN has been verified for applied load behavior and for cyclic load behavior of HT–MMC's (Chamis et al., 1988), where the influence of the interphase and limited comparisons with room-temperature data are also described. METCAN simulation of in situ behavior, how this can be used to interpret composite-measured behavior, and corresponding results for the development of an interphase between fiber and matrix, or weakening of the interfacial bond, are described in Murthy et al. (l989).

9.3 Tailoring of HT–MMC Fabrication Process

A crucial problem limiting the use of many HT–MMC's is the high residual thermal microstresses developed during the fabrication process. These high microstresses are due to the large temperature differential that results from the fabrication and the resulting mismatch between the coefficients of thermal expansion (CTE) of the fiber and the matrix. The presence of residual CTE microstresses typically degrades the mechanical performance of the composite and is primarily responsible for the reported poor thermomechanical fatigue endurance of many HT–MMC's. It is desirable, therefore, to explore possible ways to reduce, or alternatively control, the development of residual microstresses. One possibility is to use a suitable fiber coating as an interphase layer between the fibers and the matrix to reduce the effects of the fiber/matrix CTE mismatch. Also, it is possible to obtain reductions in residual stresses by tailoring the combinations of temperature and consolidation pressure during fabrication (Saravanos et al., 1990).

More recent work along these lines (Morel and Saravanos, 1990) has focused on a systematic development of concurrent tailoring methodology for optimal combination of the interphase layer, its properties, and the fabrication process variables. The computer code MMLT, which includes the above-mentioned methodology, couples METCAN with an optimizer. MMLT simulates the thermomechanical response of the laminate with incremental nonlinear micromechanics, macromechanics, and laminate theories. The structure of MMLT is shown in figure 9.4(a). MMLT can concurrently tailor the constituent materials' characteristics and the fabrication process for an a priori specified HT–MMC behavior, such as minimum residual stresses upon cooldown and maximum fatigue life. MMLT can also quantify the strong coupling, resulting from the residual stresses and the nonlinearity of the composite, between the nonlinear thermomechanical response of MMC's during the fabrication process and the subsequent thermomechanical performance of the MMC in a typical service environment. A typical thermomechanical life cycle of an MMC laminate from fabrication to failure at operational conditions (e.g., in hot engine sections) is shown in figure 9.4(b).

Representative MMLT results are reported herein to show the concept and usefulness of the methodology in achieving higher performance from HT–MMC's. A [0°/90°] P100/copper laminate was used to demonstrate the strong coupling effects. The fabrication process was tailored for three cases (Morel et al., 1992): (1) tensile in-plane load, (2) compressive in-plane load, and (3) bending load, all at a constant elevated temperature. Figure 9.5(a) shows the initial and tailored processes for the three load cases. The fabrication process for tensile in-plane load did not change with tailoring, whereas the fabrication processes for compressive in-plane and bending loads changed significantly upon tailoring: The consolidated pressure increased as the temperature decreased to room conditions, leading to an increase of about 40 percent in the in-service load capacity for compressive in-plane and bending loads (fig. 9.5(b)). For tensile in-plane load the fabrication tailoring did not affect the in-service load capacity because the bulk of the load was carried by the fibers.

9.4 HT–MMC Structural Analysis

HITCAN is a general-purpose computer code for predicting global structural and local stress-strain response of arbitrarily oriented, multilayered, high-temperature, metal-matrix composite structures both at the constituent (fiber, matrix, and interphase) and structure scales. HITCAN combines METCAN with a noncommercial finite-element code, MHOST, and a dedicated mesh generator. The code is stand-alone and streamlined for the thermal and structural analysis of hot metal-matrix composite structures. A schematic of the code
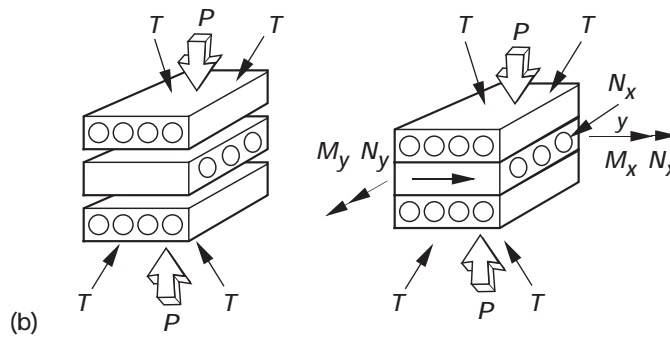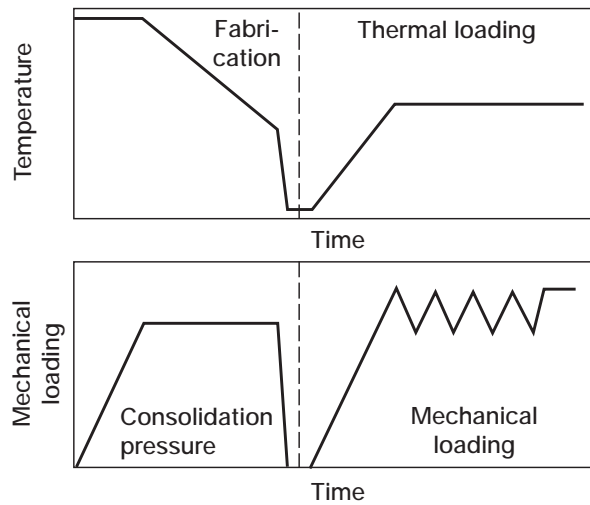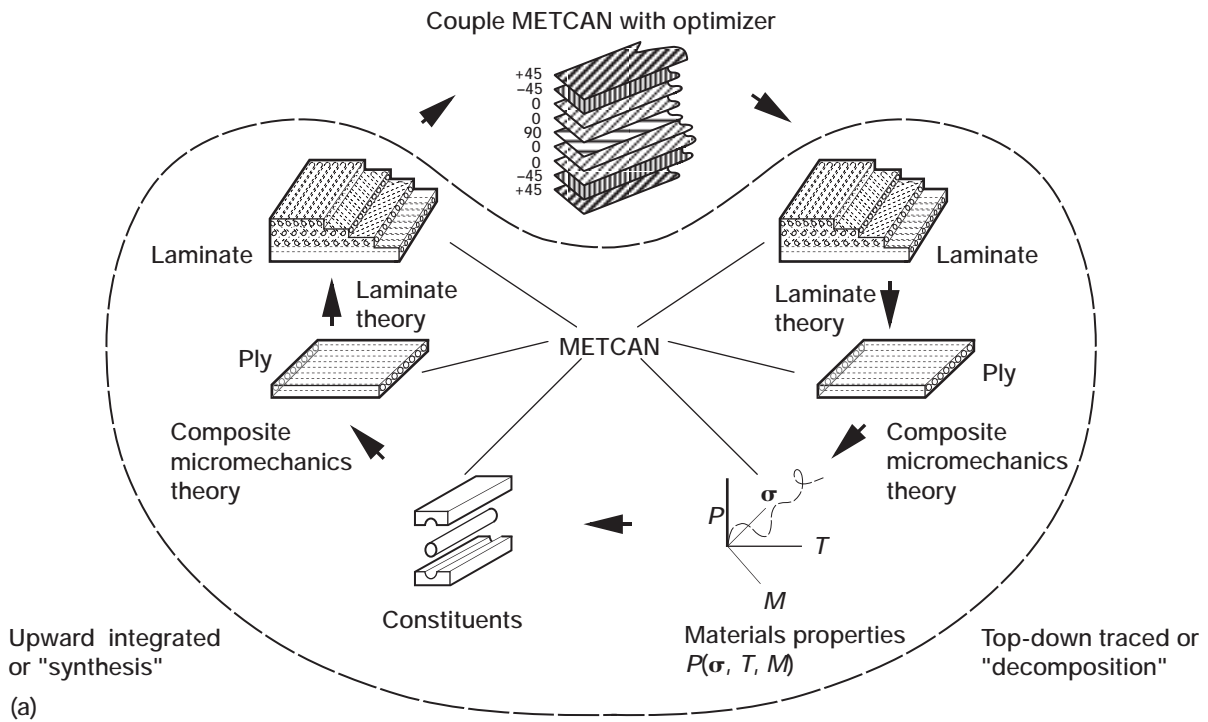
Figure 9.4—Tailoring and typical fabrication and thermomechanical cycle for metal-matrix laminate, where M denotes bending moments, N denotes in-plane load, T denotes temperature, and P denotes load. (a) Metal-matrix laminate tailoring (MMLT). (b) Typical fabrication and thermomechanical cycle of metal-matrix laminates.
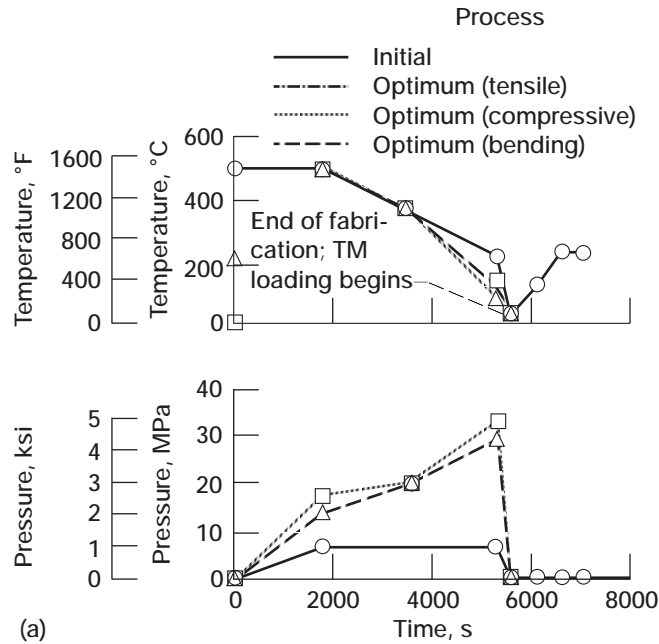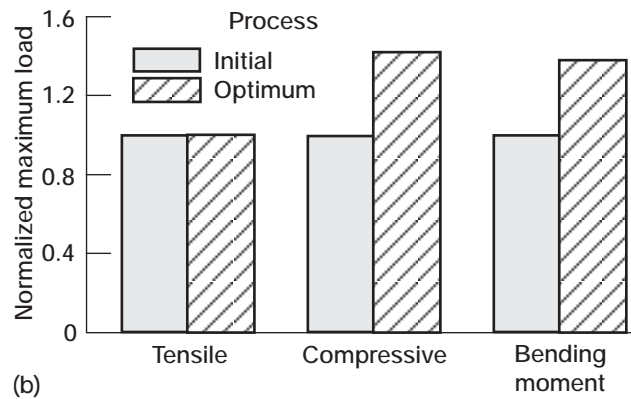
Figure 9.5.—Fabrication process and effect of fabrication optimization for P100/copper [0/90]$_s$. (a) Optimal and initial fabrication process with thermomechanical loads applied. (b) Effect of fabrication optimization on maximum in-service load.
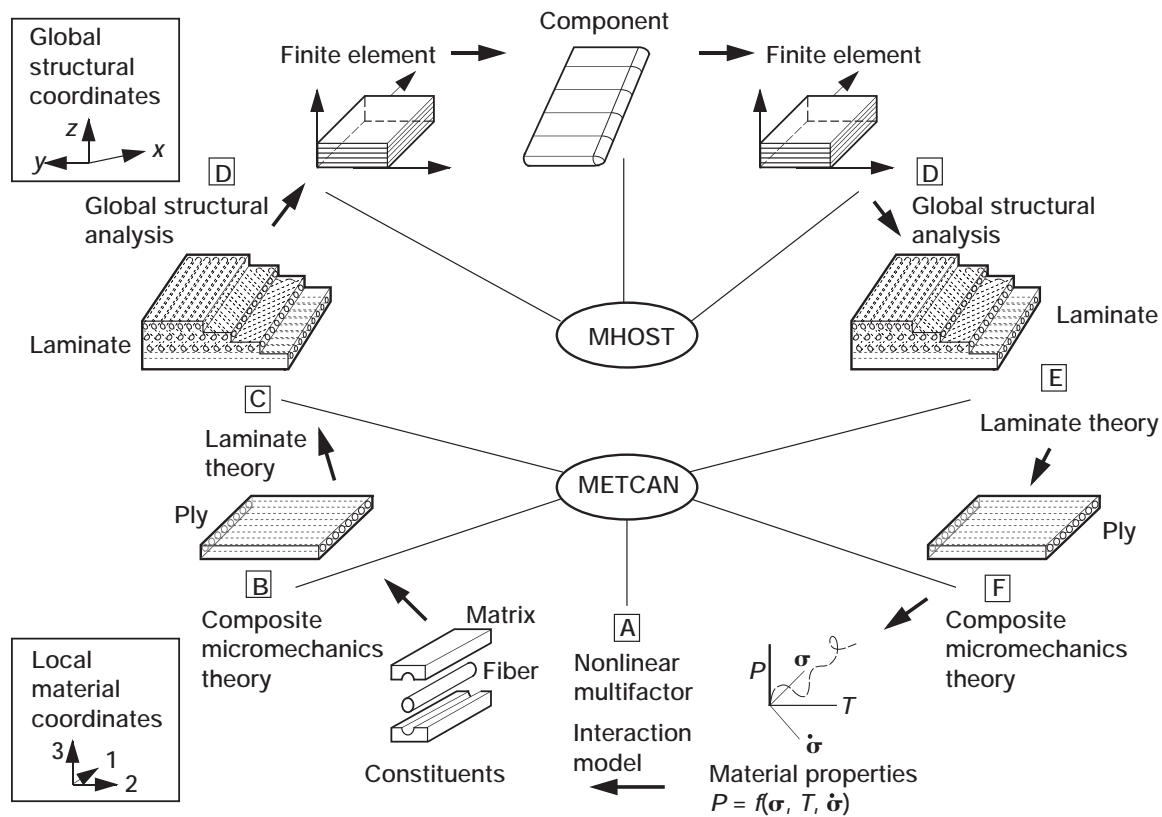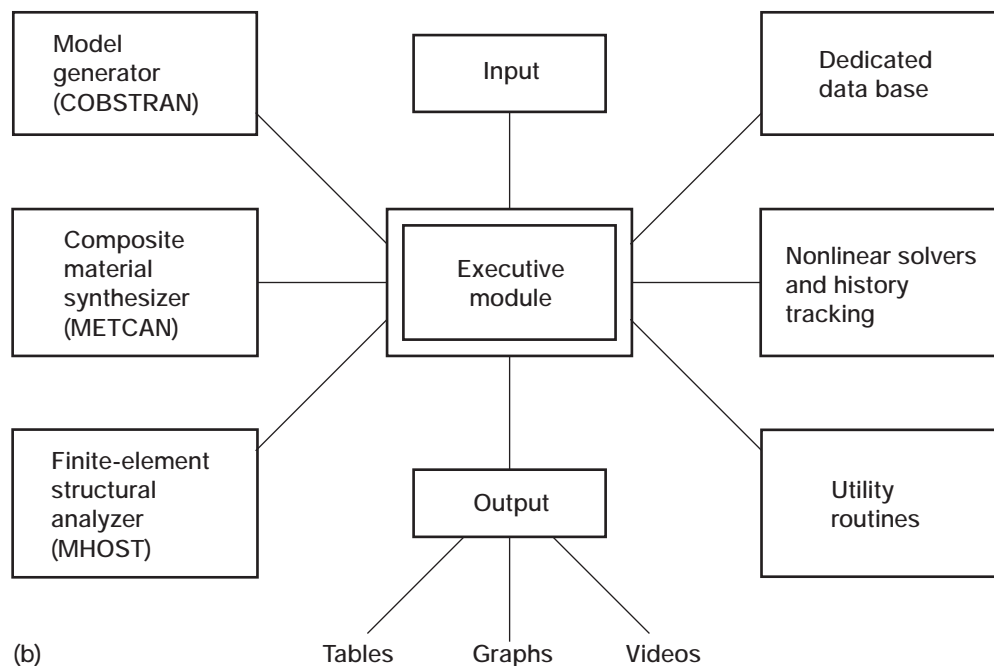
Figure 9.6—HITCAN computational simulation of hot composite structural behavior. (a) Progressive scale simulation (fabrication process to structural response), where P denotes load, T denotes temperature, σ denotes stress, and $\dot{\sigma}$ denotes stress rate. (b) Code block diagram.

TABLE 9.2.—HITCAN CAPABILITIES FOR HOT COMPOSITE STRUCTURES

| Type of analysis	Type of structure				
	Beam	Plate	Ring	Curved panel	Builtup structure
Static	Tested	Tested	Tested	Tested	Tested
Buckling[a]	Tested	Tested	Tested	Tested	Tested
Load stepping	Tested	Tested	Tested	Tested	Tested
Modal (natural vibration modes)[b]	Tested	Tested	Tested	Tested	Tested
Time domain	Not tested	Not tested	Not tested	Not tested	Not tested
Loading:					
Mechanical	Tested	Tested	Tested	Tested	Tested
Thermal	Tested	Tested	Tested	Tested	Tested
Cyclic	Not tested	Not tested	Not tested	Not tested	Not tested
Impact	Not tested	Not tested	Not tested	Not tested	Not tested
Constitutive models[c]:					
P = constant	Tested	Tested	Tested	Tested	Tested
$P = f(T)$ (temperature dependence)	Tested	Tested	Tested	Tested	Tested
$P = f(\sigma)$ (stress dependence)	Tested	Tested	Tested	Tested	Tested
$P = f(\dot{\sigma})$ (stress rate dependence)	Tested	Tested	Tested	Tested	Tested
$P = f(t)$ (creep)	Not tested	Not tested	Not tested	Not tested	Not tested
$P = f(T, \sigma, \dot{\sigma})$ (combination)	Tested	Tested	Tested	Tested	Tested
$P = f(T, \sigma, \dot{\sigma}, t)$ (creep combination)	Not tested	Not tested	Not tested	Not tested	Not tested
Fiber degradation	Tested	Tested	Tested	Tested	Tested
Fabrication-induced stresses	Tested	Tested	Tested	Tested	Tested
Ply orientations[d]	Not Tested	Not Tested	Not Tested	Not Tested	Not Tested
Arbitrary	Tested	Tested	Tested	Tested	Tested

[a]Tested one buckling mode.

[b]Tested four vibration modes.

[c]Constitutive model notation: P, material properties; T, temperature; σ, stress; $\dot{\sigma}$, stress rate; t, time.

[d]Tested three ply orientations: unsymmetric, $(0/\pm45/90)$; symmetric, $(0/45)_s$; balanced; $(0/90)_s$.
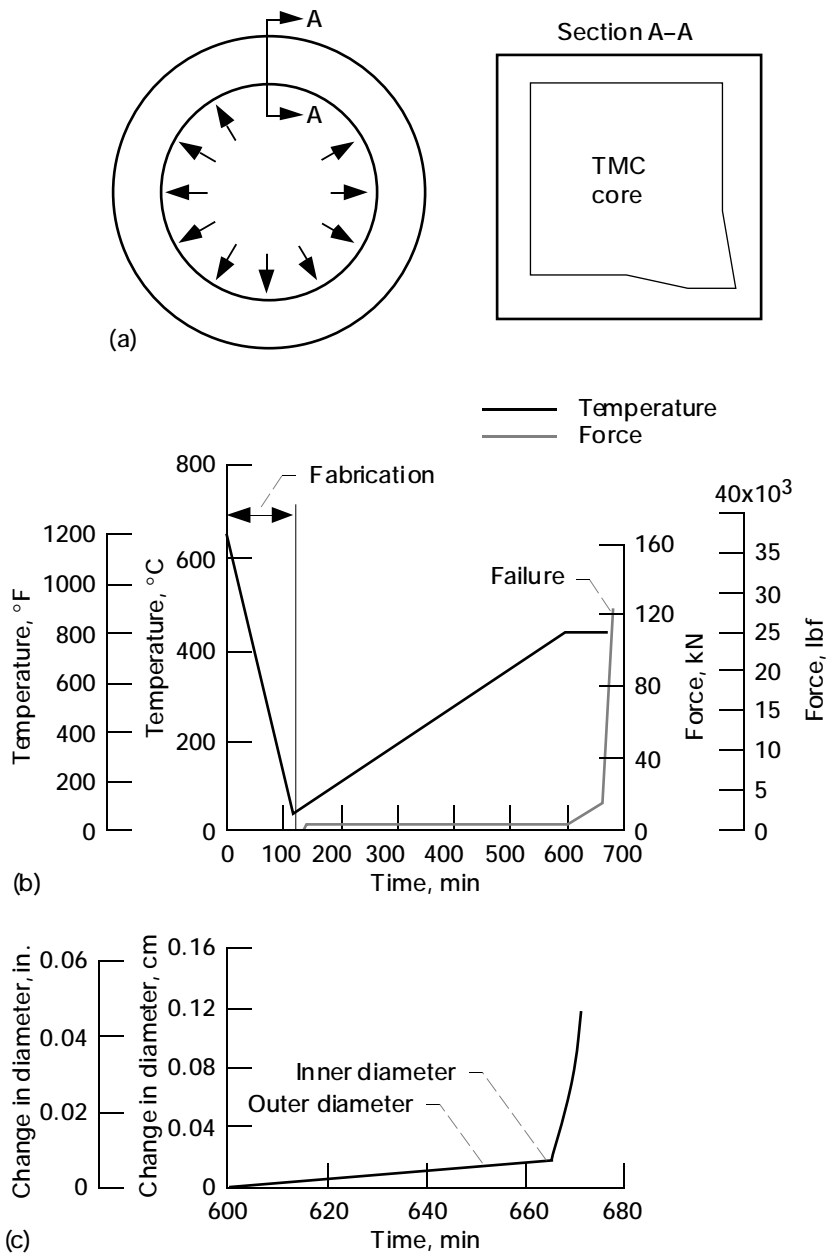
Figure 9.7.—SiC/Ti composite ring simulation using HITCAN. (a) Ring geometry and loading. (b) Loading history of ring. (c) Change in diameter of ring.

structure is shown in figure 9.6(a). HITCAN is a modular code (fig. 9.6(b)) with an executive module controlling the input, analysis modules, data bank, nonlinear solvers, utility routines, and output. HITCAN's capabilities are summarized in table 9.2. HITCAN can simulate the behavior of all types of HT–MMC structural components (beam, plate, ring, curved panel, and built-up structure) and of all types of analyses (static, buckling, vibration, and load stepping). HITCAN also accounts for degradation in material behavior from one load step to another and includes fabrication-induced stresses, fiber degradation, and interphase changes. Singhal et al. (1990) extensively described HITCAN, including a variety of sample cases to illustrate its computational capabilities.

The fabrication process cooldown, static fracture, and fatigue life responses for a ring subjected to internal pressure are included herein as specific examples. The ring overall geometry and cross section are shown in figure 9.7(a). The internal diameter was 13.599 cm (5.354 in.), the external diameter was 16.957 cm (6.676 in.), and the height was 2.078 cm (0.818 in.). The ring was made of SiC fibers and a Ti-15-3 matrix (titanium–15 wt% vanadium–3 wt% chromium–3 wt% aluminum–3 wt% tin) with 33-vol% fiber content and $[0°]_{57}$ laminate layup. The ring was subjected to a uniform temperature loading, and its internal circumferential surface was subjected to radial concentrated forces in a hydraulic rig.

The concentrated forces were applied by specially designed radial actuators to simulate uniform internal pressure. The loading history is shown in figure 9.7(b), and the ring strains in terms of change in internal and external diameter are shown in figure 9.7(c). The failure sequence (local stress exceeds corresponding strength) of the ring cross section is depicted in figure 9.8. In view of the inclusiveness of the analysis, HITCAN-predicted information can be used to minimize the number of tests during the development process and to describe post-test information on probable initiation and propagation to fracture in the prototype. For the fatigue life simulation of the ring the multifactor relationship shown in figure 9.9(a) was used. As shown in figure 9.9(b) the predicted fatigue life is a typical S/N curve. The allowable stress level S to achieve a desired number of cycles N can be estimated from the figure.

It is important to note that the HITCAN predictions of ring fracture were based on (1) calibrating only the in situ matrix behavior by using a 90°-tensile-test, room-temperature, stress-strain curve and (2) using only nominal fiber and other matrix room-temperature properties as shown in table 9.l. The specific steps consisted of selecting by "trial and success" (1) an in situ, room-temperature matrix tensile strength, (2) the exponent in the MFIM stress factor, and (3) the fabrication process to reproduce the measured 90° tensile-test, stress-strain curve to fracture.

Regions where failure does not occur

Initial failure region in Ti-15-3 at 7917 N (1780 lbf) per link (internal pressure, 14.3 MPa (2078 psi))

Failure region in Ti-15-3 at 120 541 N (27 100 lbf) per link (internal pressure, 218 MPa (31 600 psi) prior to ring fracture)

Failure region in SiC/Ti-15-3 at 120 541 N (27 100 lbf) per link (internal pressure, 218 MPa (31 600 psi) prior to ring fracture)

Figure 9.8.—Failure sequence of ring cross section.

Figure 9.9.—SiC/Ti ring fatigue life simulation using HITCAN. (a) Schematic of thermal and mechanical stress cycles. (b) Fatigue life of SiC/Ti-15-3 composite ring.

9.5 Conclusions

Three research activities pertaining to computational simulation aspects of high-temperature, metal-matrix composites (HT–MMC's) have been described. These activities have resulted in computer codes that can be used to simulate the complex behavior of hot structures made from HT–MMC's. Results from each code for select sample cases have been included to illustrate the capabilities of each code and their respective relevancy to hot structures. The results from METCAN are for the prediction of room/high-temperature strengths and stress-strain behavior for an SiC/Ti-6-4 composite. The results from the concurrent tailoring methodology are for the optimum fabrication cooldown process to achieve maximum in-service load capacity. The results from HITCAN are for static fracture (218 MPa (31 600 psi) compared to 192.5 MPa (27 900 psi) from tests) and fatigue life of an HT–MMC ring subjected to temperature and internal pressure. The predicted number of cycles is approximately 15 000 for 80-percent cyclic-stress-to-static-strength ratio.

Collectively, the results from these sample cases demonstrate that computational codes can effectively simulate the complex behavior of HT–MMC's. Verification with experimental data confirms that micromechanics-based hierarchical approaches are fundamentally sound, account for inherent attributes in the composites, require few coupon characterization tests, allow for early prototype design and fabrication, effectively assess fabrication quality, and permit identification of probable initiation and propagation to fracture in the prototype in specified loading service environments.

References

Chamis, C.C., Caruso, J.J., and Lee, H.J., 1990, "METCAN Verification Status," NASA TM–103119.

Chamis, C.C., and Hopkins, D.A., 1985, "Thermoviscoplastic Nonlinear Constitutive Relationships for Structural Analysis of High Temperature Metal Matrix Composites," NASA TM–87291.

Chamis, C.C., Murthy, P.L.N., and Hopkins, C.A., 1988, "Computational Simulation of High Temperature Metal Matrix Composites Cyclic Behavior," NASA TM–102115.

Hopkins, D.A., 1984, "Nonlinear Analysis of High-Temperature Multilayered Fiber Composite Structures Turbine Blades," NASA TM–83754.

Hopkins, D.A., and Chamis, C.C., 1985, "A Unique Set of Micromechanics Equations for High Temperature Metal Matrix Composites," NASA TM–87154.

Lerch, B.A., 1995, Private communication.

Morel, M., and Saravanos, D.A., 1990, "Concurrent Micromechanical Tailoring and Fabrication Process Optimization for Metal-Matrix Composites," NASA TM–103670.

Morel, M., and Saravanos, D.A., 1994, "Tailoring of Inelastic Metal Matrix Laminates With Simultaneous Processing Considerations," *Composites Science and Technology*, Vol. 50, pp. 109–117. (Also NASA TM–105816.)

Murthy, P.L.N., Hopkins, D.A., and Chamis, C.C., 1989, "Metal Matrix Composite Micromechanics: In-situ Behavior Influence on Composite Properties," NASA TM–102302.

Saravanos, D.A., Murthy, P.L.N., and Morel, M., 1990, "Optimal Fabrication Process for Unidirectional Metal Matrix Composites: A Computational Simulation," NASA TM–102559.

Singhal, S.N., Lackney, J.J., Chamis, C.C., and Murthy, P.L.N., 1990, "Demonstration of Capabilities of High Temperature Composite Analyzer Code HITCAN," NASA TM–102560.

Appendix—Material Data Base for NASA/P&W MMC Life Prediction Cooperative Program

Phillip W. Gravett* and Bradley A. Lerch[†]

1.0 SCS–6/Ti-15-3 MMC at 0-vol% Fiber

1.1 Test Conditions (Ref. 1)

Specimen ...	4.78-mm (0.188-in.) diameter round
Test type	isothermal
Loading	strain controlled
Temperature, °C (°F)	300 (572)

1.1.1 Tensile Properties

Modulus, GPa (Msi)	97.2 (14.1)
0.1% Yield strength, MPa (ksi)	779.1 (113)
Strength, MPa (ksi)	937.0 (135.9)
Failure strain, percent	13

*United Technologies—Pratt&Whitney Government Engines and Space Propulsion, West Palm Beach, Florida 33410.
[†]NASA Lewis Research Center, Cleveland, Ohio 44135.

1.1.2 Fatigue Properties

[R-ratio, 0.0.]

Specimen	Strainrange, percent	Life, N_f, cycles to failure
1	0.428	[a]>254 104
2	.464	[a]>161 000
3	.606	9 488
4	.850	4 274

[a]Thread failure.

Specimen	Stress range		Mean stress		Cycle	Total strainrange, percent
	MPa	ksi	MPa	ksi		
1	400	58.1	201	29.1	1	0.428
	394	57.1	197	28.6	100	.428
	380	55.1	200	29.0	127 052	.428
2	441	63.9	221	32.0	1	0.464
	418	60.6	216	31.3	100	.464
	431	62.5	216	31.3	80 500	.464
3	558	80.9	227	40.2	1	0.606
	570	82.7	261	37.8	100	.606
	570	82.7	285	41.3	4 744	.606
4	786	114	330	47.9	1	0.850
	779	113	320	46.4	100	.850
	772	112	326	47.3	2 137	.850

1.2 Test Conditions (Ref. 2)

Specimen	. . . . 4.78-mm (0.188-in.) diameter round
Test type	. . . . isothermal
Loading	. . . . strain controlled
Temperature, °C (°F)	. . . . 427 (800)

1.2.1 Tensile Properties

```
Modulus, GPa (Msi) . . . . . . . . . . . . . . . . .   83 (12)
0.2% Yield strength, MPa (ksi)  . . . . . . .   841 (122)
Strength, MPa (ksi) . . . . . . . . . . . . . . . .   883 (128)
Failure strain, percent . . . . . . . . . . . . . . . . .   20
```

1.2.2 Fatigue Properties

Specimen	R-ratio	Strainrange, percent	Life, N_f, cycles to failure
F800–1	–1.0	0.64	[b]>169 878
F800–2	–1.0	1.45	2 150
F800–3	–1.0	.98	22 971
F800–4	–1.0	1.95	1 100
F800–5	–1.0	2.75	249
F800–6	0	1.97	838
F800–7	0	.97	12 784
FRT–1[c]	–1.0	1.95	1 264

[b]Thread failure.
[c]Room temperature.

Specimen	Maximum stress		Minimum stress		Cycle	Inelastic strainrange, percent
	MPa	ksi	MPa	ksi		
F800–1	241	35.0	–236	–34.2	1	0.005
	306	44.4	–290	–42.1	84 939	.005
F800–2	525	76.1	–523	–75.8	1	0.100
	541	78.4	–557	–80.8	1 075	.045
F800–3	369	53.5	–374	–54.2	1	0.010
	427	61.9	–433	–62.8	11 458	.010
F800–4	627	90.9	–662	–96.0	1	0.380
	673	97.6	–697.7	–101.2	5 500	.300
F800–5	599	86.9	–642	–93.1	1	1.160
	651	94.4	–660	–95.7	125	1.053
F800–6	644	93.4	–549	–79.6	1	0.472
	629	91.2	–624	–90.5	419	.390
F800–7	599	86.9	–153	–22.2	1	0.008
	374	54.2	–453	–65.7	6 392	.014
FRT–1	807	117	–815	–118.2	1	0.086
	657	95.3	–676	–98.0	632	.444

1.3 Test Conditions (Ref. 1)

Specimen   . . . . 4.78-mm (0.188-in.) diameter round
Test type . . . . isothermal
Loading . . . . strain controlled
Temperature, °C (°F) 550 (1022)

1.3.1 Tensile Properties

Modulus, GPa (Msi) 75.8 (11.0)
0.1% Yield strength, MPa (ksi) 613 (89)
Strength, MPa (ksi) 670 (97.2)
Failure strain, percent 43

1.3.2 Fatigue Properties (*0.1 Hz*)

[*R*-ratio, 0.0.]

Specimen	Strainrange,[d] percent	Life, N_f, cycles to failure
1	0.578	[e]>201 793
2	.682	13 728
3	.785	16 500

[d]Mean stress approached zero.
[e]Thread failure.

Specimen	Stress range		Mean stress		Cycle	Total strainrange, percent
	MPa	ksi	MPa	ksi		
1	447	64.8	210	30.5	1	0.578
	462	67.0	56	8.1	100	.578
	476	69.0	9	1.3	100 897	.578
2	534	77.4	211	30.6	1	0.682
	542	78.6	53	7.7	100	.682
	546	79.2	17	2.5	6 864	.682
3	648	94.0	228	33.1	1	0.785
	613	88.9	52	7.5	100	.785
	607	88.0	9	1.3	8 250	.785

2.0 SCS–6/Ti-15-3 MMC at 33-vol% Fiber

2.1 Test Conditions (Ref. 3)

Specimen . . . . dogbone specimen with
6.35×25.4-mm (0.25×1.0-in.) gage section
or 6.35-mm (0.25-in.) rectangular specimen
Test type . . . . isothermal
Loading . . . . strain controlled
Temperature, °C (°F) 550 (1022)

2.1.1 Tensile Properties

Modulus		Orientation	Strength		Failure strain, percent
GPa	Msi		MPa	ksi	
190	27.6	Longitudinal	1430	207	0.86
175	25.4	Longitudinal	1344	195	.84
181	26.2	Longitudinal	1570	228	1.04
118	17.1	Transverse	410	60	1.40
123	17.8	Transverse	430	62	1.62

2.1.2 Longitudinal Fatigue Properties (0.1 Hz)

[R-ratio, 0.0.]

Specimen	Maximum stress		Life, N_f, cycles to failure
	MPa	ksi	
1	768	110	50 930
2	875	127	16 076
3	1103	160	3 375
4	1275	185	904

Specimen	Strainrange, percent	Mean strain, percent	Cycle
1	0.428	0.214	1
	.433	.220	100
	.427	.168	25 465
2	0.492	0.246	1
	.490	.252	100
	.484	.229	8 038
3	0.654	0.327	1
	.650	.329	100
	.658	.330	1 690
4	0.812	0.406	1
	.826	.463	100
	.828	.484	452

2.2 Test Conditions (Ref. 3)

Specimen	dogbone specimen with 6.35×25.4-mm (0.25×1.0-in.) gage section or 6.35-mm (0.25-in.) rectangular specimen
Test type	iso- and bi-thermal
Loading	load controlled
Temperature, °C (°F)	330 (572)

2.2.1 Tensile Properties

Modulus		Orientation	Strength		Failure strain, percent
GPa	Msi		MPa	ksi	
168	24.4	Longitudinal	1230	179	0.85
174	25.2	Longitudinal	1320	191	.85
114	16.5	Transverse	290	42	1.64

2.2.2 Longitudinal Fatigue Properties

[R-ratio, 0.0.]

Specimen	Maximum stress		Life, N_f, cycles to failure
	MPa	ksi	
1	650	95	68 299
2	758	110	13 817
3	972	141	2 810
4	1080	156	42
5	1100	159	10

Specimen	Strainrange, percent	Mean strain, percent	Cycle
1	0.398	0.199	1
	.408	.249	100
	.406	.318	34 150
2	0.470	0.235	1
	.468	.310	100
	.464	.330	6 909
3	0.552	0.276	1
	.539	.373	100
	.566	.443	1 405
4	0.626	0.313	1
	.632	.413	21
5	0.636	0.318	1
	.644	.385	5

2.2.3 Longitudinal Bithermal Fatigue Properties at 300 to 550 ℃ (572 to 1022 ℉)(See Fig. 2.2.3)

Specimen	Phasing	Maximum stress		Life, N_f, cycles to failure
		MPa	ksi	
1	IP	680	98	10 613
2	IP	761.9	110.5	5 728
3	IP	761.9	110.5	5 391
4	IP	958	139	1 615
5	IP	1068	155	299
6	OP	658	95.5	11 023
7	OP	758	110	5 867
8	OP	758	110	6 782
9	OP	841	122	4 529
10	OP	1096	159	529
11	OP	1270	184	68

Specimen	Strainrange, percent	Mean strain, percent	Cycle
1	0.374 .370 .364	0.187 .241 .291	1 100 5307
2	0.416 .410 .409	0.208 .239 .253	1 100 2864
3	0.496 .499 .488	0.248 .290 .284	1 100 2696
4	0.554 .552 .562	0.277 .316 .341	1 100 808
5	0.790 .778 .802	0.395 .489 .505	1 100 150
6	0.370 .372 .408	0.185 .192 .194	1 100 5511
7	0.426 .434 .444	0.213 .234 .297	1 100 2934
8	0.464 .468 .486	0.232 .219 .183	1 100 3391
9	0.440 .442 .454	0.220 .240 .266	1 100 2265
10	0.624 .622 .630	0.312 .317 .341	1 100 270
11	0.746 .750	0.373 .400	1 34
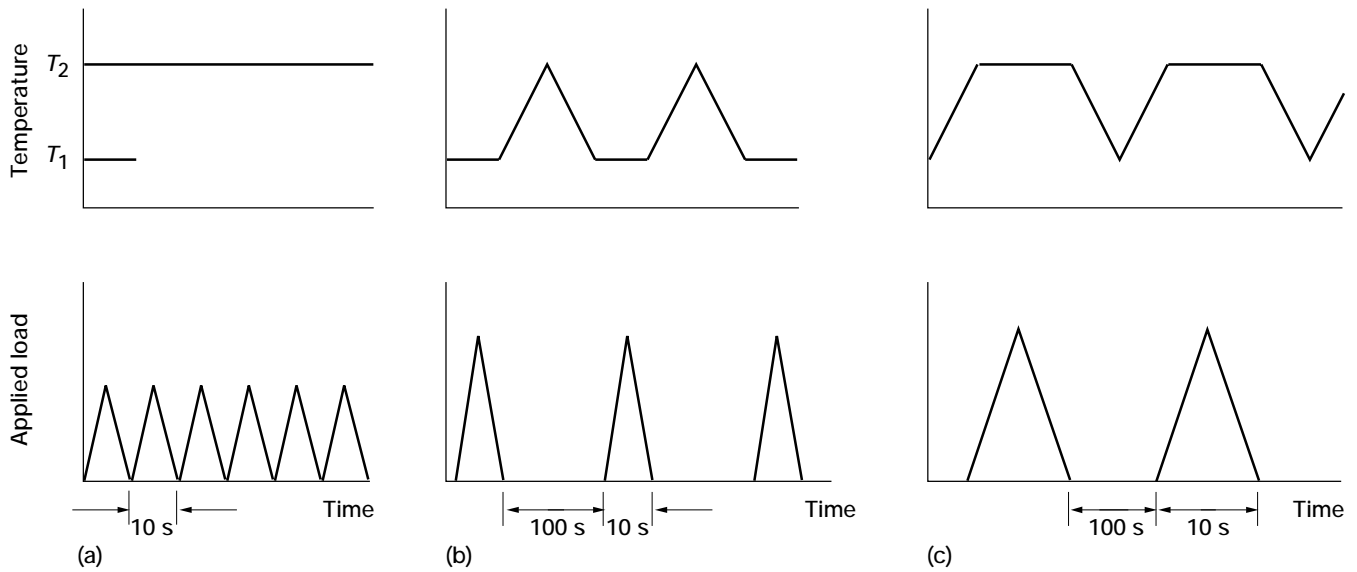
Figure 2.2.3.—TMF waveform diagrams for preceding tables. (a) Isothermal. (b) Nonisothermal and out of phase. (c) Nonisothermal and in phase.

3.0 SCS–6/Ti-15-3 MMC at 34-vol% Fiber

3.1 Test Conditions

Specimen	dogbone or rectangular specimens with 25.4×7.62-mm (1.0×3-in.) gage section
Test type	isothermal
Loading	strain controlled or tensile; load for low-cycle fatigue
Temperature, °C (°F)	21.1 (70)

3.1.1 Average Tensile Properties (Ref. 4)

Orientation, deg	Primary modulus		Secondary modulus		Strength		Failure strain, percent
	GPa	Msi	GPa	Msi	GPa	ksi	
0[f]	184±14.8	26.7±2.1	– – –	– – –	1397±103.4	202.6±15	0.90 (±0.1)
90	124	18.0	29.6	4.3	408	59.2	1.43
0/90[g]	154	22.3	111.7	16.2	1009	146.3	1.04
90/0[g]	150	22	90.0	13.0	1076	156	1.6
±30[h]	149±20	21.6±2.9	86.9	12.6	997±83.4	144.6±12.1	1.35 (±0.35)
±45[i]	117	17.0	34.0	5.0	531	77	>4.0
±60	117	17.0	21.0	3.0	393	57	1.8

[f]Average of eight specimens.
[g]Average of two specimens.
[h]Average of 14 specimens.
[i]Interrupted.

3.1.2 Fatigue Properties (Ref. 5)

Specimen	Orientation, deg	R-ratio	Initial modulus		Total strainrange,[k] percent	Maximum stress		Life, N_f, cycles to failure
			GPa	Msi		MPa	ksi	
32	0	0.05	176	25.5	0.528	981.8	142.4	9 947
35	0	.05	184	26.7	.484	913.5	132.5	18 045
38	90	.10	121	17.5	.131	174.4	25.3	35 867
45	90	.10	123	17.8	.163	209.6	30.4	9 562
B5	0/90	.05	155	22.5	.557	702.6	101.9	5 368
B1	0/90	.05	180	26.1	.540	491	71.2	17 056
B3	0/90	.05	188	27.3	.378	420	61.0	41 914
B6	0/90	.05	150	21.8	.454	350	50.8	[j]183 718
C6	90/0	.05	161	23.4	.355	419	60.7	31 935
C8	90/0	.05	– –	– –	– – –	524	76.0	10 157
C9	90/0	.05	238	34.5	.488	607	88.0	4 479
C10	90/0	.05	186	27.0	.307	365	53.0	42 293
D3	±30	.05	148	21.4	.526	683	99.0	6 232
D7	±30	.05	152	22.1	.375	469	68.0	33 288
D11	±30	.05	142	20.6	.381	552	80.0	22 477

[j]Runout.
[k]At 0.5 N_f.

3.2 Test Condition (Ref. 6)

Temperature, °C (°F) 427 (800)

3.2.1 Representative Tensile Properties at 427 °C (800 °F)

Material	Elastic modulus		0.2 % Yield strength		Ultimate tensile strength		Elongation, percent
	GPa	Msi	MPa	ksi	MPa	ksi	
[0]8	195	28.2	– – –	– – –	1510	219	0.88
[90]8	110	16.0	240	34.8	325	47.1	1.48

3.2.2 Isothermal Fatigue Data at 427 ℃ (800 ℉)

Material	Specimen	Life, N_f, cycles to failure	Maximum stress		Minimum stress		Strainrange, percent	Frequency, Hz	Control mode
			MPa	ksi	MPa	ksi			
$[0]_8^l$	Iso–1	12 352	1034	150	55	8.0	0.57	0.16	Load
	Iso–2	17 599	965	140	48	7.0	.49	.16	Load
	Iso–3	29 845	896	130	48	7.0	.48	.16	Load
		2 669	1338	194	0	0	.70	.33	Load
		3 905	1255	182	0	0	.69	.33	Load
		5 769	1110	161	0	0	.60	.33	Load
		7 207	1192	173	0	0	.59	.33	Load
		17 522	972	141	0	0	.54	.33	Load
		54 835	807	117	0	0	.44	.33	Load
$[90]_8^l$	Iso–3	1 683	172	25.0	0	0	0.31	0.33	Load
	Iso–3	3 603	137	19.9	0	0	.22	.33	Load
	Iso–3	9 863	110	16.0	0	0	.15	.33	Load
	LEI–4	166	221	32.0	0	0	.45	.83	Load
	LEI–8	1 179	172	24.9	0	0	.26	.83	Load
	LEI–2	1 340	152	22.0	0	0	.22	.83	Load
	LEI–9	8 774	138	20.0	0	0	.16	.83	Load
	LEI–3	5 265	131	19.0	0	0	.18	.83	Load
	LEI–7	23 643	110	16.0	0	0	.12	.83	Load
Ti-15-3 matrix[m]	LEI–7	100 000+	303	43.9	–290	–42.0	0.65	0.33	Strain
		22 971	428	62.1	–434	–62.9	1.00	.33	Strain
		2 150	538	78.0	–559	–81.1	1.45	.33	Strain
		100 000+	407	59.0	–393	–57.0	.87	.33	Strain
Clad $[0]_8^l$	LEI–7	25 619	483	70.1	0	0	0.41	0.33	Load
		17 027	552	80.1	0	0	.42	.33	Load
		18 314	648	94.0	0	0	.50	.33	Load
		8 783	793	115	0	0	.60	.33	Load

[l]Strainrange values taken at 0.5 N_f.
[m]Maximum and minimum stress values taken at 0.5 N_f.

3.2.3 Thermomechanical Fatigue Data (Ref. 6)

[TMF for $[0]_9$ at 93 to 538 °C (200 to 1000 °F); frequency, 5.6×10^{-3} Hz; minimum stress, 0 MPa; load control.]

Specimen	Phasing	Life, N_f, cycles to failure	Maximum stress	
			MPa	ksi
TMF–4	IP	1.5	1034	150
TMF–5	IP	1.5	1034	150
TMF–11	IP	77	965	140
TMF–12	IP	150	965	140
TMF–9	IP	1 072	896	130
TMF–14	IP	1 870	896	130
TMF–18	IP	1 171	827	120
TMF–19	IP	1 595	827	120
TMF–22	IP	25 820	690	100
TMF–6	OP	801	1241	180
TMF–15	OP	1 540	1241	180
TMF–7	OP	1 178	1034	150
TMF–16	OP	1 919	1034	150
TMF–13	OP	2 954	896	130
TMF–10	OP	3 630	896	130
TMF–21	OP	4 333	827	120
TMF–20	OP	4 916	827	120
TMF–23	OP	7 145	690	100
TMF–24	OP	9 793	621	90

[TMF for $[0]_8$ at 200 to 427 °C (400 to 800 °F); frequency, 8.3×10^{-3} Hz; minimum stress, 0 MPa; load control.]

Specimen	Phasing	Life, N_f, cycles to failure	Maximum stress	
			MPa	ksi
LE2–8	IP	149	280	40.6
LE2–5	IP	354	220	32.0
LE2–3	IP	1 455	180	26.1
LE1–11	IP	1 617	150	21.8
LE1–12	IP	3 440	140	20.3
LE1–10	IP	15 938	130	18.9
LE2–13	OP	1 013	280	40.6
LE2–4	OP	1 585	250	36.3
LE2–2	OP	3 435	220	32.0
LE2–1	OP	20 938	150	21.8

3.3 Test Conditions (Ref. 7)

Specimen	dogbone or rectangular specimens with 25.4×6.35-mm (1.0×0.25-in.) gage section
Test type	iso- and bi-thermal
Loading	load controlled
Temperature, °C (°F)	427 (800)

3.3.1 Tensile Properties

Modulus, GPa (Msi)	196 (28.4)
Orientation	Longitudinal
Strength, MPa (ksi)	1517 (220)
Failure strain, percent	0.88

3.3.2 Longitudinal Fatigue Properties (0.33 Hz)

[R-ratio, 0.0.]

Specimen	Initial modulus		Cycle	Total strainrange, percent	Maximum stress		Life, N_f, cycles to failure
	GPa	Msi			MPa	ksi	
1	193	28.0	1 250	0.70	1338	194	2 669
2	182	26.4	2 000	.69	1255	182	3 905
3	185	26.8	2 500	.60	1110	161	5 769
4	202	29.3	2 250	.59	1193	173	7 207
5	183	26.5	8 290	.54	972	141	17 522
6	183	26.4	25 000	.44	807	117	54 835

3.3.3 Longitudinal Bithermal Fatigue Properties at 100 to 427 ℃ (212 to 800 ℉)(See Fig. 3.3.3)

Specimen	Maximum stress		Life, N_f, cycles to failure	Initial modulus		Cycle	Total strainrange, percent
	MPa	ksi		GPa	Msi		
1	958	139	7609	181	26.2	4000	0.53
2	951	138	9473	194	28.1	5330	.49

[R-ratio, 0.0; load type, IP.]
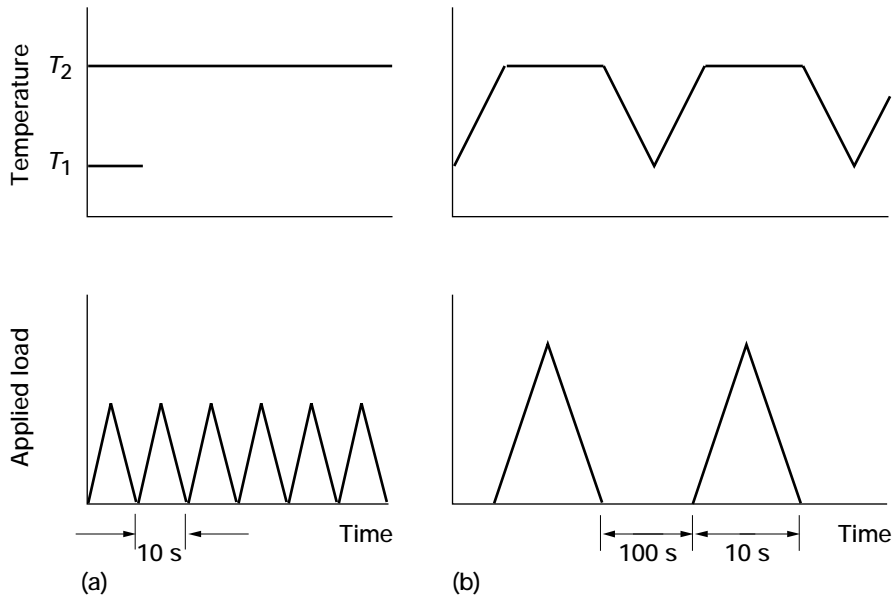


Figure 3.3.3.—TMF waveform diagrams for above table. (a) Isothermal. (b) Nonisothermal and in phase.

3.3.4 Transverse Tensile Properties at 427 ℃ (800 ℉)

Modulus, GPa (Msi) . . . . 111(16.1)
0.1% Yield strength, MPa (ksi) . . . . 221(32)
Strength, MPa (ksi) 324 (47)
Failure strain, percent 1.48

3.3.5 Transverse Fatigue Properties

[R-ratio, 0.0.]

Specimen	Maximum stress		Life, N_f, cycles to failure	Cycle	Total strainrange,[n] percent
	MPa	ksi			
1	172	25	1683	800	0.31
2	138	20	3603	1500	.22
3	103	15	9863	5250	.15

[n]Significant change in strainrange occurred as test progressed.

3.3.6 Transverse Bithermal Fatigue Properties 100 to 427 °C (212 to 800 °F) (See Fig. 3.3.6)

[R-ratio, 0.0; load type, IP; maximum stress, 138 MPa (20 ksi).]

| Specimen	Life, N_f, cycles to failure	Cycle	Total strainrange, percent
1	1258	640	0.24
2	1928	1000	.26
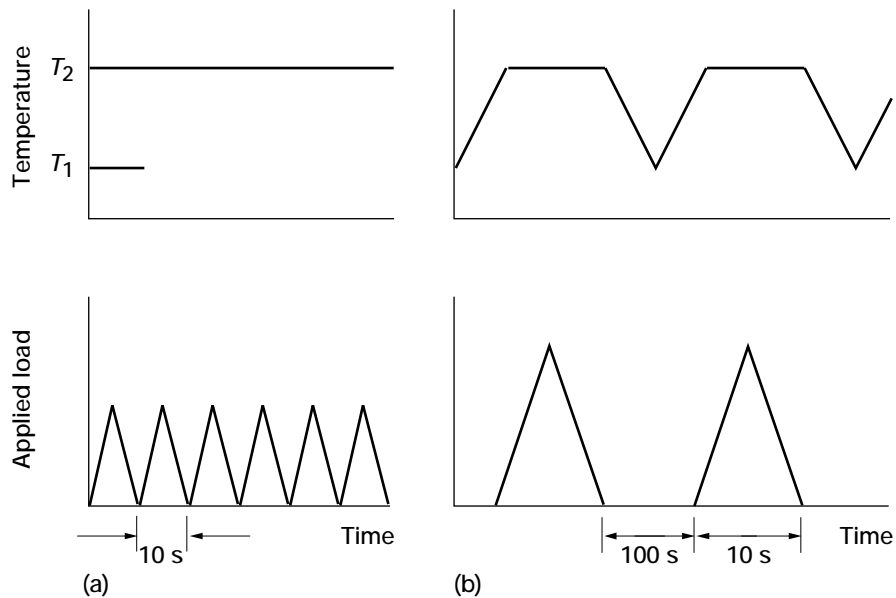
Figure 3.3.6.—TMF waveform diagrams for above table. (a) Isothermal. (b) Nonisothermal and in phase.

3.4 Test Conditions (Ref. 8)

Specimen	specimen with 152.4-mm (6.0-in.) tangent radius
Test type	isothermal LCF
Loading	load controlled
Temperature, °C (°F)	427 (800)

3.4.1 Longitudinal Tensile Properties

Test temperature, °C (°F)	427 (800)
Modulus, GPa (Msi)	185 (26.9)
Strength, MPa (ksi)	1422 (206.2)
Failure strain, percent	0.81

3.4.2 Longitudinal Fatigue Properties

Specimen	Load type	R-ratio	Maximum stress MPa	Maximum stress ksi	Life, N_f, cycles to failure
1	[o]LCF	0.1	965	140	17 274
3	LCF	.1	1103	160	7 541
5	LCF	.5	1241	180	8 772
6	LCF	.5	1103	160	13 612
7	LCF	.5	1103	160	9516
8	LCF	.5	1103	160	8 294
9	Mission	(p)	1103	160	[q]1 043

[o]SPATE, an optical stress/strain detection device based on the Lord Kelvin thermoelastic coupling effect.
[p]One mission cycle equals one cycle at an R-ratio of 0.1 plus seven cycles at an R-ratio of 0.5.
[q]Number of mission cycles.

Specimen	Initial modulus		Cycle	Total strainrange, percent
	GPa	Msi		
1	181.4	26.31	0	– – – –
	181.7	26.36	2	0.456
	166.2	24.10	8 891	.544
	155.0	22.48	13 500	.543
3	155.3	22.53	0	– – – –
	151.9	22.03	5	0.653
	153.9	22.32	3 381	.638
	150.5	21.83	6 757	.644
5	161.8	23.47	0	– – – –
	154.0	22.34	15	0.394
	152.6	22.14	4 586	.400
	156.8	22.74	8 254	.400
6	157.4	22.83	0	– – – –
	156.1	22.64	8	0.343
	157.4	22.83	6 817	.343
	146.2	21.20	12 554	.359
7	155.8	22.59	0	– – – –
	158.3	22.96	5	0.350
	150.6	21.84	4 448	.366
	146.7	21.27	8 207	.369
8	167.4	24.28	0	– – – –
	161.8	23.47	5	0.344

3.5 Test Conditions (Ref. 4)

Specimen	dogbone specimen with 25.4×7.62-mm (1.0×0.3-in.) gage section
Test type	isothermal LCF
Loading	strain controlled
Temperature, °C (°F)	427 (800)

3.5.1 Average Tensile Properties

Orientation, deg	Primary modulus		Secondary modulus		Strength		Failure strain, percent
	GPa	Msi	GPa	Msi	MPa	ksi	
0	200	29	– –	– –	1379	200	0.83
90	117	17	28	4	283	41	.85
±45	97	14	– –	– –	469	68	7.30
±60	97	14	21	3	331	48	2.95

3.6 Test Conditions (Ref. 5)

Specimen	dogbone specimen with 25.4×7.62-mm (1.0×0.3-in.) gage section
Test type	isothermal LCF
Loading	strain controlled
Temperature, °C (°F)	427 (800)

3.6.1 Fatigue Properties

Specimen	Orientation, deg	Maximum stress		Life, N_f, cycles to failure	Initial modulus		Total strainrange,[r] percent
		MPa	ksi		GPa	Msi	
36	0	914.9	132.7	17 519	193	28.0	0.459
37	0	837.7	121.5	32 804	183	26.5	.438
34[s]	0	834.3	121	139 581	185	26.8	.420
31	0	834.3	121	[t]104 000	163	23.6	.430
A3	±45	234	34	16 857	134	19.4	.332
A4	±45	228	33	14 062	117	17.0	.362
A5	±45	221	32	20 866	88.3	12.8	.288
A7	±45	269	39	6 276	80.7	11.7	.450
A8	±45	214	31	90 709	91.7	13.3	.220
A9	±45	331	48	1 954	107	15.5	.600
A14	±45	228	33	47 213	105	15.2	.400

[r]Runout.
[s]Tested in vacuum.
[t]At 0.5 N_f.

4.0 SCS–6/Ti-15-3 MMC at 35-vol% Fiber

4.1 Test Conditions (Ref. 9)

Specimen	dogbone specimen with 7.95-mm (0.313-in.) gage section
Test type	isothermal
Loading	load controlled
Temperature, °C (°F)	427 (800)

4.1.1 Longitudinal Fatigue Properties

[*R*-ratio, 0.0.]

Maximum stress		Life, N_f, cycles to failure
MPa	ksi	
1103	160	[u]4 600
1034	150	[u]9 606
1034	150	[u]10 000
965	140	[u]29 432
896	130	[u]40 794

[u]Failure in radius of dogbone.

5.0 SCS–6/Ti-15-3 MMC at 38-vol % Fiber

5.1 Test Conditions (Ref. 10)

Specimen . . . . 12.7×215.9-mm (0.5×8.5-in.) straight-sided specimen with Ti doublers
Test type . . . . isothermal
Loading . . . . load controlled
Temperature, °C (°F) 21.1 (70)

5.1.1 Longitudinal Tensile Properties

[Insufficient yielding to determine 0.1% yield.]

Modulus		Strength		Failure strain, percent
GPa	Msi	MPa	ksi	
207	30.0	1868	271	0.806
244	34.5	1902	276	[v].880
232	33.6	1758	255	.844

[v]Broke at doubler edge.

5.2 Test Conditions (Ref. 8)

Specimen . . . . . dogbone specimen with 7.95-mm (0.313-in.) gage section
Test type . . . . thermomechanical
Loading . . . . load controlled
Temperature, °C (°F) 427 (800)

5.2.1 Longitudinal Thermomechanical Fatigue Properties at 93.3 to 538 °C (200 to 1000 °F)

[R-ratio, 0.05.]

Specimen	Phasing	Maximum stress		Life, N_f, cycles to failure
		MPa	ksi	
4	OP	1241	180	1156
2	OP	1034, 1241	150, 180	[w]1385+394
3	IP	1034	150	615
16	IP	1034	150	7

[w]Load was increased to 1241 MPa (180 ksi) after 1385 cycles.

Specimen	Initial modulus		Secondary modulus		Cycle	Total strainrange, percent
	GPa	Msi	GPa	Msi		
4	208	30.1	– – –	– – –	4	0.568
	217	31.5	– – –	– – –	191	.542
	203	29.5	– – –	– – –	597	.579
2	219	31.8	– – –	– – –	6	0.448
	221	32.0	– – –	– – –	94	.446
	222	32.2	– – –	– – –	677	.442
	152	22.0	227	32.9	1387	.728
	139	20.1	230	33.3	1470	.730
3	215	31.2	– – –	– – –	3	0.457
	214	31.0	– – –	– – –	4	.460
	208	30.2	– – –	– – –	257	.478
16	185	26.9	– – –	– – –	3	0.529
	186	27.0	– – –	– – –	6	.528

5.3 Test Conditions (Ref. 10)

Specimen . . . . 12.7×215.9-mm (0.5×8.5-in.)
          straight-sided specimen with Ti doublers
Test type . . . . isothermal
Loading . . . . .load controlled
Temperature, °C (°F) 21.1 (70)

5.3.1 Longitudinal Tensile Properties

[Insufficient yielding to determine 0.1% yield strength.]

Test temperature		Modulus		Strength		Failure strain, percent
°C	°F	GPa	Msi	MPa	ksi	
21.1	70	206	30.0	1868	271	0.806
		244	35.4	1903	276	[x].880
		232	33.6	1758	255	.844
427	800	240	34.8	1820	264	0.915
		222	32.2	1448	210	.706
		214	31.1	1489	216	.735

[x]Broke at doubler edge.

5.3.2 Longitudinal Fatigue Properties

Specimen	R-ratio	Maximum stress		Life, N_f, cycles to failure
		MPa	ksi	
10L	0.1	1310	190	[y]4 711
8L	.1	1241	180	7 385
9L	.1	1103	160	23 278
11L	.1	965	140	[y]48 118
13L	.5	1379	200	9 767
12L	.5	1241	180	51 077

[y]Broke at doubler edge.

Specimen	Initial modulus		Secondary modulus		Cycle	Total strainrange, percent
	GPa	Msi	GPa	Msi		
10L	212	30.7	212	30.7	1	0.560
	212	30.8	206	29.9	5	.562
	213	30.9	207	30.0	1 000	.570
	213	31.0	203	29.5	5 000	.570
8L	215	31.2	209	30.3	1	0.529
	213	30.9	208	30.2	5	.530
	209	30.3	209	30.3	1 000	.535
9L	227	32.9	205	29.8	5	0.465
	210	30.4	210	30.4	1 000	.470
	222	32.2	209	30.3	13 100	.465
11L	202	29.4	203	29.4	1	0.435
	205	29.7	205	29.7	5	.435
	204	29.6	204	29.6	1 000	.435
	219	31.8	205	29.8	25 600	.430
13L	210	30.5	210	30.5	1	0.340
	209	30.3	206	29.9	5	.340
	214	31.0	208	30.2	1 300	.340
	213	30.9	201	29.1	3 300	.340
12L	217	31.5	217	31.5	1	0.290
	216	31.4	216	31.4	5	.290
	216	31.4	216	31.4	1 500	.290
	219	31.8	213	30.9	32 500	.290

6.0 SCS–6/Ti-15-3 MMC at 40-vol % Fiber

6.1 Test Conditions (Ref. 10)

Specimen . . . . 12.7×140-mm (0.5×5.5-in.)
straight-sided specimen with Ti doublers
Test type . . . . isothermal
Loading . . . . load controlled
Temperature, °C (°F) 21.1 (70)

6.1.1 Transverse Tensile Properties

Modulus		0.1% Yield strength		Strength		Failure strain, percent
GPa	Msi	MPa	ksi	MPa	ksi	
178	25.8	248	36.0	254	36.9	0.252
121	17.5	231	33.5	254	36.9	.402
125	18.1	234	33.9	268	38.9	.466

6.2 Test Conditions (Ref. 10)

```
Specimen  . . . . . . . . . . . 12.7×140-mm (0.5×5.5-in.)
              straight-sided specimen with Ti doublers
Test type  . . . . . . . . . . . . . . . . . . . . . . . . . isothermal
Loading  . . . . . . . . . . . . . . . . . . . . . . load controlled
Temperature, °C (°F)  . . . . . . . . . . . . . . . 427 (800)
```

6.2.1 Transverse Tensile Properties

Modulus		0.1% Yield strength		Strength		Failure strain, percent
GPa	Msi	MPa	ksi	MPa	ksi	
138	20.0	139	20.1	216	31.4	0.731
110	15.9	147	21.3	213	30.9	.658
130	18.9	144	20.9	221	32.1	.745

6.2.2 Transverse Fatigue Properties

Specimen	R-ratio	Maximum stress		Life, N_f, cycles to failure
		MPa	ksi	
8T	0.1	172	25	[z]1 054
13T	.1	172	25	203
9T	.1	138	20	427
10T	.1	138	20	489
11T	.1	103	15	24 834
12T	.5	138	20	1 575
14T	.5	103	15	69 251

[z]No strain data due to strain gage failure.

Specimen	Initial modulus		Secondary modulus		Cycle	Total strainrange, percent
	GPa	Msi	GPa	Msi		
10L	212	30.7	212	30.7	1	0.560
13T	102	14.8	64.8	9.4	1	0.220
	98.6	14.3	56.5	8.2	5	.250
	71.7	10.4	44.8	6.5	105	.320
9T	104	15.1	90.3	13.1	1	0.128
	101	14.7	76.5	11.1	5	.150
	89.6	13.0	60	8.7	100	.180
10T	98.6	14.3	98.6	14.3	1	0.130
	101	14.6	91.7	13.3	5	.135
	101	14.7	64.8	9.4	100	.170
11T	130	18.8	130	18.8	1	0.072
	127	18.4	127	18.4	5	.072
	125	18.2	125	18.2	810	.075
	132	19.1	119	17.3	9 300	.075
	127	18.4	110	15.9	23 900	.078
12T	120	17.4	120	17.4	1	0.060
	123	17.8	123	17.8	5	.058
	129	18.7	129	18.7	1 000	.062
14T	123	17.8	123	17.8	1	0.042
	120	17.4	120	17.4	5	.042
	118	17.1	118	17.1	1 000	.044
	114	16.5	114	16.5	24 460	.044
	106	15.4	106	15.4	54 135	.050
7T	107	15.5	97.9	14.2	1	0.095
	105	15.2	91.0	13.2	5	.097
	100	14.5	85.5	12.4	1 000	.100
	97.2	14.1	82.7	12.0	4 400	[aa].105

[aa]Premature failure due to power outage. Test conditions same as 11T.

7.0 SCS–6/Ti-15-3 MMC at 32- to 35-vol% Fiber

7.1 Test Conditions (Ref. 11)

Specimen	dogbone
Test type	isothermal creep
Loading	constant load
Temperature, °C (°F)	538 (1000)

7.1.1 Longitudinal Creep Testing

[R-ratio, 0.0.]

Specimen	Maximum stress		Life, N_f, hr
	MPa	ksi	
10	1103	160	2.5
11	965	140	>310
9	827	120	>323

References

1. Gayda, J., Gabb, T.P., and Freed, A.D., 1989, "The Isothermal Fatigue Behavior of a Unidirectional SiC/Ti Composite and the Ti Alloy Matrix," NASA TM–101984.
2. Gabb, T.P., Gayda, J., and Halford, G., NASA Lewis Research Center, Private communication to R. E. deLaneuville.
3. Gabb, T.P., Gayda, J., and MacKay, R.A., 1996, "Isothermal and Nonisothermal Fatigue Behavior of a Metal Matrix Composite," Submitted to Journal of Composites.
4. Lerch, B.A., and Saltsman, J.F., 1993, "Tensile Deformation of SiC/Ti-15-3 Laminates," ASTM STP–1156, pp. 161–175.
5. Lerch, B.A., 1990, "Fatigue Behavior of SiC/Ti-15-3 Laminates," *HiTEMP Review 1990*: *Advanced High-Temperature Engine Materials Technology Program,* NASA CP–10051, 1990, pp. 35–1 to 35–9.
6. Castelli, M.G. and Gayda, J., 1993, "An Overview of Elevated Temperature Damage Mechanisms and Fatigue Behavior of a Unidirectional SCS–6/Ti-15-3 Composite," *Reliability, Stress Analysis, and Failure Prevention,* R.J. Schaller, ed., DE–Vol. 55, American Society of Mechanical Engineers, New York, pp. 213–221.
7. Gayda, J., NASA Lewis Research Center, Private communication, Feb. 1990.
8. Heine, J., P&W Materials Laboratory South, Private communication.
9. Ervin, D., P&W Materials Laboratory South, Private communication.
10. Nardone, V.C., 1989, Private communication to R.E. deLaneuville.
11. Tosi, K., P&W Materials Laboratory South, Private communication.

REPORT DOCUMENTATION PAGE

Public reporting burden for this collection of information is estimated to average 1 hour per response, including the time for reviewing instructions, searching existing data sources, gathering and maintaining the data needed, and completing and reviewing the collection of information. Send comments regarding this burden estimate or any other aspect of this collection of information, including suggestions for reducing this burden, to Washington Headquarters Services, Directorate for Information Operations and Reports, 1215 Jefferson Davis Highway, Suite 1204, Arlington, VA 22202-4302, and to the Office of Management and Budget, Paperwork Reduction Project (0704-0188), Washington, DC 20503.

1. AGENCY USE ONLY (Leave blank)	2. REPORT DATE	3. REPORT TYPE AND DATES COVERED
	November 1996	Reference Publication

4. TITLE AND SUBTITLE

MMC Life System Development (Phase I)—A NASA/Pratt & Whitney Life Prediction Cooperative Program

5. FUNDING NUMBERS

WU–505–63–5B

6. AUTHOR(S)

Erwin V. Zaretsky, editor

7. PERFORMING ORGANIZATION NAME(S) AND ADDRESS(ES)

National Aeronautics and Space Administration
Lewis Research Center
Cleveland, Ohio 44135–3191

8. PERFORMING ORGANIZATION REPORT NUMBER

E–9479

9. SPONSORING/MONITORING AGENCY NAME(S) AND ADDRESS(ES)

National Aeronautics and Space Administration
Washington, DC 20546–0001

10. SPONSORING/MONITORING AGENCY REPORT NUMBER

NASA RP–1361

11. SUPPLEMENTARY NOTES

Responsible person, Erwin V. Zaretsky, organization code 5200, (216) 433–3241.

12a. DISTRIBUTION/AVAILABILITY STATEMENT

Unclassified - Unlimited
Subject Category 24

This publication is available from the NASA Center for Aerospace Information, (301) 621–0390.

12b. DISTRIBUTION CODE

13. ABSTRACT (Maximum 200 words)

Metal-matrix composites (MMC's), typically consisting of a titanium alloy matrix and ceramic reinforcement, are generally held as leading candidate materials for tomorrow's aircraft engines. Recognizing this, NASA Lewis Research Center and Pratt & Whitney Division of United Technologies Inc. entered into a four-year cooperative effort, hoping to lay the foundations of knowledge that will make these materials more reliable and ultimately less exotic. The four-year study, which began in January 1988, had several objectives: assessing life and fracture prediction methods; determining the actual fracture strength and lives of 6-in.-diameter MMC rings made from a titanium alloy designated SiC (SCS–6)/Ti-15V-3Cr-3Al-3Sn; and evaluating different means of nondestructive evaluation (NDE). Chosen for its extensive data base, this material represents the MMC's that would be used in an aircraft engine but is not the specific grade. Five separate fracture and life prediction analysis methods were applied and compared with each other and with fracture data of the rings. Manufacturing defects inherent in the rings prevented the researchers from conducting planned cyclic tests. Fatigue predictions ranged from 1000 to 15 000 cycles. Fracture predictions were less scattered, ranging from 25 to 40.1 ksi. Low-resolution x-ray computed tomography proved an effective NDE evaluation tool. The result of the various studies together with a material data base, are presented.

14. SUBJECT TERMS

Life prediction; Metal-matrix composites; Fracture; Reliability; SCS–6/Ti–15–3; Composite materials

15. NUMBER OF PAGES
144

16. PRICE CODE
A07

17. SECURITY CLASSIFICATION OF REPORT	18. SECURITY CLASSIFICATION OF THIS PAGE	19. SECURITY CLASSIFICATION OF ABSTRACT	20. LIMITATION OF ABSTRACT
Unclassified	Unclassified	Unclassified	